Jet-Quenching Signatures from Very High-p_{T} Dihadron Correlations in Pb+Pb Collisions at $\sqrt{s_{NN}} = 2.76$ TeV with the CMS Detector

By

RYLAN TOWNE CONWAY

B.S. (University of Delaware) 2009
M.S. (University of California, Davis) 2010

DISSERTATION

Submitted in partial satisfaction of the requirements for the degree of

DOCTOR OF PHILOSOPHY

in

Physics

in the

OFFICE OF GRADUATE STUDIES

of the

UNIVERSITY OF CALIFORNIA

DAVIS

Approved:

Prof. Daniel Cebra

Prof. Manuel Calderón de la Barca Sánchez

Prof. Ramona Vogt

2015

Rylan Towne Conway
June 2015
Physics

Jet-Quenching Signatures from Very High-p_{T} Dihadron Correlations in Pb+Pb Collisions at $\sqrt{s_{NN}} = 2.76$ TeV with the CMS Detector

Abstract

Experimental measurements from dihadron correlations triggered with very high-p_{T} particles in Pb+Pb collisions at 2.76 TeV are shown. The data set was collected by the Compact Muon Solenoid (CMS) detector at the Large Hadron Collider (LHC) and corresponds to an integrated luminosity of 150 μb^{-1}. The use of high-p_{T} track triggers made it possible to study dihadron correlations correlations up to $p_{\mathrm{T}} \sim 50$ GeV/c. The presence of azimuthal anisotropies of final state particles in non-central Pb+Pb collisions gives rise to single-particle correlations that are characterized by the Fourier harmonics, v_n. To isolate the jet components of the correlations, the v_2-v_4 components are subtracted from the correlations and the per-trigger-particle associated-yields on the near and away side are studied. The data are compared to correlations from $p+p$ collisions at the same center-of-mass energy over a wide range of trigger and associated-particle p_{T} and as a function of Pb+Pb event centrality. On the near-side there is evidence of moderate enhancement at low $p_{\mathrm{T}}^{\mathrm{assc}}$. On the away side there is a significant enhancement at $p_{\mathrm{T}}^{\mathrm{assc}} \sim 0.5$ GeV/c and at higher transverse momentum, $p_{\mathrm{T}}^{\mathrm{assc}} > 3$ GeV/c, there is a suppression of about 50% compared to $p+p$ collisions.

To my Father,

Who always let me know how proud he was,

I wish you could be here to read these words.

Acknowledgments

This dissertation, which is the culmination of my long academic journey, would not have been possible without the love and support of my family, friends, and teachers. During this time I have met and been influenced by a number of amazing people, many of whom I am fortunate enough to call my friend. It is not possible to thank each and every one of you and for this I am sorry. Nonetheless, I would like to thank a few select individuals who helped to make the last five years so memorable.

First and foremost I would like to thank Dan and Manuel for their guidance and wisdom, I can't imagine having two better advisors and mentors. You both taught me what it means to be a scientist and how to approach a problem from a fundamental and unbiased perspective. The friendly environment and cohesiveness you fostered in our research group made it a pleasure to come in to work everyday. Finally, I thank you both for your friendship. Most graduate students don't get to consider their advisor(s) among their friends and for this I am most grateful. I would also like to thank Wei for becoming my de facto advisor in CMS. The majority of the work presented here would not have been possible without your guidance and assistance.

I would like to thank the rest of the Nuclear Physics Group at UC Davis: Evan, for being my partner in crime and many intellectual pursuits, grad school would not have been half as fun or intellectually stimulating without you; Michael, for being my CMS compadre, without your easy going and cheerful demeanor the office would have been a gloomier place; Tony, for all the good times we've had in Davis, the Bay, Cagliari, and D.C.; Jorge, for helping me transition into CMS and for the good times on the roof of the CMS Center; Guillermo, for some interesting nights in Geneva; Rosi, for the many beers and good conversations shared late into the night; Chris, for being a great office mate and meat connoisseur; and finally Chad, for making me feel like I actually know what I'm doing in CMS and for being a great guy to hang out with in general.

I'd also like to thank some of my many good friends from Davis: Kevin, for taking ordinary situations to the next level and constantly making me aware of how much I still don't know about physics (*finger-wiggle-thingy* q.e.d.); Andrew, for sharing my love of the outdoors and music and for the many adventures we've shared (and will share) together; Marius and Ian, for all the great times skiing despite the lackluster winters these past few years; Will, for introducing me to the world of climbing and for all the great trips we went on together; and finally to Bret, Kent, Westy, and McC for all the good times on Duke Drive and elsewhere.

To my family, thank you for always being there for me. Mom, you made me who I am today and I can never thank you enough for everything you've done for me. Dad, thank you for passing on to me your love of nature and the desire to understand how it all works; I don't think I would be here without your early encouragement to pursue physics. To my siblings and sister-in-laws - Bily, Nicole, Sean, Devon, and Amy - thank you for keeping me grounded and for always being there for me. To Riley, Will, Brody, Wes, and any other future nieces and/or nephews: hopefully I will have firmly established my tenure as the cool uncle by the time you're all old enough to realize how much of a nerd I am.

Finally, to Rian, thank you for all of your love and patience, I can't imagine the past few years without you. Your smile and support has brought me through many difficult times. Mere words will never be able to explain how much you mean to me. I can't wait for the next chapter of our lives together. I love you.

Contents

List of Figures

List of Tables

Chapter 1

Introduction

1.1 The Standard Model

The Standard Model of particle physics explains three of the four fundamental forces of nature: the electromagnetic force, the weak force, and the strong force. In addition, the Standard Model also describes the building blocks of all known matter. The mathematical framework for the Standard Model is known as quantum field theory (QFT) where the dynamics of the theory are described by a Lagrangian (technically a Lagrangian *density*), which contains information about the potential and kinetic energy of the quantum fields. In total, the Standard Model Lagrangian has 19 free parameters (assuming massless neutrinos, discussed later) that have all been determined experimentally.

The basic building blocks of the theory are the fundamental particles and are classified in various ways and shown in Fig. 1.1. Half-integer spin particles are known as *fermions*. The fundamental fermions (all with spin-$\frac{1}{2}$) are displayed on the outer edge of the circle. Fermions are further classified into two groups: *quarks* (shown in red) and *leptons* (shown in green). There are six known quarks - down (d), up (u), strange (s), charm (c), bottom (b), and top (t) - which can interact via the strong force and therefore carry a color charge. The remaining six fermions are known as leptons and they do not carry a color charge. The fundamental leptons are the electron (e), muon (μ), tau (τ), electron neutrino (ν_e), muon neutrino (ν_μ), and tau neutrino (ν_τ).

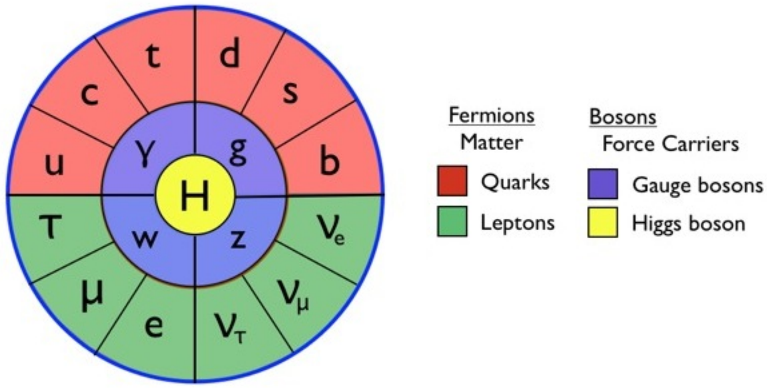

Figure 1.1: The fundamental particles that make up The Standard Model of particle phyics [1].

In addition, the Standard Model also requires the existence of an antiparticle, or "mirror particle", for each fermion listed above. Antiparticles are identical to their corresponding particle in every way except that certain quantum numbers are flipped. For charged leptons (e, μ, τ), the corresponding antiparticles have opposite electric charge and lepton number. For the massless neutral leptons (ν_e, ν_μ, ν_τ), the corresponding antiparticles have opposite helicity and opposite lepton number. For quarks, the corresponding antiparticles have opposite electric charge, opposite color charge (known as *anticolor*), and opposite baryon number.

The other type of particles, which have an integer spin, are known as *bosons*. The fundamental spin-1 bosons are the photon (γ), gluon (g), $W^\pm$, and Z. These are pictured in purple in Fig. 1.1. These are known as the "force carriers" that mediate the electromagnetic, strong, and weak forces. More formally, they are vector gauge bosons corresponding to the gauge theory (a type of quantum field theory that is invariant under continuous, local transformations) that describes each of the three forces.

The photon is the mediating gauge boson for the electromagnetic force. Quantum electrodynamics (QED) is the gauge theory that describes this interaction and the corresponding gauge invariance, colloquially known as a *symmetry*, gives rise to electric charge. As a result all particles with electric charge (e, μ, τ, $W^\pm$, and all of the quarks) can interact through the electromagnetic force by exchanging photons.

The gluon is the mediating gauge boson for the strong force. Quantum chromodynamics (QCD) is the gauge theory that describes the interaction and the corresponding gauge symmetry gives rise to color charge. The quarks (d, u, s, c, b, t) and the gluon itself are the only particles containing color charge and therefore are the only particles that interact via the strong force. The fact that the gluon carries a color charge and can interact with itself gives QCD some very interesting and unique properties that will be discussed in the next section and are the fundamental basis and motivation for all of the work presented in this thesis.

The weak force is mediated by the massive W^+, W^-, and Z bosons. The uncertainty principle tells us that the range of the weak force should be extremely small given the mass of the mediating bosons. The fact that the bosons are massive is a consequence of gauge symmetry breaking. Specifically, the Higgs mechanism is responsible for the spontaneous symmetry breaking of the electroweak interaction at low energies causing the electromagnetic and weak forces to separate [2,3]. This mechanism also predicted the existence of an additional spin-0 boson whose associated field would interact with all fermions and the $W^\pm$ and Z bosons to give them mass. This particle, known as the Higgs boson, was discovered at the LHC by the CMS and ATLAS collaborations in 2012 and was the final piece of the Standard Model [4, 5].

The Standard Model is one of the most accurate scientific theories in history. However, the Standard Model is not complete in that there are major discrepancies and gaps present in the theory. Its most notable shortcoming is its inability to explain gravity, specifically general relativity, in the same mathematical framework used for the other forces. Experimentally, one of the biggest observed discrepancies was the deficit of solar ν_e flux compared to the Standard Model predictions and the subsequent discovery of neutrino oscillation [6–8]. Neutrino oscillation can be explained by the fact that the flavor eigenstates differ from the mass eigenstates of the neutrinos, which requires neutrinos to be massive and violate flavor conservation [9, 10]. In addition, the observation of dark matter and the large baryon asymmetry in the universe are not well explained in the context of the Standard Model. Despite its shortcomings the Standard Model was still used to successfully predict the existence of the Higgs, $W^\pm$, Z bosons, and gluons as well as the charm and top quarks as well as their expected properties. Even more impressive is that it was used to correctly predict the value of the fine structure constant, α (the coupling constant in QED) out to 10 decimal places [11]!

1.2 Quantum Chromodynamics

As discussed briefly in the previous section, the theory of the strong force is known as quantum chromodynamics (QCD), which describes the interaction and dynamics of particles with color charge: quarks and gluons, collectively known as *partons*. Quarks and antiquarks are analogous to electrons and positrons in QED while the gluon, the mediating gauge boson, is a pseudo-analog of the photon. Despite this analogy, there are drastic differences between QED and QCD.

Unlike QED, which only has one type of charge, QCD contains three types of charge, called color charge - red, green, and blue - and each has a corresponding anticharge or anticolor. Another distinguishing feature is that the gluon carries color charge itself, as opposed to the electrically neutral photon of QED. This significantly complicates the theory by allowing gluons to interact with themselves which gives rise to some very unique properties of QCD (discussed in more detail later).

More formally, QCD is a non-abelian gauge theory (a specific type of quantum field theory) with an SU(3) symmetry group. SU(3) stands for the *special unitary group* and is just the group of 3×3 unitary matrices that have an additional ("special") requirement that their determinant equals one. In QCD these matrices correspond to rotations in the three dimensional color space. The SU(3) symmetry, or gauge invariance, of QCD means that the strong interaction is invariant with respect to color. The generators of SU(3) are the 3×3 matrices λ_a and do not commute which is why the theory is known as a *non-Abelian* gauge theory. The QCD Lagrangian density is given by [12,13]

$$\mathcal{L} = \sum_q \bar{\psi}_{q,i} \left(i\gamma^\mu \partial_\mu \delta_{ij} - g\gamma^\mu \frac{\lambda^a_{ij}}{2} A^a_\mu - m_q \delta_{ij} \right) \psi_{q,j} - \frac{1}{4} F^a_{\mu\nu} F^{\mu\nu}_a, \tag{1.1}$$

where $\psi_{q,i}$ are the quark fields of flavor q and color i, m_q are the quark masses, A^a_μ are the gluon fields with $a \in \{1, ..., 8\}$, g is the coupling constant, γ^μ are the gamma matrices, and $F^a_{\mu\nu}$ is the gluon field strength tensor. This is given by the following equation

$$F^a_{\mu\nu} = \partial_\mu A^a_\nu - \partial_\nu A^a_\mu + g f_{abc} A^b_\mu A^c_\nu, \tag{1.2}$$

where f_{abc} are structure constants given by the commutation relation between the $SU(3)$ generators: $\left[\frac{\lambda_a}{2}, \frac{\lambda_b}{2}\right] = i f_{abc} \frac{\lambda_c}{2}$.

Quantum corrections of the coupling constant are necessary due to the anti-screening of a color charged particle by the polarization of virtual particles from vacuum pair production. This leads to the use of an *effective coupling*, $\alpha_s(Q^2)$, which depends on the momentum transfer, Q. This momentum dependence can be better understood as probing various length scales since the de Broglie wavelength of a particle scales inversely with momentum. At high enough Q^2 and short length scales the anti-screening is reduced and the effective coupling is reduced [14]. This is known as running of the coupling and gives rise to the unique feature of QCD known as *asymptotic freedom* [15, 16].

The effective coupling, defined as $\alpha_s = g_s(Q^2)/4\pi$, scales with Q^2, to first order, as [17]

$$\alpha_s(Q^2) = \frac{4\pi}{\beta_0 \log(Q^2/\Lambda^2)}, \tag{1.3}$$

where Λ is the QCD scale parameter and β_0 is the one loop beta function for QCD. This is given by [17–19]

$$\beta_0 = \frac{11}{3} N_c - \frac{2}{3} n_f, \tag{1.4}$$

where n_f is the number of quark flavors and $N_c = 3$ is the number of colors. The fact that this quantity is positive (for $n_f < 17$) is what leads to asymptotic freedom since as $Q^2 \to \infty$, $\alpha_s \to 0$. The scaling of $\alpha_s(Q^2)$ has been verified experimentally, as shown in Fig. 1.2 [17].

At the opposite end of the energy scale, low Q^2, the QCD coupling becomes large. This leads to the phenomenon known as *confinement*, which states that only color singlet states can exist as free particles. Since individual quarks and gluons all contain a color charge, confinement implies that isolated free quarks and gluons are forbidden. This means that only color-neutral bound states of quarks and gluons can exist. These bound states are known as *hadrons* and come in two forms: *baryons* and *mesons*. Baryons, like protons and neutrons, are a bound state of three quarks (or three antiquarks for antibaryons). Mesons, like the pion, are bound states of quark and antiquark pairs.

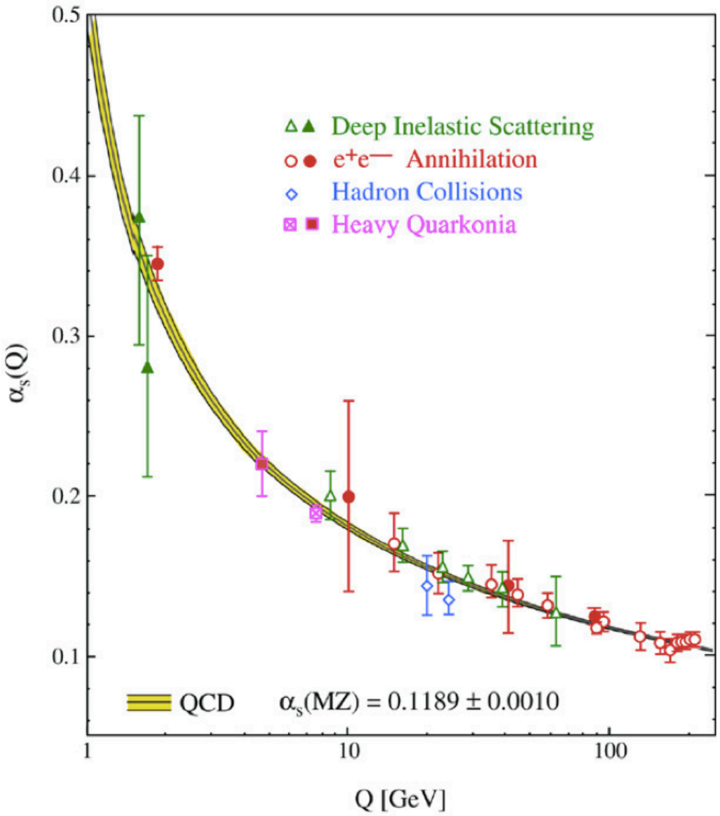

Figure 1.2: A summary of experimental measurements of α_s as a function of Q^2. The open symbols are for NLO QCD calculations and the closed symbols are for NNLO QCD calculations used in the respective analysis. The curve represents the theoretical prediction from QCD [17].

Confinement is essentially due to the fact that in QCD the strong force does not fall off with distance like gravity and the electromagnetic force do. Instead, as you pull two quarks apart the binding energy associated with the strong force actually increases. Eventually it becomes more energetically favorable to produce quark-antiquark pairs out of the vacuum for the initial two quarks to bind with, leaving two colorless, bound quark states instead of two free quarks. Although it has not been proven analytically, confinement is widely accepted as the explanation for why there has never been an observation of a free quark.

Both of these properties of QCD - asymptotic freedom and confinement - lead to consequences that provide the foundation and motivation for the research presented in this thesis. Specifically, studying a strongly coupled form of matter called the quark gluon plasma (QGP), the formation of which is a corollary of the idea of asymptotic freedom, using high energy “jets” as a probe, which are a directly related to the concept of confinement. The QGP and jets will both be discussed in more detail in the next section.

1.3 The Quark Gluon Plasma

As discussed at the end of the last section, confinement tells us that QCD does not allow completely free quarks to exist, they must always be “confined” to a bound state. However, the running coupling and asymptotic freedom in QCD indicate that at high energies (small length scales) the coupling constant decreases so that partons can behave “freely” across small enough distance scales. At high enough energies (such that $\langle Q^2 \rangle$ is large and α_s is small) and hadron densities this effect causes the confined states of quarks and gluons to “melt”, meaning that the constituent quarks are no longer bound in colorless doublets or triplets. Since the quarks and gluons are only allowed to act freely within the boundaries of such an energetically dense region, they are not truly free but “quasifree” particles. This phenomenon is known as *deconfinement* and is a defining characteristic of the state of matter known as the quark-gluon plasma (QGP).

The energy density needed to create the QGP is estimated from lattice QCD calculations to be $\epsilon \sim 1$ GeV/fm^3 [20]. One of the only known ways to create and observe this type of system is through high energy collisions of *heavy ions*, such as the nuclei of lead (Pb) and gold (Au) atoms [21–24]. These experiments can only be conducted at large specialized particle accelerators, namely the Relativistic Heavy Ion Collider (RHIC) and the Large Hadron Collider (LHC).

One of the main experimental techniques for inferring the existence of the QGP is by comparing to a baseline measurement of the null hypothesis, which in this case just means that we assume the QGP was not created in heavy-ion collisions. If this were the case then it is expected that results from heavy-ion collisions would be analogous to a superposition of individual proton-proton ($p+p$) collisions, where it is assumed that the neutron and proton will behave identically in such collisions. Therefore, by scaling the results from $p + p$ collisions by the expected number of nucleon-nucleon collisions they should match the results from heavy-ion collisions if there was no QGP formation. The first step for making such comparisons is estimating how many nucleon-nucleon collisions occur in a given heavy-ion collision, which is done using a *Glauber Model*.

1.3.1 The Glauber Model and N_{coll} Scaling

A Glauber model is Monte Carlo-based technique for modeling heavy-ion collisions. This is done by modeling each colliding nucleus as a collection of nucleons that are randomly distributed by a Fermi distribution. More specifically it is a Woods-Saxon distribution given by [25]

$$\rho(r) = \rho_0 \frac{1 + \omega(\frac{r}{R})^2}{1 + e^{\frac{r-R}{a}}}, \tag{1.5}$$

where ρ_0 is the nucleon density at the center of the nucleus, R is the nuclear radius, a is the skin depth, and ω accounts for spherical deviations in the shape. Studying the overlap geometry of two such nuclei at various impact parameters can provide important insights into the role that *centrality* (how overlapping the two colliding nuclei are) plays in heavy-ion collisions.

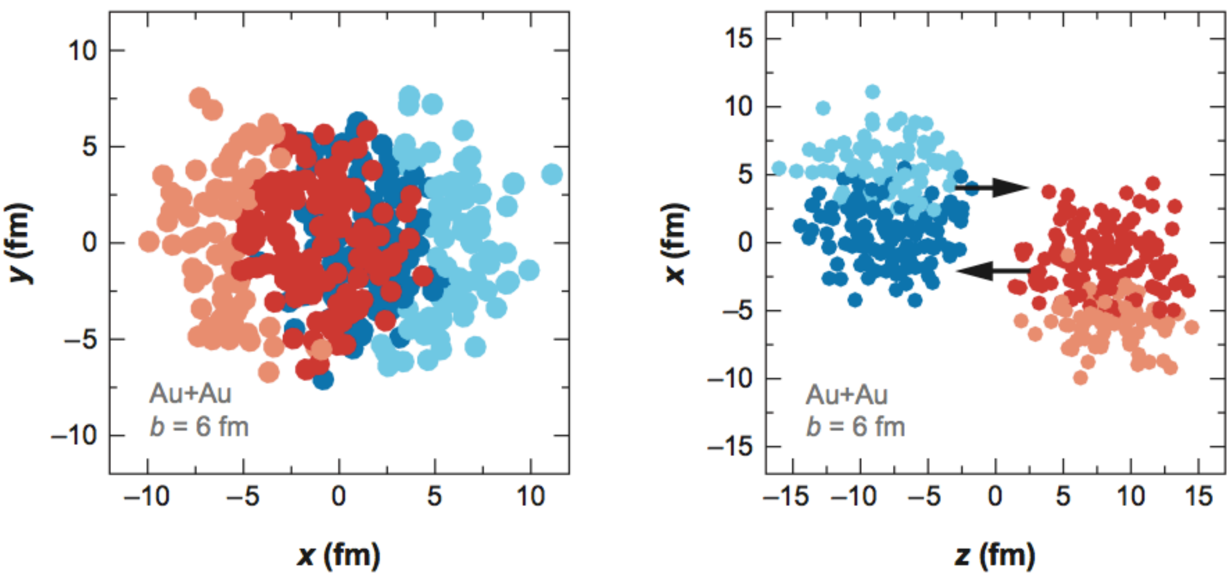

Figure 1.3: A Glauber Model event with $b = 6$ fm for two colliding Au nuclei. The left plot shows the plane transverse to the beam direction while the right plot shows the plane containing the impact parameter and the beam direction. The participating nucleons are shown in dark red/blue [25]. Note: the right plot does not depict the Lorentz contraction that occurs in high energy heavy-ion collisions.

A diagram showing the geometry of a non-central collision ($b = 6$ fm) of gold nuclei is shown in Fig. 1.3 [25]. The left figure shows the geometry of the collision in the plane transverse to the beam pipe and the right plot shows a longitudinal view of the collision. Individual nucleons are darkened if they participate in the collision (determined by whether or not they overlap with a nucleon of the other nucleus), these are the so called *participant nucleons* and the total number of them in each collision is denoted as N_{part}. The total number of individual nucleon-nucleon collisions in each even is denoted by N_{coll}.

The Glauber model can be used to scale $p+p$ collisions by the expected number of binary collisions, N_{coll}, in a given heavy-ion event to compare certain results. If the heavy-ion collision just behaved as a superposition of individual nucleon-nucleon collisions then the ratio of certain quantities, like charged particle yield, should be ~ 1 (within the given statistical precision). The ratio of charged particle yields in heavy-ion collisions to $p+p$ collisions as a function of p_{T} and η is called the *nuclear modification factor* and is given by [26, 27]

$$R_{AA} = \frac{1}{\langle N_{\text{coll}} \rangle} \frac{d^2 N_{AA}/dp_{\text{T}}dy}{d^2 N_{pp}/dp_{\text{T}}dy}. \tag{1.6}$$

This is perhaps the most fundamental heavy-ion observable since it only requires charged particle p_{T} spectra in both heavy-ion and $p+p$ collisions, as well as a Glauber model to determine the N_{coll} scaling. A collection of various R_{AA} results from the SPS fixed target experiment (17.3 GeV) to the most recent from the LHC (2.76 TeV) is shown in Fig. 1.4 [28]. It is clear that at RHIC and LHC energies, 200 GeV and 2.76 TeV respectively, there is a significant suppression (R_{AA}) for the entire p_{T} range shown. This is consistent with the idea of a strongly interacting medium, the QGP, causing colored particles to lose energy as they pass through and thus resulting in a reduced p_{T} measured in the detector. This shift from high to low p_{T} combined with the rapid drop off in spectra with increasing p_{T} leads to an $R_{AA} < 1$ The exact behavior is not trivial and is due to numerous other effects, some of which will be discussed in the following sections.

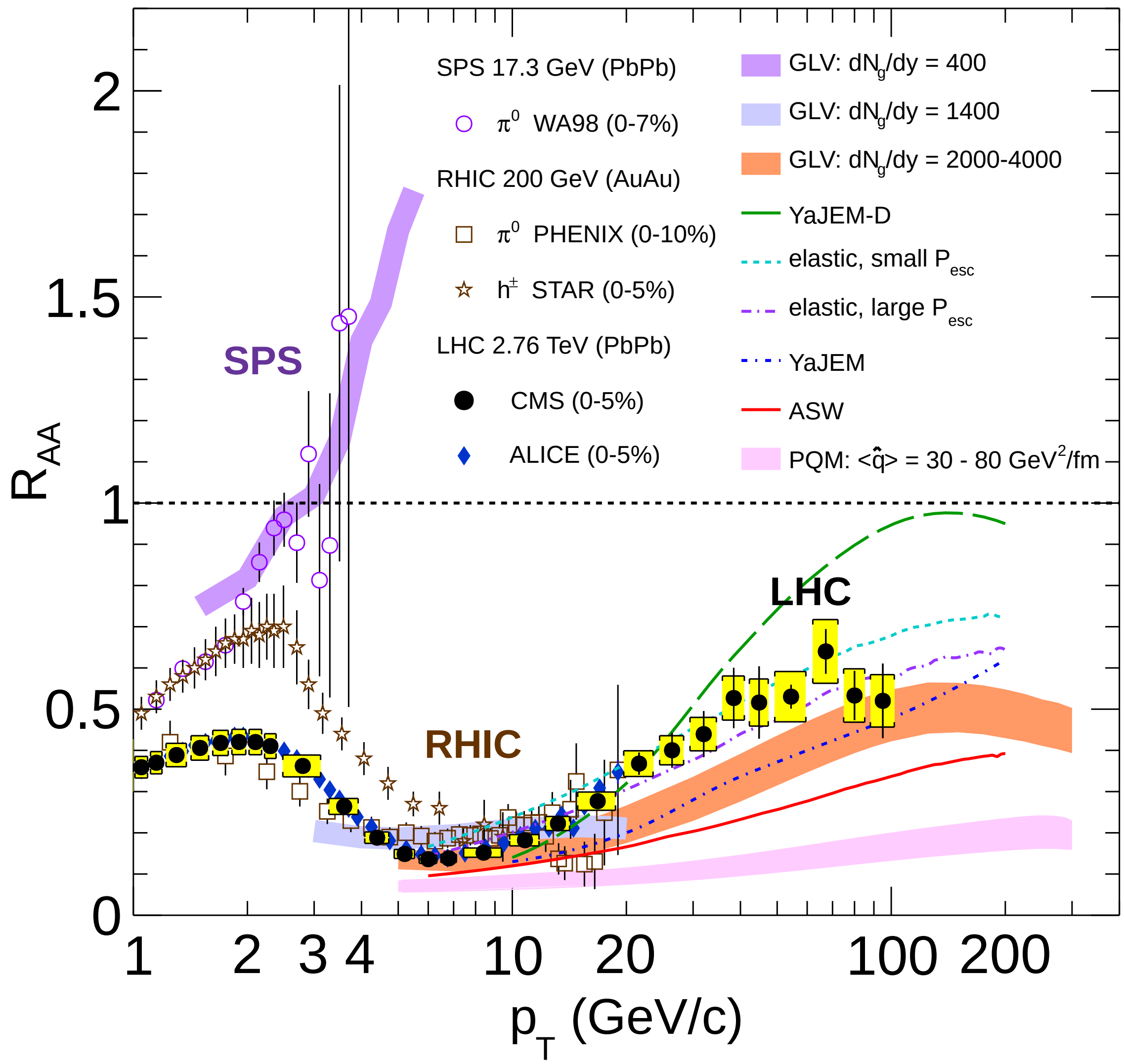

Figure 1.4: The nuclear modification factor, R_{AA}, as a function of p_{T} from various experiments at various center-of-mass energies. Also shown are curves from various theoretical predictions based on different models of the QGP. The error bars denote statistical uncertainty while the shaded boxes represent systematic uncertainties. A significant suppression is seen at RHIC and LHC energies, which suggests a modification due to the presence of a strongly interacting medium: the QGP [28].

1.3.2 Collective Behavior and Elliptic Flow

Another important feature of the QGP is that it is a thermalized medium. Since it is not really in a completely asymptotically free state the medium is still strongly interacting which implies that it will exhibit collective behavior. As result, in non-central heavy-ion collisions the interaction region will be azimuthally anisotropic. When the interaction region thermalizes, pressure gradients will also form in an anisotropic manner that preferentially emits particles in the plane containing the impact parameter and beam direction, the *reaction plane*. This is illustrated in Fig. 1.5.

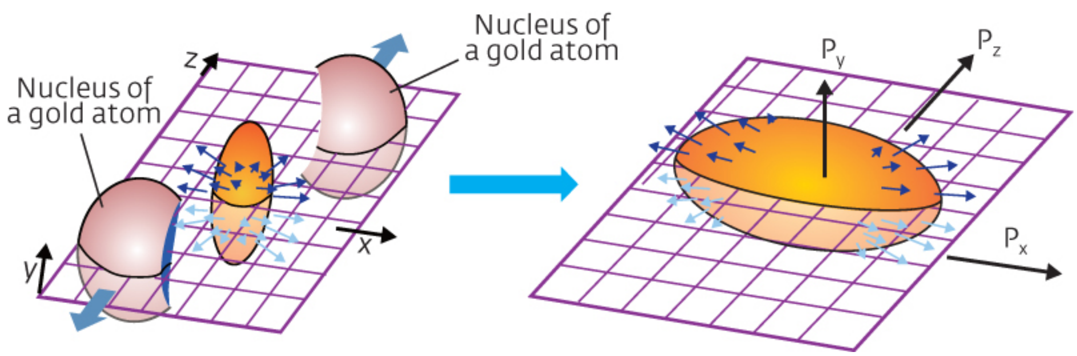

Figure 1.5: A cartoon showing how the initial spatial anisotropy in non-central heavy-ion collisions can lead to a final state momentum anisotropy [29].

This phenomenon is known as *elliptic flow* and can be modeled using relativistic hydrodynamics [30, 31]. It was predicted theoretically prior to experimental observation and is one of the key pieces of evidence supporting the claim that the QGP is a thermalized medium [31]. Experimentally this can be measured using the azimuthal anisotropy parameter, v_2. This can be done by first looking at the Lorentz-invariant final-state particle distribution given by [32]

$$E\frac{d^3N}{d^3p} = \frac{1}{2\pi}\frac{d^2N}{p_{\mathrm{T}}dp_{\mathrm{T}}dy}\left(1 + \sum_{n=1}^{\infty} 2v_n \cos n(\phi - \Psi_r)\right), \tag{1.7}$$

where the azimuthal component is expanded in a Fourier series (shown on the r.h.s. in parenthesis). The Fourier coefficients, given by the $2v_n$ terms, can then be used to characterize the azimuthal distribution of final-state particles. The v_2 coefficient is known as the *elliptic flow coefficient* and should be non-zero in non-central collisions for the reasons explained in the beginning of this section. More importantly, v_2 can actually be measured experimentally, unlike the energy density and pressure gradients, and can be used to test the validity of various models of relativistic hydrodynamics.

Figure 1.6 shows v_2 measurements from two separate RHIC experiments: STAR and PHENIX. The v_2 values for all charged hadrons and various identified particles are shown as a function of p_{T} at $\sqrt{s_{NN}} = 200$ GeV. The solid and dashed curves represent theoretical predictions from relativistic hydrodynamics for specific identified particles. In the low-p_{T} region we see that the models and the data agree extremely well, supporting the claim that the QGP is thermalized. At higher p_{T} the data diverges drastically from the models. However this is not unexpected due to the increased presence of particles from hard scatterings at high p_{T}, which are not part of the thermalized, collective medium. The origin and effects of these hard processes and how they behave in the presence of a QGP medium is discussed in the next section.

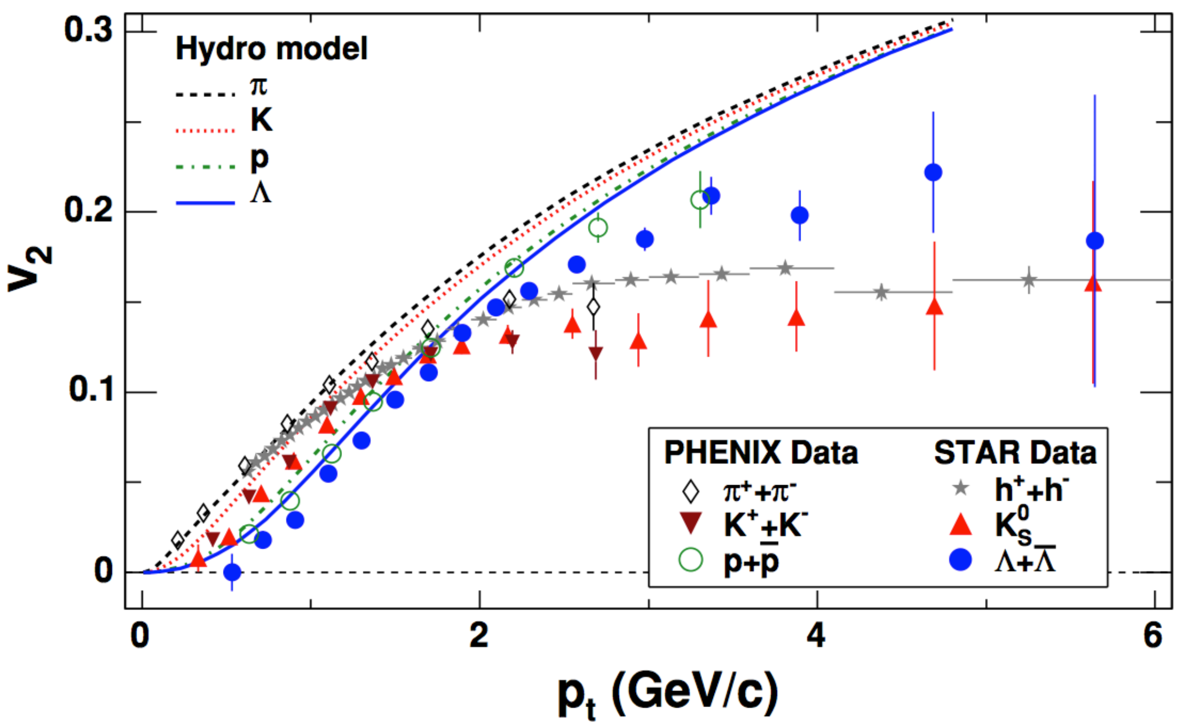

Figure 1.6: Elliptic flow measurements, v_2, as a function of p_{T} for various identified particles at $\sqrt{s_{NN}} = 200$ GeV from the STAR and PHENIX collaborations. The curves represent the theoretical predictions from relativistic hydrodynamics [33].

The centrality dependence of v_2 in heavy-ion collisions is an important characteristic as well, given that it is a consequence of the geometrical anisotropy in the initial interaction region in non-central collisions. Therefore, in central collisions, where the anisotropy in the initial overlap region is at a minimum, v_2 should be at a minimum compared to more peripheral collisions. This is indeed the case and can be seen in Fig. 1.7, which shows v_2 for charged hadrons as a function of p_{T} for five different centrality bins. The data were collected from CMS at $\sqrt{s_{NN}} = 2.76$ TeV and from PHENIX at $\sqrt{s_{NN}} = 200$ GeV. In both cases a clear centrality dependence is visible where v_2 is at a minimum in the most central collisions.

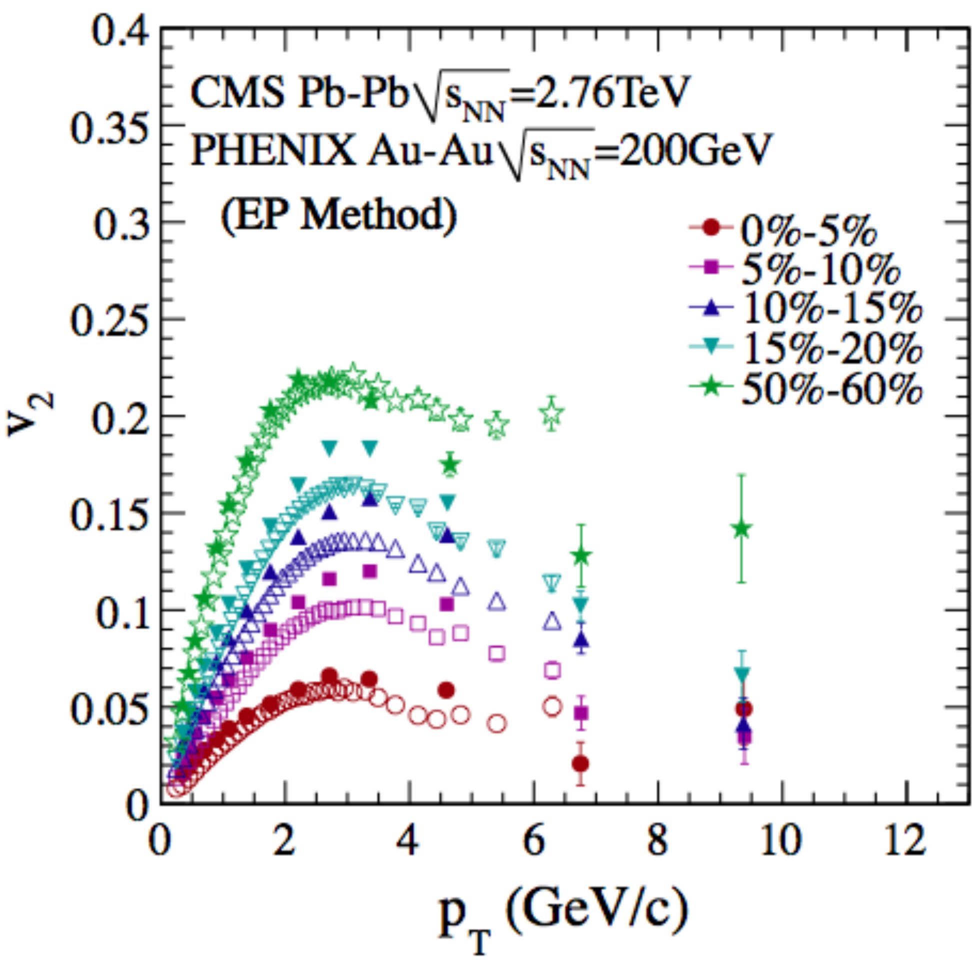

Figure 1.7: Elliptic flow measurements of charged particles, v_2, as a function of p_{T} for five different centrality bins. The filled points are from CMS at $\sqrt{s_{NN}} = 2.76$ TeV and the open points are from PHENIX at $\sqrt{s_{NN}} = 200$ GeV [34].

1.3.3 Parton Energy Loss and Jet Quenching

Another important characteristic of a QGP medium is the amount of energy loss that colored particles will undergo as they pass through. Unlike $p + p$ collisions, where scattered particles are essentially passing through a QCD vacuum, high-p_{T} particles produced in heavy-ion collisions should experience medium-induced collisional (elastic scattering) and radiative (inelastic scattering) energy loss [35]. There are a number of ways to observe this and it was the basis for one of the earliest proposed signatures of the QGP: *jet quenching* [36].

1.3.3.1 Jets in High Energy Collisions

Qualitatively, a *jet* is a highly collimated stream of (typically) high-p_{T} hadrons that is produced in high energy collisions. Hard scattering events can lead to the production of high-p_{T} partons that are "knocked out" of their bound state. However, the concept of confinement in QCD says that colored particles can not exist freely. This means that as the individual quark or gluon begins to fly away from its confining hadron the binding energy from the strong force increases (since the strong force does not diminish with distance). Eventually, it becomes more energetically favorable for the free parton to undergo the process of *hadronization* (also known as fragmentation), which is where numerous quark-antiquark pairs are produced from the vacuum and bind together to form a collection of hadrons, also known as jet fragments. Since momentum must be conserved, the p_{T} of the initial parton must be split between its fragmentation products, thus leading to a stream of high-p_{T} particles being measured in a detector.

These situations are typically caused (to first order) by a $2 \to 2$ hard scattering. This results in a large momentum transfer between the two colliding quarks or gluons which results in two high-p_{T} partons that eventually form jets. Again, momentum must be conserved so the final state p_{T} should always balance (i.e. sum to zero), which means that the pair of jets (collectively called a *dijet*) should be created "back-to-back" from each other, i.e. $\Delta\phi = \pi$. It is possible for hard scatters to lead to three-jet (or multiple-jet) events which would clearly not be aligned back-to-back in azimuth. These are much less common than back-to-back dijet events since the cross sections require additional factors of α_s for each additional gluon that is split off.

1.3.3.2 Jet Quenching in Heavy-Ion Collisions

In heavy-ion collisions dijet events can be used as an extremely useful tool for measuring any medium-induced energy loss. As perviously discussed, in $p + p$ collisions where there is no QGP medium with which to interact, the p_{T} of every dijet should balance (to first order). In reality there are higher order terms that are non-negligible in these interactions that lead to multi-jet events that can make it very difficult to measure the momentum balance. Nonetheless, the leading order interaction is a dijet and these should always be balanced. This is shown on the left in Fig. 1.8.

In heavy-ion collisions there are events where a dijet is created on the edge of the QGP medium such that one jet escapes into the QCD vacuum while undergoing minimal energy loss while the other jet plows directly through the QGP undergoing significant energy loss along the way (its energy is "quenched"). This is pictured on the right in Fig. 1.8. In these situations there should be a significant discrepancy in the transverse momentum balance of the dijet, which should be observable experimentally. This is the signature that Bjorken first proposed as evidence of the formation of a quark-gluon plasma [36].

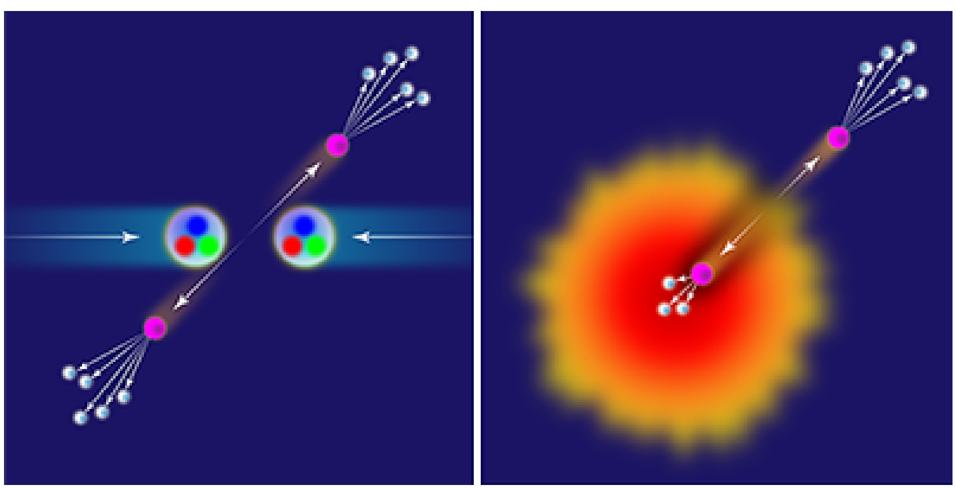

Figure 1.8: Left: A dijet event occurring in $p + p$ collisions. Since the event takes places in a QCD vacuum the dijet must be perfectly balanced in p_{T}. Right: A dijet event occurring in a heavy-ion collision. The dijet pair is created near the surface of the medium such that one jet escapes into the vacuum and undergoes minimal energy loss while the other jet traverses through the strongly coupled medium where it undergoes significant energy loss before being measured in the detector. [37].

Some of the first experimental evidence of jet quenching was observed at RHIC by the STAR and PHENIX collaborations. This was done by looking at the azimuthal distributions of high-p_{T} dihadron (two-particle) correlations from Au+Au, p+Au, and $p+p$ collision data at $\sqrt{s_{NN}}$ = 200 GeV [21,22]. In these studies high-p_{T} tracks were used a proxy for jets since full jet reconstruction was not possible with either the STAR or PHENIX detectors. These results will be discussed more in the next chapter. With the advent of more modern (and more expensive) detectors designed for complete event reconstruction in $p+p$ collisions at the LHC, jet reconstruction is now possible in heavy-ion collisions. This involves using information from the tracker, electromagnetic calorimeter (ECAL), and hadronic calorimeter (HCAL) to reconstruct, as accurately as possible, the total transverse momentum in an event to identify jets on an event-by-event basis. An example of a reconstructed dijet event from Pb+Pb collisions in the CMS detector is shown in Fig. 1.9. The effects from jet quenching are clearly visible where one jet (the *leading jet*) has $p_{\mathrm{T}} = 205.1$ GeV/c and the second jet (the *subleading jet*) has $p_{\mathrm{T}} = 70.0$ GeV/c.

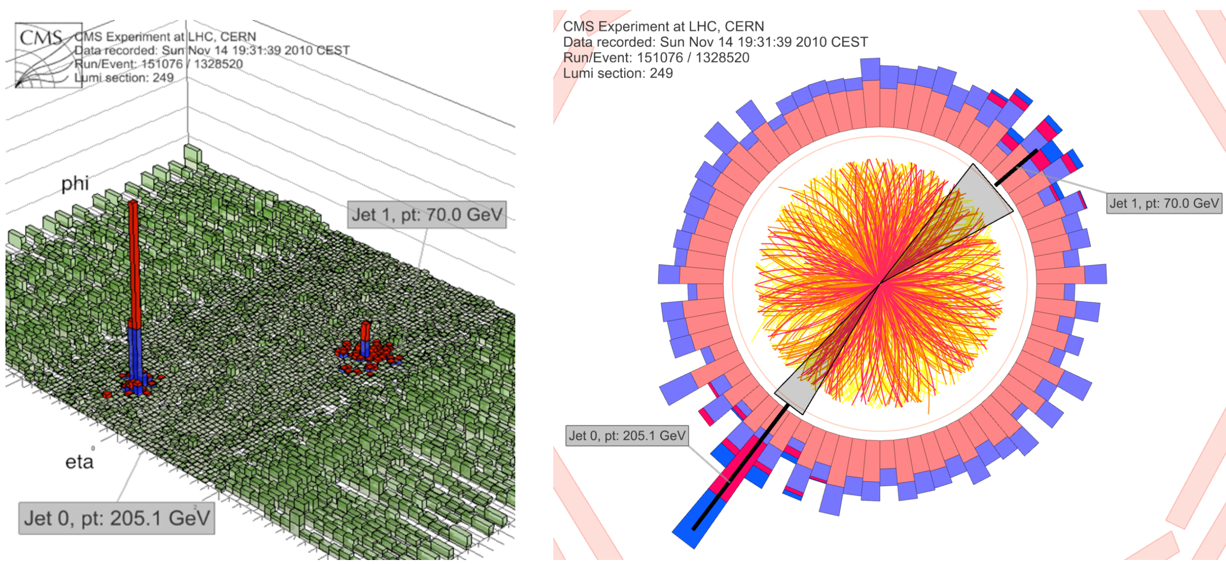

(a) The $\eta - \phi$ plane of the calorimeters

(b) Radial view showing tracks and calorimeter data

Figure 1.9: An example of an unbalanced dijet event reconstructed with the CMS detector in Pb+Pb collisions at $\sqrt{s_{NN}} = 2.76$ TeV. Left: the $\eta - \phi$ plane showing the amount of energy deposited in the ECAL (red) and HCAL (blue). Right: a transverse cross section of the event showing the charged particle tracks and η-averaged deposited energy in the ECAL (red) and HCAL (blue) [38].

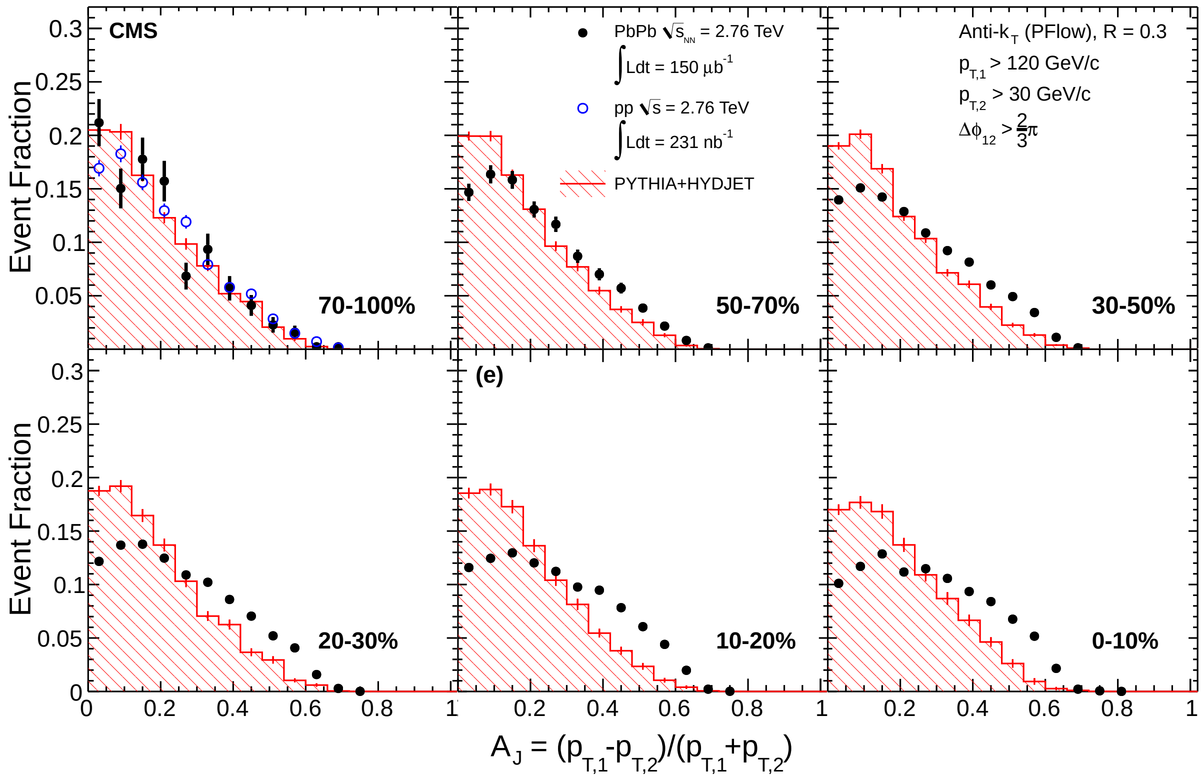

Figure 1.10: Dijet asymmetry ratio, A_{J}, in six different centrality bins for Pb+Pb collisions (black points), $p+p$ collisions (open blue points), and Pb+Pb simulations (red histograms). The leading jet was required to have $p_{\mathrm{T}} > 120$ GeV/c and the subleading jet was required to have $p_{\mathrm{T}} > 30$ GeV/c while the angular separation between the two was required to be $\Delta\phi > \frac{2}{3}\pi$ [39].

Using full jet reconstruction, measurements of the dijet asymmetry ratio, which is given by $A_{\mathrm{J}} = (p_{T,1} - p_{T,2})/(p_{T,1} + p_{T,2})$, as a function of event centrality are possible. As with flow, the effects from jet quenching are expected to be strongly dependent on centrality except that in this case it should be most significant in central collisions. Figure 1.10 shows this measurement in six different centrality classes in Pb+Pb collisions (black points) for leading jets with $p_{\mathrm{T}} > 120$ GeV/c and subleading jets with $p_{\mathrm{T}} > 30$ GeV/c and an azimuthal separation between the two of $\Delta\phi > \frac{2}{3}\pi$ (which filters out multi-jet events) [39]. The results are compared to simulated Pb+Pb dijet events (shown in red) and the most peripheral Pb+Pb bin is also compared to the results from $p+p$ collisions (shown in blue). Very good agreement is seen between the data from $p+p$ collisions and the most peripheral events from Pb+Pb data and simulations. In all but the most peripheral events a significant discrepancy is seen between simulation and data. In particular, the data show a large number of events with imbalanced dijets ($A_{\mathrm{J}} \to 1$) and relatively smaller number of balanced dijets ($A_{\mathrm{J}} = 0$) compared to unquenched dijet simulations and peripheral events. This is consistent with the idea of jet quenching and is evidence for the existence of the QGP in Pb+Pb collisions at the LHC at $\sqrt{s_{NN}} = 2.76$ TeV.

In addition to A_{J} measurements we can measure the nuclear modification factor for reconstructed jets in the same way it was done for charged particle p_{T} spectra (Sec. 1.3.1). The R_{AA} for reconstructed inclusive jets from 0-5% central Pb+Pb events is shown in black triangles within green boxes in Fig. 1.11 for jets with $100 < p_{\mathrm{T}} < 300$ GeV/c [40]. It shows a clear a suppression for the entire p_{T} range studied which is also consistent with the jet quenching picture. On average, jets from heavy-ion collisions will undergo energy loss so they will be measured with a lower-p_{T} in the detector compared to their initial p_{T}. Additionally, since the cross section for high-p_{T} jets drops off rapidly with jet-p_{T} it will appear that jets at the measured p_{T} value are suppressed since there are far fewer jets measured at a given p_{T} than jets that had that same initial p_{T}.

In addition to fully reconstructed inclusive jets, the R_{AA} for b-jets - jets produced from a hard-scattered bottom quark - are shown in red squares within orange boxes for $80 < p_{\mathrm{T}} < 250$ GeV/c. These results represent the first results with successfully reconstructed b-jets in heavy-ion collisions and show a significant suppression ($\sim$0.4) for the entire p_{T} range studied. This is also consistent with the jet quenching picture but provides additional information indicating that jet quenching does not have a strong dependence on the mass of the original parton resulting in a jet [41].

Also shown in Fig. 1.11 is the R_{AA} for the production of three color-neutral probes: isolated photons [42], inclusive W's [43], and Z's [44]. Since these particles are not colored they shouldn't be affected by the presence of a strongly-coupled medium like the QGP and this is exactly what is observed. The R_{AA} for all of these processes is unity (within statistical and systematic uncertainties). Lastly, the R_{AA} for the production of B-mesons is also shown in light brown in Fig. 1.11. Since B-mesons originate from a b quark, which should undergo medium-induced energy loss, these are expected to show signs of suppression (but not as much as the light quark hadrons) which is exactly what is observed [45].

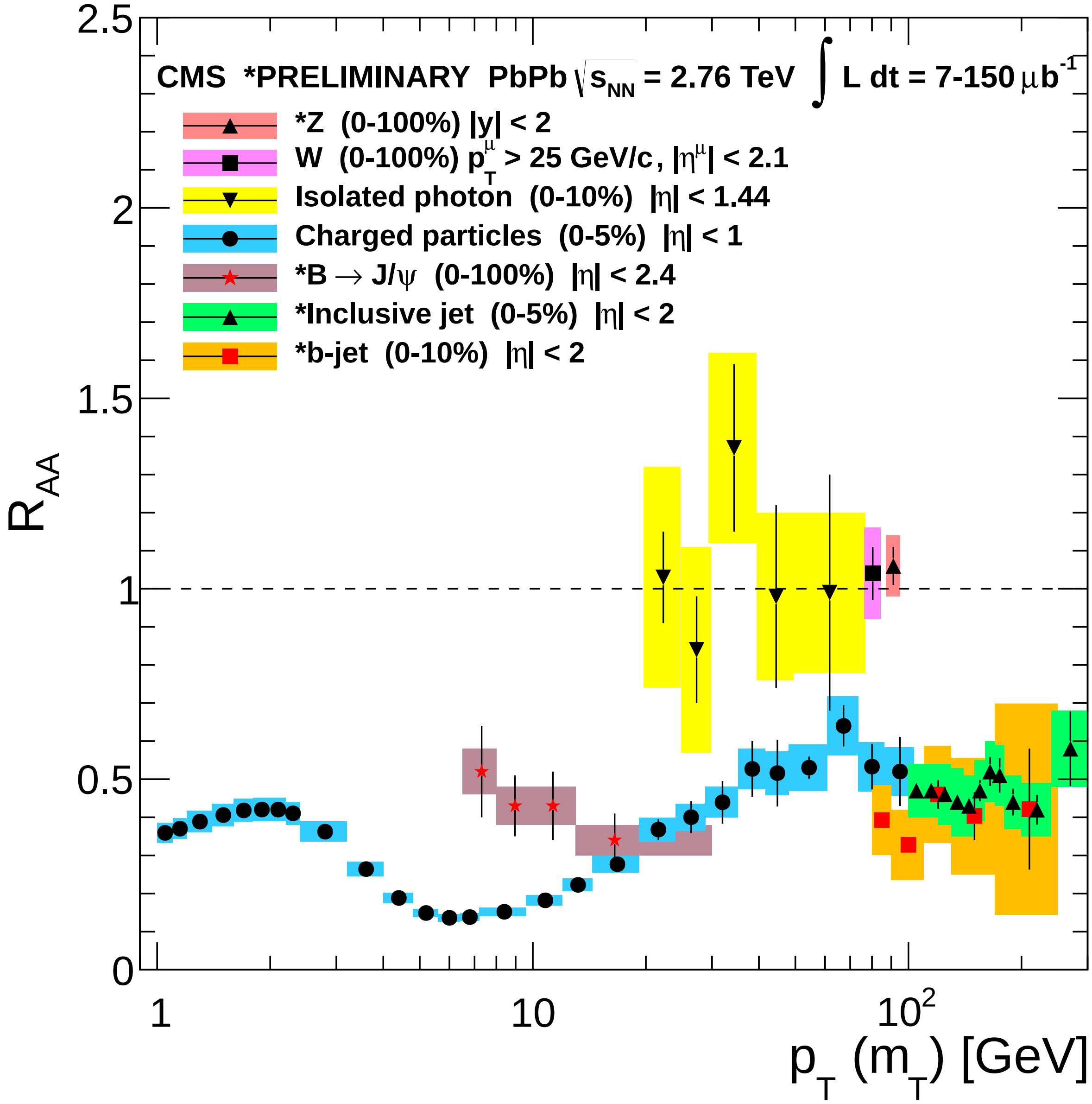

Figure 1.11: Nuclear modification factor, R_{AA} for charged particles and various hard processes as a function of p_{T}. Fully reconstructed inclusive jets are shown in green from 100-300 GeV/c. Reconstructed b-jets are shown in orange from 80-250 GeV/c. Charged particles are shown in light blue from 0-100 GeV/c. Isolated photons are shown in yellow, Z boson production is shown in light red, inclusive $W^{\pm}$ boson production is shown in light magenta, and B-meson production is shown in light brown [40].

Chapter 2

Experimental Studies Using Dihadron Angular Correlations

2.1 Jet Suppression

Dihadron Correlations, discussed in detail in Sec. 6.1, are used to study the relative ϕ and η distributions between pairs of particles produced in high energy collisions. One of the most significant and landmark results using this technique was from the STAR collaboration and is shown in Fig. 2.1 [22,46]. This figure shows the two-particle azimuthal distribution of all "high-p_T" hadrons ($p_\mathrm{T} > 2$ GeV/c) for p+p, central p+Au, and central Au+Au collisions at $\sqrt{s_{NN}} = 200$ GeV.

The $p + p$ dataset, represented by the black histogram, shows the characteristic azimuthal structure we expect from dijet correlations, namely the peaks at $\Delta\phi = 0$ and $\Delta\phi = \pi$. The p+Au dataset, shown in red, is largely consistent with the $p + p$ data and also shows two prominent dijet peaks. However, the central Au+Au dataset, shown in blue, shows one major difference: the most striking is the disappearance of the "away-side" jet peak ($\Delta\phi = \pi$). This was taken as one of the first signs of jet quenching in heavy-ion collisions.

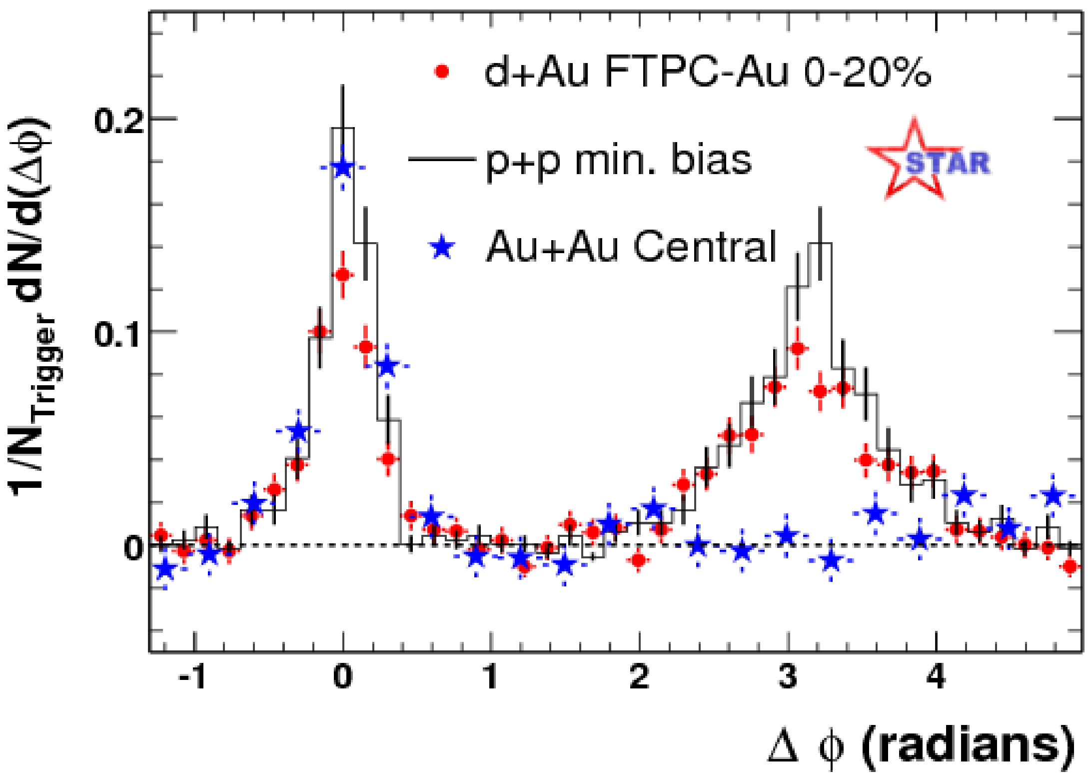

Figure 2.1: Dihadron correlations shown as a function of $\Delta\phi$ for $p+p$ (black histogram), central p+Au (red circles) and central Au+Au (blue stars) collisions at $\sqrt{s_{NN}} = 200$ GeV [22, 46].

2.2 Higher Order Flow Coefficients

In addition to jet quenching studies, dihadron correlations can be used for flow measurements as well. When constructing dihadron correlations in heavy-ion collisions, a prominent long-range ($\Delta\eta > 1$) structure is visible in the low-p_{T} region. This can be seen in Fig. 2.2 which shows 2-D dihadron correlations as a function of $\Delta\phi$ and $\Delta\eta$ for 12 different centrality bins with $3.0 < p_{\mathrm{T}}^{\mathrm{trig}} <$ 3.5 GeV/c and $1.0 < p_{\mathrm{T}}^{\mathrm{assc}} < 1.5$ GeV/c in Pb+Pb collisions at $\sqrt{s_{NN}} = 2.76$ TeV [47].

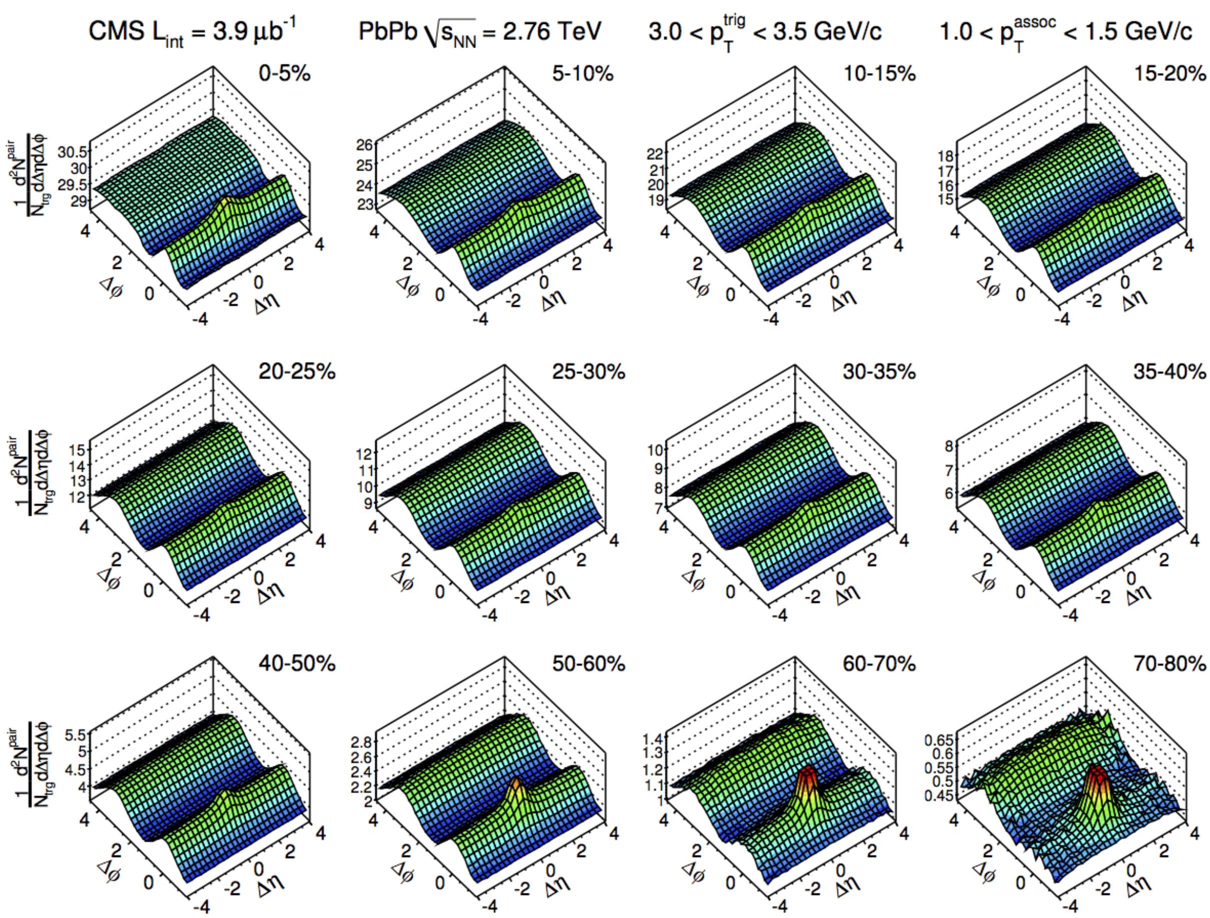

Figure 2.2: 2-D dihadron correlations as a function of $\Delta\eta$ and $\Delta\phi$ with $3 < p_{\mathrm{T}}^{\mathrm{trig}} < 3.5$ GeV/c and $1 < p_{\mathrm{T}}^{\mathrm{assc}} < 1.5$ GeV/c in twelve different centrality bins for Pb+Pb collisions at $\sqrt{s_{NN}} =$ 2.76 TeV [47].

This long-range structure is attributed to flow-like effects in heavy-ion collisions. In addition to elliptic flow (v_2), discussed in the previous chapter, there are contributions from higher-order flow coefficients, v_n, due to fluctuations in the initial collision geometry, which arise due to the quantum nature of the nucleus [48]. These coefficients can be measured by fitting the long-range structure of the dihadron correlations with a Fourier series. The results indicate that higher order flow terms are non-negligible in heavy-ion collisions and can explain the interesting long-range structure seen. The flow coefficients, v_2-v_5, are shown in Fig. 2.3 as a function of N_{part} in three different $p_{\mathrm{T}}^{\mathrm{trig}}$ bins and with $1 < p_{\mathrm{T}}^{\mathrm{assc}} < 3$ GeV/c [47]. The centrality dependence of v_2 is very apparent here but the higher order coefficients, $v_3 - v_5$, are largely independent of centrality. This is expected since initial-state fluctuations are related to the individual nuclei, not the collision geometry.

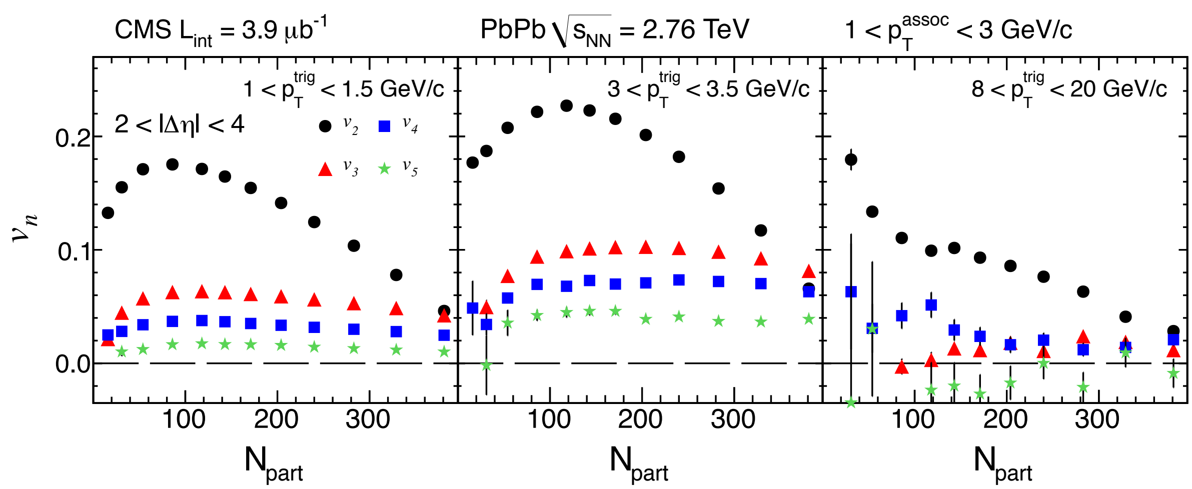

Figure 2.3: Flow coefficients, v_2-v_5, as a function of N_{part} with $1 < p_{\mathrm{T}}^{\mathrm{assc}} < 3$ GeV/c in three different $p_{\mathrm{T}}^{\mathrm{trig}}$ bins in Pb+Pb collisions at $\sqrt{s_{NN}} = 2.76$ TeV [47].

2.3 Surprises in $p+p$ and p+Pb Collisions

In addition to heavy-ion collisions, dihadron correlations are used to study $p+p$, p+Pb, and p+Au (shown in Fig. 2.1) collision systems as well. In fact, one of the first results from the LHC was a study of the dihadron correlation functions in high-multiplicity $p+p$ collisions at $\sqrt{s} = 7$ TeV. The results, shown in Fig. 2.4, show a near-side ($\Delta\phi \sim 0$) long-range $|\Delta\eta| < 4$ ridge in the underlying event structure [49]. This is indicative of some type of collective behavior that had never been observed before. The cause of this long-range ridge structure is still unknown and is a major open question in the high energy physics community. It is postulated that it could be from the formation of a small QGP medium in the highest multiplicity $p+p$ collisions.

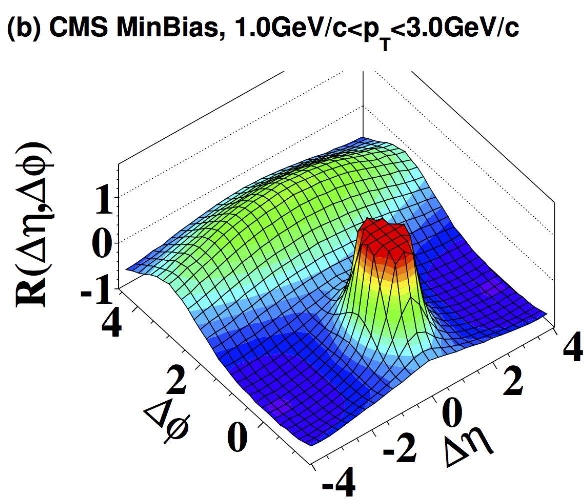

(a) Minimum-bias

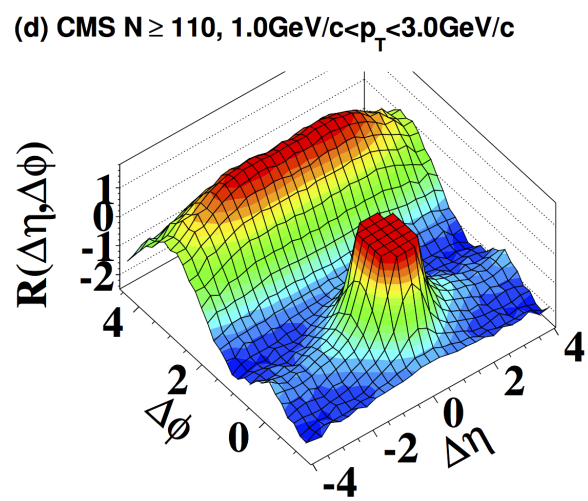

(b) $N_{trk} > 110$

Figure 2.4: 2-D dihadron correlations as a function of $\Delta\eta$ and $\Delta\phi$ in $p+p$ collisions at $\sqrt{s} = 7$ TeV. The left plot is minimum-bias data and the right plot is from a high-multiplicity trigger with $N_{\text{trk}} > 110$ [49].

The first p+Pb collisions at 5.02 TeV were recorded at the LHC in 2013. Again, one of the first major results were from dihadron correlations in high-multiplicity events [50]. These results also showed the appearance of a near-side long-range ridge structure. Further investigation found that there were significant v_2 and v_3 values associated with this structure that were much higher than expected for a p+Pb collision system [51]. The dihadron correlation function with $1 < p_{\mathrm{T}}^{\mathrm{assc}}, p_{\mathrm{T}}^{\mathrm{trig}} < 3$ GeV/c and $220 \leq N_{\mathrm{trk}} < 260$ in p+Pb events at $\sqrt{s_{NN}} = 5.02$ TeV is shown on the left in Fig. 2.5. The right side of this figure shows the v_2 values calculated from two and four-particle correlations with $0.3 < p_{\mathrm{T}} < 3$ GeV/c as a function of N_{part}. The results are compared to a similar (but not identical) ATLAS analysis [52] and shows decent agreement. Both sets of data indicate a non-negligible elliptic flow value for high-multiplicity p+Pb collisions. The explanation of this phenomenon remains an open question in the field.

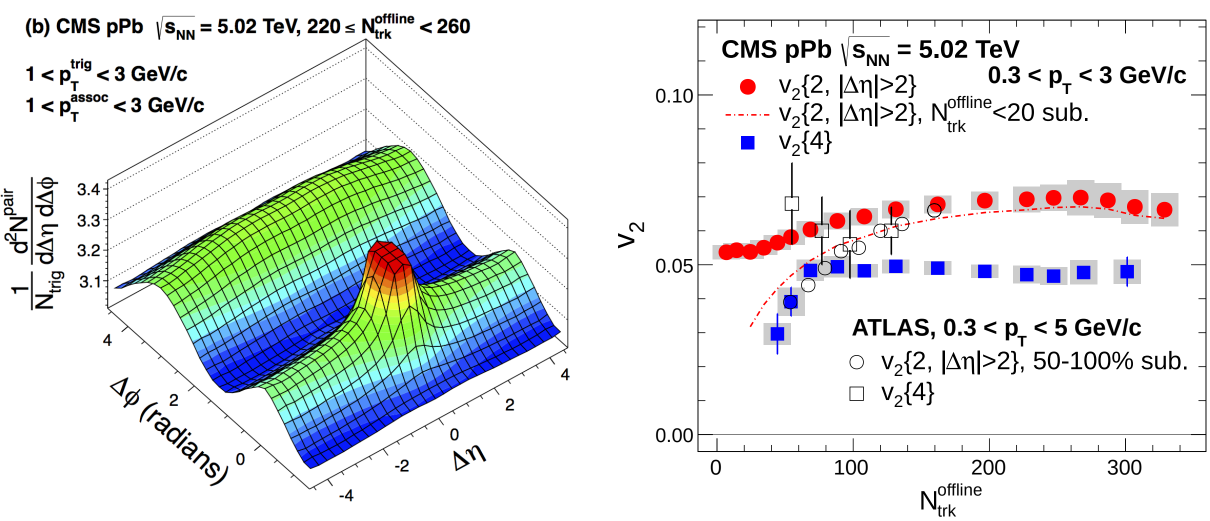

(a) 2-D correlation function

(b) v_2 vs N_{trk}

Figure 2.5: Right: 2-D dihadron correlations as a function of $\Delta\eta$ and $\Delta\phi$ with $1 < p_{\mathrm{T}}^{\mathrm{trig}}, p_{\mathrm{T}}^{\mathrm{assc}} < 3$ GeV/c and $220 < N_{\mathrm{trk}} < 260$ for p+Pb collisions at $\sqrt{s_{NN}} = 5.02$ TeV. Left: v_2 from two (red) and four-particle (blue) correlations with $0.3 < p_{\mathrm{T}} < 3$ GeV/c as a function of N_{trk}. The v_2 results from a similar (but not identical) ATLAS analysis are shown in the open white symbols. [51, 52].

Chapter 3

Experimental Facilities

The data used in this analysis were collected from the Compact Muon Solenoid (CMS) experiment. This is a large, multi-purpose detector that operates at the Large Hadron Collider (LHC) at the European Organization for Nuclear Research (CERN) outside of Geneva, Switzerland. Even though it was built mainly as a $p + p$ detector, the CMS experiment is extremely well suited for Pb+Pb studies. In particular, the superconducting solenoidal magnet and the extremely precise silicon tracker provide excellent high-p_{T} resolution for charged tracks which allows us to significantly extend the p_{T} range for heavy-ion analyses.

3.1 The Large Hadron Collider

The Large Hadron Collider (LHC) is the world's largest and most powerful particle accelerator ever built. It provides the most energetic $p + p$ and Pb+Pb collisions ever produced in a laboratory setting at 8 TeV and 2.76 TeV per nucleon, respectively (the LHC is currently ramping up to provide 13 TeV $p+p$ collisions) [53]. It is the largest machine ever built and took over two decades to design and build [54].

Although the main purpose of the LHC is to provide $p + p$ collisions, it was designed from its inception to be able to provide high energy heavy-ion collisions as well. For roughly one month during every operational year the LHC collides $^{208}_{82}$Pb ions. This particular type of Pb nucleus is well suited for heavy-ion collisions since it is doubly magic (containing 126 neutrons and 82 protons, both of which are closed nuclear shells) and thus highly spherical, which simplifies the collision geometry.

The peak collision energy for the Pb+Pb collisions is lower than that for $p+p$ collisions. This is because each Pb nucleus contains 126 neutrons that do not have an electromagnetic charge, which makes them impossible to accelerate on their own using RF waves in the synchrotron. Thus, the charge of the Pb nucleus is +82 but the mass number, A, is 208, meaning it is ~ 208 times more massive than the proton. This means that the maximum collision energy for ^{208}Pb is 39% (82/208) of the maximum energy for $p+p$ collisions. Since the maximum center-of-mass collision energy for $p+p$ collisions in 2011 was 7 TeV, the maximum center-of-mass collision energy for Pb+Pb collisions is 2.76 TeV per nucleon (574 TeV total) for the 2010 and 2011 heavy-ion runs at the LHC.

By the end of 2013, prior to the first scheduled long shutdown for maintenance and upgrades, the LHC had delivered a total integrated luminosity of 23.2 fb^{-1} for $p+p$ collisions at $\sqrt{s} = 8$ TeV, 160 μb^{-1} for Pb+Pb collisions at $\sqrt{s_{NN}} = 2.76$ TeV, and 31 nb^{-1} for p+Pb collisions at $\sqrt{s_{NN}} = 5.02$ TeV [55].

3.1.1 Design

The LHC is a synchrotron with two superconducting rings that accelerate charged hadrons in opposite directions. The LHC was installed in the existing 26.7 km tunnel that previously housed the Large Electron-Positron Collider (LEP) at CERN. The tunnel itself is between 45 m and 170 m underground and has four interaction points where the beams are focused to collide with each other. These four interaction points correspond to the locations of the four main experiments at the LHC (shown in Fig. 3.1 [56]): A Toroidal LHC Apparatus (ATLAS), Compact Muon Solenoid (CMS), LHC-beauty (LHCb), and A Large Ion Collider Experiment (ALICE) [54].

The high energy beams of protons and lead ions are guided around the circumference of the LHC using a series of 1,232 superconducting dipole magnets. These bending magnets need to be operated below 10 K ($-263.2°C$) in order to reach the superconducting state. In order to provide enough bending power required to keep 7 TeV protons inside of the 27 km ring the magnets need to be able to produce a 8.3 T magnetic field, which requires an actual operating temperature of 1.9

Figure 3.1: An aerial view of the LHC and CERN. The locations of the four major experiments at the LHC (CMS, ATLAS, LHCb, and ALICE) are shown. Lake Geneva and Mont Blanc are also visible in the background [56].

K ($-271.3°C$) [53–55].

The beams are kept focused by a series of 393 quadrupole magnets that provide a magnetic field of 6.85 T at an operating temperature of 1.9 K. In addition, there are a number of specialized superconducting and non-superconducting magnets that are used to focus the beams for optimal luminosity at the interaction points where ATLAS and CMS are located [53, 54].

3.1.2 $p + p$ Acceleration Chain

The LHC is really just the last phase in the long acceleration process required to accelerate protons and lead ions up to 8 TeV and 2.76 TeV, respectively. By the time the protons are injected into the LHC from the Super Proton Synchrotron (SPS) they are already at 450 GeV. The full accelerator complex at CERN used for the acceleration of protons and lead ions into the LHC is shown in

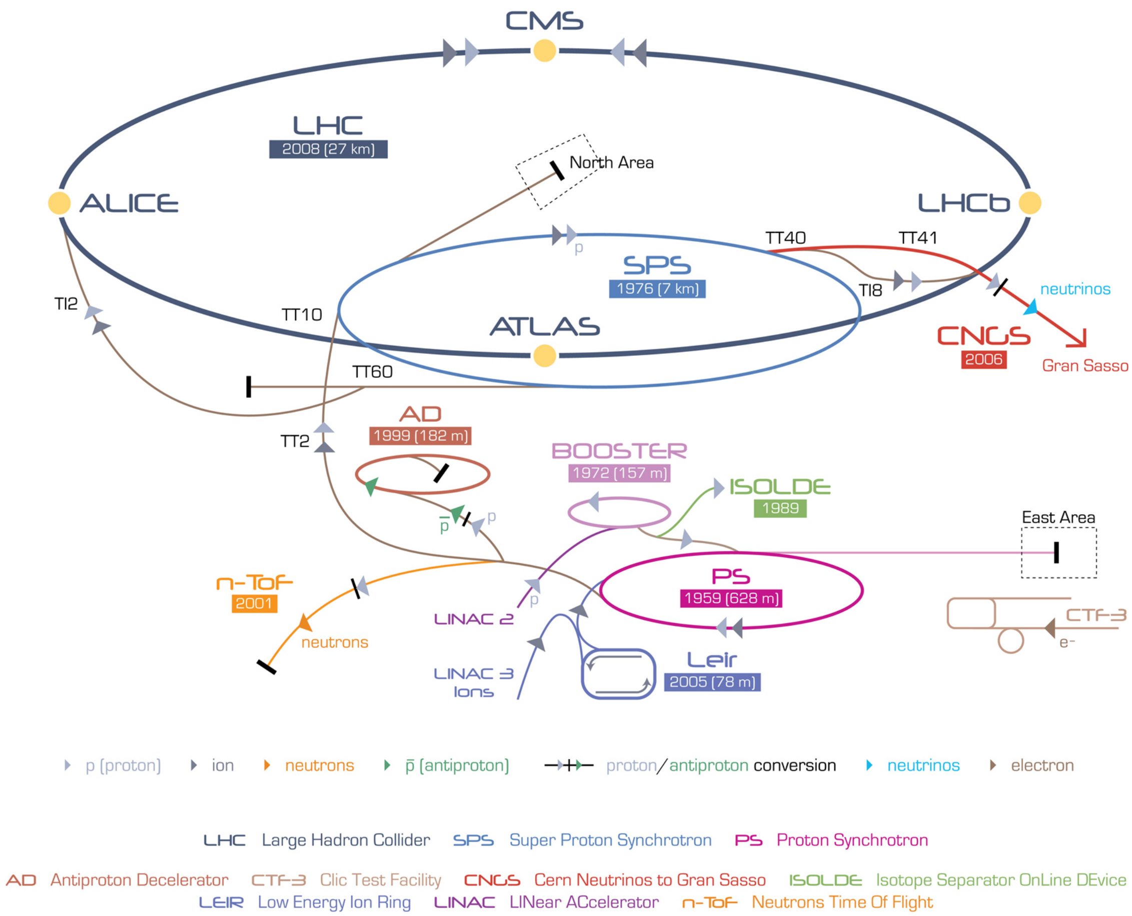

Figure 3.2: A diagram of the accelerator complex at CERN. The various steps in the $p+p$ and Pb+Pb acceleration process are indicated by the various colors [55].

Fig. 3.2 [55].

All of the protons that are collided in the LHC come from a 5 kg bottle of hydrogen gas. The hydrogen atoms are pulled apart into their constituent protons and electrons by placing the gas inside a sufficiently strong electric field. The protons are then accelerated by the Linear Accelerator 2 (Linac 2) up to 50 MeV before being injected into the Proton Synchrotron Booster (PSB). The PSB then accelerates the protons up to 1.4 GeV before being injected into the Proton Synchrotron (PS). The PS was actually CERN's first synchrotron, beginning operation in 1958, and was for a brief time the world's most energetic particle accelerator. The PS accelerates the protons up to 25 GeV before injecting them into the SPS. The SPS is the second largest accelerator at CERN, having a circumference of almost 7 km, and was used, among other things, for the discovery of the $W^{\pm}$

and Z bosons by the UA1 and UA2 experiments [57, 58]. In the SPS the protons are accelerated up to 450 GeV where they are finally injected into the LHC where they will be accelerated up to the desired collision energy [53, 54].

3.1.3 Pb+Pb Acceleration Chain

The acceleration chain for heavy-ions is slightly different than that for protons. The process begins by heating up a source of pure ^{208}Pb to about $500°C$ to vaporize some of the atoms. As with the hydrogen gas, an electric field is applied to rip off a few of the electrons from the vaporized Pb atoms, ionizing them. These are then accelerated by the Linear Accelerator 3 (Linac 3) up to about 4.5 MeV per nucleon.

After the Linac 3, the ions pass through a number of stripping foils on their way to the Low Energy Ion Ring (LEIR). By the time they make it into the LEIR all of the remaining ions have a charge of +54. From here the ions are accelerated up to 72 MeV per nucleon before being injected into the PS, where they follow the same remaining acceleration process as the proton beams. The PS accelerates the ions up to 5.9 GeV per nucleon and strips the last of the electrons away from the ions before they get injected into the SPS. The SPS then accelerates the ions up to 177 GeV per nucleon before they are finally injected into the LHC where they are accelerated the rest of the way up to 2.76 TeV [53, 59].

A summary of the various accelerator parameters for $p+p$ and Pb+Pb collisions at peak luminosity is shown in Table 3.1 [53–55].

Table 3.1: LHC beam parameters for $p+p$ and Pb+Pb collisions during peak luminosity [53–55].

Beam Parameters	$p+p$ **Collisions**	**Pb+Pb Collisions**
Maximum Collision Energy	8 TeV	574 TeV (2.76 TeV per nucleon)
Number of Bunches	2808	592
Number of protons/ions per bunch	1.15×10^{11}	7×10^{7}
Bunch Spacing	25 ns	100 ns
Peak Luminosity	1.0×10^{34} cm^{-2}s^{-1}	1.0×10^{27} cm^{-2}s^{-1}

3.2 The Compact Muon Solenoid Detector

The Compact Muon Solenoid (CMS) detector, shown in Fig. 3.3, is a general-purpose particle detector designed to operate at the LHC and to conduct a wide variety of new physics searches. One of its main goals was to search for the elusive Higgs boson and on July 4th, 2012, along with the ATLAS collaboration, the announcement of the discovery of a new particle consistent with the Higgs was made at CERN, at which I was fortunate enough to be present [4, 5]. In addition to the search for the Higgs, the CMS detector is used to study other aspects of the Standard Model, to look for physics beyond the Standard Model such as supersymmetry and potential dark matter particles, and to study to the strongly-coupled nuclear matter created with heavy-ion collisions.

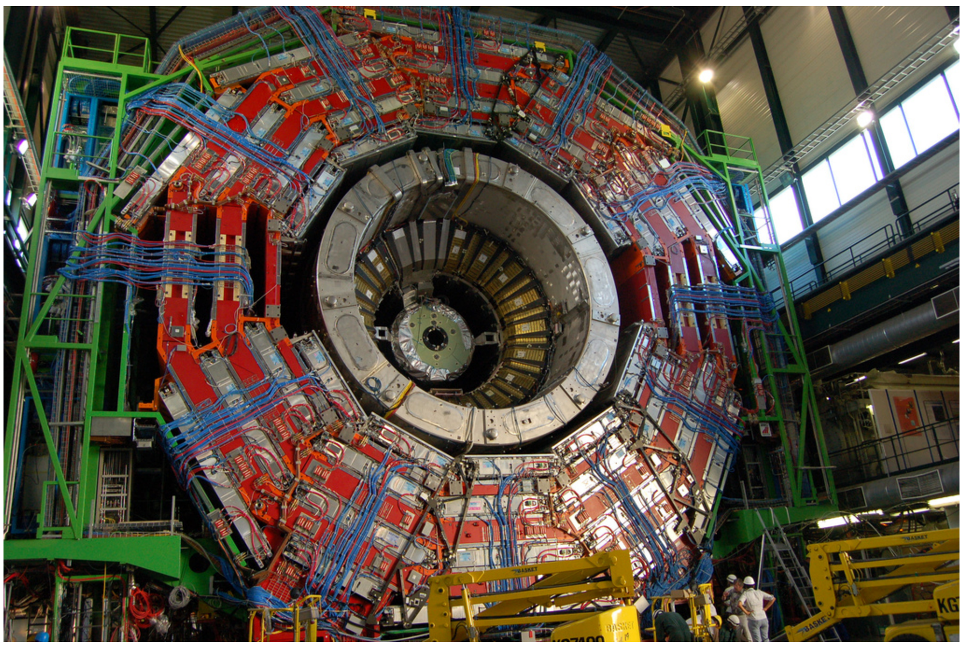

Figure 3.3: A picture of one end of the barrel region of the CMS detector [60].

The CMS detector was built to be very robust and versatile since it had a number of different physics objectives in mind when it was being designed and commissioned. It consists of a number of different subdetectors that all measure different aspects of high energy collisions that can then be combined to provide as complete a picture as possible of the underlying physics governing the interactions.

3.2.1 Overview of the CMS Experiment

The CMS detector was designed around the goals of the LHC; namely, to deal with high luminosity, high energy collisions. In peak operation with bunch crossings happening every 25 ns and up to 20 collisions occurring per crossing, the CMS detector needed to be fast and accurate enough to distinguish between 20 individual yet simultaneous collisions. The details of the design can be summed up with four main goals [60]:

- Good muon identification and momentum resolution out to high p_{T}. In addition, the ability to distinguish between μ^{+} and μ^{-} up to 1 TeV/c.

- Good charged particle reconstruction and momentum resolution with the ability to use fast online tracking in triggers. Accurate vertex resolution is also necessary for high pile-up scenarios.

- Good electromagnetic energy resolution for accurate reconstruction of electrons and photons. Good π^{0} rejection is also necessary for accurate dielectron and diphoton mass reconstruction.

- Hermetic hadronic energy coverage for dijet reconstruction and accurate missing-transverse-energy resolution.

These requirements resulted in the construction of the CMS detector. The "C" stands for "Compact" since all of the primary tracking, electromagnetic and hadronic calorimetry fit within the large solenoidal magnet. The engineering ingenuity that went into this is beyond the scope of this thesis but resulted in a detector with an average density of just under 3000 kg/m^{3}. The "M" stand "Muon" since the extensive muon system built around the magnet gives the CMS detector unparalleled muon identification and reconstruction capabilities. Finally, the "S" stands for "Solenoid" since the large magnetic field provided by the solenoidal magnet provides high-p_{T} resolution that is essential for measuring collisions at energies reached by the LHC [61].

A to-scale diagram of the detector and its major subdetectors is shown in Fig. 3.4. As with most modern particle detectors, CMS is built in layers with successive subdetectors being built around the others. As seen in the figure, the innermost layer of the CMS detector (the subdetector

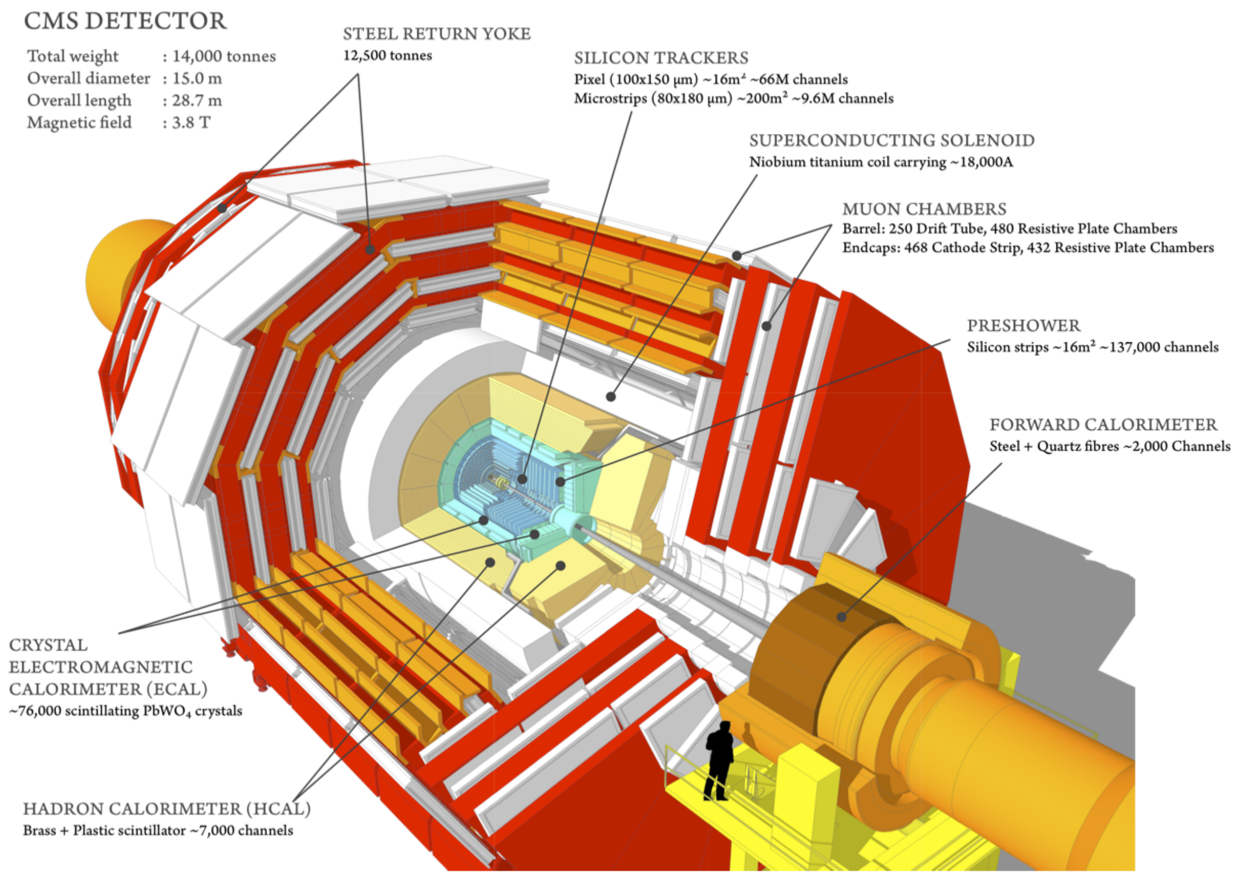

Figure 3.4: A to scale diagram of the CMS detector. The various subsystems are indicated and an averaged sized human is placed in the foreground to help provide a sense of scale [60].

closest to the interaction point) is the inner silicon tracker. The tracker itself consists of two main parts: the pixel detector and the strip detector. The pixel detector consists of the inner three layers of the tracker that contains silicon pixels with extremely high granularity providing accurate 3-D spatial information about each hit. The strip detector consists of the next 11 layers of the tracker consisting of long silicon strips that provide 2-D spatial information about each hit. Together, the pixel and strip detectors provide extremely fast and accurate tracking for charged particles [60,61]. They will be discussed in more detail in Sec. 3.2.2.

3.2.1.1 Electromagnetic Calorimeter

Outside of the tracker sits the electromagnetic calorimeter (ECAL). This is made of lead tungstate crystals, $PbWO_4$, that are extremely dense, have a short radiation length, and scintillate when electrons or photons pass through. The energy of the incident electron or photon is directly proportional to the amount of scintillation light, or number of photons produced, which can be accurately measured by avalanche photodetectors attached to the end of each crystal. The total length of each crystal in the barrel region of the ECAL is 25.8 radiation lengths, ensuring that essentially all of the photons and electrons produced from collisions will be absorbed [60, 61].

In total, the ECAL contains about 76,000 lead tungstate crystals. The barrel region of the ECAL covers $|\eta| < 1.48$ and the endcap covers $1.48 < |\eta| < 3.0$ [60]. Figure 3.5 shows the lead tungstate scintillating crystals being installed on one of the ECAL endcaps [62]

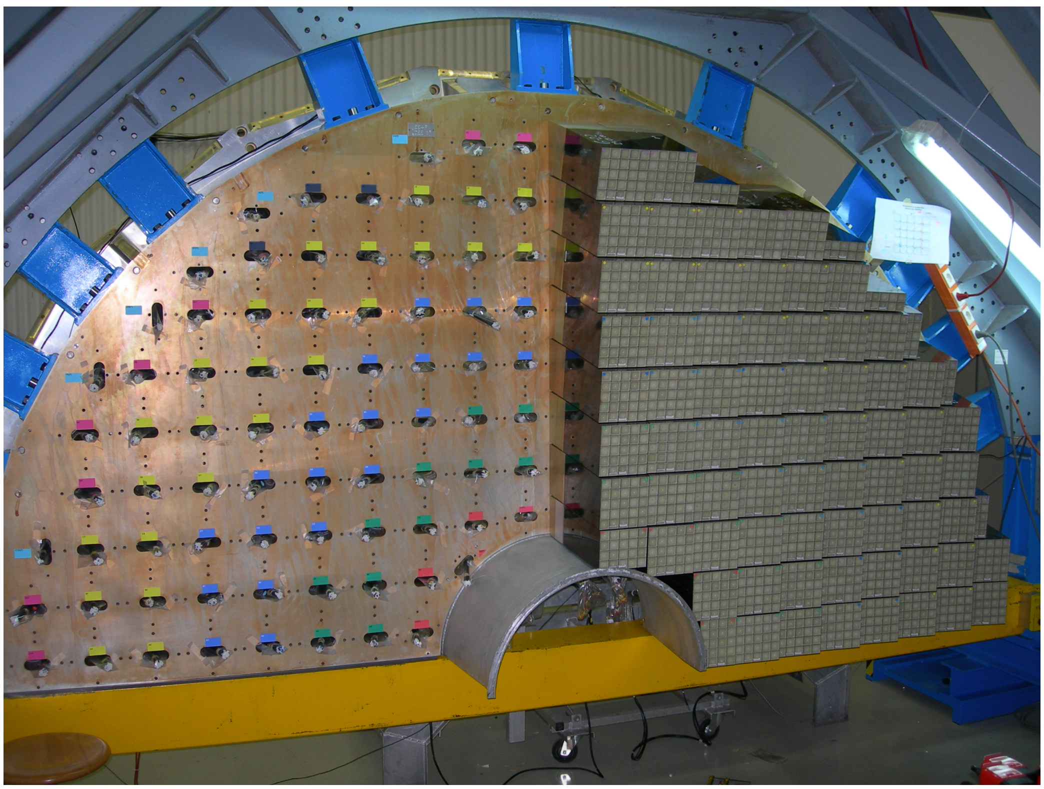

Figure 3.5: Lead tungstate scintillating crystals being installed on one of the ECAL endcaps [62].

3.2.1.2 Hadronic Calorimeter

Outside of the ECAL sits the hadronic calorimeter (HCAL). The HCAL is a sampling calorimeter that consists of alternating layers of brass absorber and plastic scintillator. When a hadronic particle passes through a sufficient amount of the dense absorber material it will interact with a nucleus and produce a shower of secondary particles. As these secondary particles pass through the scintillator layers they emit flashes of blue-violet light that are absorbed by tiny optical fibers embedded in the HCAL. After passing through the scintillator the secondary particles will pass through another absorber layer and cause their own shower of secondary particles to be picked up by the next scintillator layer. The number of secondary particles produced, measured by the amount of light emitted by the scintillators, is used to determine the energy of the original incident hadron.

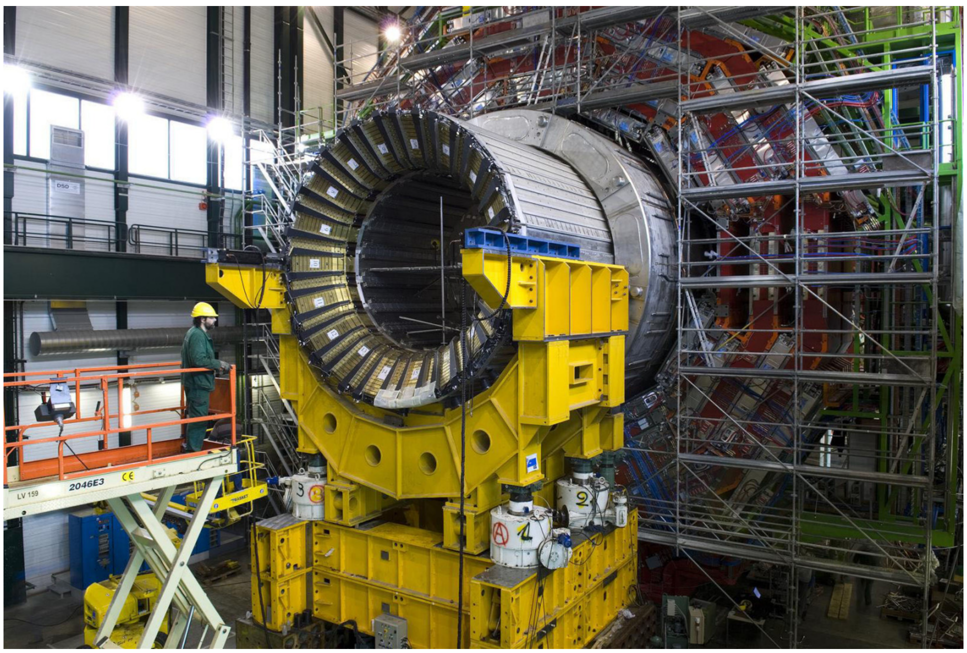

Figure 3.6: The barrel region of the HCAL being installed in the CMS detector [63].

In order to ensure that a hadron-nucleus interaction occurs in each absorbing layer, a material with a small nuclear interaction length was chosen. The specific composition of the brass used in the HCAL is 70% Cu and 30% Zn and has a nuclear interaction length of 16.42 cm. At midrapidity this gives the HCAL a total thickness of 5.82 nuclear interaction lengths with the ECAL providing an additional 1.1 nuclear interaction lengths of material [60, 61].

Figure 3.6 shows the barrel region of the HCAL being installed into the CMS detector where it fits snugly inside of the solenoidal magnet [63]. The 36 wedges that make up the barrel region, each weighing 26 tons, are clearly visible in the photo. The barrel region of the HCAL covers $|\eta| < 1.4$

and the endcap region covers from $1.3 < |\eta| < 3.0$ [60].

An interesting side-note about the brass used in the HCAL endcap detector is that it came from used artillery cartridges from the Russian Navy during World War II. In total over one million shells were used to provide enough brass for the endcaps [61].

3.2.1.3 Superconducting Solenoidal Magnet

The inner tracker, ECAL, and HCAL all sit within the large solenoidal magnet. The magnet is capable of providing a peak field of 4 T, about 100,000 times stronger than the magnetic field of the Earth. With a diameter of six meters it is the largest superconducting magnet ever built. The strong magnetic field produced by the magnet causes charged particles to bend more due to the Lorenz force. This allows the CMS detector to have extremely accurate momentum resolution for high-p_{T} particles ($\sim 1\%$ for charged particles with $p_{\mathrm{T}} = 100$ GeV/c) [61, 64].

Figure 3.7: The superconducting solenoidal magnet being installed inside of the iron return yoke in the CMS detector [65].

Constructing a magnet that was powerful enough to produce a 4 T field and large enough to fit all of the barrel calorimetry and tracking provided a number of engineering challenges. The solenoid needed four layers of winding NbTi conductor in order to produce the desired 4 T magnetic field, twice as many layers as any other superconducting magnet used in high energy physics experiments. The magnet also had to be built with a reinforced conductor so it could support its own weight, 220 tons, and withstand the force of its own magnetic field. The nominal current applied to the magnet is 19.14 kA giving it a total stored energy of 2.6 GJ. During operation the magnet is only applied a current of 18.16 kA, providing a 3.8 T field with 2.3 GJ of stored energy. This is done to increase the longevity of the magnet [60].

Outside of the magnet is an iron return yoke that helps guide and maintain as close to a uniform field as possible outside of the solenoid. In addition, the return yoke provides most of the structural support for the rest of the detector. In total, the return yoke consists of 12,000 tons of iron, almost twice the amount used in the Eiffel Tower.

In the barrel region of the detector the magnetic field is extremely uniform, even outside of the magnet due to the presence of the iron return yoke. This can be seen in Fig. 3.8 which shows the magnetic field strength on the left and the field lines on the right, as measured by cosmic rays [66]. In the endcaps the magnetic field becomes far less uniform, making the track reconstruction for charged particles more difficult in the forward regions.

3.2.1.4 Muon Systems

Outside of the magnet lie the muon systems. Muons have a small interaction cross section with matter. They are thus able to penetrate through the inner layers of the detector. They are essentially minimum ionizing particles in the expected p_T range for particles emitted from collisions at LHC energies. This can be seen in Fig. 3.9 which shows the stopping power, $\langle -dE/dx \rangle$, of muons in copper as a function of momentum [67]. The energy loss in this region is typically described by the Bethe-Bloch formula which is dominated by atomic excitation and ionization at low p_T and radiative processes at high p_T. In general, the amount of energy loss is inversely proportional to the mass of the interacting particle and since $m_\mu/m_e \approx 200$, muons will interact significantly less with

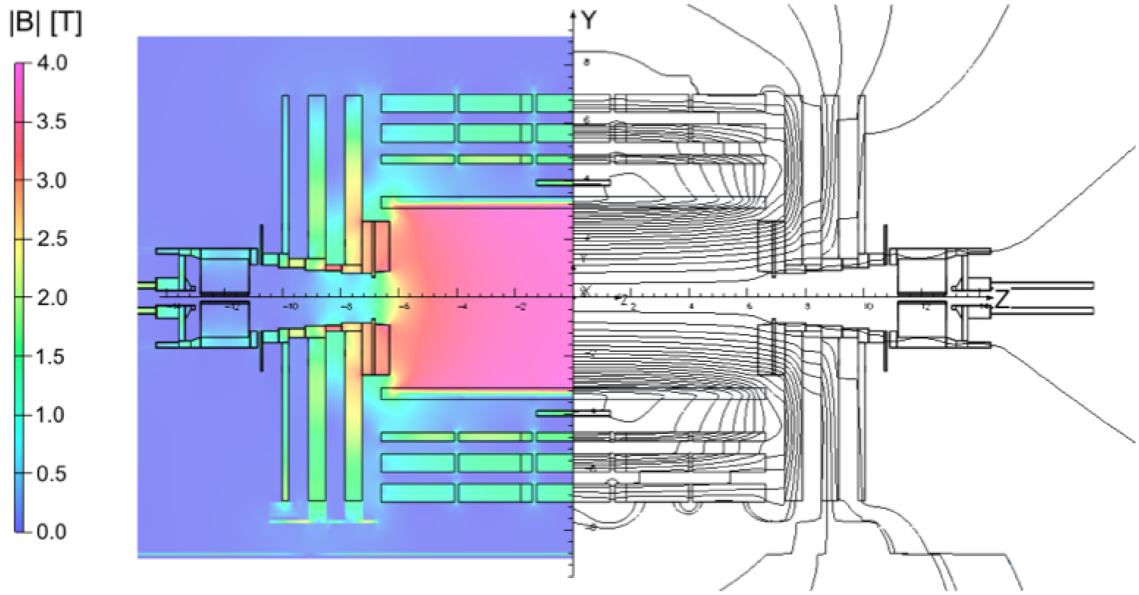

Figure 3.8: A map of the magnetic field strength (left) and the field lines (right) in the CMS detector [66].

matter than electrons [67]. In addition, muons do not have a color charge so they won't interact via the strong force like neutral hadrons which otherwise pass through the ECAL largely unaffected.

These properties make muons unique in that they are, to good approximation, the only charged particles that pass through all of the layers of the detector, including the magnet, and make it into the muon detectors (hence their name). It is worth noting that neutrinos will also escape undetected and a small number of "punch through" hadrons will also make it into the muon detectors. These are easy to distinguish though since neutrinos don't leave any trace in the detector (as opposed to the charged track of the muons) and the punch through hadrons will get absorbed by the inner layers of the iron return yoke, making it easy to reject them as muon candidates.

The muon systems consist of a series of different tracking detectors placed between various layers of the iron return yoke (pictured in red in Fig. 3.4). Around the barrel region of the detector ($|\eta| < 1.2$) there are drift tube (DT) chambers and resistive plate chambers (RPC). The endcap muon system ($0.9 < |\eta| < 2.4$) consists of RPCs as well as cathode strip chambers (CSC). All of these systems are able to detect the charge of the muon as it passes through them so even though it does not lose much energy in the detectors we can still determine its trajectory and, therefore, its momentum. In total there are 250 DTs, 610 RPCs, and 540 CSCs in the CMS muon system [60,61].

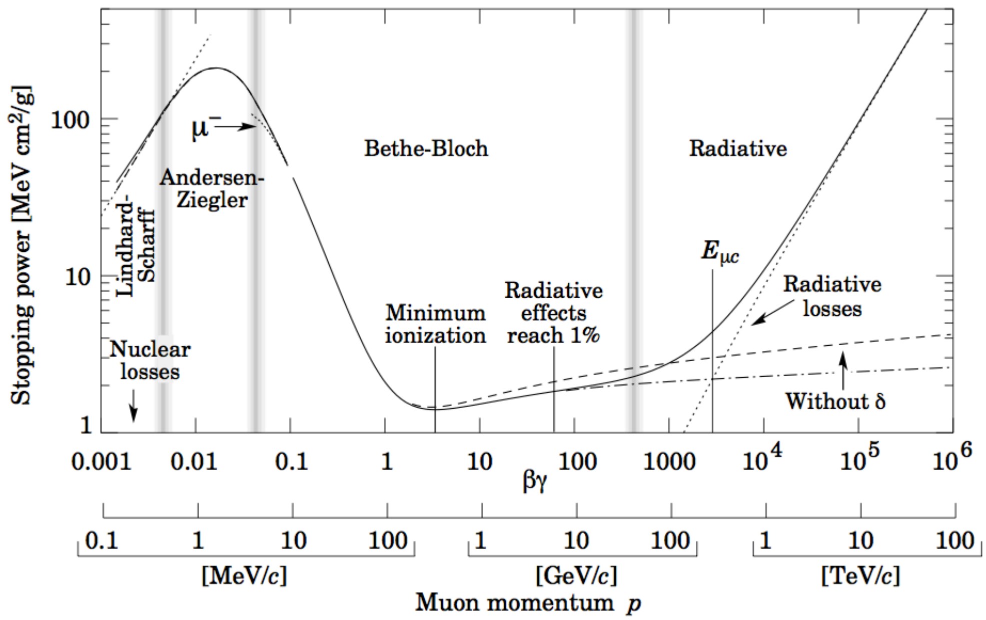

Figure 3.9: Stopping power or energy loss, $\langle -dE/dx \rangle$, as a function of momentum for muons passing through copper [67].

The alternating layers of iron return yoke and muon detectors (RPCs and DTs) around the barrel of the CMS detector can be seen in Fig. 3.3. The tracker, magnet, and calorimeters are also visible. The total diameter of the detector is about 15 m compared to the 25 m ATLAS detector, making it very "compact" (at least as far as state-of-the-art, all-purpose particle detectors go).

3.2.1.5 Forward Hadronic Calorimeter

Two forward hadronic calorimeters (HF) are located outside of the muon endcaps, roughly 11 m on either side of the interaction point, covering the pseudorapidity region $2.9 < |\eta| < 5.2$. These improved the CMS detectors capabilities for measuring missing E_T, which is a crucial measurement for some Higgs searches, by making the calorimetry almost completely hermetic. They will also improve the identification and reconstruction of forward jets, an important signature for some heavy Higgs searches and an important background veto in certain SUSY searches. Additionally, the HF detectors provide a way to measure transverse energy, or centrality (Sec. 4.3), in heavy-ion events that is uncorrelated with measurements in the rest of the detector [68].

Since the majority of the particle and energy flux coming from the high energy collisions will

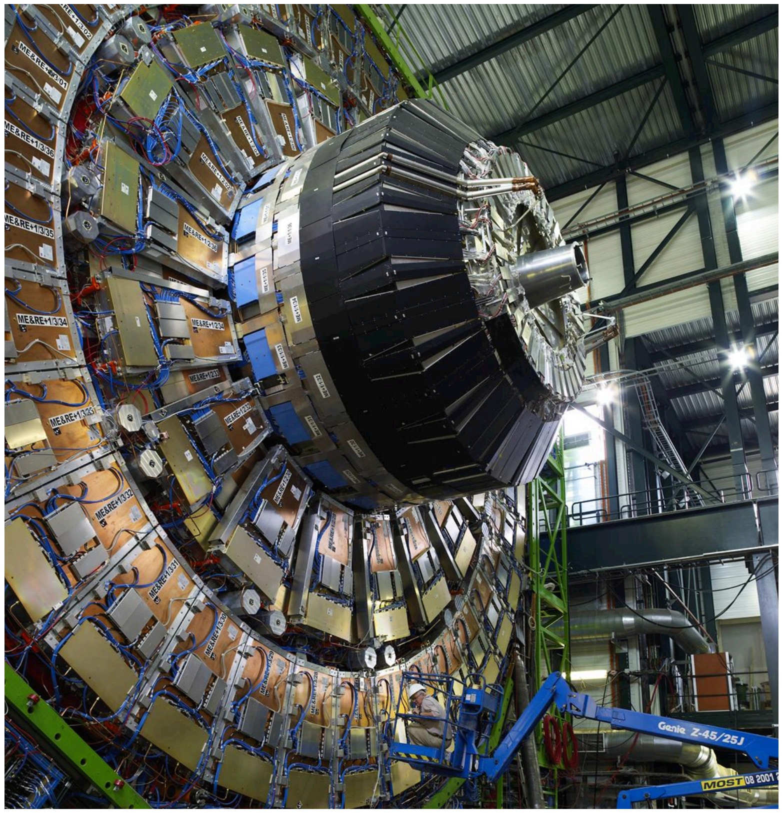

Figure 3.10: One of the CMS forward hadronic calorimeters (HF) attached to the endcap of the detector [66].

be directed in the forward regions - on average, about 760 GeV will be deposited into the HFs per $p + p$ collision compared to 100 GeV in the rest of the detector - the detectors needed to be designed to withstand an unprecedented amount of radiation damage. For this reason a Cherenkov detector built with quartz-fibers, which are very resistant to radiation damage, embedded in a copper absorber was chosen [60, 68].

The photomultiplier tubes (PMT) that measure the Cherenkov radiation, which determines the amount of deposited energy, are shielded from the intense radiation by a 40 cm slab of steel and borated polyethylene. The entire HF is surrounded by 30 cm of steel, 30 cm of magnetite concrete, and 10 cm of borated polyethylene to protect the readout electronics from the high levels of radiation. The HF has a total depth of 1.65 m or about 10 nuclear interaction lengths (enough to sufficiently contain and measure a Cherenkov signal from a 1 TeV hadron) [60, 68]. A picture of one of the HF detectors attached to the muon system endcap is shown in Fig. 3.10 [66].

Combining the information from all of the subdetectors provides an almost complete picture of the event. Figure 3.11 shows how various particles are picked up by different subdetectors. The charged particles, shown in solid red, green, and light blue, all have curved trajectories due to the presence of the magnetic field and are picked up by the inner tracker. The electron, the red curve, leaves a curved track in the tracker and then deposits all of its energy in the ECAL. The photon, dashed dark blue, is invisible to the tracker since it does not have an electric charge but still ends up depositing all of its energy in the ECAL. Charged hadrons, green, leave a curved track in the tracker but pass through the ECAL (where they still lose some energy) and end up depositing all of their energy in the HCAL. Neutral hadrons, dashed green, pass through the tracker and ECAL unaffected but end up depositing all of their energy in the HCAL. Muons leave a curved track in the tracker but pass through the ECAL, HCAL, and magnet before they leave additional track information in the muon systems before exiting the detector. Neutrinos are completely invisible to the detector but are identifiable in certain events due to the presence of missing transverse energy/momentum. This is only possible to detect in a reliable fashion due to the hermetic nature of the CMS calorimetry, discussed previously.

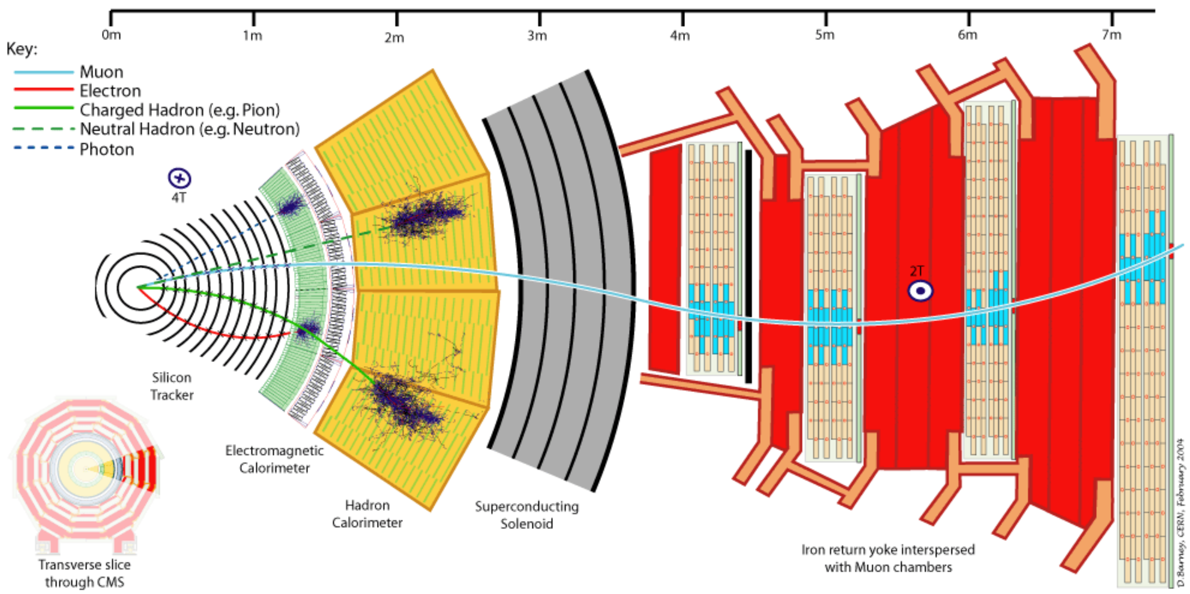

Figure 3.11: A diagram showing a transverse (to the beamline) slice of the CMS detector and the various subdetectors. Examples of how the different subdetectors help identify different types of particles are shown by the different colored trajectories passing through different parts of the detector [61].

3.2.2 Sillicon Tracker

Dihadron correlations deal with the spatial distribution of charged particles produced in high energy collisions, as discussed in the previous chapter. This is done by reconstructing the trajectory of each charged particle that passes through the detector (see Chapter 5.1 for more detail on tracking). Therefore, the CMS tracking detector is paramount to any dihadron correlation analysis.

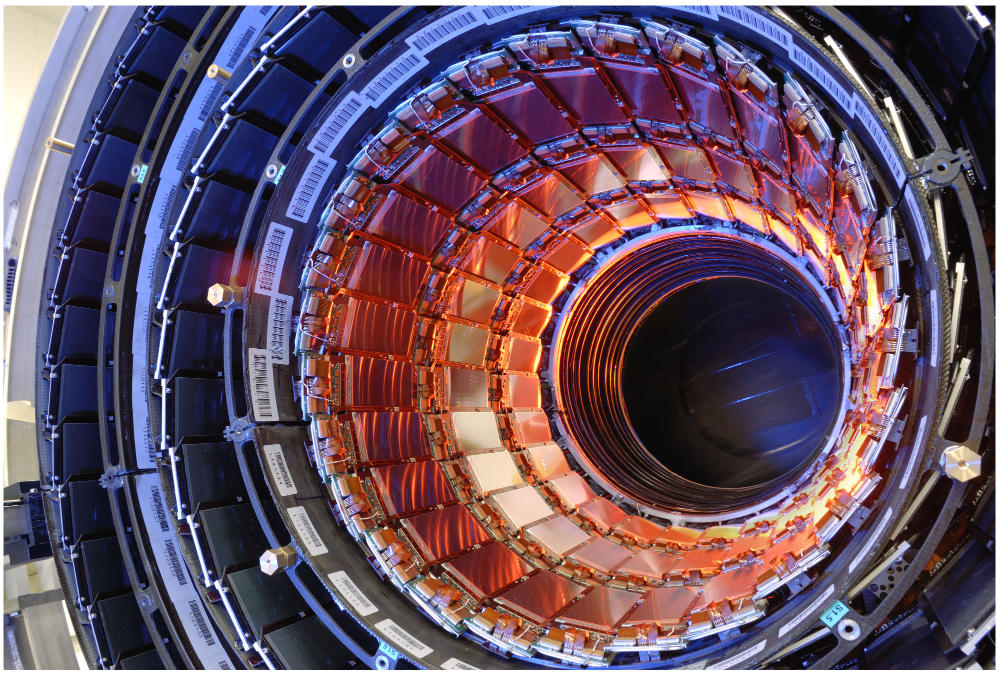

Figure 3.12: A picture of the silicon strip detectors in the barrel region of the tracker [69].

3.2.2.1 Tracking Requirements

The CMS tracker was designed with a number of physics goals in mind which can essentially be boiled down to three general requirements: it had to be accurate, fast, and resistant to radiation damage. With the expectation of high pile-up conditions (estimated to reach up to 20 p+p collisions per bunch crossing) at the LHC the ability to distinguish between multiple collision (primary) vertices was crucial, which requires an extremely accurate tracking detector. Furthermore, since the expected bunch spacing at the LHC was 25 ns (during the design phase) the tracker was also required to have an extremely fast response and readout time. Lastly, due to the tracker's proximity to the interaction region, with the innermost layer being only 4 cm away, it needed to have sufficient radiation hardness to withstand the intense particle flux for its expected lifetime of 10 years. Table 3.2 shows the expected radiation dose (in SI units of Gy) and particle flux through different layers of the tracker, which shows why radiation damage concerns are significant for the innermost part of the detector in the barrel region [60, 70]. With these considerations in mind it was decided that the tracker should be an all silicon tracking detector.

Table 3.2: The radiation dose, particle flux, hit rate density at different layers of the barrel region of the tracking detector [60].

Radius	**Tracker Layer**	**Radiation Dose**	**Charged Particle Flux**	**Hit Rate Density**
4 cm	1st Pixel Layer	840 kGy	10^8 cm^{-2}s^{-1}	1000 kHz mm^{-2}
11 cm	3rd Pixel Layer	190 kGy		
22 cm	1st Strip Layer	70 kGy	6×10^6 cm^{-2}s^{-1}	60 kHz mm^{-2}
75 cm	7th Strip Layer	7 kGy		
115 cm	Outer Edge	1.8 kGy	3×10^5 cm^{-2}s^{-1}	3 kHz mm^{-2}

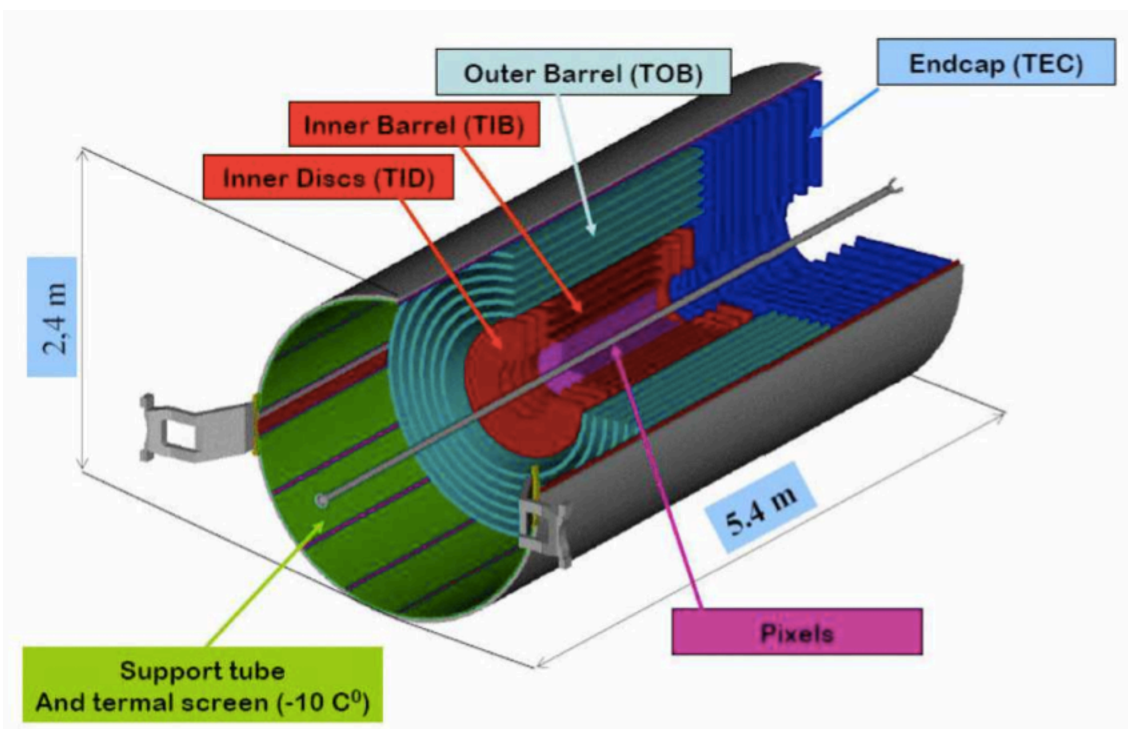

Figure 3.13: A diagram of the CMS tracking detector [64].

3.2.2.2 Detector Design and Layout

The tracking detector consists of 13 layers of silicon detectors in the barrel region and 14 layers in the endcap. It was made with over 200 m^2 of silicon, making it the largest silicon detector in the world and the most expensive part of the CMS detector, taking up about 60% of the total ∼$500,000,000 budget for the entire CMS detector. In total it contains over 76 million individual readout channels [60, 69].

The detector is split up into two main parts: an inner pixel detector and an outer strip detector. A diagram of the final design is shown in Fig. 3.13. A diagram showing a longitudinal slice of the entire tracker and the position of each pixel layer and strip module is shown in Fig. 3.14. A diagram showing a radial slice of the barrel region of the tracker and the position of each pixel layer and individual strip module is shown in Fig. 3.15 [60, 64, 71, 72].

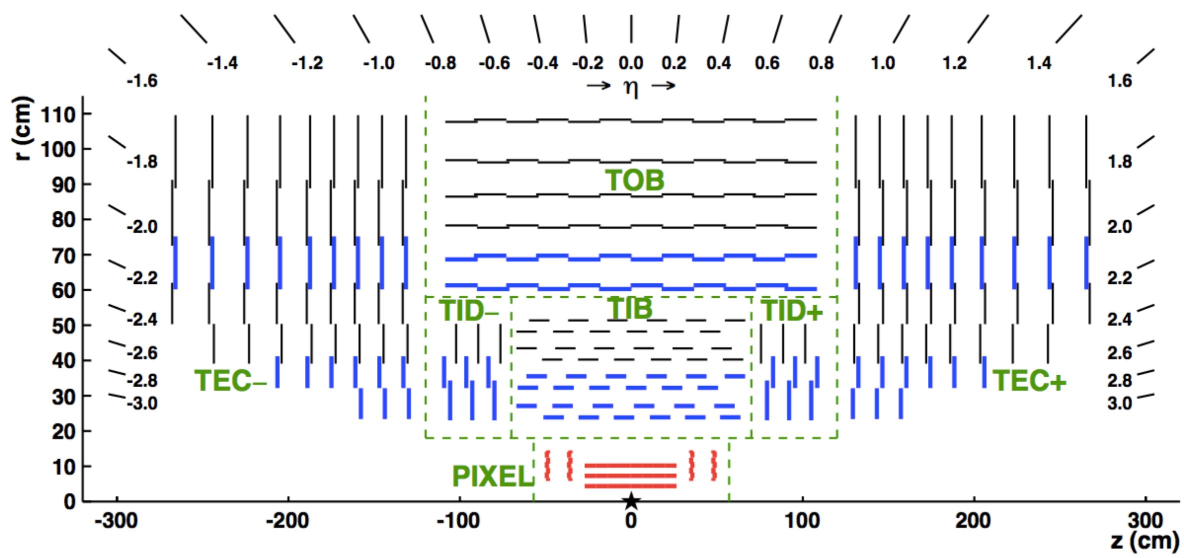

Figure 3.14: A diagram showing a longitudinal slice of the configuration of the silicon pixels and strips in the CMS inner tracking detector [71].

The pixel detector consists of the inner three layers of the tracking detector in the barrel region, located 4, 7, and 11 cm from the beam pipe, and two endcap layers. These layers are indicated in magenta in Fig. 3.13, in red in Fig. 3.14, and in green in Fig. 3.15. These layers are made of 66 million individual silicon pixels that are 100 μm by 150 μm giving a spatial resolution of the range of 15-20 μm by using a Gaussian interpolation of the shared charge from multiple pixels. In total, the three pixel layers are made of only 1 m^2 of silicon, which corresponds to over 6,000 readout channels per cm^2 [60, 69]

The silicon strip detector consists of the outer 10 layers of the barrel region of the tracker, extending from 22 and 110 cm from the beam pipe, and 12 layers in the endcap. The barrel region of the strip detector is further split up into the tracker inner barrel (TIB) and tracker outer barrel (TOB). The TIB has four layers of 10 cm by 180 μm silicon strips and the TOB has six layers of 25 cm by 180 μm silicon strips. Due to their length, the strips can only provide accurate spatial information in two dimensions for each hit. However, two layers in the TIB and two layers in the TOB have back-to-back strips installed with a slight stereo angle between them which provides these layers with 3-D spatial resolution capabilities. These double-sided stereo strips are pictured in blue in Fig. 3.14 and Fig. 3.15. In total there are 9.6 million silicon strips and associated readout channels in the strip detector [60, 72].

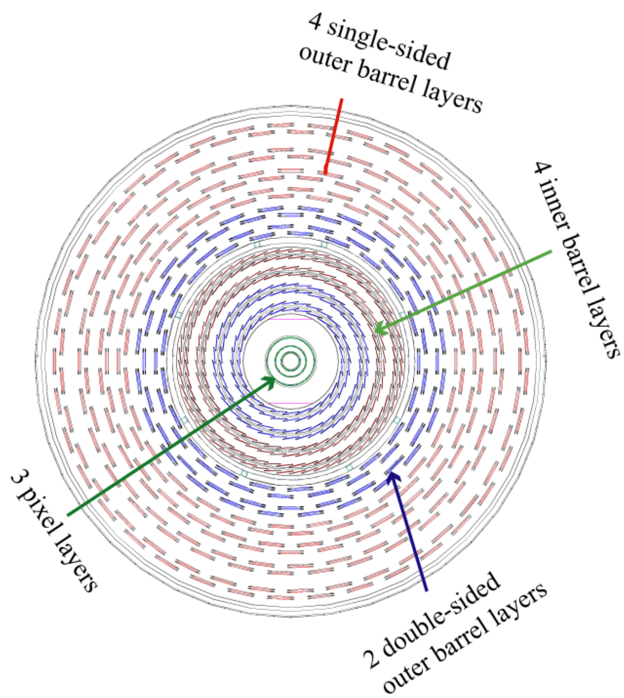

Figure 3.15: A diagram showing a transverse slice of the configuration of the silicon pixels and strips in the CMS inner tracking detector. [72].

3.2.2.3 Further Considerations

The high granularity in the pixel detector means that, even though it experiences a particle flux over an order of magnitude larger than the inner strip layer, its channel occupancy is almost two orders of magnitude less. This can be seen in Fig. 3.16 which shows the average channel occupancy for all of the pixel and strip layers with typical pileup $p + p$ interactions. The average channel occupancy is 0.002-0.02% for the pixel layers and 0.1-0.8% for the strip layers. This means that individual pixels in the innermost region will be less affected by intense radiation from the collision zone [71].

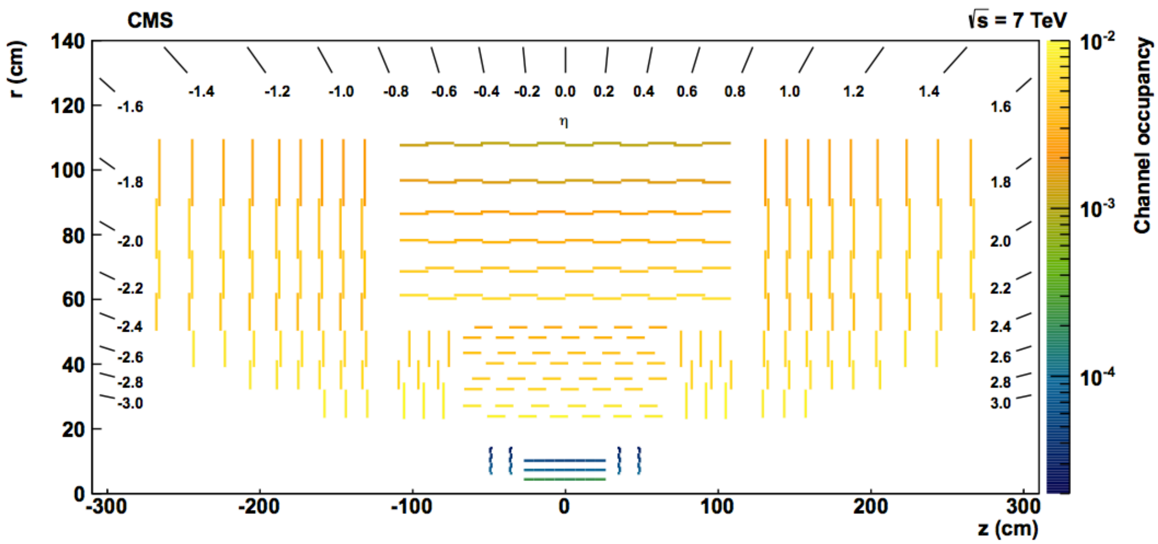

Figure 3.16: A schematic diagram of the CMS tracking system in the longitudinal plane, only half of it is shown since it is symmetric about the x-axis. The color-axis represents the channel occupancy which is the just fraction of minimum-bias $p + p$ events that cause each channel to fire. The extremely high granularity of the three pixel layers gives it a much lower occupancy even though it is significantly closer to the interaction region than the silicon strip detectors [71].

Another important consideration for any tracking detector is the total material budget used. For example, if too much silicon is used then it will interact too much with the particles it is trying to track causing them to deviate from their initial trajectory, thus making it much more difficult to determine the particle's initial momentum and track reconstruction in general. This is why the CMS tracker was limited to 13 layers of silicon detectors, which corresponds to about 5.135 mm of silicon that a particle traverses at midrapidity. The total radiation length and nuclear interaction length for every component of the tracker and the beampipe as a function of pseudorapidity (determined from simulations) is shown in Fig. 3.17. In the barrel region, $|\eta| < 1$, the total material budget is significantly less than in the forward regions, adding to the difficulties of track reconstruction in that part of the detector [60, 71].

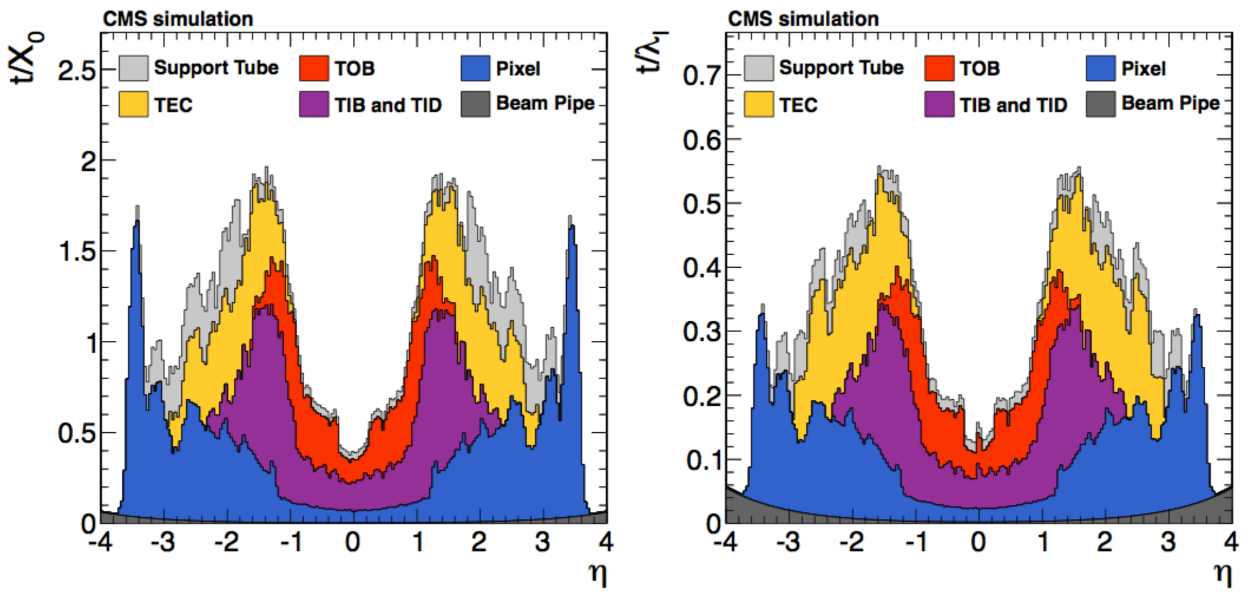

Figure 3.17: The material budget of the CMS tracking detector as a function of η in units of radiation length (left) and nuclear interaction length (right). The contribution from the various subsystems of the tracker are represented by the different colored histograms [71].

Chapter 4

Event Selection

The first step in a heavy-ion analysis is to filter out any unwanted collisions. in other words, we want to *trigger* the data acquisition system to record events only when they are of interest to the physics goals of the analysis. Since the CMS collaboration involves a number of people conducting different heavy-ion analyses there are many different event types of interest. This means that there are multiple event triggers running during the data-taking period. The most basic trigger is called the *minimum-bias trigger* and serves to make sure that data is only recorded when an actual Pb+Pb collision happens and to filter out all of the "junk" from the data sets (e.g. events where a Pb ion collides with a gas molecule in the collision zone). However, since the minimum-bias interaction rate was ~ 4 KHz during the 2011 heavy-ion run, it had to be *prescaled* by a factor of 200 (meaning that only one out of every 200 minimum-bias events was recorded) to prevent the data read-out system from overloading. Therefore, in order to collect enough events with high-p_{T} tracks for this analysis a special high-p_{T} track trigger had to be implemented.

4.1 Minimum-Bias Data

The minimum-bias Pb+Pb data are recorded with a trigger that requires coincident signals from both ends of the detector in the beam scintillator counters (BSC) or in the forward hadron calorimeters (HF), discussed in Sec. 3.2. The minimum-bias trigger is also required to coincide with a bunch crossing in the interaction region, which is determined by the beam pick-up timing detector (BPTX), to minimize contamination due to cosmic rays, beam background, and other noise. The minimum-bias trigger is more than 97% efficient for inelastic Pb+Pb collisions [38].

Offline event selection is then applied to reduce the background from beam-gas events, beam-halo events, cosmic-ray muons, and electromagnetic interaction from ultra-peripheral collisions (UPCs) which can lead to a breakup of either of the colliding Pb nuclei [73]. This was done by first requiring that the coinciding HF signals, one on either side of the interaction point, each contained at least three towers with a total deposited energy of 3 GeV. Each event is then required to have a primary reconstructed vertex that is consistent with the transverse beam spot and contains at least two tracks with $p_{\mathrm{T}} > 75$ MeV/c. Finally, the length of each pixel cluster is used to require that only tracks originating from the primary vertex are present in the event [38, 74, 75].

4.2 Single-Track High-p_{T} Event Trigger

During the 2011 Pb+Pb run the total interaction rate during peak performance was 4 kHz. Given that the total trigger rate that was feasible for the CMS detector during the run was only 100 Hz the minimum-bias trigger had to be heavily prescaled [76]. Since the goal of this analysis is to look at high-p_{T} dihadron correlations, $p_{\mathrm{T}} > 20$ GeV/c, it was not feasible to rely solely on the minimum-bias trigger to get sufficient statistics at high p_{T}. For this reason a dedicated trigger was needed to identify events that contain high-p_{T} tracks.

The result was the development and deployment of a dedicated high-level trigger (HLT) that made use of the full track reconstruction in heavy-ion events. This trigger is seeded by two level-1 (L1) trigger paths: `L1_ETT100`, which requires 100 GeV of transverse energy in the entire calorimeter, and `L1_SingleJet16_NotETT140`, which requires the presence of a 16 GeV jet and the calorimeter to have less than 140 GeV of total energy. The first L1 trigger is used to find candidate events from central Pb+Pb collisions and the second is used to find candidate events from peripheral Pb+Pb collisions [76].

The events that pass the two L1 triggers discussed above are passed to the HLT for the final step in the trigger path. In the HLT each event undergoes track reconstruction that is almost identical to that done in the offline reconstruction process for Pb+Pb data, which is discussed in

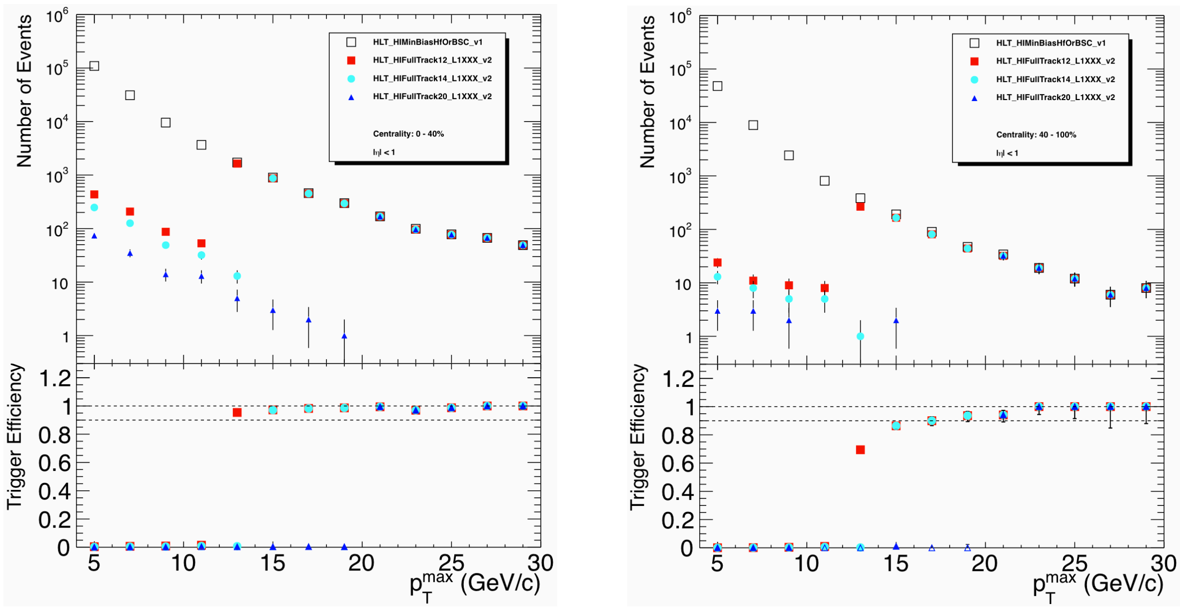

(a) The 0-40% most central collisions

(b) The 40-100% most peripheral collisions

Figure 4.1: The leading track p_{T} distribution (top) and trigger efficiency (bottom) with $|\eta| < 1$ for minimum-bias (open white squares) and single-track high-p_{T} triggered events with p_{T} thresholds of 12 (red squares), 14 (cyan circles) , and 20 GeV/c (blue triangles) in two centrality ranges: 0-40% (a) and 40-100% (b) [77].

the next section. This is done to maximize the efficiency of selecting events with high-p_{T} tracks. However, since track reconstruction is a very computationally-intensive process to run in an online setting, such as in the HLT, two additional requirements were added to the track reconstruction algorithm.

First, prior to undergoing the most time-consuming step in the track reconstruction algorithm (extending the reconstruction from the pixel detector to include all the information from the strip detectors) each event is required to have a single calorimeter tower with $E_T > 4$ GeV and a pixel-only track with $p_{\mathrm{T}} > 10$ GeV/c, where a "pixel-only" track is a track that is reconstructed using only the information from the three innermost pixel layers of the tracker. This requirement rejects 75% of the events that pass the L1 requirements while maintaining a total trigger efficiency of almost 100% for events with at least one track with $p_{\mathrm{T}} > 20$ GeV/c. The second requirement speeds up the total CPU time by only running the full track reconstruction on track candidates with $p_{\mathrm{T}} > 11$ GeV/c. Due to this last requirement, the lowest p_{T} threshold was set to 12 GeV/c

in the HLT with two additional trigger thresholds of 14 and 20 GeV/c [76].

The leading track (the track with the highest p_{T} in each event) p_{T} distribution for $|\eta| < 1$ is shown in Fig. 4.1 for minimum-bias events as well as minimum-bias events that are also found in at least one of the 12, 14, and 20 GeV/c single-track high-p_{T} trigger paths. The trigger efficiency for each of the high-p_{T} track triggers is shown below the p_{T} distributions as a function of leading track p_{T}. The results for 0-40% central collisions are shown in Fig. 4.1(a) and for 40-100% peripheral collisions in Fig. 4.1(b). The same results are shown for events with the leading track $|\eta| < 2$ in Fig. 4.2. The presence of high-p_{T} track triggered events with a leading track p_{T} below 12 GeV/c is likely caused by events where a high-p_{T} track caused the trigger to fire but did not pass the final selection criteria for track reconstruction (discussed in the next chapter).

The trigger efficiency curve has a sharp turn-on at $p_{\mathrm{T}} \sim 12$ GeV/c in central Pb+Pb events with an efficiency around 95%, increasing to almost 100% above $p_{\mathrm{T}} \sim 20$ GeV/c. The trigger efficiency turn-on isn't as sharp or as high in peripheral events but it still reaches an efficiency of over 95% above $p_{\mathrm{T}} \sim 20$ GeV/c.

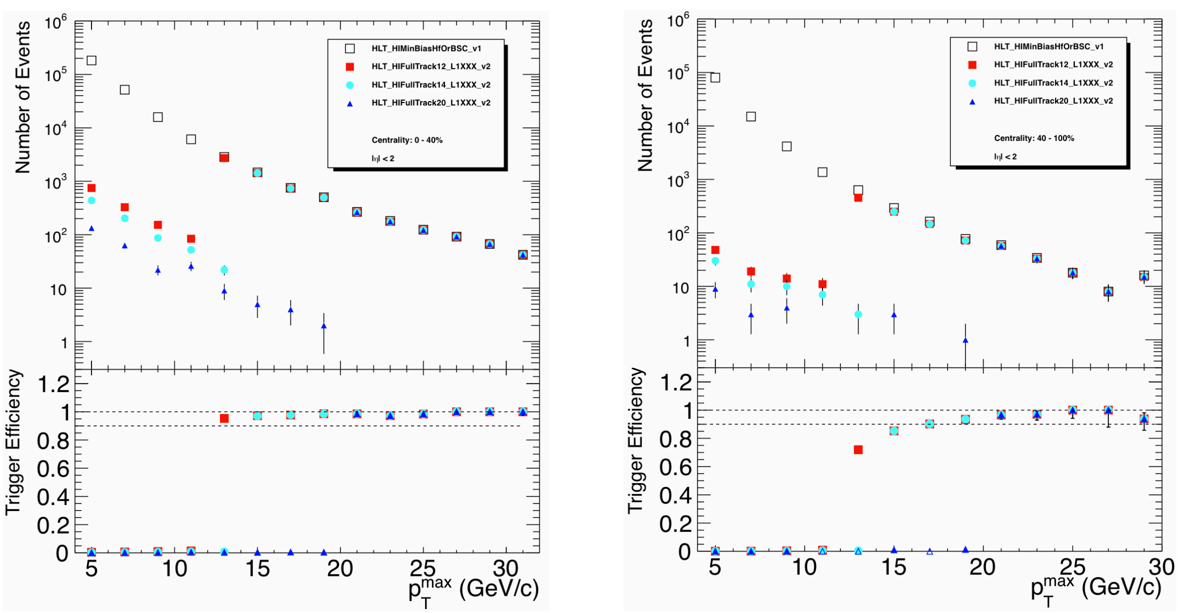

(a) The 0-40% most central collisions

(b) The 40-100% most peripheral collisions

Figure 4.2: The leading track p_{T} distribution (top) and trigger efficiency (bottom) with $|\eta| < 2$ for minimum-bias and single-track high-p_{T} triggered events with p_{T} thresholds of 12, 14, and 20 GeV/c in two centrality ranges: 0-40% (a) and 40-100% (b) [76].

The full dataset collected by the CMS detector from the 2011 Pb+Pb run corresponds to a total integrated luminosity of about 150 μb^{-1}, which contains over 750 million minimum-bias events after offline event selection is applied. The final single-track high-p_{T} triggered dataset used in this analysis contains roughly 1.55 million events with at least one track with $p_{\mathrm{T}} > 20$ GeV/c. To illustrate the effectiveness of the high-p_{T} track triggers, during the 2010 run only 50,000 events were recorded that contained a track with $p_{\mathrm{T}} > 20$ GeV/c [76].

4.3 Centrality Determination

As discussed previously, determining the centrality of a heavy-ion collision is a vital step in trying to understand the underlying physics. In CMS, the total transverse energy deposited in the forward hadronic calorimeters ($\sum E_T$) is used to divide the centrality of each event into bins representing 2.5% of the total inelastic cross section. The distribution of $\sum E_T$ has the characteristic "horse's back" shape that is commonly associated with variables that are used for centrality determination in heavy-ion collisions and is shown in Fig. 4.3. The figure also shows the boundaries of the centrality bins used by all CMS heavy-ion analyses during the first two heavy-ion runs at the LHC.

Soft particle production is strongly correlated with event centrality in heavy-ion collisions. In central events there are a large number of nucleon-nucleon interactions which produce a lot of particles and, in more peripheral events, there are only a few interacting nucleons so a smaller number of particles are produced as a result. A good measure of event multiplicity in the CMS detector is the number of hits in the innermost pixel detector, which has a low occupancy even in central Pb+Pb events due to its extremely high granularity. Figure 4.4 shows the correlation between the number of hits in the inner pixel layer and total energy deposited in the HF detectors.

Given the tight correlation between $\sum E_T$ and event multiplicity (as determined by the number of inner pixel hits) we can be sure that background events are not contaminating the dataset. We can then estimate the total number of interacting nucleons, N_{part}, that experience at least one inelastic collision for each centrality bin. This was done using a Glauber model Monte Carlo simulation at LHC energies [38]. The centrality bins used in this analysis and their associated average N_{part} values are shown in Table 4.1.

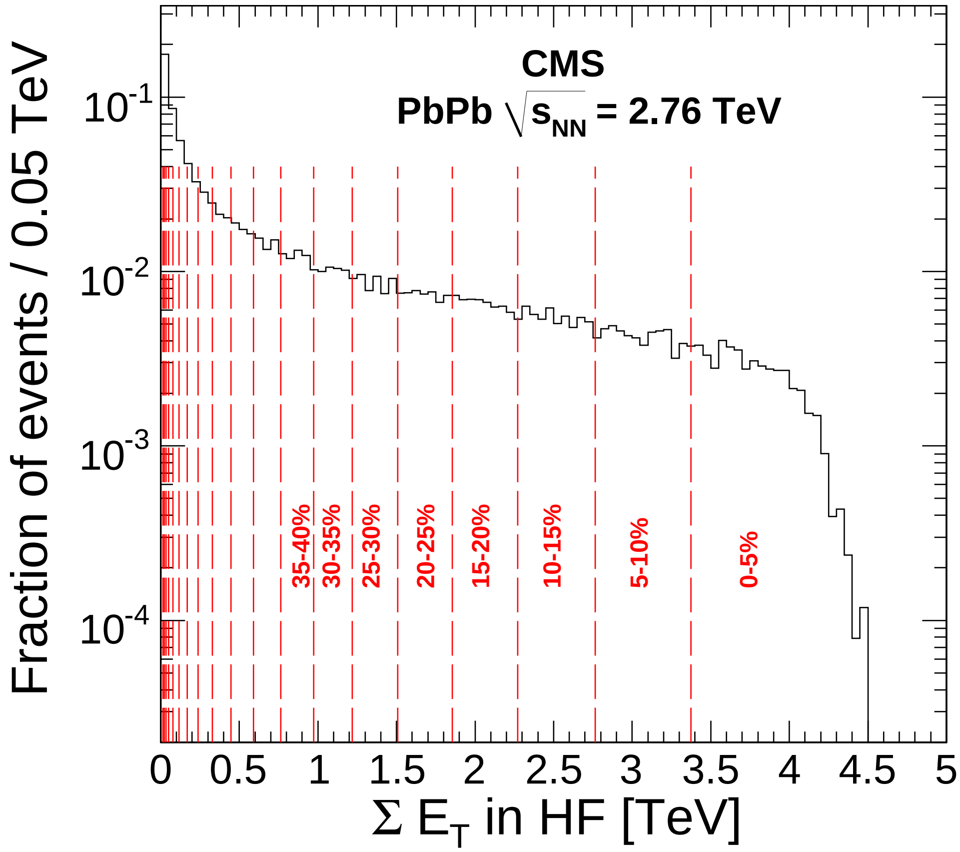

Figure 4.3: The distribution of the total transverse energy deposited in the forward hadronic calorimeters ($\sum E_T$). The distribution is divided into bins representing 5% of the total hadronic inelastic cross section for Pb+Pb collisions at the LHC. [78].

Table 4.1: The centrality bins used in the analysis along with the average number of participating nucleons in each bin. The values were obtained using a Glauber model Monte Carlo simulation with the same parameters as in Ref. [38].

Centrality	0-10%	10-20%	20-30%	30-40%	40-50%	50-60%
$\langle N_{part} \rangle$	355 ± 3	262 ± 4	187 ± 4	130 ± 4	86 ± 3	53 ± 3

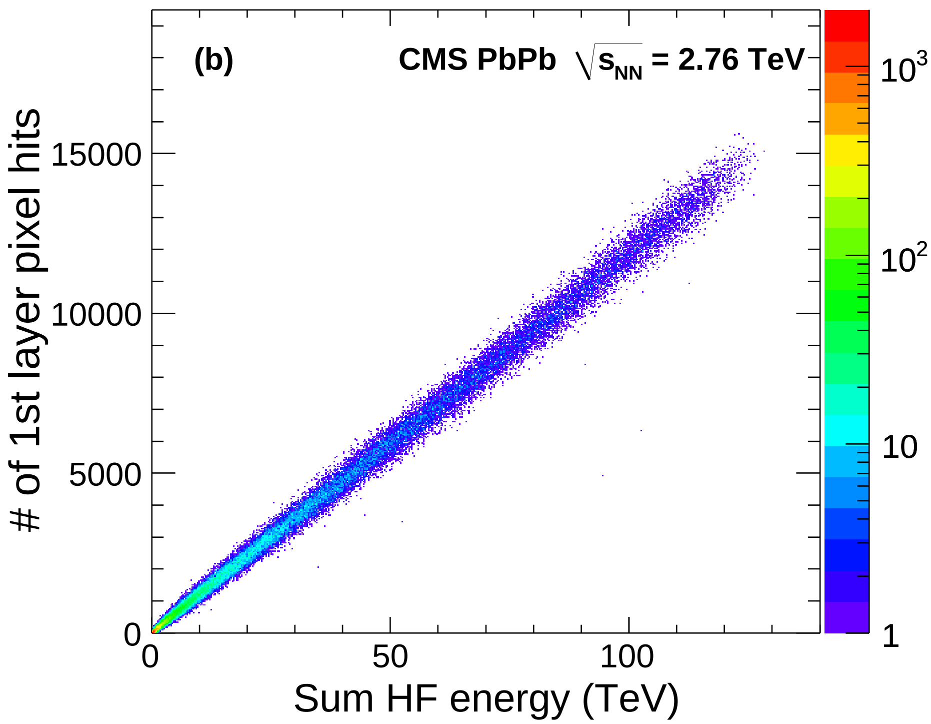

Figure 4.4: A 2-D histogram showing the tight correlation between the number of hits in the first pixel layer of the tracker and the total energy deposited in the forward hadronic calorimeters (HF) [38].

Despite the inefficiencies in the minimum-bias trigger, the distribution of events in each centrality bin should be roughly flat since each bin is constructed so that it contains an equal fraction of the total inelastic cross section for Pb+Pb collisions, as shown on the left in Fig. 4.5. Each bin represents 2.5% of the total centrality where bin 1 corresponds to the most central events and bin 40 corresponds to the most peripheral. For rare processes, like the hard scatters that produce high-p_{T} tracks, there is an inherent bias towards more central events since the number of nucleon-nucleon interactions is large. This centrality bias can easily be seen on the right side of Fig. 4.5 which shows the number of events in each centrality bin for the three single-track high-p_{T} trigger thresholds. As a cross check the centrality bins for minimum-bias events that have a leading track, $p_{\mathrm{T}} > 12$, GeV/c are also included and show excellent agreement with the high-p_{T} triggered data.

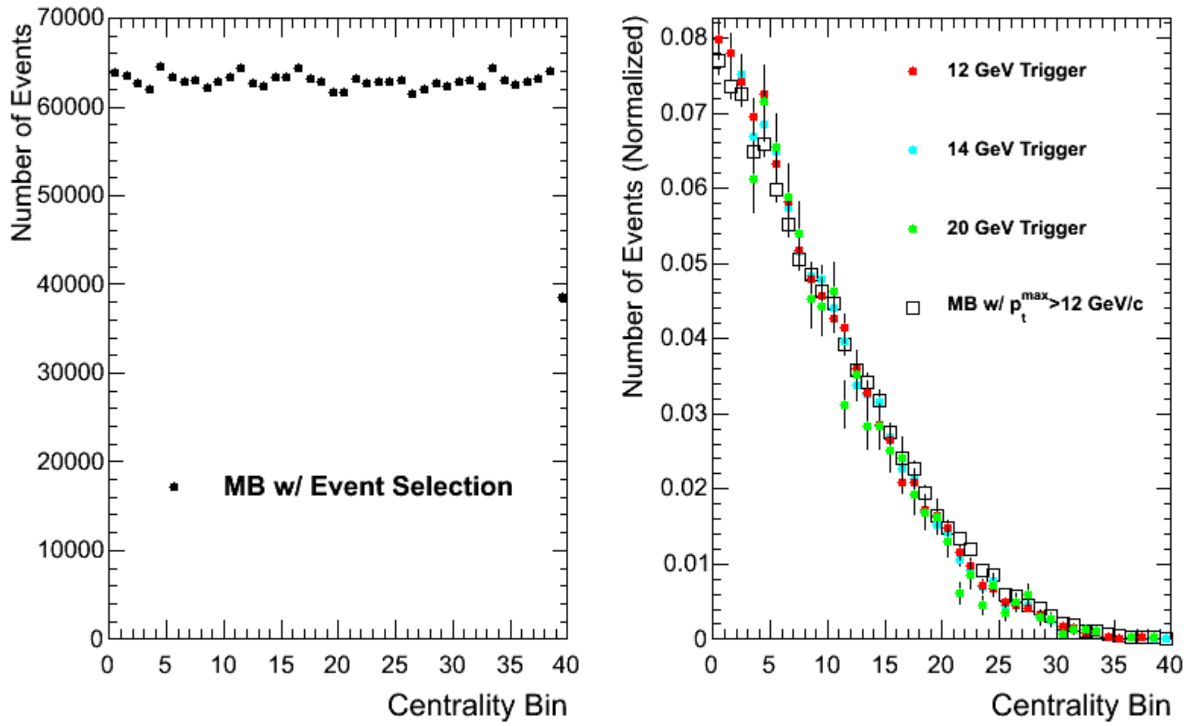

Figure 4.5: The distribution of events in each centrality bin for minimum-bias data (left) and the three single-track high-p_{T} triggers (right). The right plot also shows minimum-bias data with at least one track with $p_{\mathrm{T}} > 12$ GeV/c as a cross check to verify that the centrality bias is not a systematic effect arising from the triggers.

Chapter 5

Track Reconstruction

Dihadron angular correlations depend on accurate measurements of track trajectories. Thus, track reconstruction in the CMS detector is a major component of this analysis. In particular, track reconstruction for heavy-ion collisions is significantly more challenging than in $p + p$ collisions due to extremely high event multiplicities. As a result, there are some important differences between the track reconstruction algorithm used in $p + p$ and heavy-ion collisions. In addition, the accuracy or *efficiency* of the track reconstruction algorithm is important to know for any track-based analysis. Appropriate efficiency corrections can then be applied in order to minimize any systematic bias resulting from the finite acceptance of the detector and the tracking algorithm itself.

5.1 Track Reconstruction in CMS

In the CMS detector, tracks from $p + p$ collisions are reconstructed by starting with a *seed*, which are initial estimates of tracks that are compatible with the beam spot or vertex. There are six different types of seeds, which are various combinations of hits in the pixel and strip layers of the tracker that are comparable with the expected trajectory of a charged particle in a magnetic field, i.e. a helix, above some minimum p_{T} value. Each type of seed is searched for one at a time in an iterative fashion. In each step the track seeds are propagated out to all of the layers of the tracker to find compatible hits using a combinatorial Kalman filter. At the end of each step, all of the hits associated with a reconstructed track are removed before the next iteration of seed finding and track fitting begins. The tracking algorithm is described generally in Ref. [79] and in detail in Ref. [80], the performance of the tracking detector during the 2010 run can be found in Ref. [81].

This algorithm is not computationally feasible in Pb+Pb collisions due to the drastic increase in the occupancy of the pixel layers in central events. The combinatorics of the seed generation steps blow up as particle multiplicity increases. For this reason specific heavy-ion tracking algorithms were developed based on the existing $p+p$ algorithm.

5.2 Heavy-Ion Track Reconstruction in CMS

In heavy-ion collisions a two-step iteration process is used for track reconstruction to reduce the computational requirements. The first step uses pixel triplet seeds that are propagated to the other layers of the tracker to reconstruct tracks with a low fake rate (misidentified reconstructed tracks) above $p_{\mathrm{T}} = 1.5$ GeV/c. These tracks are referred to as `hiGoodTightTracks`. The second step uses tracks that are only constructed from the pixel detector and constrained to originate from the beam spot to find tracks with a low fake rate below $p_{\mathrm{T}} = 1.8$ GeV/c. These tracks are referred to as "pixel tracks".

After these two steps, the two track collections are merged together. Duplicate tracks are identified by shared hits among tracks in both collections and removed from the pixel track set. Additionally, all pixel tracks above $p_{\mathrm{T}} = 1.8$ GeV/c and all full tracks below $p_{\mathrm{T}} = 1.5$ GeV/c are removed from the final merged track collection, known as `hiGoodTightMergedTracks`. The two tracking iterations are described more below but the full detail of the heavy-ion track reconstruction algorithm can be found in Refs. [82] and [34].

1. **hiGoodTightTracks:** As described above, this iteration is intended to provide quality tracks with a low fake rate and acceptable efficiency above $p_{\mathrm{T}} = 1.5$ GeV/c. There are five main steps in this algorithm: identifying and reconstructing the primary vertex; identifying track seeds; finding track candidates; performing a final track fit; and making quality cuts for the final track collection.

   (a) **Primary Vertex Reconstruction:** Using the beam spot as an initial estimate of the transverse position of the primary vertex and the shapes of the pixel clusters found in the inner tracker, the z-vertex position can be estimated with a 1 mm accuracy. This is then used as a constraint for finding pixel triplets (three hits in the pixel detector that are consistent with a compatible track). A subset of these pixel triplets is then passed to an adaptive vertex fitter to reconstruct the primary vertex with a resolution of ~ 10 μm in the most peripheral events.

   (b) **Pixel Triplet Seed Identification:** With the primary vertex from the previous step, pixel triplet seeds are found with the requirements that their distance of closest approach to the primary vertex be less than 0.1 cm in the longitudinal direction ($d_z < 0.1$ cm) and 0.2 cm in the transverse plane ($d_{xy} < 0.2$ cm). In addition, each pixel triplet is required to have $p_{\mathrm{T}} \geq 0.9$ GeV/c. These requirements significantly reduce the combinatorics and CPU time involved in finding possible track seeds, which can be orders of magnitude higher in central Pb+Pb collisions compared to even the highest multiplicity p+p events.

   (c) **Finding Track Candidates:** The trajectories from the pixel-triplet seeds are then successively propagated out to the outer layers of the tracker using a combinatorial Kalman filter. At each step the five best possible trajectories are propagated to the next layer based on the normalized χ^2 of each trajectory and its associated hits in the various layers of the tracker. Once the outer layer is reached, trajectories with at least six associated hits are passed to the final track fitter.

   (d) **Track Fitting:** Since the track candidates from the previous step only contain a collection of associated hits and estimates of the track parameters, which could be biased based on the primary vertex constraint, the trajectories are refit with a Kalman filter, making use of the full information about the trajectory, and smoothed with a Runge-Kutta propagator. The latter is able to account for material effects and inhomogeneities in the magnetic field by numerically extrapolating the track between each hit in the detector.

(e) **Track Quality Selection:** Finally, the track collection produced from the previous four steps is filtered with a few "tight" quality cuts. These cuts are designed to minimize the fake rate and maximize the efficiency of the track collection, improving the so-called "purity" of the track collection. Tighter quality cuts are applied producing the standard `highPurity` track collection that is used in most CMS heavy-ion analyses. The specific cuts applied to each track collection are shown in Table 5.1.

The efficiency and fake rate (discussed in more detail in Sec. 5.4) of the `hiGoodTighTracks` collection is shown in Fig. 5.1 for 5-10% central Pb+Pb events. The events were simulated with the HYDJET MC event generator [83].

Table 5.1: The track cuts applied for the "tight" and "highPurity" quality selections. The uncertainty in the estimate of track parameter X is represented by $\sigma(X)$ [34, 76].

Cut Description	**Cut Parameter**	**Tight**	**highPurity**
Minimum number of hits per track	N_{hits}	12	13
Maximum relative p_{T} error	$\sigma(p_{\mathrm{T}})/p_{\mathrm{T}}$	0.075	0.05
Max. normalized transverse dist. from vertex	$d_{xy}/\sigma(d_{xy})$	5	3
Max. normalized longitudinal dist. from vertex	$d_z/\sigma(d_z)$	5	3
Maximum χ^2 per degree of freedom per signal	$\chi^2/\mathrm{NDF}/N_{\mathrm{hits}}$	0.25	0.15

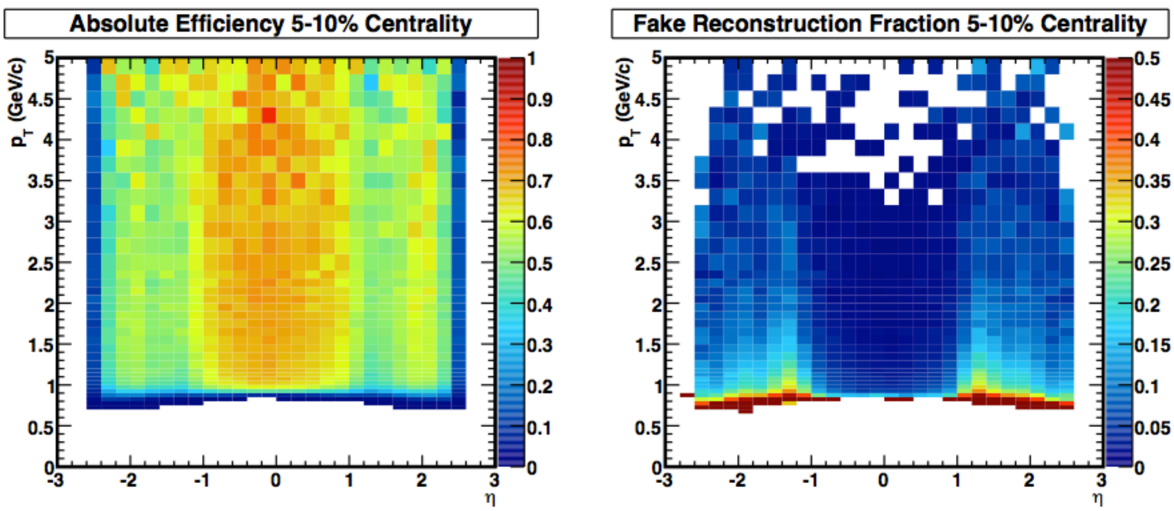

Figure 5.1: Left: The absolute efficiency (algorithmic efficiency times the geometric acceptance) as a function of p_{T} and η for `hiGoodTightTracks` in 5-10% central Pb+Pb collisions simulated with HYDJET. Right: The fake rate for the same track collection shown on the left as a function of p_{T} and η [34].

2. **Pixel Tracks:** The second iteration of the heavy-ion tracking algorithm is intended to compliment the first by providing high purity tracks below $p_\mathrm{T} = 1.8$ GeV/c, where the `hiGoodTightTracks` do not behave as well. In this step only hits from the pixel tracker are considered and the minimum p_T threshold is lowered to 0.2 GeV/c. The pixel triplets are then fit using a conformal map and the requirement that they originate from the beam spot such that $d_{xy} = 0$. These tracks are then filtered based on their statistical goodness of fit, χ^2/NDF, and the longitudinal distance of closest approach to the vertex, d_z. This is done to minimize the fake rate in the large η and low p_T regions.

Below $p_\mathrm{T} \sim 400$ MeV/c the reconstruction efficiency of pixel tracks drops significantly and the fake rate starts to rise, particularly outside of midrapidity. This can be seen in Fig. 5.2, which shows the efficiency and fake rate of the `pixelTrack` collection reconstructed from simulated Pb+Pb events from HYDJET.

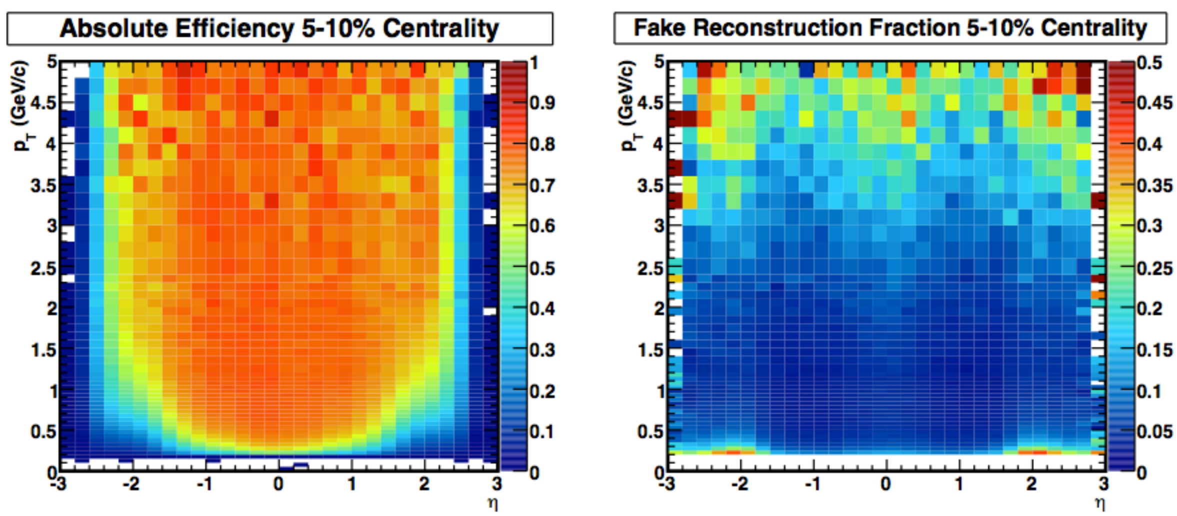

Figure 5.2: Left: The absolute efficiency (algorithmic efficiency times the geometric acceptance) as a function of p_T and η for pixelTracks in 5-10% central Pb+Pb collisions simulated with HYDJET. Right: The fake rate for the same track collection shown on the left as a function of p_T and η [34].

5.3 High-p_{T} Track Kinematics

Since this analysis is focused specifically on high-p_{T} dihadron correlations, high-p_{T} tracks are of particular interest. The CMS detector with its 3.8 T magnetic field (Sec. 3.2) is particularly well suited to measure high-p_{T} tracks. In addition, the single-track high-p_{T} trigger is able to significantly increase the number of events containing high-p_{T} tracks, which allows us to significantly extend the p_{T} range of what was previously possible for any track-based heavy-ion analysis. This can be seen in Fig. 5.3 which shows the high-p_{T} spectra (> 12 GeV/c) for `highPurity` tracks from minimum-bias events and single-track high-p_{T} triggered events.

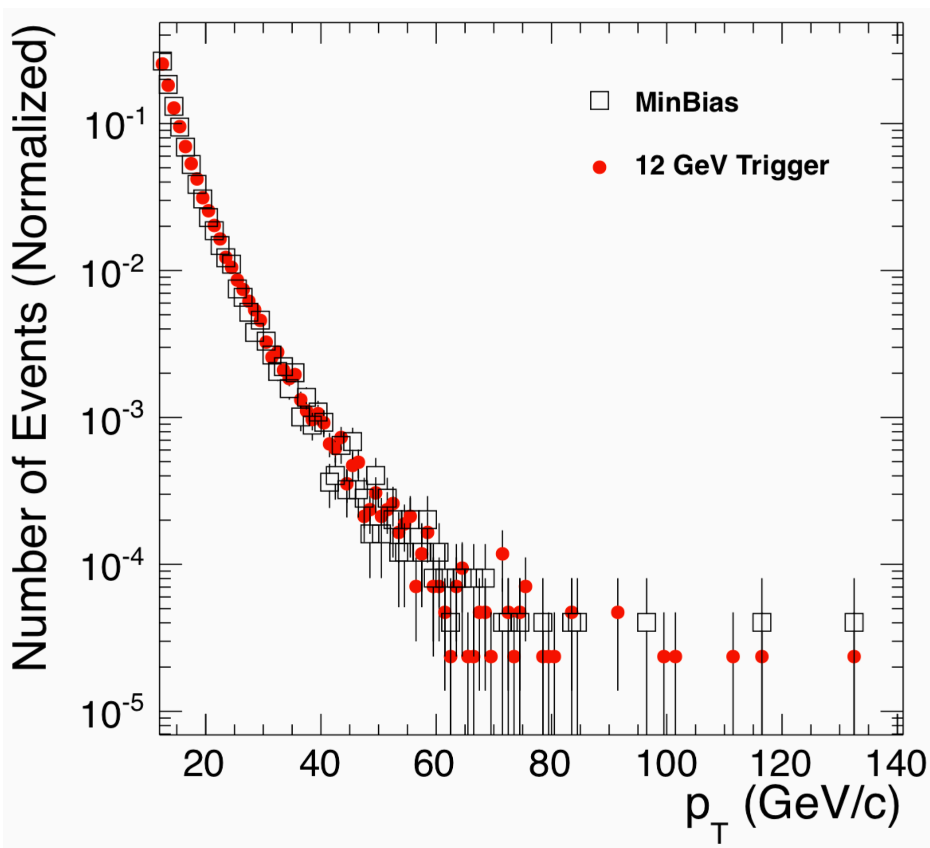

Figure 5.3: The p_{T} spectra for tracks above $p_{\mathrm{T}} = 12$ GeV/c from minimum-bias events (open squares) and high-p_{T} track triggered events from the 12 GeV/c threshold (red circles) [76].

It is important to ensure that the events from the high-p_{T} track trigger dataset and their subsequent high-p_{T} tracks are not biased in an unintended way. This can be evaluated by comparing various vertex and track kinematic variables to those from minimum-bias events. Figure 5.4 shows the longitudinal and transverse vertex distributions. On the left is the distribution of the vertex positions along the beam direction, z_{vtx}, for minimum bias events containing at least one track with $p_{\mathrm{T}} > 12$ GeV/c (open squares) and high-p_{T} track triggered events above the 12 GeV/c threshold (red circles). Events with $|z_{\mathrm{vtx}}| > 15$ cm were not included in this analysis and most other CMS heavy-ion analyses since they can lead to biases in the η distribution of tracks (and consequently the $\Delta\eta$ distribution) [34]. The distribution of the vertex position in the transverse plane is shown in Fig. 5.4 for minimum-bias events with at least one high-p_{T} track in the center plot and for high-p_{T} track triggered events in the right plot. Within statistics, there is very good agreement between the vertex positions from the two event samples.

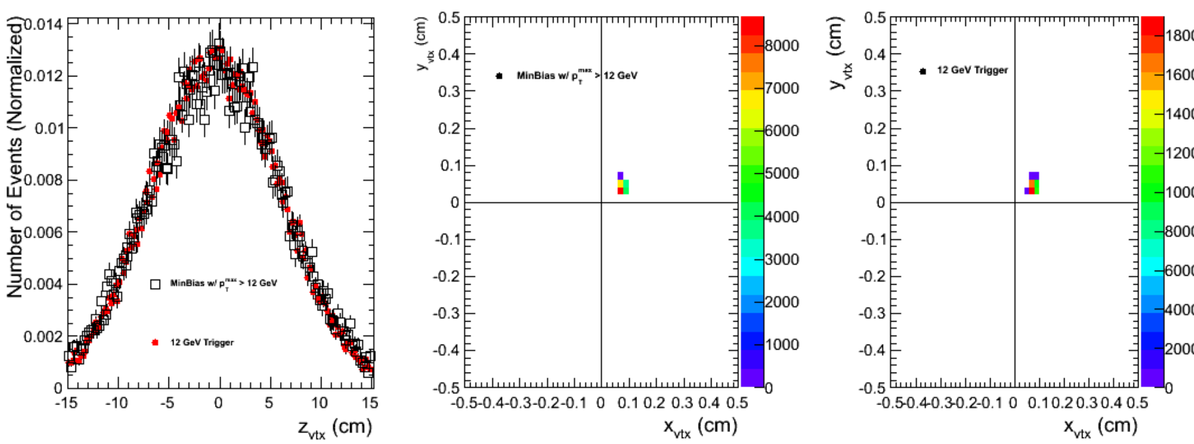

Figure 5.4: Left: the distribution of vertex positions along the beamline, z_{vtx}, for minimum bias events with at least one track above $p_{\mathrm{T}} = 12$ GeV/c (open squares) and for high-p_{T} track triggered events above the 12 GeV/c threshold (red circles). Center: the distribution of vertex positions in the transverse plane for minimum bias events with a high-p_{T} track. Right: the distribution of vertex positions in the transverse plane for high-p_{T} track triggered events above the 12 GeV/c threshold [76].

Additional track kinematic variables are shown for minimum-bias events with at least one high-p_{T} track (always represented by the open white squares) and for single-track high-p_{T} triggered events above the 12 GeV/c threshold (always represented by the red circles) in Figures 5.5- 5.8. The comparisons between the two event samples shows very good agreement within the statistical uncertainty.

Figure 5.5 shows the η distribution for the two event samples for low (left) and high-p_{T} tracks (right). Figure 5.6 shows the ϕ distribution for the two event samples for low (left) and high-p_{T} tracks (right). The track quality variables, shown in Table 5.1, are plotted for the two event samples for low-p_{T} tracks in Fig. 5.7 and for high-p_{T} tracks in Fig. 5.8. The distance of closest approach for each track from the vertex position in the longitudinal direction normalized by the uncertainty, $d_z/\sigma(d_z)$, is shown in the top left plot. The distance of closest approach, normalized by the uncertainty, in the transverse plane is shown in the top center plot. the number of hits in the tracker associated with each track, N_{hits} is shown in the top right plot. The relative momentum uncertainty, $p_{\mathrm{T}}/\sigma(p_{\mathrm{T}})$, is shown in the bottom left plot. Finally, the statistical goodness of fit for each track trajectory, χ^2/NDF, is shown in the bottom center plot.

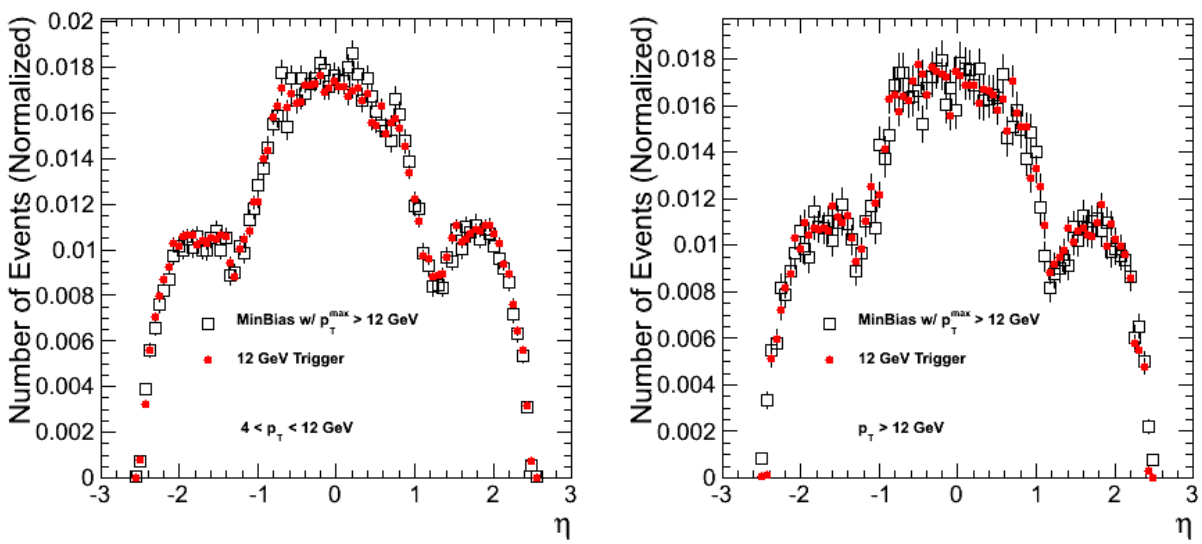

Figure 5.5: The η distribution for tracks from minimum-bias events containing at least one track with $p_{\mathrm{T}} > 12$ GeV/c (open squares) and for single-track high-p_{T} triggered events (red circles). The left plot shows the distribution for tracks with $4 < p_{\mathrm{T}} < 12$ GeV/c and the right plot shows the distribution for tracks with $p_{\mathrm{T}} > 12$ GeV/c [76].

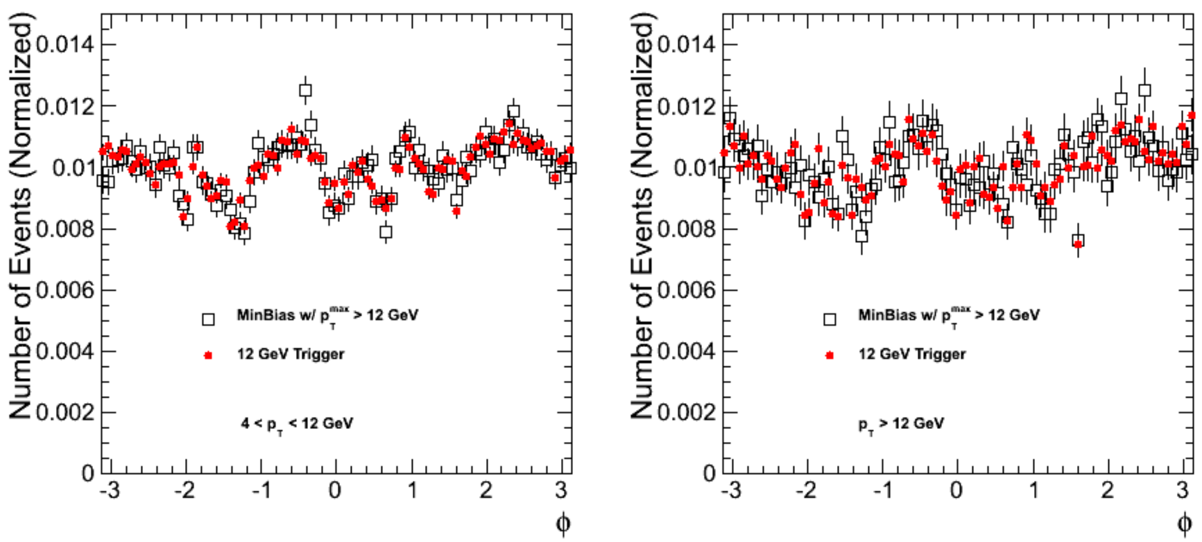

Figure 5.6: The ϕ distribution for tracks from minimum-bias events containing at least one track with $p_{\mathrm{T}} > 12$ GeV/c (open squares) and for single-track high-p_{T} triggered events (red circles). The left plot shows the distribution for tracks with $4 < p_{\mathrm{T}} < 12$ GeV/c and the right plot shows the distribution for tracks with $p_{\mathrm{T}} > 12$ GeV/c [76].

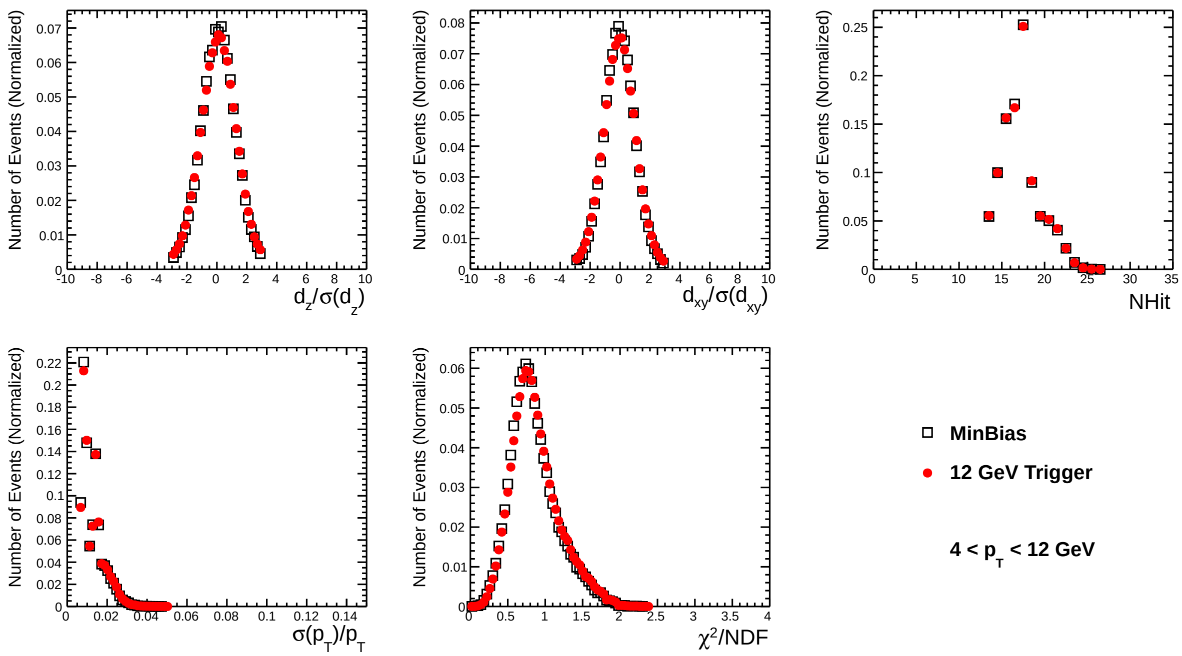

Figure 5.7: Track quality variables for minimum-bias events containing at least one track with p_{T} > 12 (open squares) and high-p_{T} track triggered events above the 12 GeV/c threshold (red circles) for tracks with $4 < p_{\mathrm{T}} < 12$ GeV/c. The distance of closest approach to the vertex in the z-direction (normalized by the uncertainty in the measurement) is shown in the top left plot, the distance of closest approach to the vertex in the xy-plane is shown in the top center plot, the number of tracker hits associated with each track is shown in the top right plot, the relative momentum uncertainty is shown in the bottom left plot, and the statistical goodness of fit is shown in the bottom center plot [76].

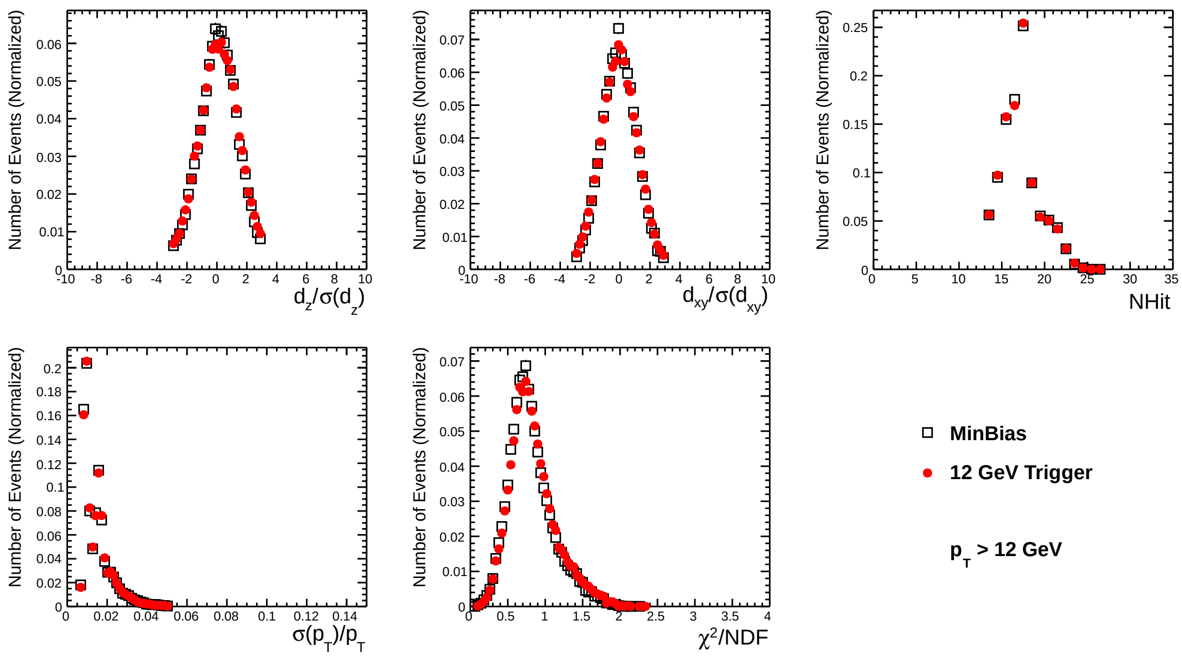

Figure 5.8: Track quality variables for minimum-bias events containing at least one track with $p_{\mathrm{T}} > 12$ (open squares) and high-p_{T} track triggered events above the 12 GeV/c threshold (red circles) for tracks with $p_{\mathrm{T}} > 12$ GeV/c. The distance of closest approach to the vertex in the z-direction (normalized by the uncertainty in the measurement) is shown in the top left plot, the distance of closest approach to the vertex in the xy-plane is shown in the top center plot, the number of tracker hits associated with each track is shown in the top right plot, the relative momentum uncertainty is shown in the bottom left plot, and the statistical goodness of fit is shown in the bottom center plot [76].

5.4 Track Reconstruction Performance and Efficiency Corrections

The final track collection used in this analysis was created by merging `hiGoodTightTracks` and `pixelTracks`, which was discussed in Sec. 5.2. The absolute track reconstruction efficiency (algorithmic efficiency times the geometric acceptance) as a function of p_T and η, is shown on the left in Fig. 5.9. The fraction of misidentified tracks, known as the fake rate, as a function of p_T and η is shown on the right in Fig. 5.9. The efficiency and fake rate are also shown as a function of p_T with $|\eta| < 1$ for various centralities in Fig. 5.10. We can see that the efficiency for both the `hiGoodTightTracks` and the `pixelTracks` is slightly worse for central events compared to peripheral. For the pixel tracks, the fake rate is also worse for central events but remains below 5% for the entire p_T region.

The efficiency and fake rate for the high-p_T track collection was calculated using dijet signals generated from PYTHIA [84] and embedding them into HYDJET events. To improve the statistics out to high p_T several different minimum jet p_T thresholds, known as $\hat{p}_T$, were used between 30 and 300 GeV/c. The various $\hat{p}_T$ samples were then combined by weighting each with their corresponding jet cross section from PYTHIA. The trajectories of the particles produced from the event generators are then compared to the tracks that are passed through a GEANT4 [85] simulation of the CMS detector response and then reconstructed using the full offline track reconstruction algorithm. In this way we can get a good handle of the track reconstruction efficiency and fake rate. However, it should be noted that, even with the PYTHIA embedded HYDJET samples, the statistics at high-p_T are still limited and affect our ability to assign an accurate systematic uncertainty for the tracking efficiency at high p_T (discussed later in Sec. 6.3.3).

To correct for the imperfections in track reconstruction efficiency and contamination from fake tracks, each reconstructed track is weighted be the efficiency correction factor, ϵ_trk, which is calculated as a function of p_T, η, and event centrality, and is given by,

$$\epsilon_\mathrm{trk}(p_\mathrm{T}, \eta, \mathrm{cent}) = \frac{1 - f(p_\mathrm{T}, \eta, \mathrm{cent})}{A(p_\mathrm{T}, \eta, \mathrm{cent}) E(p_\mathrm{T}, \eta, \mathrm{cent})}, \tag{5.1}$$

where $A(p_\mathrm{T}, \eta, \mathrm{cent})$ is the geometric detector acceptance, $E(p_\mathrm{T}, \eta, \mathrm{cent})$ is the algorithmic reconstruction efficiency, and $f(p_\mathrm{T}, \eta, \mathrm{cent})$ is the fraction of misidentified tracks [82, 86]. The correction factor was calculated in the same centrality bins used in the analysis. The effect of applying the efficiency correction factor to reconstructed tracks only changes the scale of the 2D correlation functions being produced since they are just the ratio of signal and background distributions (discussed in Sec. 6.1.1), which are a also functions of p_{T}, η, and centrality

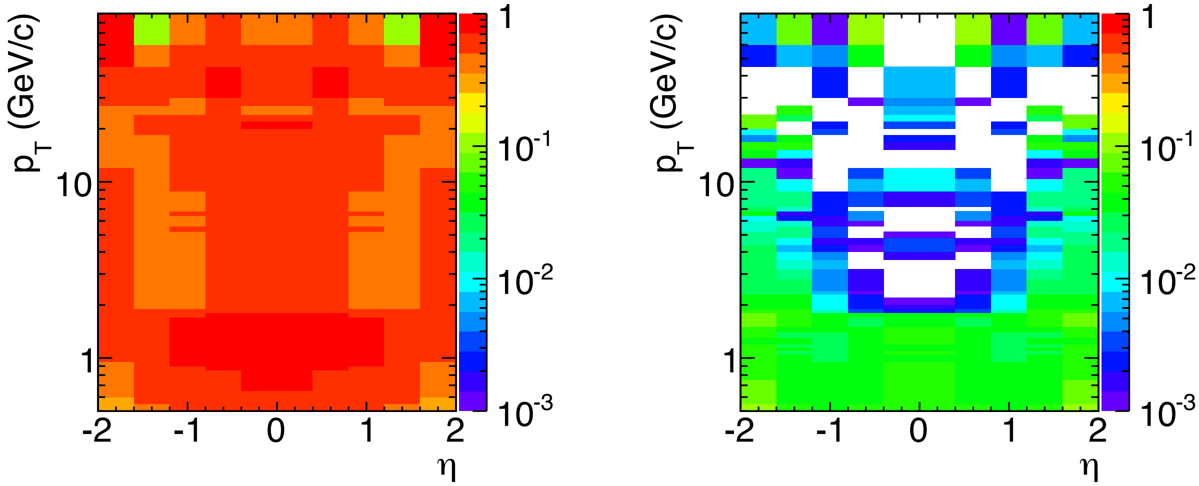

Figure 5.9: Left: Track reconstruction efficiency as a function of p_{T} and η. Right: The fake rate or fraction of misidentified reconstructed tracks as a function p_{T} and η. Both values were calculated using PYTHIA dijets embedded in 0-5% central HYDJET simulated Pb+Pb events.

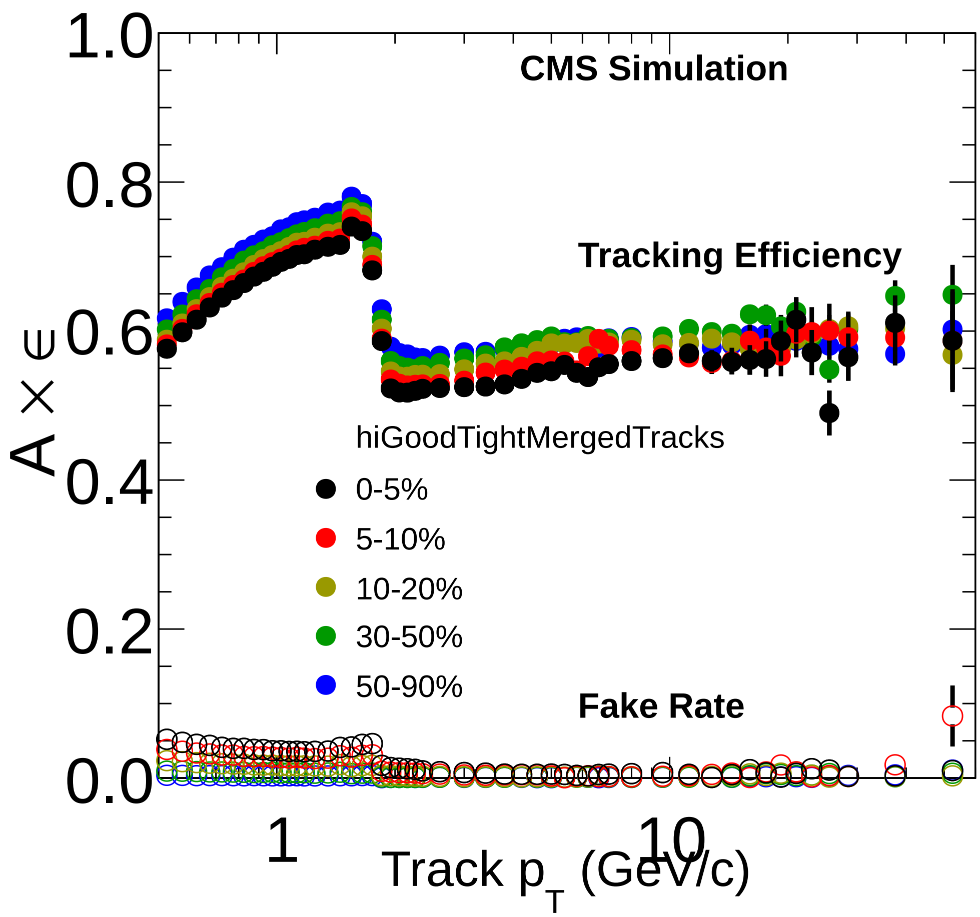

Figure 5.10: The track reconstruction efficiency (solid circles) and fake rate (open circles) as a function of p_{T} for $|\eta| < 1$ for various collision centralities with PYTHIA dijets embedded in HYDJET simulated Pb+Pb events for the entire p_{T} range used in this analysis: $0.5 < p_{\mathrm{T}} < 48$ GeV/c.

Chapter 6

Analysis

6.1 Very High-p_{T} Dihadron Correlations

With the advent of modern detectors like CMS and ATLAS jets can be accurately reconstructed above $p_{\mathrm{T}} \sim 100$ GeV/c in Pb+Pb collisions at LHC energies. However, below $p_{\mathrm{T}} \sim 50$ GeV/c standard jet reconstruction is not feasible due to the presence of large background fluctuations [87]. Using high-p_{T} dihadron correlations we can look below this lower limit for jet reconstruction to study jet energy loss. In this region it is possible to subtract the underlying flow background to isolate the jet correlations. In order to extract this information we first need to calculate the per-trigger-particle associated yield distributions using the dihadron-correlation method [47, 88].

6.1.1 Dihadron-Correlation Method

In this method, all charged particles that came from the primary vertex, are within a specified $p_{\mathrm{T}}^{\mathrm{trig}}$ range, and have $|\eta| < 2.4$ are defined as *trigger particles.* Hadron pairs are then formed by associating every charged particle with $|\eta| < 2.4$ and in a specified $p_{\mathrm{T}}^{\mathrm{assc}}$ range with each trigger particle. The per-trigger-particle associated yield distribution is then given by:

$$\frac{1}{N_{\mathrm{trig}}} \frac{d^2 N^{\mathrm{pair}}}{d\Delta\eta d\Delta\phi} = B(0,0) \times \frac{S(\Delta\eta, \Delta\phi)}{B(\Delta\eta, \Delta\phi)}, \tag{6.1}$$

where $N_{\rm trig}$ is the number of trigger particles in each event (which can be more than one per event), $N^{\rm pair}$ is the total number of hadron pairs in the event, and $\Delta\eta$ and $\Delta\phi$ are the differences in η and ϕ of the pair, respectively. The signal distribution, $S(\Delta\eta, \Delta\phi)$, is the measured per-trigger-particle distribution composed from same-event pairs,

$$S(\Delta\eta, \Delta\phi) = \frac{1}{N_{\rm trig}} \frac{d^2 N^{\rm same}}{d\Delta\eta d\Delta\phi}. \tag{6.2}$$

The background distribution, $B(\Delta\eta, \Delta\phi)$, is the measured per-trigger-particle distribution of mixed-event pairs defined by,

$$B(\Delta\eta, \Delta\phi) = \frac{1}{N_{\rm trig}} \frac{d^2 N^{\rm mix}}{d\Delta\eta d\Delta\phi}, \tag{6.3}$$

where $N^{\rm mix}$ is the number of pairs taken from the mixed events. This is constructed by forming hadron pairs between the trigger particles in each event with the associated particles from ten different pseudo-random events (discussed below), excluding the event that contains the trigger particle. The background distribution effectively accounts for pair-acceptance effects and random combinatorial background. The value $B(0, 0)$ represents the mixed-event associated yield where both particles of the hadron pair are going in approximately the same direction ($\Delta\eta \simeq 0$ and $\Delta\phi \simeq 0$, where the bin widths are 0.3 and $\pi/16$, respectively), which means it has the maximum possible geometric pair acceptance. Thus, the ratio $B(0, 0)/B(\Delta\eta, \Delta\phi)$ is the pair-acceptance correction factor that is applied to the signal distribution, Eq. (6.2), to give the corrected per-trigger-particle associated yield distribution.

The associated yield distribution in Eq. (6.1) is calculated in each centrality bin (2.5% of the total inelastic cross section, discussed in Sec. 4.3) and then averaged into 10% centrality bins for the analysis. In addition, the distribution is calculated in 0.5 cm bins for the vertex position along the beam line ($z_{\rm vtx}$) for $|z_{\rm vtx}| < 15$ cm. This is done to ensure that the event mixing that goes into the background distribution, Eq. (6.3), does not introduce any systematic biases from differences between central and peripheral events or variations in detector acceptance at different $z_{\rm vtx}$ positions.

It is important to note that in this analysis the absolute values of $\Delta\eta$ and $\Delta\phi$ are used in the construction of all associated yield distributions. This is done to maximize the statistical accuracy of the correlation measurements. This also means that only one quadrant in the 2-D correlation functions shown below is actually filled, the rest are all filled for illustrative purposes only by reflecting about the axis $\Delta\phi = 0$ and $\Delta\eta = 0$.

An example per-trigger-particle associated yield distribution is shown in Fig. 6.1 [86] for trigger particles with $p_{\mathrm{T}}^{\mathrm{trig}} > 20$ GeV/c and $1 < p_{\mathrm{T}}^{\mathrm{assc}} < 2$ GeV/c for the $0-30\%$ most central Pb+Pb collisions [86]. Fig. 6.1(a) shows a 2-D associated yield distribution as a function of $\Delta\eta$ and $\Delta\phi$, the same distribution projected onto the $\Delta\phi$ axis is shown in Fig. 6.1(b). The near-side peak ($\Delta\eta \sim 0$, $\Delta\phi \sim 0$), which is truncated to emphasize the surrounding structure, is formed mostly by single jet fragmentation. The away-side structure ($|\Delta\eta| < 3$, $|\Delta\phi| \sim \pi$) is believed to be mainly a consequence of the dijet contribution, which, along with the near-side peak, is also observed in $p+p$ collisions [89]. The full set of 2-D correlation functions for all $p_{\mathrm{T}}^{\mathrm{trig}}$ and $p_{\mathrm{T}}^{\mathrm{assc}}$ combinations used in this analysis are shown for all Pb+Pb centralities and $p+p$ collisions in Appendix A.

6.1.2 Estimating the v_n-Background Contribution

The long-range ($2 < |\Delta\eta| < 4$) near-side ($\Delta\phi \sim 0$) ridge structure at low p_{T} in Fig. 6.1(a) is generally believed to be a result of anisotropies in single-particle azimuthal distributions (e.g. hydrodynamic flow effects) in heavy-ion collisions [48, 90–94]. In order to isolate the jet signal this background must be subtracted from our associated-yield distributions, which means we have to estimate the flow contribution.

The component of the 1-D $\Delta\phi$-projected per-trigger-particle associated yield distribution that is attributed to the flow background is typically described with a Fourier series and given by [88],

$$\frac{1}{N_{\mathrm{trig}}}\frac{dN_{\mathrm{bkg}}^{\mathrm{pair}}}{d\Delta\phi} = \frac{N_{\mathrm{assc}}}{2\pi}\left[1 + 2\sum_{n=1}^{\infty} v_n(p_{\mathrm{T}}^{\mathrm{trig}})v_n(p_{\mathrm{T}}^{\mathrm{assc}})\cos n\Delta\phi\right], \tag{6.4}$$

where N_{assc} is the total number of hadron pairs formed in each $p_{\mathrm{T}}^{\mathrm{trig}}$ and $p_{\mathrm{T}}^{\mathrm{assc}}$ bin. The Fourier coefficients, $v_n(p_{\mathrm{T}}^{\mathrm{trig}})$ and $v_n(p_{\mathrm{T}}^{\mathrm{assc}})$, which characterize the above distribution are the standard

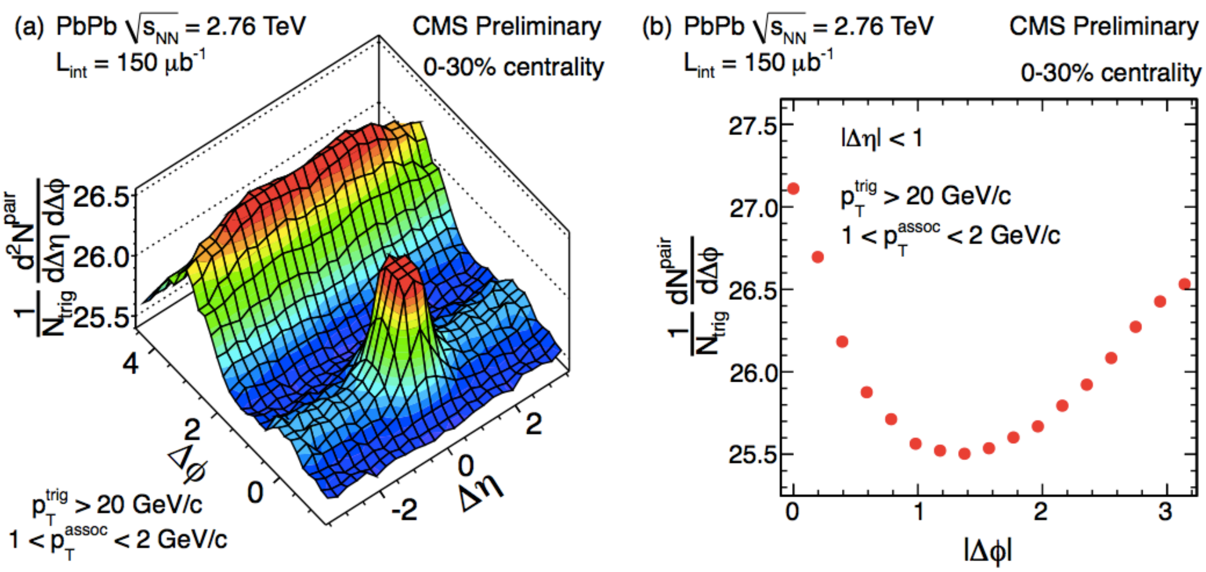

Figure 6.1: The per-trigger-particle associated yield of charged particles with $p_{\mathrm{T}}^{\mathrm{trig}} > 20$ GeV/c and $1 < p_{\mathrm{T}}^{\mathrm{assc}} < 2$ GeV/c from the $0-30\%$ centrality range of Pb+Pb collisions at $\sqrt{s_{NN}} = 2.76$ TeV. The results are shown in (a) two-dimensions as a function of $\Delta\eta$ and $\Delta\phi$ after symmetrization (see text) and (b) one-dimension as a function of $|\Delta\phi|$. The near-side peak in (a) is truncated to display better the surrounding structure. [86]

single-particle azimuthal anisotropy harmonics [32,95] for the trigger and associated particle respectively. The deconvolution (usually referred to as a *factorization* in this context) of the single-particle azimuthal anisotropies of the trigger and associated particles can be assumed if the observed correlation is driven solely by hydrodynamic expansion of the medium (e.g. flow) [47, 48, 95, 96]. Since this is exactly what we are trying to model we can use the single-particle v_n coefficients for the trigger and associated particles independently in the associated yield distribution for the flow background, Eq.(6.4).

Therefore, in order to estimate the flow background using the Fourier expansion shown in Eq.(6.4) the flow coefficients, v_n (p_{T}), need to be measured in the same p_{T} range $(0.5 < p_{\mathrm{T}} < 50$ GeV/c) and centrality bins $(0-60\%)$ used in this analysis. The second-order coefficient, v_2, was previously measured using the Event Plane method [32, 82] up to $p_{\mathrm{T}} \approx 60$ GeV/c in two η ranges, $|\eta| < 1$ and $1 < |\eta| < 2$ in Ref. [77].

The presence of the near-side ridge, discussed in the previous section, indicates that the higher-order flow coefficients, v_n with $n > 2$, also need to be taken into account at high p_{T}. For this reason, v_3

and v_4 were also measured using the Event Plane method for higher-order coefficients described in Ref. [97]. The measurements were extended from a p_{T} of 7 GeV/c to 60 GeV/c in two different η ranges, as with v_2, so they could be used in this analysis [86]. The fifth-order Fourier coefficient was also calculated out to high p_{T} but was found to be consistent with zero above $\sim$ 10 GeV/c. Since this analysis was done for trigger-particles with $p_{\mathrm{T}}^{\mathrm{trig}} \approx 20$ GeV/c these results are not shown since including the v_5 term would have no effect on the results.

In order to extract the high-p_{T} v_n data in various p_{T} bins the measurements were parameterized by fitting the low and high-p_{T} regions with various functions. The v_n values were restricted to particles with $|\eta| < 1$ in the parameterization fits. For v_2 the data were fit with a fifth-order polynomial at low p_{T} from $0.3 - 6$ GeV/c. The high-p_{T} range, $5.5 - 60$ GeV/c was fit with a function of the form $c_1(p_{\mathrm{T}})^{c_2}$, where c_1 and c_2 are fit parameters. The fit ranges overlap in p_{T} to ensure that the transition between fits is smooth. In the analysis the high-p_{T} fit is always used in the overlap region so there is no ambiguity.

The higher-order coefficients were fit in a similar manner. The v_3 and v_4 coefficients were fit with a third-order polynomial at low p_{T} from $0.3 - 4.5$ GeV/c and $0.3 - 5$ GeV/c, respectively, In the high p_{T} range they were both fit with a function of the form $c_1(p_{\mathrm{T}})^{c_2}$ from $4 - 50$ GeV/c and $3.5 - 50$ GeV/c, respectively. The fit functions and the fit ranges used in the analysis were all chosen to fit the data as smoothly as possible as a function of p_{T} to avoid any side effects from statistical fluctuations. The systematic effects resulting in this parameterization are discussed in Sec. 6.3.1.

6.1.3 The ZYAM Method

Once the flow coefficients have been accurately measured the flow background can be subtracted from the 1-D $\Delta\phi$-projected associated-yield distribution. Assuming the flow background is roughly constant as a function of η, which has been shown for $|\eta| < 1$ in Ref. [77, 82], we can calculate the background subtracted associated yield distribution with the following equation,

$$\frac{1}{N_{\mathrm{trig}}}\frac{dN_{\mathrm{sub}}^{\mathrm{pair}}}{d\Delta\phi} = \frac{1}{N_{\mathrm{trig}}}\frac{dN^{\mathrm{pair}}}{d\Delta\phi} - a_0\left[1 + 2\sum_{n=1}^{\infty} v_n(p_{\mathrm{T}}^{\mathrm{trig}})v_n(p_{\mathrm{T}}^{\mathrm{assc}})\cos n\Delta\phi\right], \tag{6.5}$$

where the Fourier term is taken directly from Eq. (6.4). The parameter a_0 is determined such that the minimum of the difference is around zero, as prescribed by the Zero Yield At Minimum (ZYAM) procedure [98].

To find the minimum between the associated yield distribution and the flow background we have to assume that the 1-D $\Delta\phi$-projected associated yield can be expressed as:

$$C(\Delta\phi) = a_0 C_H(\Delta\phi) + J(\Delta\phi), \tag{6.6}$$

where $C(\Delta\phi)$ is the raw 1-D per-trigger-particle associated yield distribution given by

$$C(\Delta\phi) = \frac{1}{N_{\mathrm{trig}}}\frac{dN^{\mathrm{pair}}}{d\Delta\phi}, \tag{6.7}$$

$C_H(\Delta\phi)$ is the harmonic correlation function representing the collective flow background,

$$C_H(\Delta\phi) = 1 + 2\sum_{n} v_n(p_{\mathrm{T}}^{\mathrm{trig}})v_n(p_{\mathrm{T}}^{\mathrm{assc}})\cos n\Delta\phi, \tag{6.8}$$

and $J(\Delta\phi)$ represents dijet correlations. There is no assumption made about the functional form of $J(\Delta\phi)$. It is assumed that the when $C(\Delta\phi)$ is at a minimum the contribution from dijets, $J(\Delta\phi)$, is essentially zero [98], giving us,

$$C(\Delta\phi_{\mathrm{min}}) \simeq a_0 C_H(\Delta\phi_{\mathrm{min}}). \tag{6.9}$$

From this we can easily determine a_0 by

$$a_0 = \frac{C(\Delta\phi_{\min})}{C_H(\Delta\phi_{\min})}. \tag{6.10}$$

Therefore, in order to determine a_0 we just need to find the minimum of the 1-D $\Delta\phi$-projected associated yield distribution divided by the Fourier expansion of the flow background. Once a_0 is determined we can use Eq. (6.5) to effectively isolate the jet correlations.

To minimize the influence of statistical fluctuations in the 1-D $\Delta\phi$-projected associated yield distributions, Eq. (6.10) is fitted with a second-order polynomial between $0.5 < |\Delta\phi| < 1.5$. The minimum of the fit function is then taken as the value of the parameter a_0 to be used in the ZYAM subtraction. This procedure found that the position the minimum of the fit function, $\Delta\phi_{\min}$, was always near 1 radian. Therefore, to reduce systematic uncertainties from an additional fit parameter it is assumed that $\Delta\phi_{\min} = 1$ for all $p_{\mathrm{T}}^{\mathrm{assc}}$ and $p_{\mathrm{T}}^{\mathrm{trig}}$ bins used in the analysis. The value of $\Delta\phi_{\min}$ was then varied to determine the corresponding systematic uncertainties (discussed in Sec. 6.3.2).

In cases where collective flow dominates and the near and away-side peaks overlap it is uncertain whether the assumptions made in the ZYAM procedure are valid [99]. However, these issues are not relevant in this analysis given the large amplitude and narrow widths of the correlation signals in the high p_{T} range [100].

Examples of the 1-D $\Delta\phi$-projected per-trigger-particle associated yield distributions with $|\Delta\eta| < 1$ and for various $p_{\mathrm{T}}^{\mathrm{trig}}$ and $p_{\mathrm{T}}^{\mathrm{assc}}$ combinations are shown in Fig. 6.2 for 0-10% central Pb+Pb collisions, Fig. 6.3 for 50-60% peripheral Pb+Pb collisions, and in Fig. 6.4 for $p+p$ collisions at $\sqrt{s_{NN}} = 2.76$ TeV. The solid curves in Fig. 6.2 and Fig. 6.3 represent the estimated flow background contribution from the v_n harmonics, scaled by the a_0 parameter as in Eq. (6.5). In $p+p$ collisions it is assumed so that there is no collective behavior so the pedestal background is flat by assumption and is represented by the dashed red lines in Fig. 6.4 [86].

Subtracting the flow background from the per-trigger-particle associated yield distributions produces jet-like dihadron correlations, as shown in Fig. 6.5 for 0-10% central Pb+Pb collisions (red), 50-60% peripheral Pb+Pb collisions (blue), and $p+p$ collisions (open white circles). These results are displayed for $|\Delta\eta| < 1$ and for various $p_{\mathrm{T}}^{\mathrm{trig}}$ and $p_{\mathrm{T}}^{\mathrm{assc}}$ combinations. It is worth noting that Figures 6.2, 6.3, 6.4, and 6.5 do not show all of the $p_{\mathrm{T}}^{\mathrm{assc}}$ bins used in the analysis. Only a subset at low $p_{\mathrm{T}}^{\mathrm{assc}}$ is shown to give an idea of how the distributions evolve in $p_{\mathrm{T}}^{\mathrm{trig}}$ and $p_{\mathrm{T}}^{\mathrm{assc}}$ [86]. The method outlined above will be referred to as the v_n-*subtraction* method to distinguish between an alternative method of isolating jet correlations, that will be discussed in Sec. 6.2.

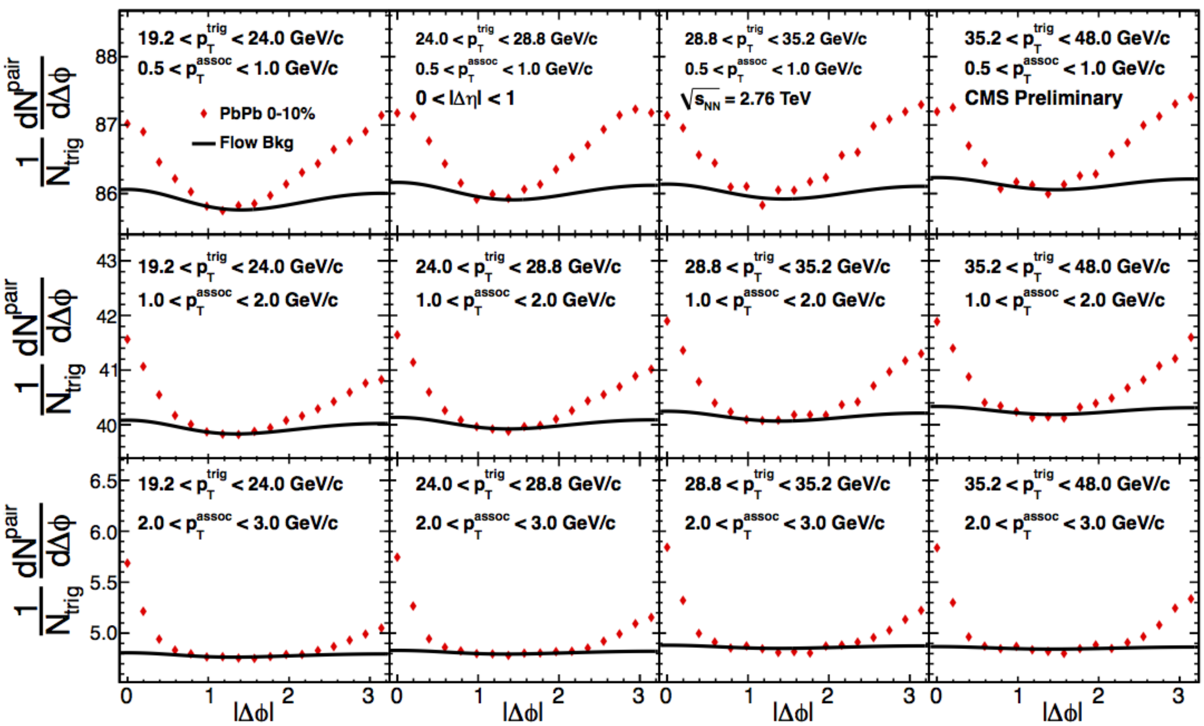

Figure 6.2: The 1-D $\Delta\phi$-projected associated yield distributions for 0-10% central Pb+Pb collisions with $|\Delta\eta| < 1$ are shown with the red points and the estimated flow backgrounds (scaled by the a_0 parameter from the ZYAM procedure) are represented by the solid black curves. The distributions are shown for various combinations of $p_{\mathrm{T}}^{\mathrm{trig}}$, increasing from left to right, and $p_{\mathrm{T}}^{\mathrm{assc}}$, increasing from top to bottom [86].

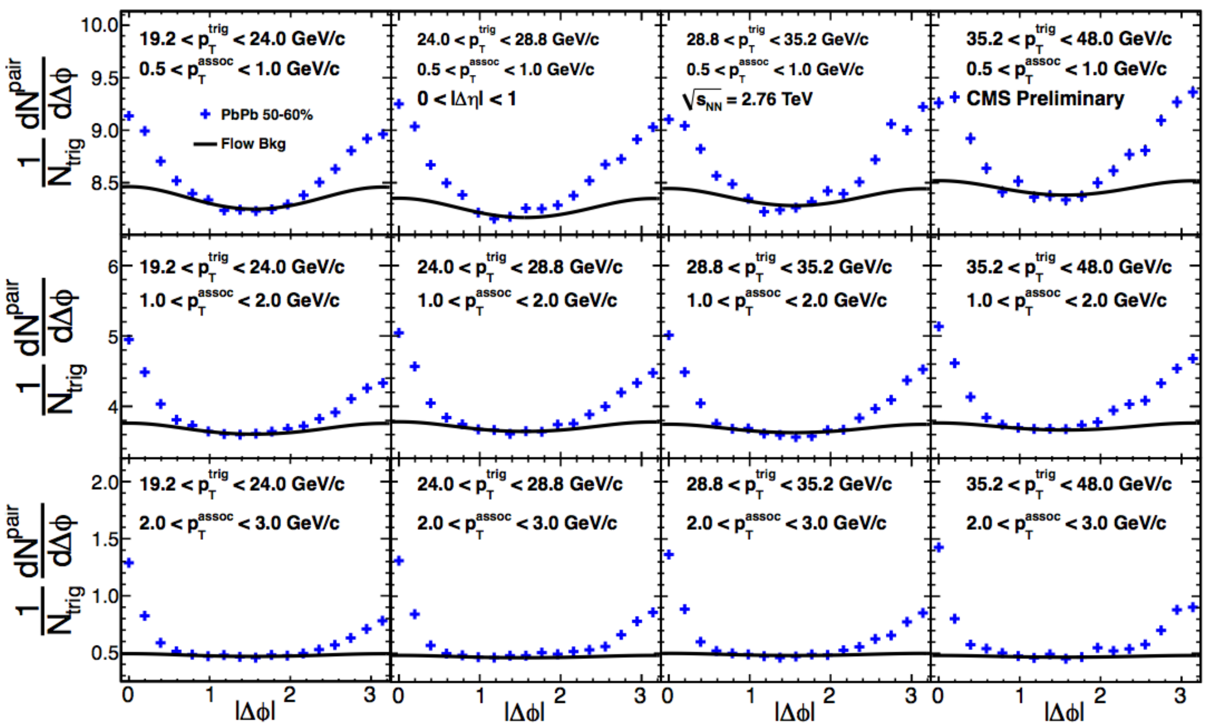

Figure 6.3: The 1-D $\Delta\phi$-projected associated yield distributions for 50-60% peripheral Pb+Pb collisions with $|\Delta\eta| < 1$ are shown with the blue points and the estimated flow backgrounds (scaled by the a_0 parameter from the ZYAM procedure) are represented by the solid black curves. The distributions are shown for various combinations of p_T^{trig}, increasing from left to right, and p_T^{assc}, increasing from top to bottom [86].

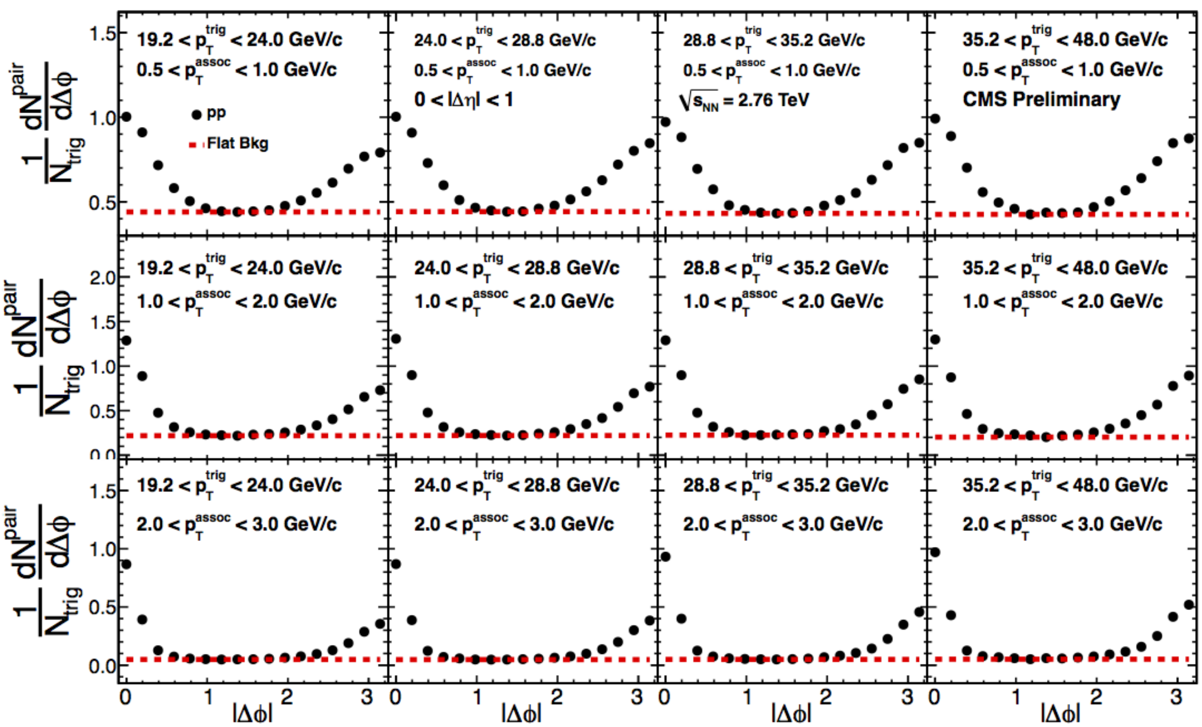

Figure 6.4: The 1-D $\Delta\phi$-projected associated yield distributions for $p+p$ collisions with $|\Delta\eta| < 1$ are shown with the black points and the pedestal backgrounds (scaled by the a_0 parameter from the ZYAM procedure) are represented by the dashed red lines. The distributions are shown for various combinations of $p_{\mathrm{T}}^{\mathrm{trig}}$, increasing from left to right, and $p_{\mathrm{T}}^{\mathrm{assc}}$, increasing from top to bottom [86].

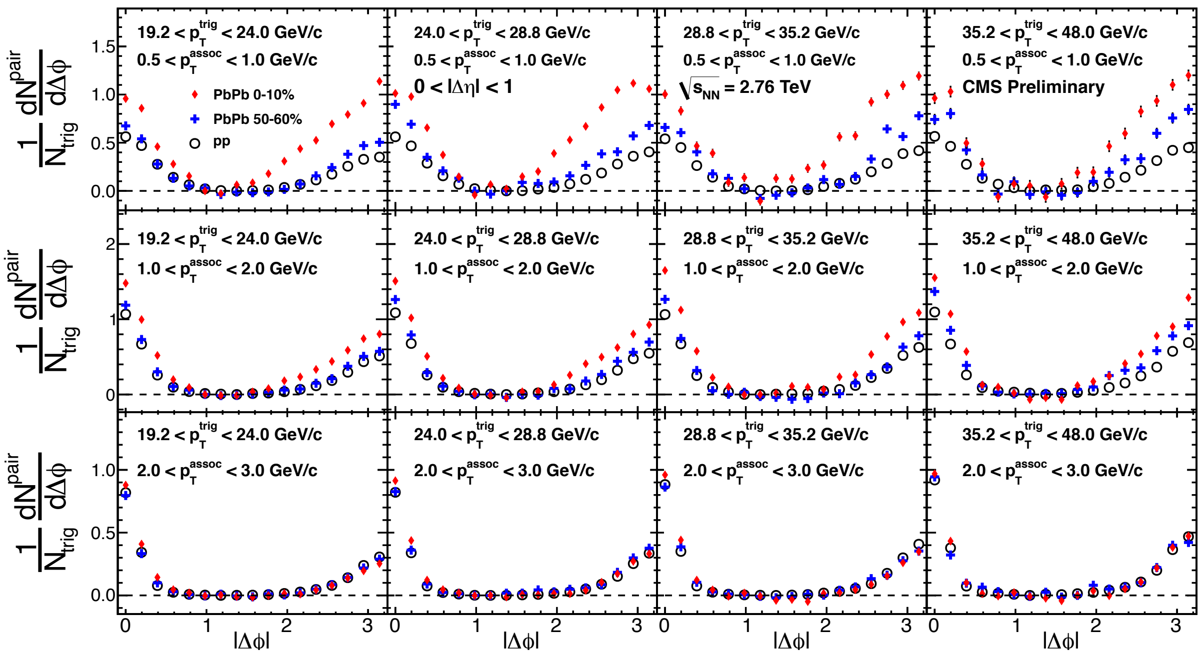

Figure 6.5: The 1-D $\Delta\phi$-projected associated yield distributions after the background subtraction (via the ZYAM procedure) for $|\Delta\eta| < 1$. The distributions are shown for various combinations of $p_{\rm T}^{\rm trig}$, increasing from left to right, and $p_{\rm T}^{\rm assc}$, increasing from top to bottom. The distributions for $0 - 10\%$ central Pb+Pb collisions are shown in red, $50 - 60\%$ peripheral Pb+Pb collisions are shown in blue, and $p + p$ collisions are shown with open black circles [86].

6.1.4 Integrated Yields and I_{AA} Ratios

In order to study jet-suppression and QGP energy loss using the background subtracted per-trigger-particle associated yield distributions, described in the previous section, we need to quantify the yields of the near and away-side jet peaks. This will allow meaningful, quantitative comparisons between different Pb+Pb centralities and p+p collisions. This can be done by first calculating the integrated yields under the near ($0 < |\Delta\phi| < 1$) and away-side ($1 < |\Delta\phi| < \pi$) jet peaks,

$$Y^{\text{near}}(p_{\text{T}}^{\text{trig}}, p_{\text{T}}^{\text{assc}}) = \frac{1}{N_{\text{trig}}} \int_{0}^{\Delta\phi_{\min}} \int_{0}^{\Delta\eta'} \frac{d^2 N_{\text{sub}}^{\text{pair}}}{d\Delta\phi d\Delta\eta} d\Delta\eta d\Delta\phi \tag{6.11}$$

and

$$Y^{\text{away}}(p_{\text{T}}^{\text{trig}}, p_{\text{T}}^{\text{assc}}) = \frac{1}{N_{\text{trig}}} \int_{\Delta\phi_{\min}}^{\pi} \int_{0}^{\Delta\eta'} \frac{d^2 N_{\text{sub}}^{\text{pair}}}{d\Delta\phi d\Delta\eta} d\Delta\eta d\Delta\phi \tag{6.12}$$

where $\Delta\phi_{\min} = 1$ and $\Delta\eta' = 1$ in this analysis. An illustration of the calculations shown in Eq. (6.11) and Eq. (6.12) are shown in Fig. 6.6(a) and Fig. 6.6(b), respectively.

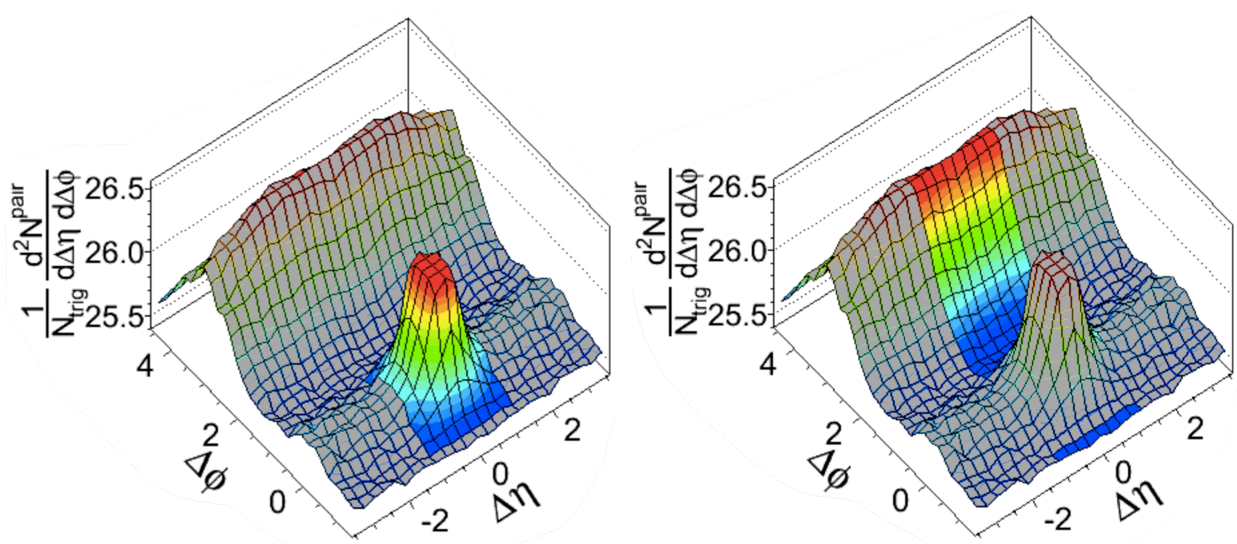

(a) The near-side integrated yield contribution

(b) The away-side integrated yield contribution

Figure 6.6: An illustration showing what would go into the near-side integrated yield (a) and the away-side integrated yield (b) from the example per-trigger-particle associated yield distribution shown in Fig. 6.1.

Figure 6.7 shows the integrated yields for 0-10% central Pb+Pb collisions (red), 50-60% peripheral Pb+Pb collisions (blue), and p+p collisions (open white circles). The results are shown as a function of $p_{\mathrm{T}}^{\mathrm{assc}}$ in the four $p_{\mathrm{T}}^{\mathrm{trig}}$ bins used in this analysis. The top row shows the near-side integrated yields and the bottom row shows the away-side integrated yields.

We can then quantify the amount of jet suppression observed in Pb+Pb collisions compared to $p+p$ collisions by calculating the I_{AA} modification factor. This is just the ratio of integrated yields in Pb+Pb collisions to that in $p+p$ collisions. As a function of $p_{\mathrm{T}}^{\mathrm{trig}}$ and $p_{\mathrm{T}}^{\mathrm{assc}}$ this ratio is given by,

$$I_{\mathrm{AA}}(p_{\mathrm{T}}^{\mathrm{trig}}, p_{\mathrm{T}}^{\mathrm{assc}}) = \frac{Y^{AA}\left(p_{\mathrm{T}}^{\mathrm{trig}}, p_{\mathrm{T}}^{\mathrm{assc}}\right)}{Y^{pp}\left(p_{\mathrm{T}}^{\mathrm{trig}}, p_{\mathrm{T}}^{\mathrm{assc}}\right)}, \tag{6.13}$$

where Y^{AA} and Y^{pp} are the integrated yields in Pb+Pb and $p+p$ collisions, respectively. As with the integrated yields, Eq. (6.11) and Eq. (6.12), the I_{AA} ratios can be calculated for the near and away-side separately. These can also be calculated as a function of Pb+Pb event centrality to compare jet suppression between central and peripheral events. These results will be shown in Sec. 7.2.

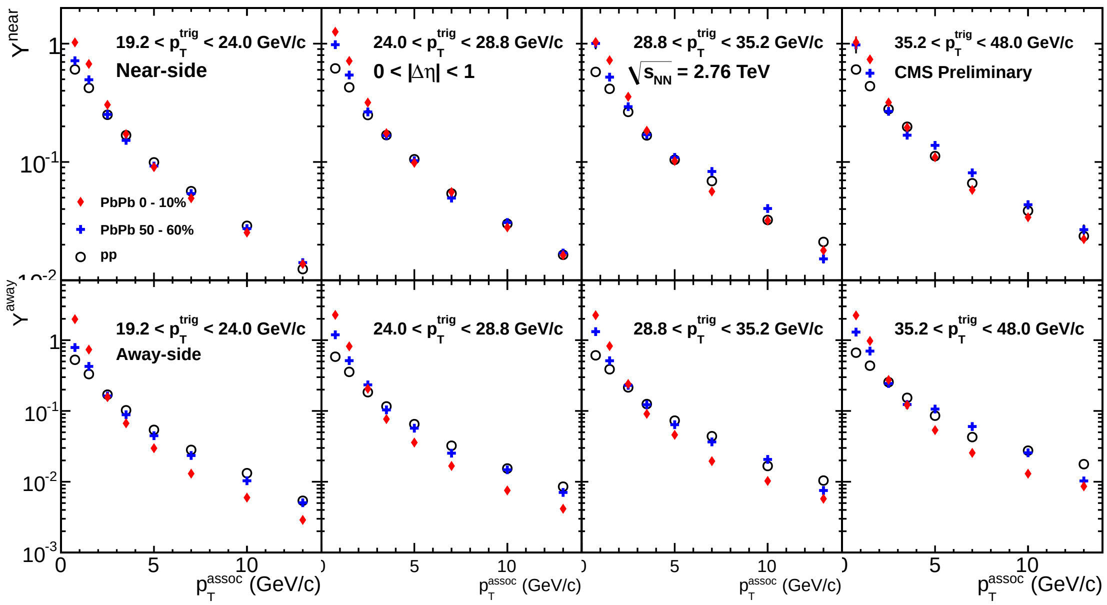

Figure 6.7: The near (top) and away-side (bottom) integrated yields for $|\Delta\eta| < 1$ as a function of $p_{\mathrm{T}}^{\mathrm{assc}}$ for four different $p_{\mathrm{T}}^{\mathrm{trig}}$ bins. The red data points are for 0-10% central Pb+Pb collisions, the blue points are for 50-60% peripheral Pb+Pb collisions, and the open circles are for $p+p$ collisions. The error bars only correspond to the statistical uncertainty in this measurement. [86].

6.2 Long-Range $\Delta\eta$ Subtraction

As a consistency check for the ZYAM based v_n-subtraction method another method for isolating the jet correlations and calculating the integrated yields, henceforth referred to as the *long-range $\Delta\eta$ subtraction method*, was used for comparison. This method relies on the assumption that the long-range ridge correlation in $\Delta\eta$ (henceforce referred to as just the *long-range* correlation) observed in the near-side of the per-trigger-particle associated yield distributions, such as in Fig. 6.1, does not contain any jet-like correlations. In other words, it is assumed to be a result of only flow effects and will contain contributions from all of the v_n coefficients. It is also assumed that the long-range near-side ridge, resulting from the v_n contributions, is constant in $\Delta\eta$ since the v_n values have been shown to be almost independent of η [77, 82].

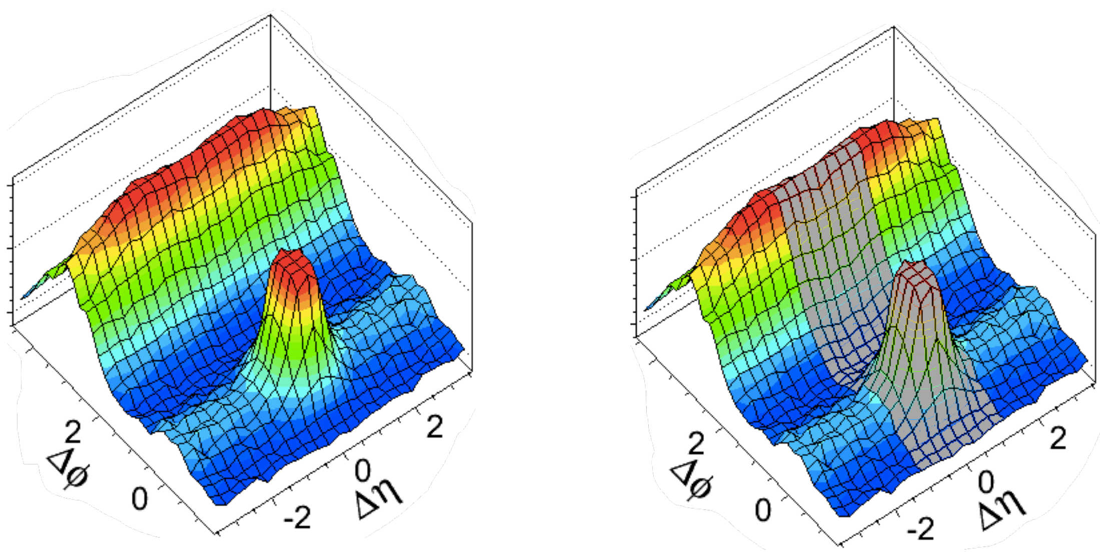

(a) The full per-trigger-particle associated yield distribtion

(b) The long-range $\Delta\eta$ component of the per-trigger-particle associated yield distribution

Figure 6.8: An illustration showing the difference between the long-range component of the per-trigger-particle associated yield distribution (a) and the full per-trigger-particle associated yield distribution (b).

Under these assumptions, we can remove the correlations from flow by estimating their contribution with the 1-D projection of the long-range $\Delta\eta$ region ($1 < |\Delta\eta| < 4$) onto the $\Delta\phi$ axis. The lower limit was chosen to ensure that no component of the near-side jet peak is included in the correlation since this is always contained within $|\Delta\eta| < 1$. The upper limit was chosen due to limited statistics from the basic tracker geometry which covers $|\eta| < 2.4$. Therefore, we can remove the flow background and isolate the jet-like correlations if we subtract this from the 1-D $\Delta\phi$ projection of the entire per-trigger-particle assisted yield distribution ($0 < |\Delta\eta| < 4$). An illustration showing the difference between the full 2-D per-trigger-particle associated yield distribution and the long-range region is shown in Fig. 6.8.

The near-side integrated yields can then be calculated with this method by the following equation,

$$Y^{\mathrm{near}}(p_{\mathrm{T}}^{\mathrm{trig}}, p_{\mathrm{T}}^{\mathrm{assc}}) = \frac{1}{N_{\mathrm{trig}}} \int_0^{\Delta\phi_{\mathrm{min}}} d\Delta\phi \left[\int_0^4 \frac{d^2N^{\mathrm{pair}}}{d\Delta\phi d\Delta\eta} d\Delta\eta - \int_1^4 \frac{d^2N^{\mathrm{pair}}}{d\Delta\phi d\Delta\eta} d\Delta\eta \right] \tag{6.14}$$

where, again, in this analysis $\Delta\phi_{\mathrm{min}} = 1$. Figure 6.9 shows the 1-D $\Delta\phi$ projected distributions of the full per-trigger-particle associated yield (red) and the long-range region (white) corresponding to the example shown in Fig. 6.8. With the near-side integrate yield it is then straightforward to calculate the near-side I_{AA} ratio using the procedure outlined in the previous section.

This method can only be used as a cross check for the near-side I_{AA} ratios since the assumptions made for the long-range near-side ridge do not hold for the away-side. Specifically, jet correlations are not limited to a small $\Delta\eta$ region like in the near-side, they contribute in the entire $\Delta\eta$ region. Thus, subtracting the long-range region on the away-side will remove parts of the jet correlations that we are trying to isolate. This can be seen in Fig. 6.9 where the 1-D $\Delta\phi$ projections of the full $\Delta\eta$ range and the long-range region are almost identical on the away-side. Despite the limitations of this method it can still provide an important consistency check with the v_n-subtraction method and help validate necessary assumptions.

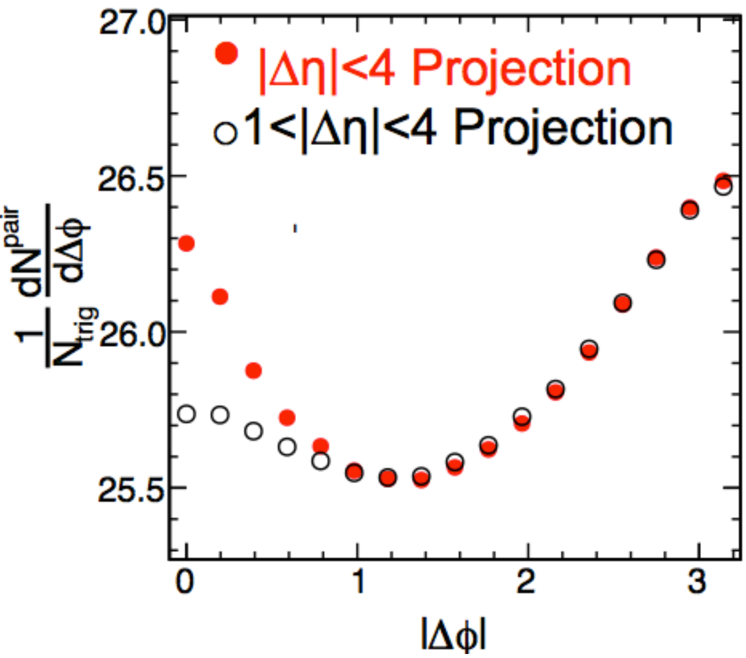

Figure 6.9: The 1-D $\Delta\phi$ projected per-trigger-particle associated yield distributions corresponding to the 2-D distributions shown in Fig. 6.8. The red points correspond to the $\Delta\phi$ projection of the full distribution (shown in Fig. 6.8(a)) and the open white points correspond to the $\Delta\phi$ projection of the long-range component of the distribution (shown in Fig. 6.8(b)).

6.3 Systematic Uncertainties

The final systematic uncertainties associated with the final I_{AA} results come from three main areas: the v_n parameterization, the ZYAM method, and the tracking corrections. Each one will be discussed in more detail in the following subsections but a table quantifying the corresponding uncertainties in various p_{T} and centrality ranges is shown for both the near (Table 6.1) and away-side (Table 6.2) I_{AA} results below. It is worth noting that the tables are just for reference, the actual systematic uncertainties were calculated explicitly in each ($p_{\mathrm{T}}^{\mathrm{trig}}, p_{\mathrm{T}}^{\mathrm{assc}}$) from each source and added in quadrature for the final results.

Table 6.1: Systematic uncertainties of the near-side associated yields [86].

	Centrality	00-10%	10-60%
Source	$p_{\mathrm{T}}^{\mathrm{assc}}$ (GeV/c)		
v_n parameterization	$[0.5; 2.0]$	5%	7%
	$[2.0; 6.0]$	2%	2%
	$[> 6.0]$	1%	1%
ZYAM method	$[0.5; 2.0]$	5%	5%
	$[2.0; 6.0]$	2%	2%
	$[> 6.0]$	1%	1%
Tracking corrections	All	10%	10%
Total	$[0.5; 2.0]$	12%	13%
	$[2.0; 6.0]$	10%	10%
	$[> 6.0]$	10%	10%

Table 6.2: Systematic uncertainties of the away-side associated yields [86].

	Centrality	00-10%	10-60%
Source	$p_{\mathrm{T}}^{\mathrm{assc}}$ **(GeV/c)**		
v_n parameterization	$[0.5; 2.0]$	3%	6%
	$[2.0; 6.0]$	1%	2%
	$[> 6.0]$	1%	1%
ZYAM method	$[0.5; 2.0]$	8%	10%
	$[2.0; 6.0]$	6%	5%
	$[> 6.0]$	1%	2%
Tracking corrections	All	10%	10%
Total	$[0.5; 2.0]$	13%	15%
	$[2.0; 6.0]$	11%	11%
	$[> 6.0]$	10%	10%

6.3.1 Systematic Uncertainties in the v_n Parameterization and Subtraction

The parameterization of the high-p_T v_n results was done so the p_T binning could be changed if necessary, as discussed in Sec. 6.1.2. The upper and lower limits of the fit uncertainties were calculated and used to determine how much the parameterization affects the final I_{AA} results. Specifically, the standard deviation of the fit function as a function of p_T was calculated analytically using the functional form of the fit where the parameter uncertainties were determined from the covariance matrix returned from `TMinuit`. The v_3 and v_4 values were only parameterized up to 25 GeV/c and 20 GeV/c, respectively, due to the lack of statistics at high p_T. Above these values both coefficients were assumed to be zero.

The upper (lower) bound of the parameterization uncertainty was then calculated by adding (subtracting) $\sigma(p_\mathrm{T})$ to the fit for the entire p_T range. The fits at $\pm\sigma(p_\mathrm{T})$ are shown in blue for v_2, v_3, and v_4 in Figures 6.10, 6.11, and 6.12, respectively. The near and away-side I_{AA} results were then calculated using the upper and lower bounds on the parameterization uncertainty. These results were compared to those found with the nominal parameterization obtained by the fitting procedure to determine the systematic effect. The results of using these limits on the parameterization for the I_{AA} calculations are shown for both the near and away-side values as well as the 0-10% and 50-60% most central events in Figures 6.13, 6.14, 6.15, and 6.16. It should be noted that the statistical error bars on the bottom ratios plots are not really meaningful since it is the ratio of the same dataset subtracted by a different parameterized background. The systematic effect from the v_n parameterization was calculated in the same way for the other centrality bins used in the analysis: 10-20%, 20-30%, 30-40%, and 40-50%.

The effect of the parameterization is only significant at low-p_T, in particular on the near-side. Each bin in $(p_\mathrm{T}^\mathrm{trig}, p_\mathrm{T}^\mathrm{assc})$ is subtracted by a background modulated by the $v_n(p_\mathrm{T}^\mathrm{trig}) \times v_n(p_\mathrm{T}^\mathrm{assc})$ terms. Since the lowest $p_\mathrm{T}^\mathrm{trig}$ bin starts at 19.2 GeV/c the amount of flow modulation starts to drop off drastically above p_T 2-3 GeV/c. Above p_T 5 GeV/c the flow background is essentially flat, which is why the effect of the parameterization are almost negligible at high-p_T despite the fact that the uncertainty in the parameterization is largest here.

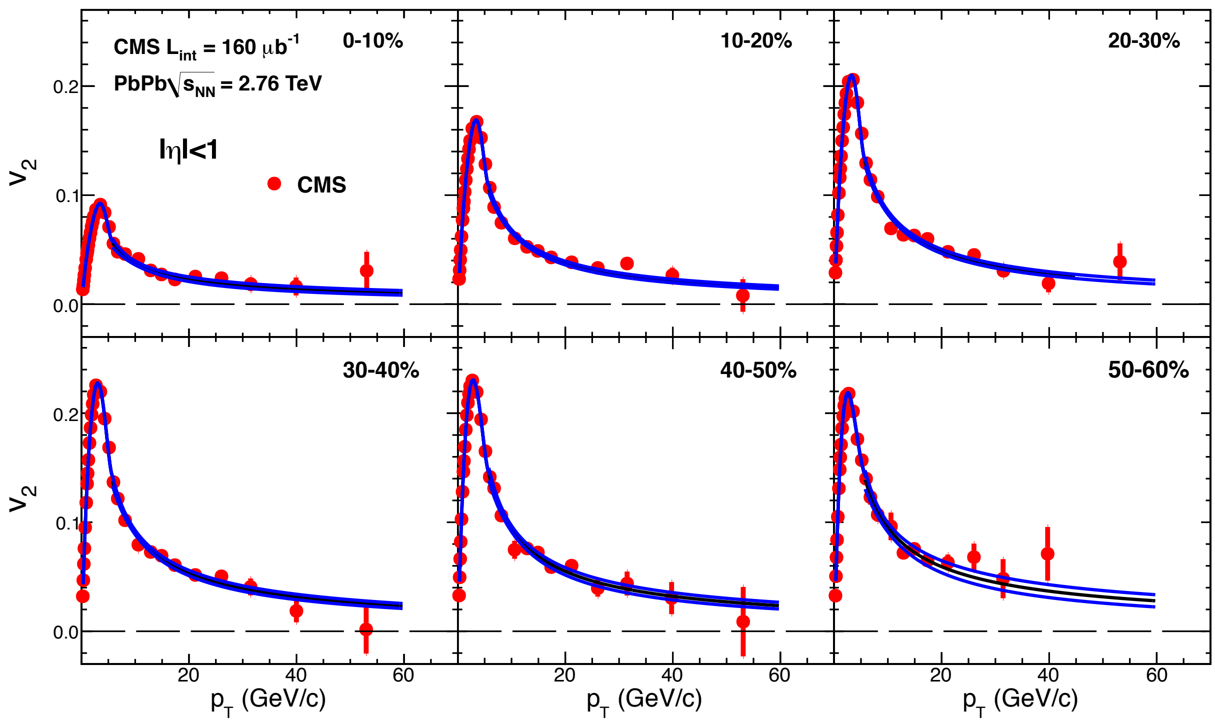

Figure 6.10: v_2 as a function of p_{T} for $\eta < 1$ in six different centrality bins with the most central 0-10% in the top left and the most peripheral 50-60% in the bottom right. The blue curves represent the one sigma bounds of the fit parameterization, which is shown in black.

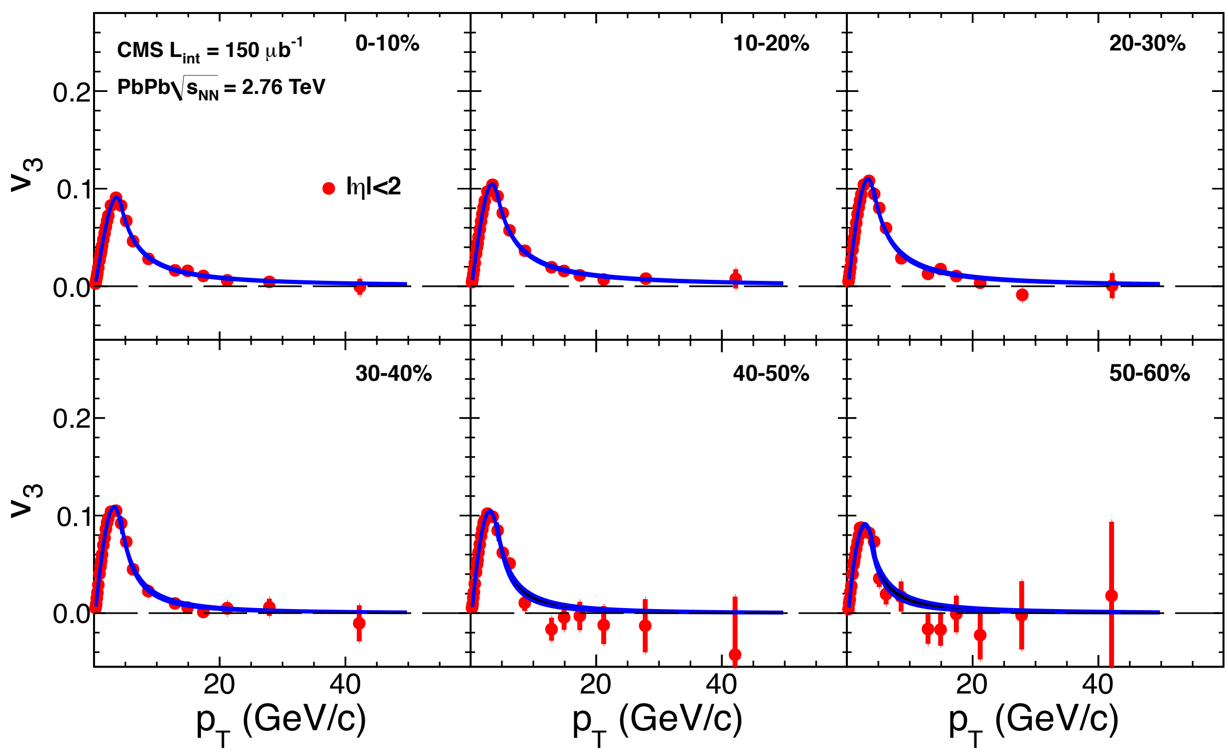

Figure 6.11: v_3 as a function of p_{T} for $\eta < 1$ in six different centrality bins with the most central 0-10% in the top left and the most peripheral 50-60% in the bottom right. The blue curves represent the one sigma bounds of the fit parameterization, which is shown in black.

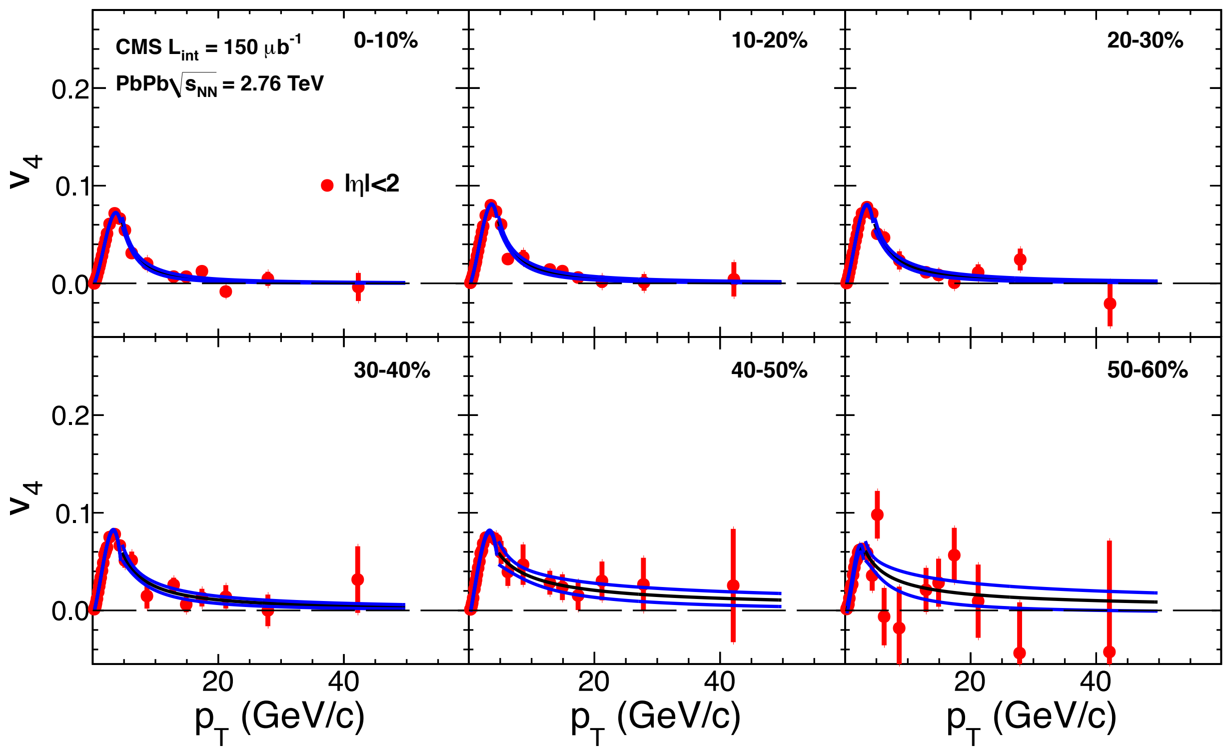

Figure 6.12: v_4 as a function of p_T for $\eta < 1$ in six different centrality bins with the most central 0-10% in the top left and the most peripheral 50-60% in the bottom right. The blue curves represent the one sigma bounds of the fit parameterization, which is shown in black.

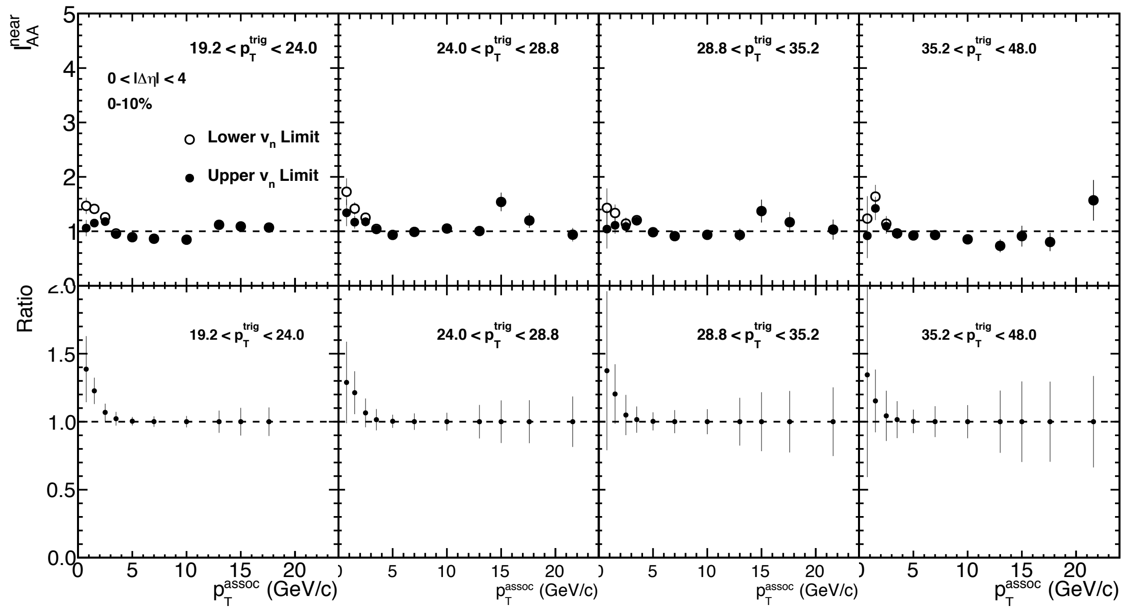

Figure 6.13: The top row shows I_{AA}^{near} as a function of $p_{\text{T}}^{\text{assc}}$ in four different $p_{\text{T}}^{\text{trig}}$ bins for the 0-10% most central collisions. The open circles represent the values calculated using the upper limit of the v_n parameterization and the closed circles represent the values calculated using the lower limt. The bottom row shows the ratio of the I_{AA} values obtained with the upper and lower limits.

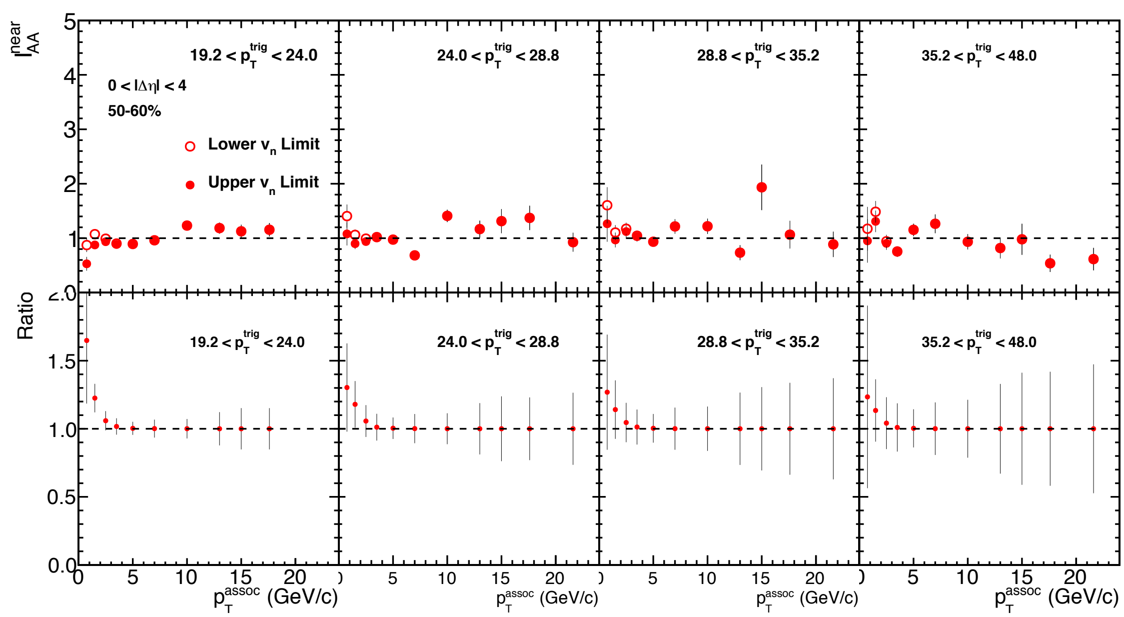

Figure 6.14: The top row shows I_{AA}^{near} as a function of $p_{\text{T}}^{\text{assc}}$ in four different $p_{\text{T}}^{\text{trig}}$ bins for the 50-60% most central collisions. The open red circles represent the values calculated using the upper limit of the v_n parameterization and the closed red circles represent the values calculated using the lower limt. The bottom row shows the ratio of the I_{AA} values obtained with the upper and lower limits.

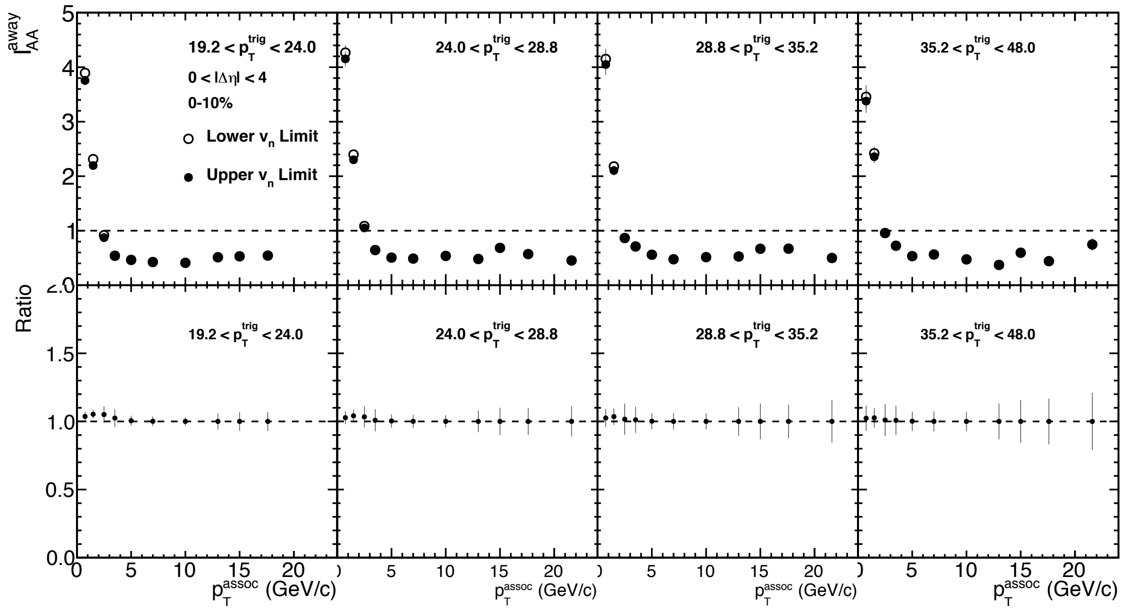

Figure 6.15: The top row shows I_{AA}^{away} as a function of $p_{\text{T}}^{\text{assc}}$ in four different $p_{\text{T}}^{\text{trig}}$ bins for the 0-10% most central collisions. The open circles represent the values calculated using the upper limit of the v_n parameterization and the closed circles represent the values calculated using the lower limt. The bottom row shows the ratio of the I_{AA} values obtained with the upper and lower limits.

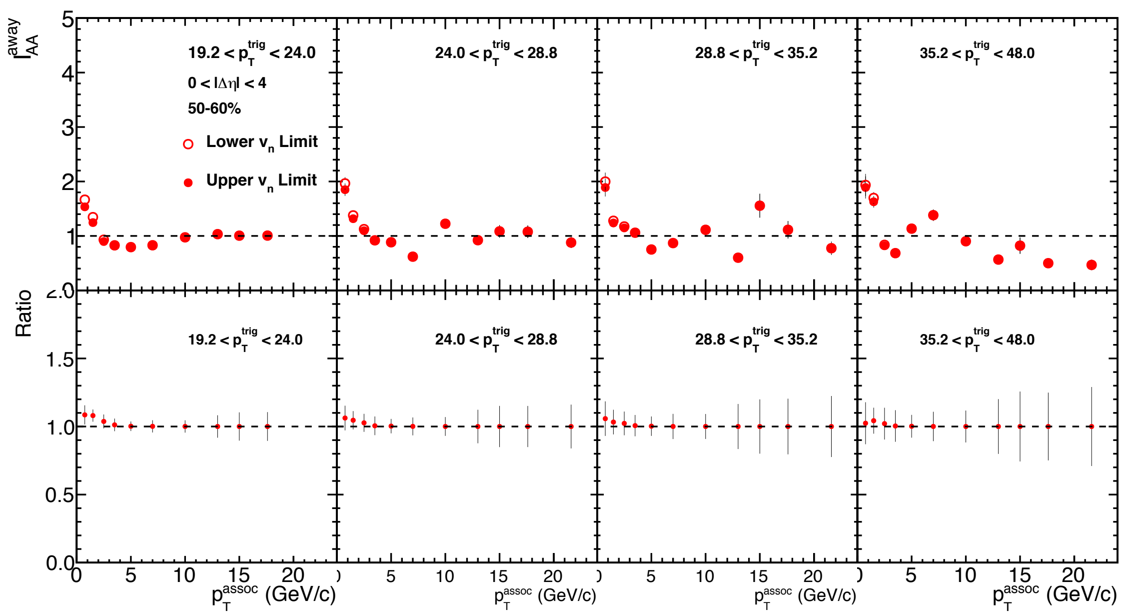

Figure 6.16: The top row shows I_{AA}^{away} as a function of $p_{\text{T}}^{\text{assc}}$ in four different $p_{\text{T}}^{\text{trig}}$ bins for the 50-60% most central collisions. The open red circles represent the values calculated using the upper limit of the v_n parameterization and the closed red circles represent the values calculated using the lower limt. The bottom row shows the ratio of the I_{AA} values obtained with the upper and lower limits.

6.3.2 Systematic Uncertainties from the ZYAM Method

The Zero Yield at Minimum (ZYAM) method that is used to subtract the flow background is another source of systematic uncertainty in the analysis. As discussed in Sec. 6.1.3 this method depends heavily on the parameter $\Delta\phi_{min}$ (also referred to as $\Delta\phi_{\mathrm{ZYAM}}$). Specifically, this point is used as the minimum for the ZYAM criteria and also separates the near and away-side for the integrated yield calculations. In this analysis this parameter was set to $\Delta\phi_{\mathrm{ZYAM}} = 1.0$. In order to determine the systematic effect of fixing this parameter the results were calculated by allowing the parameter to vary in a given range. The value of $\Delta\phi_{\mathrm{ZYAM}}$ is then determined by the minimum of the parabola fit to the data within the allowed range.

The I_{AA} results calculated with $\Delta\phi_{\mathrm{ZYAM}} = 1$ and $0.4 < \Delta\phi_{\mathrm{ZYAM}} < 1.6$ are shown for the near and away-side measurements in the 0-10% and 50-60% centrality bins in Figures 6.17, 6.18, 6.19, and 6.20. Similarly, the allowed range of the parameter $\Delta\phi_{\mathrm{ZYAM}}$ was shifted to determine the effect on the results. Thus the I_{AA} results were also calculated with $0.6 < \Delta\phi_{\mathrm{ZYAM}} < 1.8$ (open circles) and $0.2 < \Delta\phi_{\mathrm{ZYAM}} < 1.4$ (close circles) on both the near and away-side in the same centrality bins. These results are shown in Figures 6.21, 6.22, 6.23, and 6.24.

The differences are only large at low-p_{T}. This is due to the fact that as p_{T} is increased the near and away-side jet peaks become narrow, leaving a large flat region in between. This means that the exact value of $\Delta\phi_{\mathrm{ZYAM}}$ becomes less important at high-p_{T} since the minimum is constant in the flat region between the peaks. The total systematic effect of the ZYAM procedure is largest below $p_{\mathrm{T}} \sim 2$ GeV/c but remain non-negligible up to $p_{\mathrm{T}} \sim 6$ GeV/c. There is almost no effect above $p_{\mathrm{T}} \sim 6$ GeV/c but an uncertainty of 1% is quoted in the table as a conservative estimate.

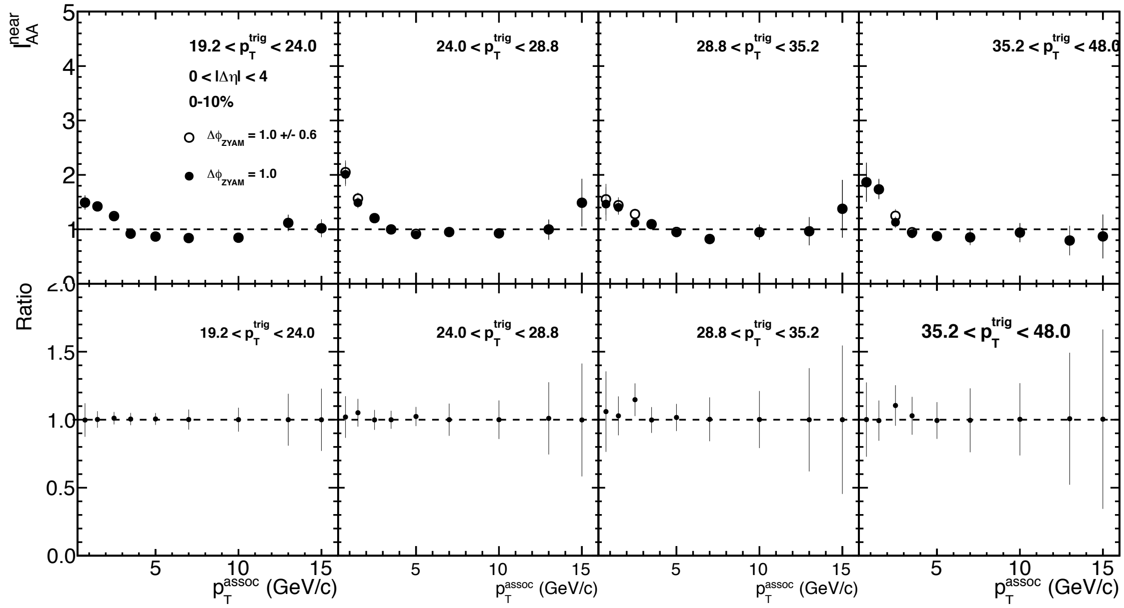

Figure 6.17: I_{AA}^{near} as a function of $p_{\text{T}}^{\text{assc}}$ for four different $p_{\text{T}}^{\text{trig}}$ bins for the 0-10% most central collisions. The filled circles show the results with $\Delta\phi_{\text{ZYAM}} = 1.0$ and the open circles show the results when $\Delta\phi_{\text{ZYAM}}$ is allowed to vary in the range $0.4 < \Delta\phi_{\text{ZYAM}} < 1.6$. The bottom row shows the ratio of the two different sets of results.

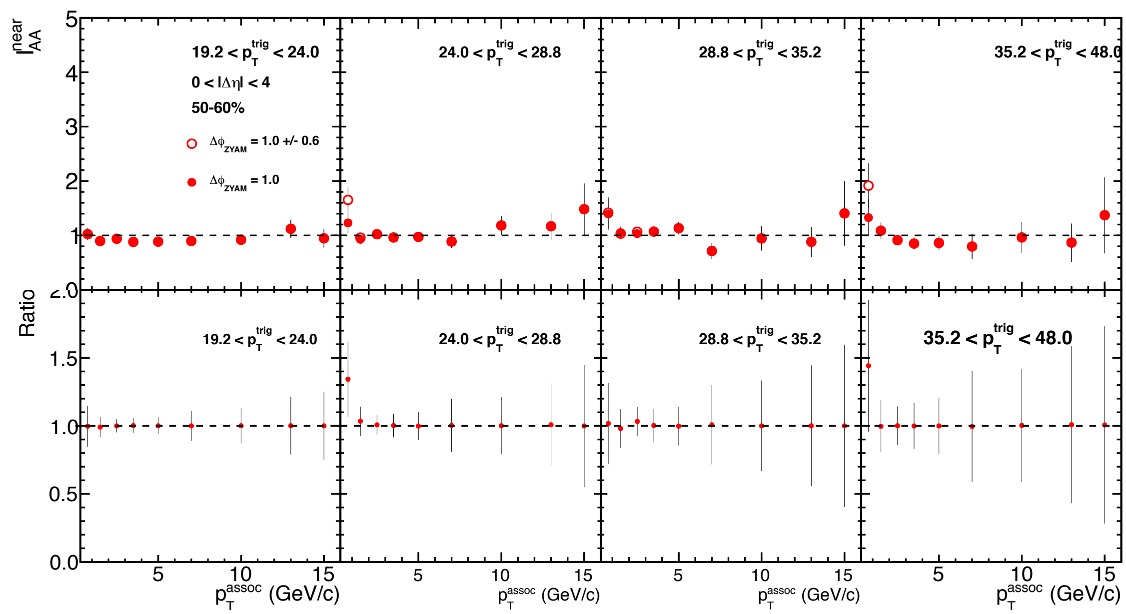

Figure 6.18: I_{AA}^{near} as a function of $p_{\text{T}}^{\text{assc}}$ for four different $p_{\text{T}}^{\text{trig}}$ bins for the 50-60% most central collisions. The filled red circles show the results with $\Delta\phi_{\text{ZYAM}} = 1.0$ and the open red circles show the results when $\Delta\phi_{\text{ZYAM}}$ is allowed to vary in the range $0.4 < \Delta\phi_{\text{ZYAM}} < 1.6$. The bottom row shows the ratio of the two different sets of results.

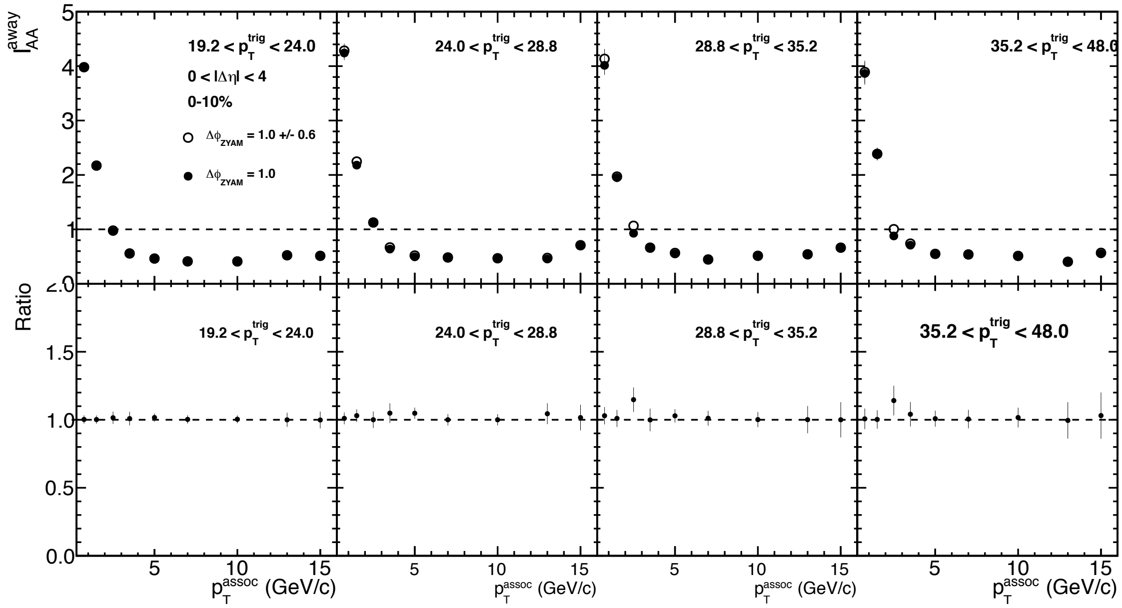

Figure 6.19: I_{AA}^{away} as a function of $p_{\text{T}}^{\text{assc}}$ for four different $p_{\text{T}}^{\text{trig}}$ bins for the 0-10% most central collisions. The filled circles show the results with $\Delta\phi_{\text{ZYAM}} = 1.0$ and the open circles show the results when $\Delta\phi_{\text{ZYAM}}$ is allowed to vary in the range 0.4,1.6. The bottom row shows the ratio of the two different sets of results.

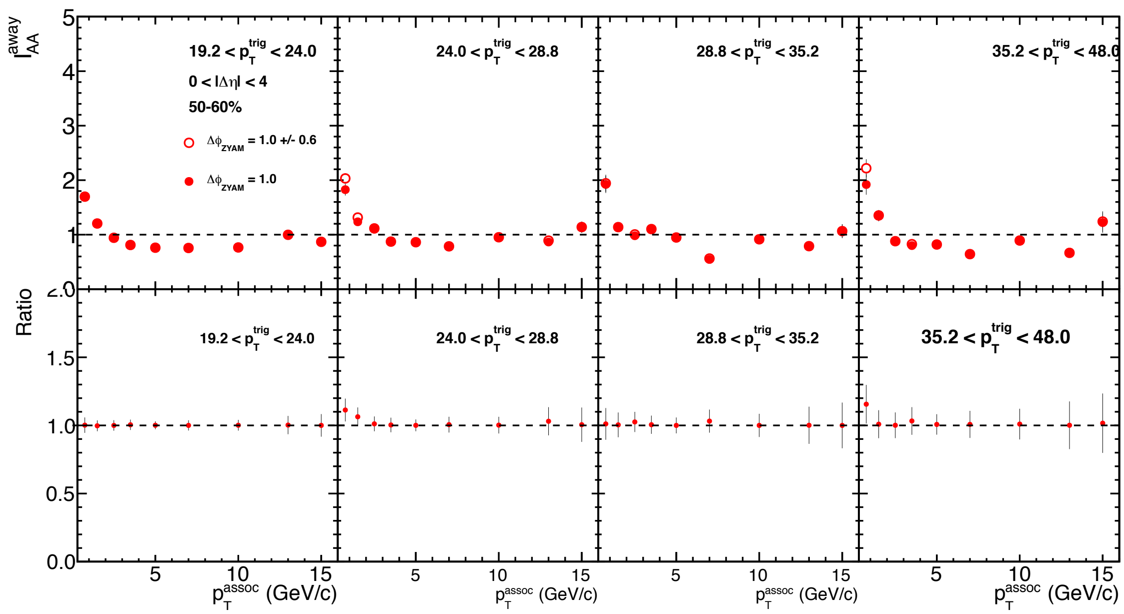

Figure 6.20: I_{AA}^{away} as a function of $p_{\text{T}}^{\text{assc}}$ for four different $p_{\text{T}}^{\text{trig}}$ bins for the 50-60% most central collisions. The filled red circles show the results with $\Delta\phi_{\text{ZYAM}} = 1.0$ and the open red circles show the results when $\Delta\phi_{\text{ZYAM}}$ is allowed to vary in the range $0.4 < \Delta\phi_{\text{ZYAM}} < 1.6$. The bottom row shows the ratio of the two different sets of results.

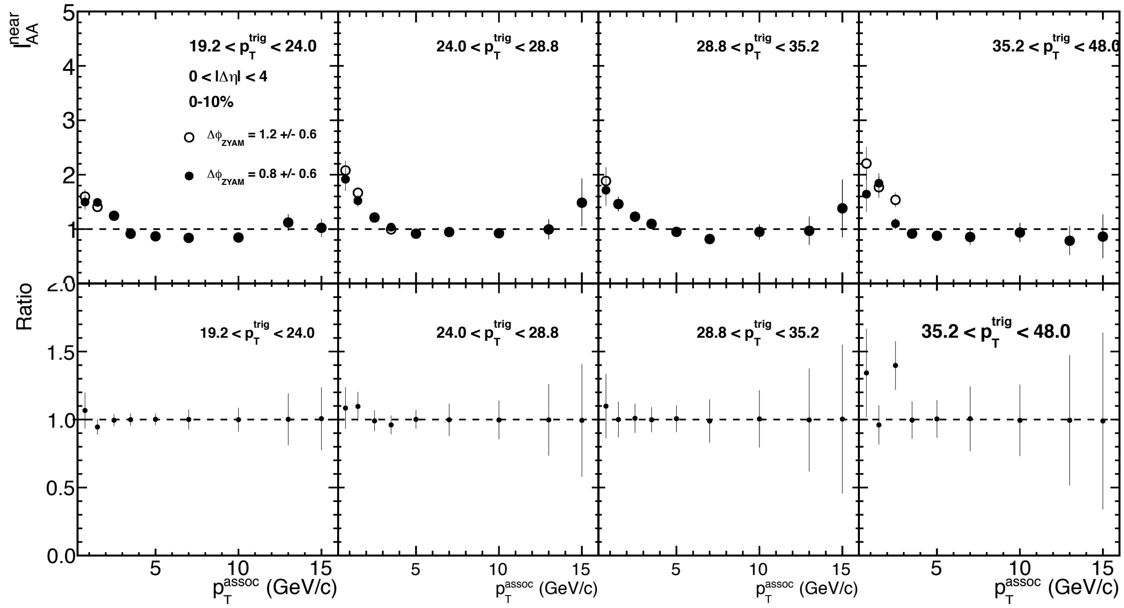

Figure 6.21: I_{AA}^{near} as a function of $p_{\mathrm{T}}^{\mathrm{assc}}$ for four different $p_{\mathrm{T}}^{\mathrm{trig}}$ bins for the 0-10% most central collisions. The results were calculated using two different ranges for the $\Delta\phi_{\mathrm{ZYAM}}$ parameter: $0.6 < \Delta\phi_{\mathrm{ZYAM}} < 1.8$ (open circles) and $0.2 < \Delta\phi_{\mathrm{ZYAM}} < 1.4$ (closed circles). The bottom row shows the ratio of the two different sets of results.

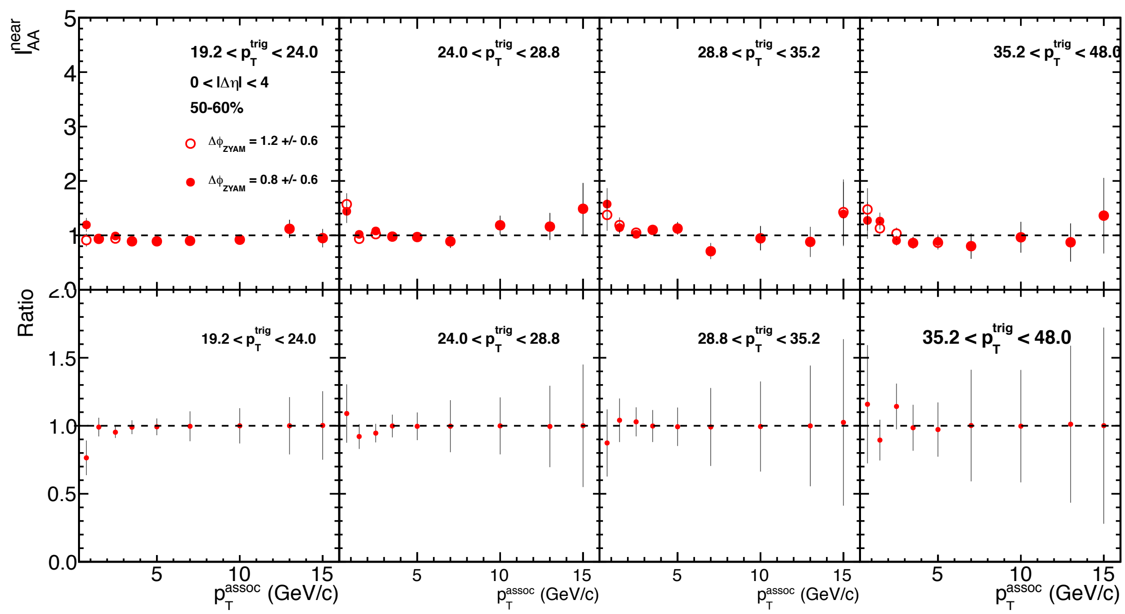

Figure 6.22: I_{AA}^{near} as a function of $p_{\mathrm{T}}^{\mathrm{assc}}$ for four different $p_{\mathrm{T}}^{\mathrm{trig}}$ bins for the 50-60% most central collisions. The results were calculated using two different ranges for the $\Delta\phi_{\mathrm{ZYAM}}$ parameter: $0.6 < \Delta\phi_{\mathrm{ZYAM}} < 1.8$ (open red circles) and $0.2 < \Delta\phi_{\mathrm{ZYAM}} < 1.4$ (closed red circles). The bottom row shows the ratio of the two different sets of results.

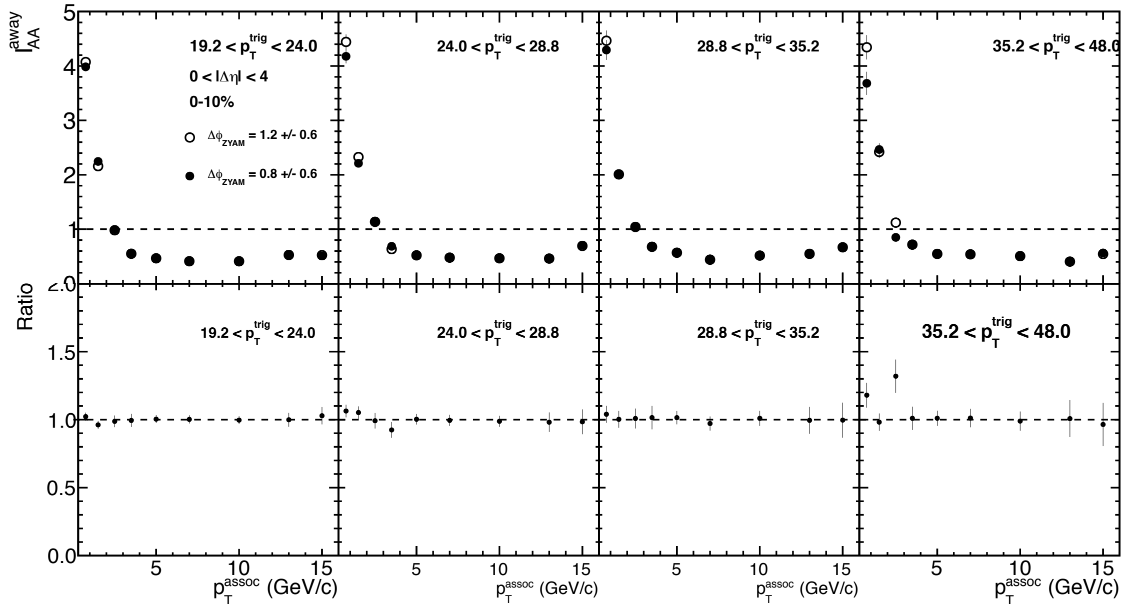

Figure 6.23: $I_{AA}^{\rm away}$ as a function of $p_{\rm T}^{\rm assc}$ for four different $p_{\rm T}^{\rm trig}$ bins for the 0-10% most central collisions. The results were calculated using two different ranges for the $\Delta\phi_{\rm ZYAM}$ parameter: $0.6 < \Delta\phi_{\rm ZYAM} < 1.8$ (open circles) and $0.2 < \Delta\phi_{\rm ZYAM} < 1.4$ (closed circles). The bottom row shows the ratio of the two different sets of results.

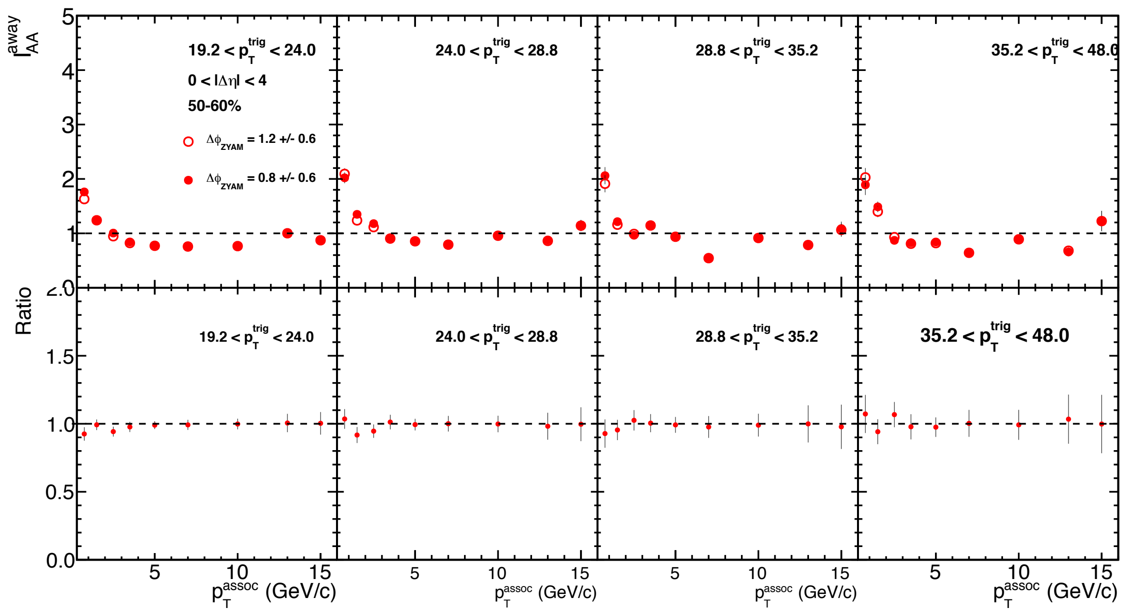

Figure 6.24: $I_{AA}^{\rm away}$ as a function of $p_{\rm T}^{\rm assc}$ for four different $p_{\rm T}^{\rm trig}$ bins for the 50-60% most central collisions. The results were calculated using two different ranges for the $\Delta\phi_{\rm ZYAM}$ parameter: $0.6 < \Delta\phi_{\rm ZYAM} < 1.8$ (open red circles) and $0.2 < \Delta\phi_{\rm ZYAM} < 1.4$ (closed red circles). The bottom row shows the ratio of the two different sets of results.

6.3.3 Systematic Uncertainties from Track Corrections

To determine the effect of applying the efficiency correction to each reconstructed track before constructing the dihadron correlations, which was discussed in Sec. 5.4, a closure test was done. This was done by looking at PYTHIA dijets embedded into HYDJET Pb+Pb events and constructing the dihadron correlation functions from the generator level tracks, reconstructed tracks, and efficiency corrected reconstructed tracks.

The 1-D $\Delta\phi$ projected dihadron correlations from these three track collections with $|\Delta\eta| < 4$ are shown in Figures 6.25-6.28. Fig. 6.25 shows the results for 0-30% central Pb+Pb events with $15 < p_{\mathrm{T}}^{\mathrm{trig}} < 30$ GeV/c in six different $p_{\mathrm{T}}^{\mathrm{assc}}$ bins. Fig. 6.26 shows the same results for the 30-60% central Pb+Pb events. Fig. 6.27 shows the results with $30 < p_{\mathrm{T}}^{\mathrm{trig}} < 50$ GeV/c for 0-30% central Pb+Pb events and Fig. 6.28 shows them for 30-60% central Pb+Pb events. The ratio of the generator-level and efficiency corrected reconstructed dihadron correlations is shown below each corresponding plot.

In general the agreement is better at low $p_{\mathrm{T}}^{\mathrm{assc}}$ but a lack of sufficient statistics at high $p_{\mathrm{T}}^{\mathrm{assc}}$ make it difficult to accurately determine the effect introduced from the efficiency corrections. A significant increase in computing resources is required to generate MC simulated events with the full track information necessary for tracking studies, especially at high p_{T}, which is why it was difficult to get enough statistics for this study. For this reason it was decided to apply an additional 10% systematic error for all of the data points in the final I_{AA} results to account for the efficiency corrections.

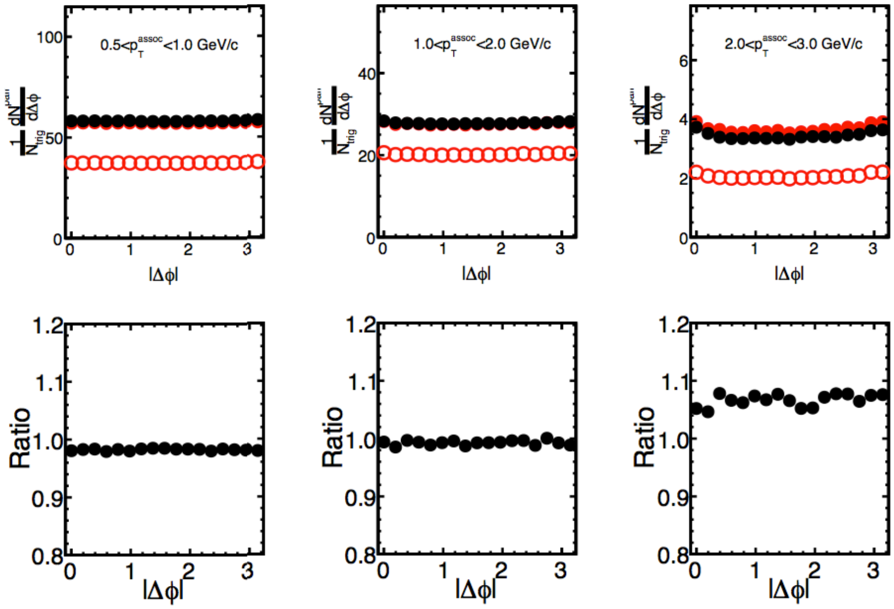

(a) $0.5 < p_{\mathrm{T}}^{\mathrm{assc}} < 3.0$ GeV/c

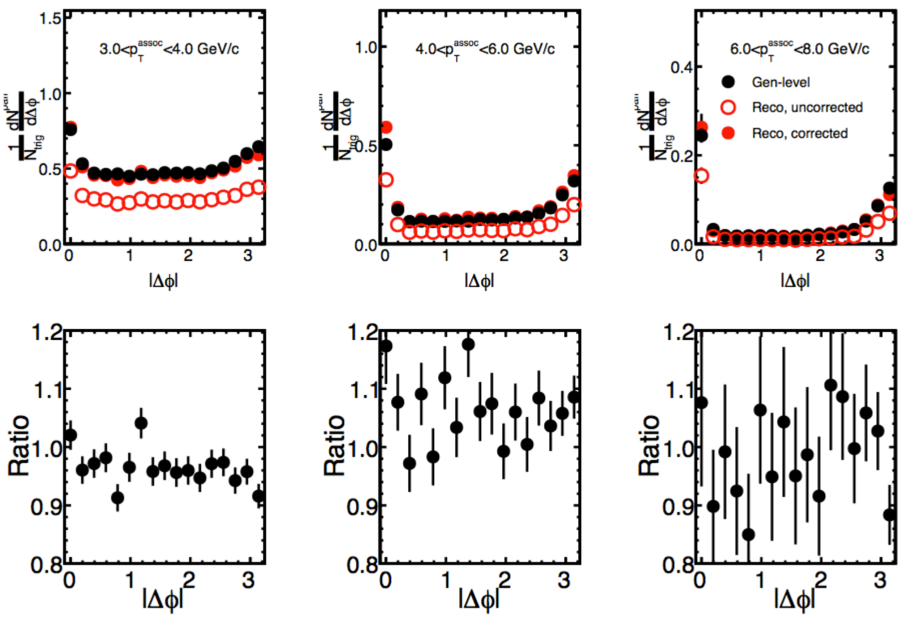

(b) $3.0 < p_{\mathrm{T}}^{\mathrm{assc}} < 8.0$ GeV/c

Figure 6.25: Top: 1-D $\Delta\phi$ projected dihadron correlations with $|\eta| < 4$ and $15 < p_{\mathrm{T}}^{\mathrm{trig}} < 30$ GeV/c in various $p_{\mathrm{T}}^{\mathrm{assc}}$ bins for the 0-30% most central Pb+Pb collisions. The black points are from generator-level tracks, the open red circles are reconstructed tracks, and the solid red circles are efficiency corrected reconstructed tracks.

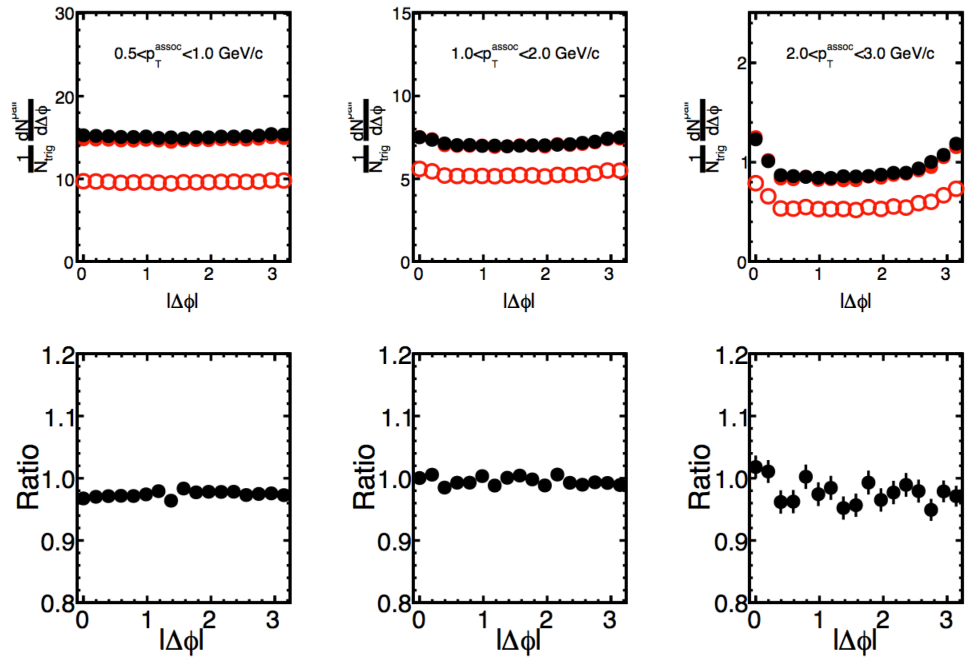

(a) $0.5 < p_{\mathrm{T}}^{\mathrm{assc}} < 3.0$ GeV/c

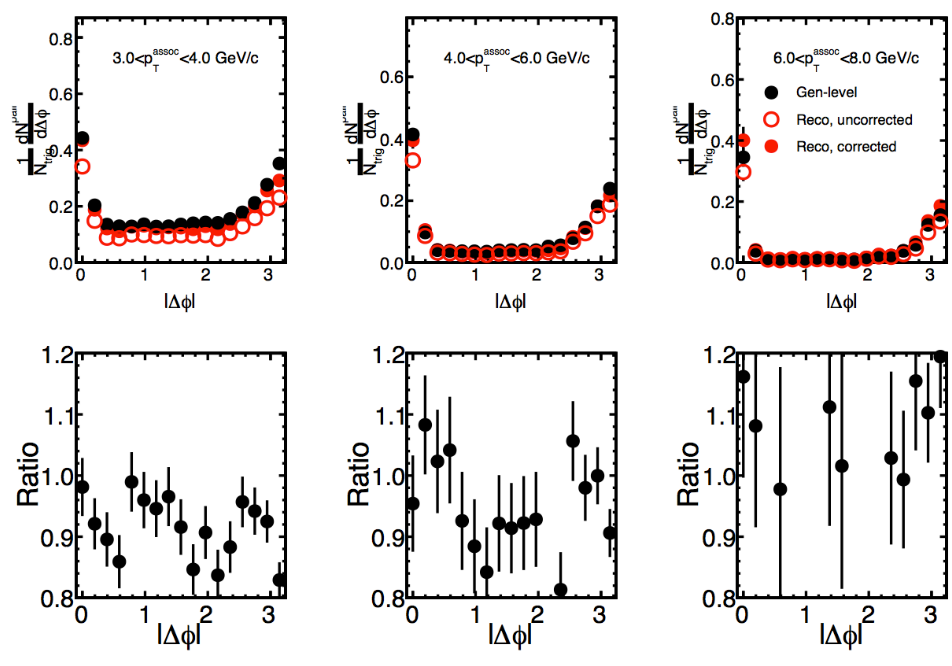

(b) $3.0 < p_{\mathrm{T}}^{\mathrm{assc}} < 8.0$ GeV/c

Figure 6.26: Top: 1-D $\Delta\phi$ projected dihadron correlations with $|\eta| < 4$ and $15 < p_{\mathrm{T}}^{\mathrm{trig}} < 30$ GeV/c in various $p_{\mathrm{T}}^{\mathrm{assc}}$ bins for the 30-60% central Pb+Pb collisions. The black points are from generator-level tracks, the open red circles are reconstructed tracks, and the solid red circles are efficiency corrected reconstructed tracks. Bottom: the ratio of the 1-D $\Delta\phi$ projected dihadron correlations from generator-level tracks to efficiency corrected reconstructed tracks.

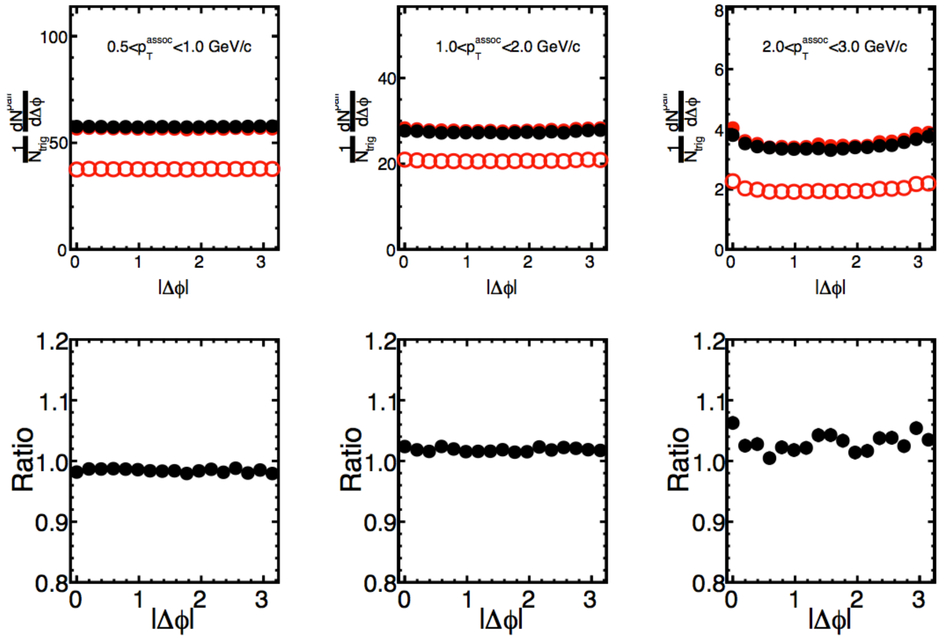

(a) $0.5 < p_{\mathrm{T}}^{\mathrm{assc}} < 3.0$ GeV/c

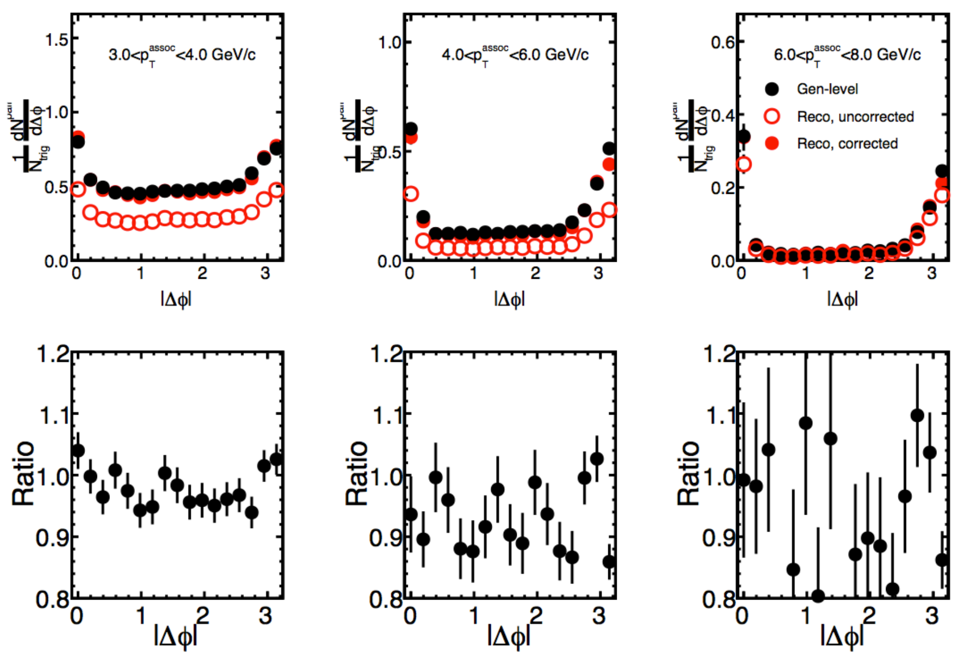

(b) $3.0 < p_{\mathrm{T}}^{\mathrm{assc}} < 8.0$ GeV/c

Figure 6.27: Top: 1-D $\Delta\phi$ projected dihadron correlations with $|\eta| < 4$ and $30 < p_{\mathrm{T}}^{\mathrm{trig}} < 50$ GeV/c in various $p_{\mathrm{T}}^{\mathrm{assc}}$ bins for the 0-30% most central Pb+Pb collisions. The black points are from generator-level tracks, the open red circles are reconstructed tracks, and the solid red circles are efficiency corrected reconstructed tracks. Bottom: the ratio of the 1-D $\Delta\phi$ projected dihadron correlations from generator-level tracks to efficiency corrected reconstructed tracks.

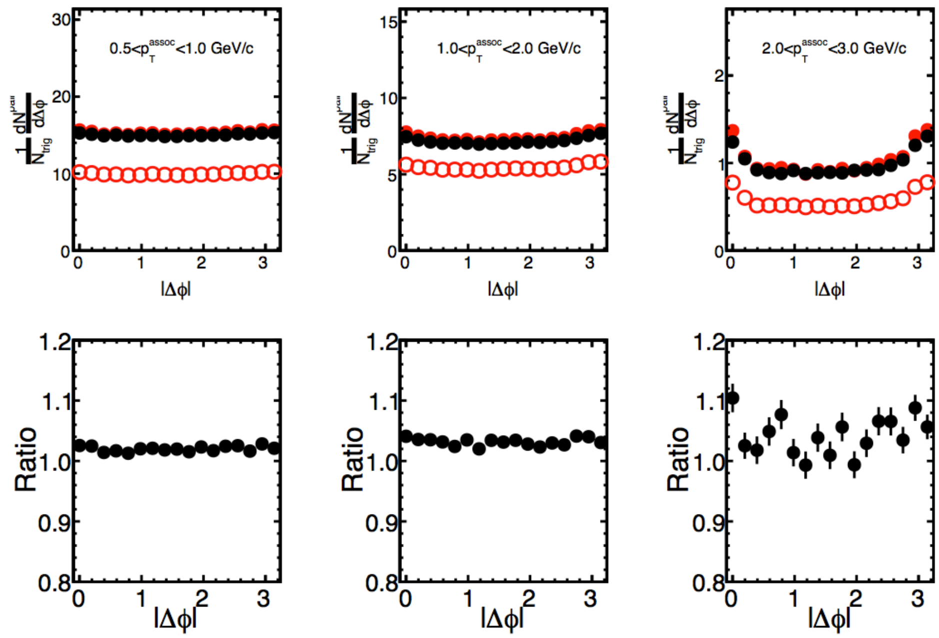

(a) $0.5 < p_{\mathrm{T}}^{\mathrm{assc}} < 3.0$ GeV/c

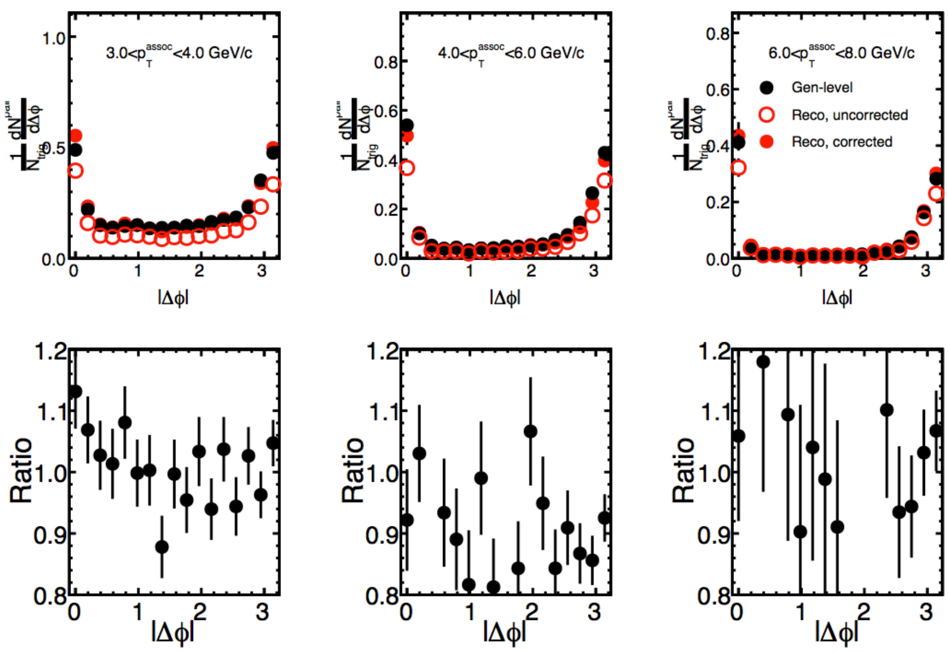

(b) $3.0 < p_{\mathrm{T}}^{\mathrm{assc}} < 8.0$ GeV/c

Figure 6.28: Top: 1-D $\Delta\phi$ projected dihadron correlations with $|\eta| < 4$ and $30 < p_{\mathrm{T}}^{\mathrm{trig}} < 50$ GeV/c in various $p_{\mathrm{T}}^{\mathrm{assc}}$ bins for the 30-60% central Pb+Pb collisions. The black points are from generator-level tracks, the open red circles are reconstructed tracks, and the solid red circles are efficiency corrected reconstructed tracks. Bottom: the ratio of the 1-D $\Delta\phi$ projected dihadron correlations from generator-level tracks to efficiency corrected reconstructed tracks.

6.3.4 Systematic Uncertainties in the High p_{T} v_n Measurements

The event plane method was used to calculate the high-p_{T} v_3 and v_4 measurements. The systematic uncertainties were calculated in the same way as for the high-p_{T} v_2 measurement. The details of this measurement and the sources of the associated uncertainties can be found in Ref. [77].

The primary source of systematic uncertainty comes from the tracking efficiency and misidentification (fake rate) at low-p_{T}. The resolution correction factor used in the Event Plane measurements, the particle composition, and the centrality determination also contribute to the total systematic uncertainty, although these are all at a level of 1% or below. The uncertainties from these sources for v_3 (Table 6.3) and v_4 (Table 6.4) are summarized in the tables below.

Table 6.3: Systematic uncertainties of $v_3\{\Psi_3\}(p_{\mathrm{T}})$ with $|\eta| < 1.0$ in event plane method [86].

	Centrality	00-10%	10-60%
Source	p_T(GeV/c)		
Particle composition	All	0.5%	0.5%
Centrality Determination	All	1.0%	1.0%
Track selection & misidentified track	[0.5; 0.8]	3.0%	2.0%
	[> 0.8]	1.0%	1.0%
Resolution correction	All	1.0%	1.0%
Total	[0.5; 0.8]	4%	3%
	[> 0.8]	2%	2%

Table 6.4: Systematic uncertainties of $v_4\{\Psi_4\}(p_{\mathrm{T}})$ with $|\eta| < 1.0$ in event plane method [86].

	Centrality	00-10%	10-60%
Source	p_T(GeV/c)		
Particle composition	All	0.5%	0.5%
Centrality Determination	All	1.0%	1.0%
Track selection & misidentified track	[0.5; 0.8]	6.0%	4.0%
	[> 0.8]	1.0%	1.0%
Resolution correction	All	5.0%	5.0%
Total	[0.5; 0.8]	8%	7%
	[> 0.8]	6%	6%

Chapter 7

Results

7.1 High-p_{T} Azimuthal Anisotropy Harmonics (v_n)

High-p_{T} v_n measurements can provide information to help constrain the path length (l) dependence of parton energy loss (ΔE) in a QGP medium. Specifically, these measurements can help determine which energy-loss models are dominant at LHC energies: collisional energy loss which predicts $\Delta E \sim l$, radiative energy loss which predicts $\Delta E \sim l^2$, and an AdS/CFT (anti-de Sitter/conformal field theory correspondence) based energy-loss mechanism which predicts $\Delta E \sim l^3$ [101–106]. Recent π^0 v_2 studies from the Relativistic Heavy Ion Collider at $\sqrt{s_{NN}} = 200$ GeV have shown that pQCD calculations of collisional and radiative energy loss underpredict the measured v_2 values for $6 < p_{\mathrm{T}} < 10$ GeV/c while the AdS/CFT-based models compare well with the data [107].

The high-p_{T} v_n measurements shown here significantly extend the p_{T} range of previous v_2 measurements out to $p_{\mathrm{T}} \sim 60$ GeV/c and v_3 and v_4 measurements out to $p_{\mathrm{T}} \sim 50$ GeV/c. In the very high-p_{T} region that these measurements probe, it is expected that effects from hydrodynamic flow are completely negligible and that jet fragmentation dominates particle production, thus making energy-loss measurements less ambiguous.

The results of the high-p_{T} v_2 measurements are shown in Fig. 7.1 for six different centrality bins ranging from $0-10\%$ to $50-60\%$ and two different η ranges, $|\eta| < 1$ and $1 < |\eta| < 2$ [77, 82]. The dashed curves represent the parameterizations used for the I_{AA} measurements, as discussed in Sec. 6.1.2. The low-p_{T} dependence of v_2 shows the characteristic rise up to $2-3$ GeV/c, which is roughly where the thermal spectrum ends. Above 3 GeV/c we see a rapid decrease out to ~ 10 GeV/c as the hydrodynamic contribution diminishes. This is followed by a more gradual decrease out to ~ 60 GeV/c (the extent of the measurement). Although the statistics are limited in the highest p_{T} bins we see that the trend for v_2 remains non-zero all the way out to 60 GeV/c for central collisions.

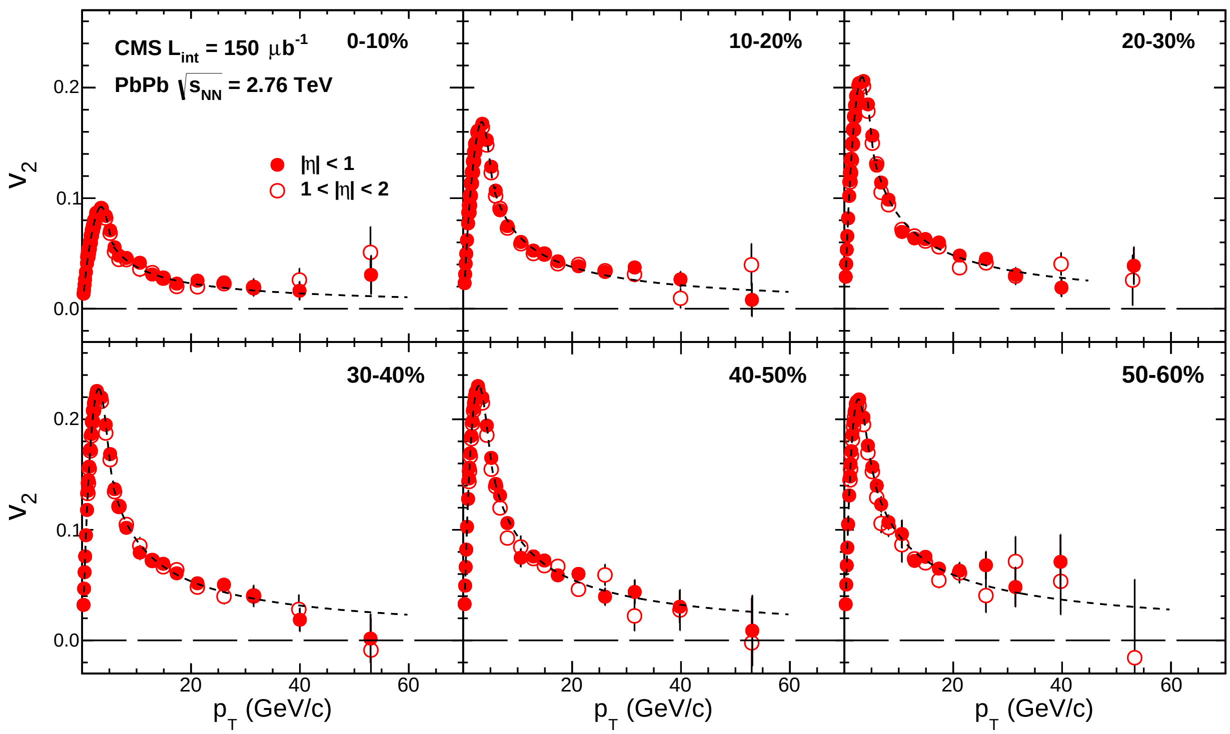

Figure 7.1: The single-particle azimuthal anisotropy coefficient, v_2, as a function of charged particle transverse momentum for $0.3 < p_{\mathrm{T}} < 60$ GeV/c. The red circles are for all charged particles with $|\eta| < 1$ and the open red circles are for all charged particles with $1 < |\eta| < 2$, for six different centrality classes in Pb+Pb collisions at $\sqrt{s_{NN}} = 2.76$ TeV. The error bars only denote statistical uncertainties. The dashed lines show the parameterization used in this analysis. Smooth polynomial functions were used at low-p_{T} and an inverse power law fit was used at high-p_{T}. [77]

The results for the high-p_{T} v_3 and v_4 measurements are shown in Fig. 7.2 and Fig. 7.3, respectively. As in Fig. 7.1, the results are shown for six different centrality bins ranging from $0-10\%$ to $50-60\%$ and two different η ranges, $|\eta| < 1$ and $1 < |\eta| < 2$ [86]. Here we see a similar rise of v_3 and v_4 at low-p_{T} up to ~ 3 GeV/c followed by a rapid decrease from $3-10$ GeV/c.

Above 10 GeV/c v_3 continues to decrease while staying above zero up to $\sim$ 30 GeV/c for central collisions. The v_4 measurement decreases more rapidly and is largely consistent with zero above $\sim$ 20 GeV/c. The statistical uncertainties for the peripheral v_4 measurements at high p_{T} are too large to make any meaningful conclusion about the behavior.

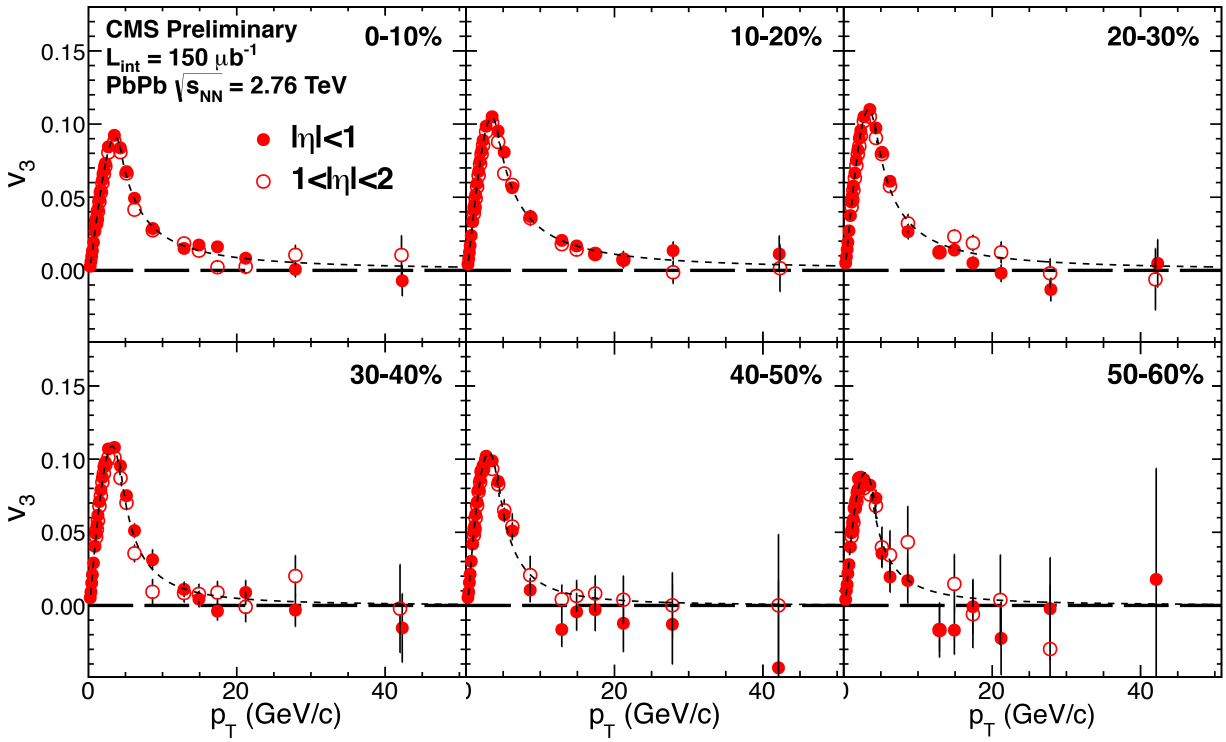

Figure 7.2: The single-particle azimuthal anisotropy coefficient, v_3, as a function of charged particle transverse momentum for $0.3 < p_{\mathrm{T}} < 60$ GeV/c. The red circles are for all charged particles with $|\eta| < 1$ and the open red circles are for all charged particles with $1 < |\eta| < 2$, for six different centrality classes in Pb+Pb collisions at $\sqrt{s_{NN}} = 2.76$ TeV. The error bars only denote statistical uncertainties. The dashed lines show the parameterization used in this analysis. Smooth polynomial functions were used at low-p_{T} and an inverse power law fit was used at high-p_{T}. [86]

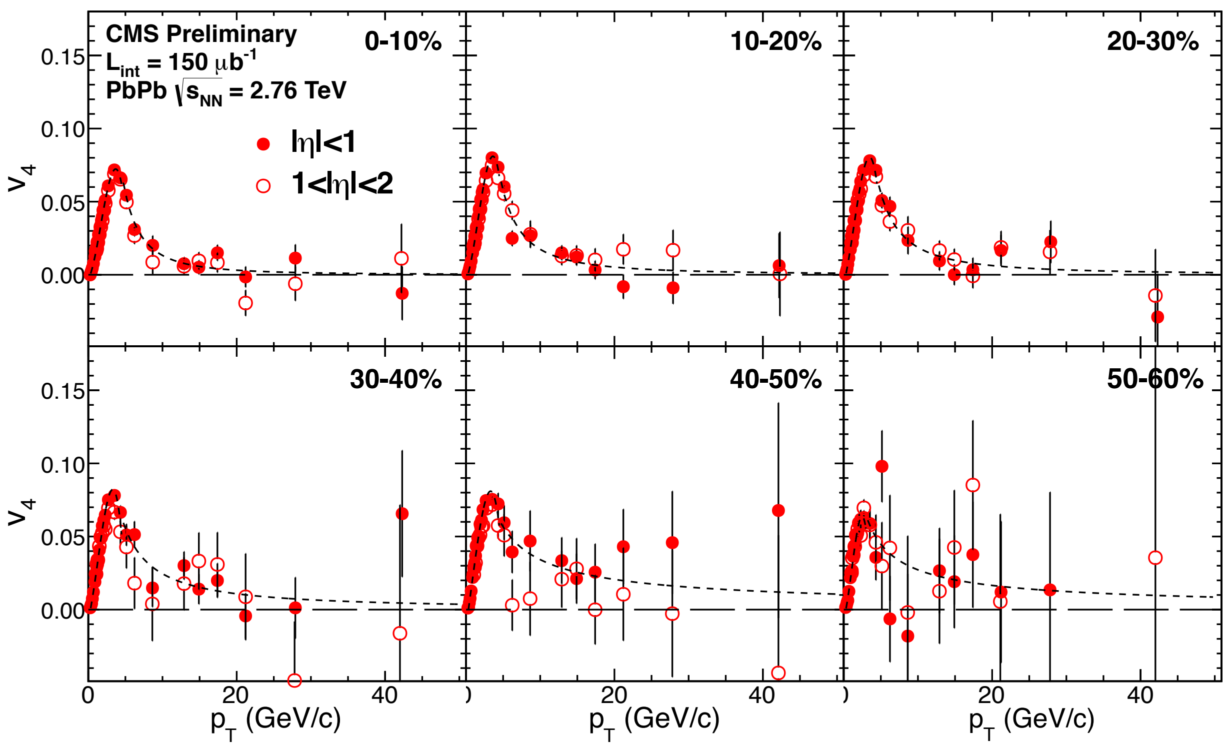

Figure 7.3: The single-particle azimuthal anisotropy coefficient, v_4, as a function of charged particle transverse momentum for $0.3 < p_T < 60$ GeV/c. The red circles are for all charged particles with $|\eta| < 1$ and the open red circles are for all charged particles with $1 < |\eta| < 2$, for six different centrality classes in Pb+Pb collisions at $\sqrt{s_{NN}} = 2.76$ TeV. The error bars only denote statistical uncertainties. The dashed lines show the parameterization used in this analysis. Smooth polynomial functions were used at low-p_T and an inverse power law fit was used at high-p_T. [86]

7.2 Near and Away-Side I_{AA} Ratios

The near-side I_{AA} ratios, which are the ratios of integrated yields in Pb+Pb collisions to $p + p$ collisions (Sec. 6.1.4), are shown in Fig. 7.4 as a function of $p_{\mathrm{T}}^{\mathrm{assc}}$ in four different $p_{\mathrm{T}}^{\mathrm{trig}}$ bins at $\sqrt{s_{NN}} = 2.76$ TeV. The top row shows the near-side I_{AA} values for 0-10% central collisions and the bottom row shows the values for 50-60% peripheral collisions. The red and blue points represent the data obtained from the v_n-subtraction method for $|\eta| < 1$ (Sec. 6.1.3), the black squares in the background represent the data obtained from the long-range $\Delta\eta$ subtraction method (Sec. 6.2). The error bars represent statistical uncertainties while the brackets represent the systematic uncertainties at each point.

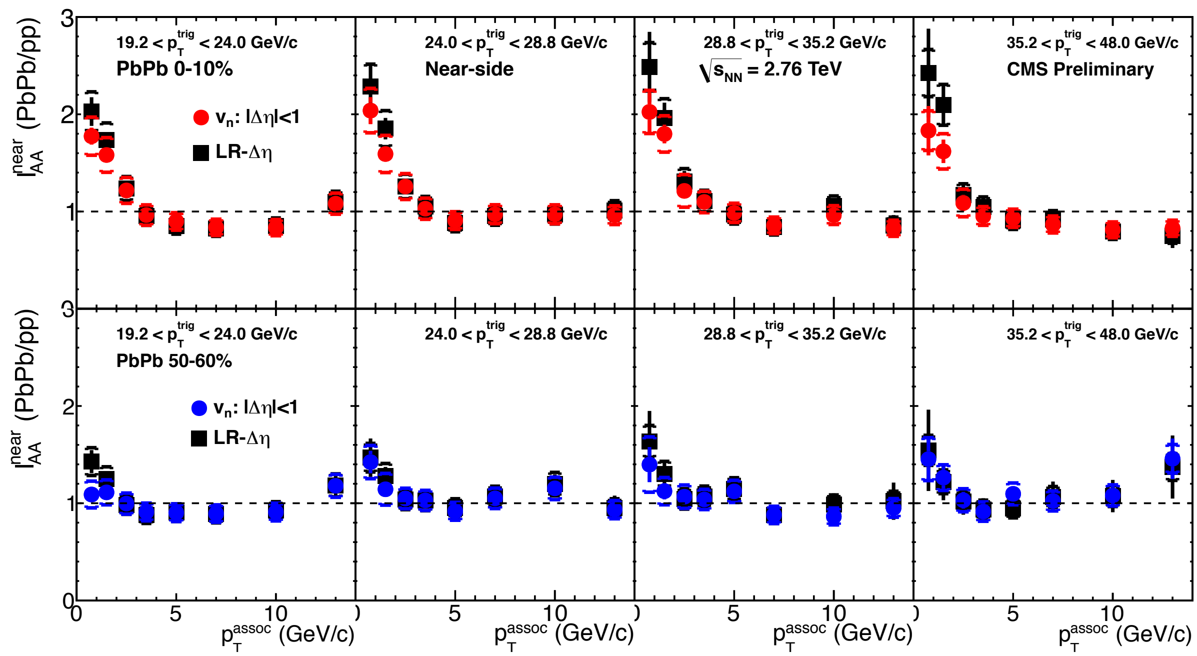

Figure 7.4: Near-side I_{AA} as a function of $p_{\mathrm{T}}^{\mathrm{assc}}$ in four different $p_{\mathrm{T}}^{\mathrm{trig}}$ bins in Pb+Pb collisions at $\sqrt{s_{NN}} = 2.76$ TeV. The top row shows the results for the $0-10\%$ centrality bin and the bottom row shows the results for the $50-60\%$ centrality bin. The blue and red circles represent the results calculated from the v_n-subraction method with $|\Delta\eta| < 1$ while the black squares in the background represent the results calculated from the long-range $\Delta\eta$ subtraction method. The vertical error bars represent statistical uncertainties while the brackets represent the systematic uncertainties.

The v_n-subtraction method and the long-range $\Delta\eta$ subtraction method show excellent agreement for the near-side I_{AA} values above $p_{\mathrm{T}}^{\mathrm{assc}} \sim 2$ GeV/c. In this region the near-side I_{AA} ratios are consistent with 1.0 with some bins showing at most a ∼10% discrepancy, indicating a negligible modification from the $p+p$ reference. At very low $p_{\mathrm{T}}^{\mathrm{assc}}$, $\sim 0.5-1$ GeV/c, there is up to a 25% discrepancy between the v_n-subtraction method and the long-range $\Delta\eta$ subtraction method in some cases, although the statistical and systematic errors are largest in these bins. The discrepancy could be due to a potential contribution from the v_1 term, which was not included in the v_n-subtraction procedure since the data were not available at high p_{T}. Despite the discrepancy, both methods show an enhancement of up to a factor of two for the near-side I_{AA} ratio for $p_{\mathrm{T}}^{\mathrm{assc}} < 2$ GeV/c in the 0-10% central Pb+Pb collisions. A slight enhancement is also seen in the 50-60% peripheral Pb+Pb collisions at low $p_{\mathrm{T}}^{\mathrm{assc}}$ but the significance is small given the size of the uncertainties.

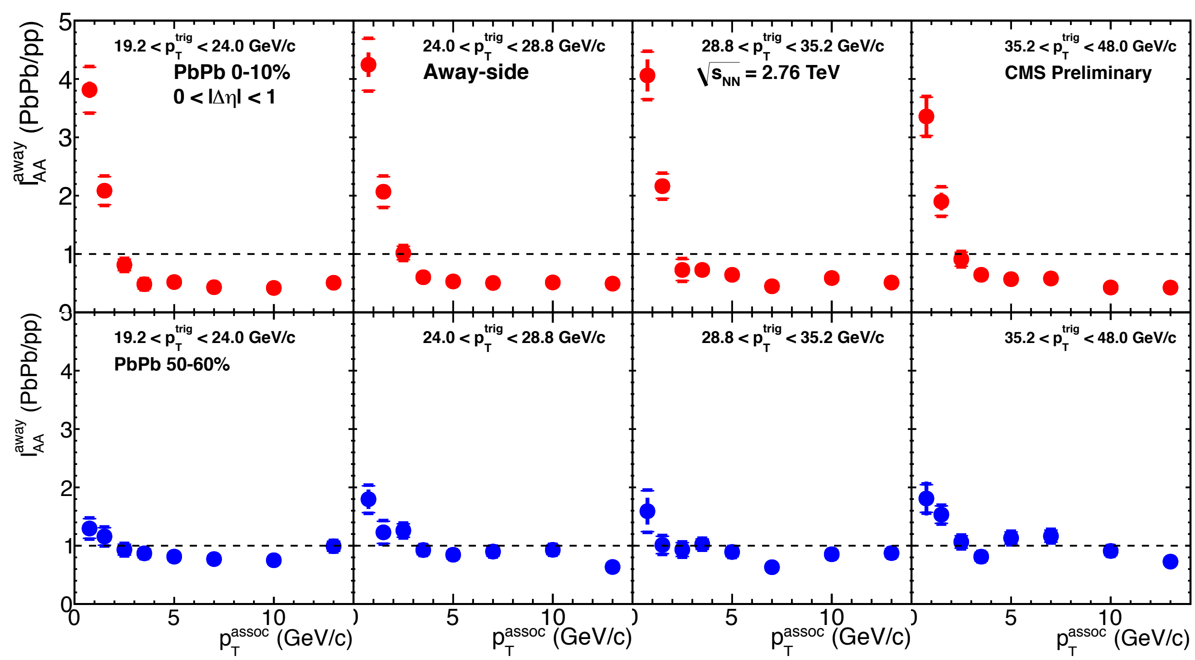

Figure 7.5: Away-side I_{AA} calculated from the v_n-subtraction method with $|\Delta\eta| < 1$ as a function of $p_{\mathrm{T}}^{\mathrm{assc}}$ in four different $p_{\mathrm{T}}^{\mathrm{trig}}$ bins in Pb+Pb collisions at $\sqrt{s_{NN}} = 2.76$ TeV. The top row shows the results for the $0-10\%$ centrality bin and the bottom row shows the results for the $50-60\%$ centrality bin. The vertical error bars represent statistical uncertainties while the brackets represent the systematic uncertainties.

The away-side I_{AA} ratios are shown in Fig. 7.5 as a function of $p_{\mathrm{T}}^{\mathrm{assc}}$ in four different $p_{\mathrm{T}}^{\mathrm{trig}}$ bins at $\sqrt{s_{NN}} = 2.76$ TeV, in a similar manner to the near-side I_{AA} ratios in Fig. 7.4. The red circles in the top row show the away-side I_{AA} values for 0-10% central collisions and the bottom row shows the values for 50-60% peripheral collisions. The error bars represent statistical uncertainties while the brackets represent the systematic uncertainties at each point. Since the long-range $\Delta\eta$ subtraction method is not applicable on the away-side, discussed in Sec. 6.2, only the values obtained from the v_n-subtraction method are shown.

A suppression of about 50% is seen in the away-side I_{AA} ratios for $p_{\mathrm{T}}^{\mathrm{assc}} > 4-5$ GeV/c in 0-10% central Pb+Pb collisions. The amount of suppression appears to be largely independent of $p_{\mathrm{T}}^{\mathrm{trig}}$ and $p_{\mathrm{T}}^{\mathrm{assc}}$ in this range. This behavior is qualitatively consistent with what is expected as a result of jet quenching effects on high-p_{T} partons. As $p_{\mathrm{T}}^{\mathrm{assc}}$ is decreased, the away-side I_{AA} suppression turns to an enhancement around $p_{\mathrm{T}}^{\mathrm{assc}} \sim 3$ GeV/c. In the lowest $p_{\mathrm{T}}^{\mathrm{assc}}$ bin, $0.5 < p_{\mathrm{T}}^{\mathrm{assc}} < 1.0$ GeV/c, an enhancement up to a factor of 3-4 is seen in the 0-10% most central collisions. This can be understood from an energy conservation and energy loss perspective where the high-p_{T} partons lose energy in the medium (and become subsequently suppressed) which is then converted into low-p_{T} associated particles, providing the enhancement. A similar trend is seen in the 50-60% peripheral collisions, shown in blue in the bottom row of Figure 7.5, although the level of enhancement and suppression is significantly less than that observed in central collisions. This indicates that there is a difference in the away-side partonic energy loss between central and peripheral collisions.

The near-side I_{AA} values are shown in Fig. 7.6 as function of the number of participating nucleons, N_{part} in four different $p_{\mathrm{T}}^{\mathrm{assc}}$ ranges. The top row shows the results for $19.2 < p_{\mathrm{T}}^{\mathrm{trig}} < 24$ GeV/c and the bottom row shows the results for $35.2 < p_{\mathrm{T}}^{\mathrm{trig}} < 48$ GeV/c. The number of participating nucleons associated with each centrality bin were calculated using a Glauber model [108]. Again, as in Fig. 7.4, two methods for obtaining the near-side I_{AA} ratios are shown: the v_n-subtraction method (blue) and the long-range $\Delta\eta$ subtraction method (black). The data points from the two different methods were offset slightly on the x-axis for clarity.

We see good agreement between the two methods except in the lowest $p_{\mathrm{T}}^{\mathrm{assc}}$ range. Again, they show a moderate enhancement for $p_{\mathrm{T}}^{\mathrm{assc}} < 2$ GeV/c but indicates a slight suppression in the range

$4 < p_{\mathrm{T}}^{\mathrm{assc}} < 6$ GeV/c. The enhancement at low $p_{\mathrm{T}}^{\mathrm{assc}}$ also shows a correlation with N_{part}, indicating that the enhancement is larger in more central Pb+Pb collisions. This suggests that near-side jets also undergo some energy loss which isn't too surprising since they have, on average, a non-zero path length through the medium. This could also explain the low-p_{T} enhancement seen on the near side.

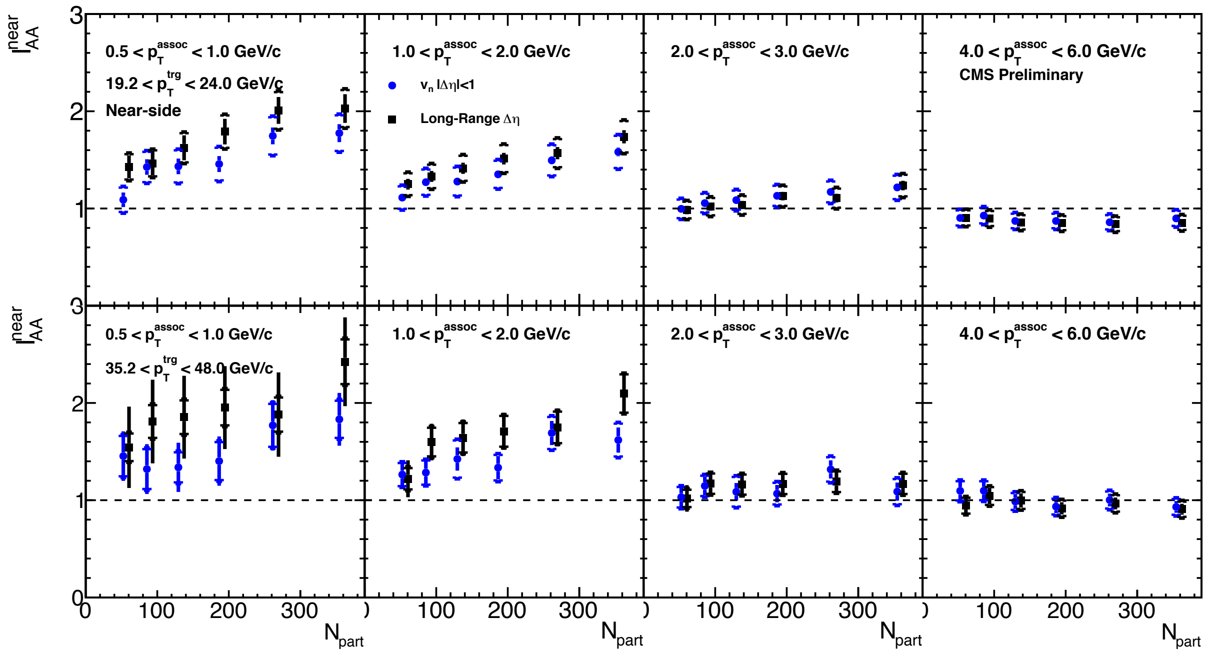

Figure 7.6: Near-side I_{AA} as a function of N_{part} for combinations of four $p_{\mathrm{T}}^{\mathrm{assc}}$ bins (increasing from left to right) and two $p_{\mathrm{T}}^{\mathrm{trig}}$ bins (increasing from top to bottom) in Pb+Pb collisions at $\sqrt{s_{NN}} = 2.76$ TeV. The solid blue circles shows represent the results calculated from the v_n-subtraction method with $|\Delta\eta| < 1$ while the black squares in the background represent the results calculated from the long-range $\Delta\eta$ subtraction method. The vertical error bars represent statistical uncertainties while the brackets represent the systematic uncertainties.

The away-side I_{AA} values are shown in Fig. 7.7 as function of N_{part} in four different $p_{\mathrm{T}}^{\mathrm{assc}}$ ranges. The top row shows the results for $19.2 < p_{\mathrm{T}}^{\mathrm{trig}} < 24$ GeV/c and the bottom row shows the results for $35.2 < p_{\mathrm{T}}^{\mathrm{trig}} < 48$ GeV/c. Here we see a significant correlation between I_{AA}^{away} and N_{part} with larger enhancement/suppression seen in central collisions (high N_{part}) compared to peripheral collisions (low N_{part}). This is again consistent with the jet quenching picture where greater high-p_{T} suppression is expected in more central Pb+Pb collisions.

The reduced enhancement and suppression seen in the near-side I_{AA} values is also expected as a result of surface bias. Specifically, the jets on the near side, which are identified by their high-p_{T} trigger particles, are selected with a bias towards high-p_{T} partons originating on or near the surface of the QGP volume created in a heavy-ion collision. Due to the rapid fall in particle multiplicity with p_{T}, a high-p_{T} trigger particle is much less likely to have originated from a jet within the QGP medium, which will undergo energy loss and will consequently be measured at lower p_{T}, than a jet near the surface that undergoes minimal energy loss and fragments producing a high-p_{T} hadron. Therefore, on average, the particles from the near-side jet will traverse a much smaller distance through the QGP medium than the particles from the away-side jet and, as a result, will undergo less modification induced by the medium.

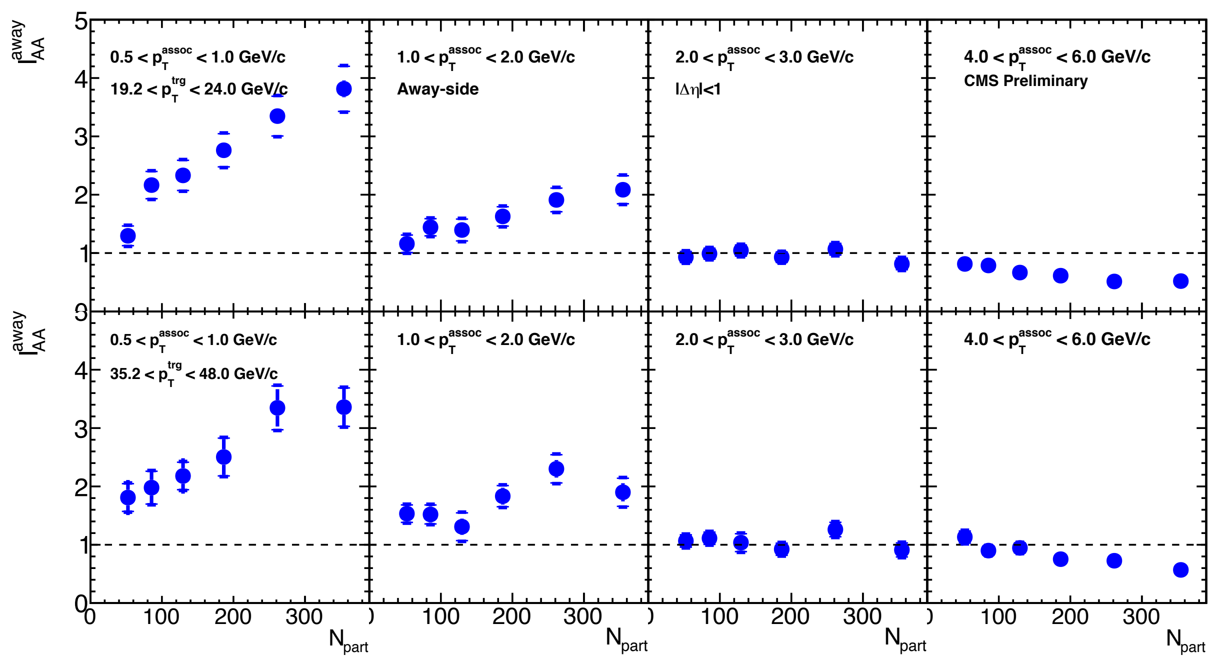

Figure 7.7: Away-side I_{AA} calculated from the v_n-subtraction method with $|\Delta\eta| < 1$ as a function of N_{part} for combinations of four $p_{\mathrm{T}}^{\mathrm{assc}}$ bins (increasing from left to right) and two $p_{\mathrm{T}}^{\mathrm{trig}}$ bins (increasing from top to bottom) in Pb+Pb collisions at $\sqrt{s_{NN}} = 2.76$ TeV. The vertical error bars represent statistical uncertainties while the brackets represent the systematic uncertainties.

7.3 Comparisons and Discussion

As mentioned previously, the high-p_{T} range studied in this analysis is well above what has been studied in track-based dihadron correlations. This makes it difficult to do meaningful comparisons with other work. However, a recent jet-hadron study done with the STAR detector at RHIC looked at angular correlations between reconstructed jets and associated tracks [109]. The jets were studied in three different p_{T} bins, the largest one is $20 < p_{\mathrm{T}}^{\mathrm{jet}} < 40$ GeV/c which is "comparable" to the $p_{\mathrm{T}}^{\mathrm{trig}}$ ranges used in the analysis presented in this dissertation.

The comparison between the away-side I_{AA} results as a function of $p_{\mathrm{T}}^{\mathrm{assc}}$ for the STAR jet-hadron correlations and the dihadron correlations from CMS, shown in the previous section, is shown in Fig. 7.8. The STAR jet-hadron I_{AA}^{away} results are shown with $20 < p_{\mathrm{T}}^{\mathrm{jet}} < 40$ GeV/c for the 0-20% most central events at $\sqrt{s_{NN}} = 200$ GeV (blue) and the CMS dihadron I_{AA}^{away} results are shown for the lowest two $p_{\mathrm{T}}^{\mathrm{trig}}$ bins, $19.2 < p_{\mathrm{T}}^{\mathrm{trig}} < 24$ GeV/c (red) and $24 < p_{\mathrm{T}}^{\mathrm{trig}} < 28.8$ GeV/c (green) for the 0-10% most central events at $\sqrt{s_{NN}} = 2.76$ TeV. The statistical uncertainties are shown with error bars and the systematic uncertainties are shown by the color bands. The measurements agree very well, an enhancement of around a factor of four at low p_{T} and a suppression of about 50% at high p_{T} is also observed in the STAR data.

Both results paint a clear and consistent picture of jet-quenching in heavy-ion collisions. The suppression of high-p_{T} particles due to QCD energy loss in the quark-gluon plasma is clearly visible for away-side jets that, on average, traverse through more of the medium than the near-side jets. We subsequently see an enhancement of low-p_{T} particles on the away side which can also be understood from the energy loss of high-p_{T} particles. As a jet traverses through the QGP the lost energy is still conserved and some of it ends up being "absorbed" by the medium which provides an enhancement to the thermal part of the p_{T} spectrum ($p_{\mathrm{T}} < 2$ GeV/c). This is also clearly visible in both the STAR and CMS results presented here in Fig. 7.8.

It is important to point out that this comparison has a number of caveats due to the fact that this is not an "apples-to-apples" comparison. Aside from the differences in the centrality bins and the center-of-mass collision energy, the fact that the STAR measurement was done using reconstructed jets as the trigger instead of a high-p_{T} track makes the comparison far less straightforward. High-p_{T}

tracks are a good proxy for events containing jets but they don't provide much information about the total energy of the jet. Since jets typically fragment into a number of high-p_T particles, the p_T of a single fragmented particle is not the same as the full jet p_T. Jet reconstruction attempts to reconstruct the total jet energy/p_T which corresponds to the p_T of the initial hard scattered parton. Therefore, a single track with $p_\mathrm{T} = 20$ GeV/c is likely from a jet with a much larger p_T (a jet will rarely fragment in such a way that gives almost all of its energy to a single fragment) so it is not directly comparable to a jet with $p_\mathrm{T}^{\mathrm{jet}} = 20$ GeV/c.

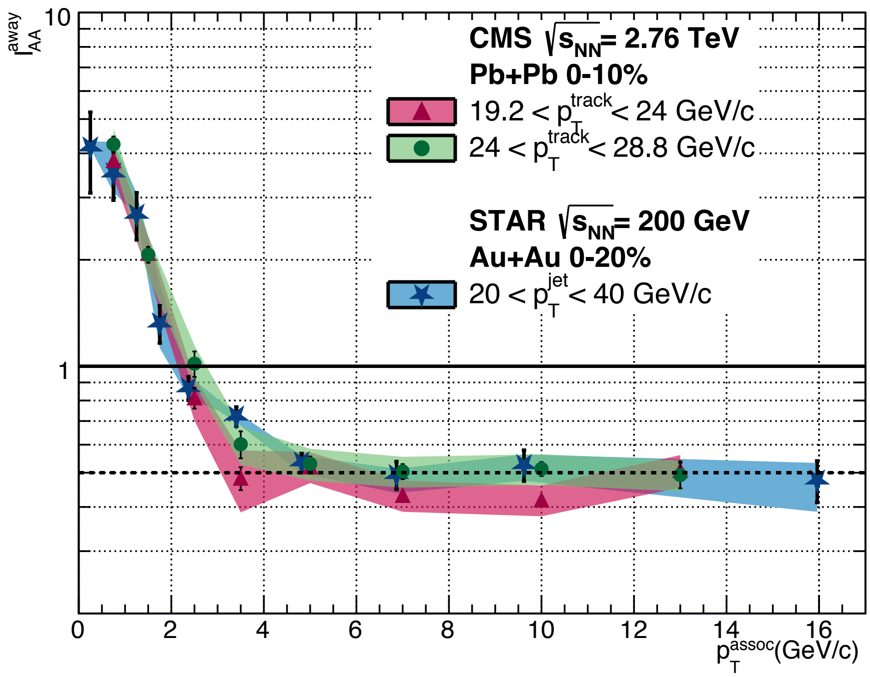

Figure 7.8: The away-side I_{AA} results as a function of $p_\mathrm{T}^{\mathrm{assc}}$ from jet-hadron correlations in STAR and dihadron correlations in CMS. The STAR data are shown in blue for the 0-20% most central Au+Au collisions at $\sqrt{s_{NN}} = 200$ GeV with $20 < p_\mathrm{T}^{\mathrm{jet}} < 40$ GeV. The CMS data are from the 0-10% most central Pb+Pb collisions at $\sqrt{s_{NN}} = 2.76$ TeV with $19.2 < p_\mathrm{T} < 24$ GeV/c (shown in red) and $24 < p_\mathrm{T} < 28.8$ GeV/c (shown in green). Statistical uncertainties are shown with error bars and the systematic uncertainties are shown with color bands [86, 109].

In addition, the STAR analysis only took into consideration the v_2 and v_3 terms of the flow-like background. The high-p_T v_2^{jet} and v_3^{jet} terms were also not measured directly but estimated from a parameterization. The uncertainties for these are included in the systematic errors for the STAR measurements. Despite these differences it is still the closest analysis to the one presented in this dissertation and provides a good qualitative comparison. The consistency between the results also provides stronger evidence for the idea of jet-quenching in heavy-ion collisions.

Another (almost) comparable analysis of I_{AA} from dihadron correlations was done by the ALICE collaboration, shown in Fig. 7.9 [110]. The figure shows the near (left) and away-side (right) I_{AA} results as a function of $p_{\mathrm{T}}^{\mathrm{assc}}$ with $8 < p_{\mathrm{T}}^{\mathrm{trig}} < 15$ GeV/c for the 0-5% most central events. The results done with a flat background subtraction are shown by the red points and the results from a v_2 background subtraction are shown by the red line. A number of model predictions are also shown by other black and white symbols [111].

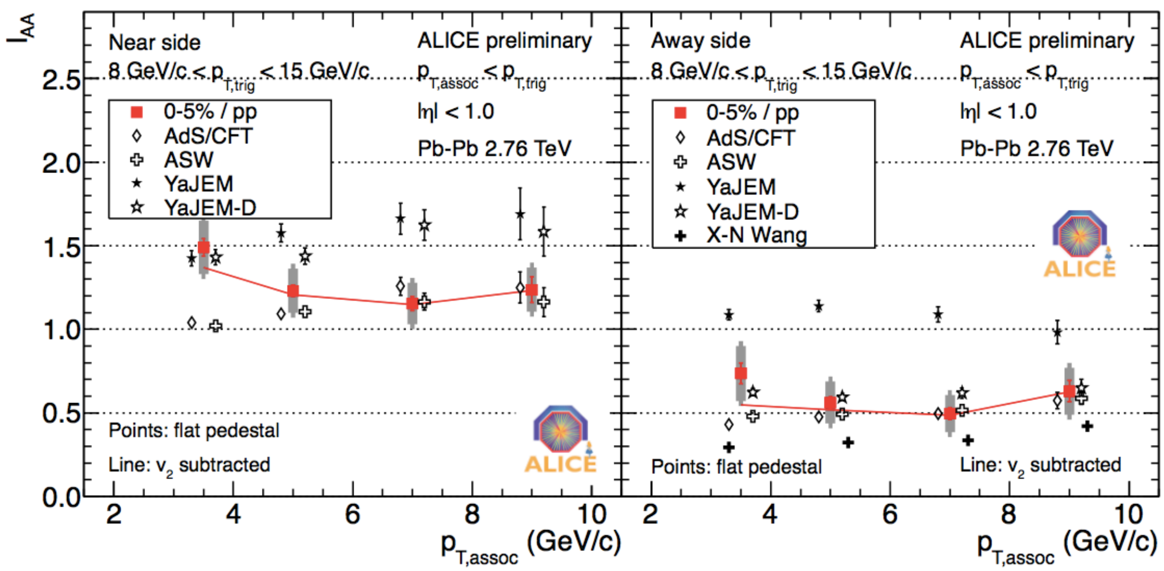

Figure 7.9: The near (left) and away-side (right) I_{AA} results as a function of $p_{\mathrm{T}}^{\mathrm{assc}}$ with $8 < p_{\mathrm{T}}^{\mathrm{trig}} < 15$ GeV/c for the 0-5% most central events. The results done with a flat background subtraction are shown by the red points and the results from a v_2 background subtraction is shown by the red line [110]. Numerous theory predictions are shown in black and white symbols for comparison [111].

The away-side I_{AA} results from ALICE also show a $\sim 50\%$ suppression above $p_{\mathrm{T}} \sim 3$ GeV/c which is very comparable to the results presented in this dissertation and the STAR results. The near side results are above one for the entire $p_{\mathrm{T}}^{\mathrm{assc}}$ range shown although the higher p_{T} points are consistent with one within the statistical and systematic uncertainties. It is important to note that this is not an apples-to-apples comparison either since the trigger-particle p_{T} range ($8 < p_{\mathrm{T}}^{\mathrm{trig}} < 15$

GeV/c) is significantly lower than in this dissertation.

The model comparisons with the ALICE results also provide some insight into the energy-loss mechanism within a QGP medium. The away-side I_{AA} calculation using a next-to-leading-order (NLO) perturbative QCD (pQCD) model by X-N Wang, et al. [112], underpredicts the measured data from ALICE across the entire $p_{\mathrm{T}}^{\mathrm{assc}}$ range shown. We also see that the YaJEM model (Yet another Jet Energy-loss Model), which is another pQCD model with a fixed minimum virtuality scale (Q_0), is shown in black stars and agrees very poorly with the data on both the near and away side, significantly overestimating the I_{AA} values except in the lowest $p_{\mathrm{T}}^{\mathrm{assc}}$ bin on the near side. A variant of YaJEM, YaJEM-D (for dynamical computation of Q_0) is shown in open white stars and shows much better agreement on the away side while being largely consistent with the default YaJEM results on the near side. The ASW model (Armesto-Salgado-Wiedemann), which uses exact calculations of scattering along finite path lengths in QCD matter using the multiple soft scattering approximation (the BDMPS limit [113]), is shown with open crosses and shows very good agreement with data on the away side. It agrees well on the near side as well except in the lowest $p_{\mathrm{T}}^{\mathrm{assc}}$ bin. Finally, an AdS/CFT-QCD hybrid model (denoted as AdS) is shown in open diamonds. This is a phenomenological model that uses pQCD for radiative energy-loss calculations and an AdS/CFT model to calculate interactions with the medium. This model also agrees well with the data and is very comparable to the ASW results across the entire $p_{\mathrm{T}}^{\mathrm{assc}}$ range shown on the near and away side. This is somewhat expected though since the AdS model uses the jet-quenching weights calculated with the ASW formalism.

These comparisons suggest that pQCD calculations alone are not enough to describe the energy-loss mechanism of high-p_{T} particles in a QGP medium in the context of near and away-side I_{AA} measurements. The away side appears to be very well explained by the YaJEM-D, ASW, and AdS models although they each show discrepancies on the near side. Overall, it appears that the near-side I_{AA} results are best described by the ASW and AdS models except for the significant disagreement in the lowest $p_{\mathrm{T}}^{\mathrm{assc}}$ bin.

Chapter 8

Conclusion

We successfully measured the associated hadron yields from dihadron correlations on the near and away side in Pb+Pb and compared them with the associated yields from $p+p$ collisions by constructing I_{AA} ratios at $\sqrt{s_{NN}} = 2.76$ TeV with the CMS detector. The associated yields and I_{AA} ratios were presented in central (0-10%) and peripheral (50-60%) heavy-ion collisions as a function of $p_{\mathrm{T}}^{\mathrm{assc}}$ in four different $p_{\mathrm{T}}^{\mathrm{trig}}$ bins that were significantly above the $p_{\mathrm{T}}^{\mathrm{trig}}$ range studied in any previous measurement. The I_{AA} ratios were also presented as a function of N_{part} in four different $p_{\mathrm{T}}^{\mathrm{assc}}$ bins and two different $p_{\mathrm{T}}^{\mathrm{trig}}$ bins.

The near-side I_{AA} results were largely consistent with one for all centralities except in the lowest p_{T} bins which is expected from the surface bias of near-side jets which preferentially select for shorter path lengths. In the most central events the away-side I_{AA} results show a $\sim 50\%$ suppressions for high-p_{T} ($p_{\mathrm{T}} > 3$ GeV/c) GeV/c and an enhancement by a factor of ~ 4 at low-p_{T} ($p_{\mathrm{T}} < 2$ GeV/c). In the most peripheral events we find that the low-p_{T} enhancement and the high-p_{T} suppression are significantly reduced indicating that there is little modification compared to $p+p$ collisions. In general, a strong dependence on centrality was observed for the away-side I_{AA} measurements.

The flow-like background associated with the underlying heavy-ion event was determined for the first time from high-p_{T} measurements of v_2-v_4. This was subtracted from the high-p_{T} correlations to produce the isolated jet correlations used in the I_{AA} measurements. To test the v_n-subtraction method an additional background subtraction technique was presented that used the long-range correlations as an estimate for the underlying event background on the near side. Both approaches gave near-side I_{AA} results that agree very well except for the lowest $p_{\mathrm{T}}^{\mathrm{assc}}$ bins and even these were consistent within statistical and systematic uncertainties.

The away-side I_{AA} results were compared with results from a recent jet-hadron correlation analysis from STAR. The data, although not directly comparable, agree very well across the entire $p_{\mathrm{T}}^{\mathrm{assc}}$ range presented. The results are consistent with the jet-quenching model of jet suppression in heavy-ion collisions.

Appendix A

Correlation Functions

The correlation functions for every point shown in the final I_{AA} results are presented here. The first section will show the correlation functions with the full near side jet peak and the second section will show the correlation functions with a truncated jet peak to highlight the underlying event structure in each bin. They will be presented for each $p_{\mathrm{T}}^{\mathrm{trig}}$ bin (increasing from left to right) and $p_{\mathrm{T}}^{\mathrm{assc}}$ bin (increasing from top to bottom) combination. They are shown for each of the six centrality bins used in the analysis along with the $p+p$ dataset.

A.1 With Full Near Side Jet Peak

A.1.1 Pb+Pb: 0-10% Centrality

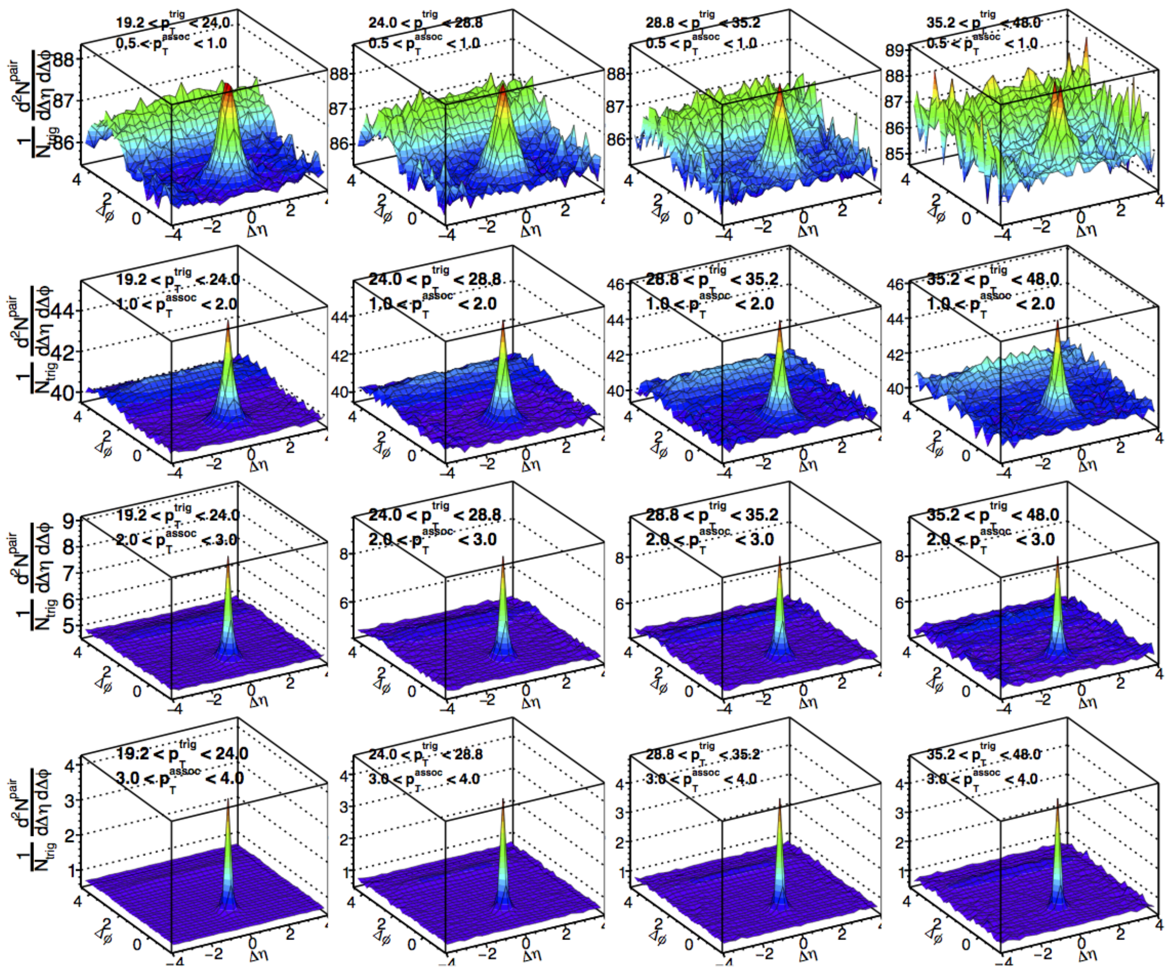

Figure A.1: The 2-D correlation functions as a function of $\Delta\eta$ and $\Delta\phi$ in all four $p_{\mathrm{T}}^{\mathrm{trig}}$ bins and the lowest four $p_{\mathrm{T}}^{\mathrm{assc}}$ bins ($0.5 < p_{\mathrm{T}}^{\mathrm{assc}} < 4$ GeV/c) in the 0-10% most central Pb+Pb collisions.

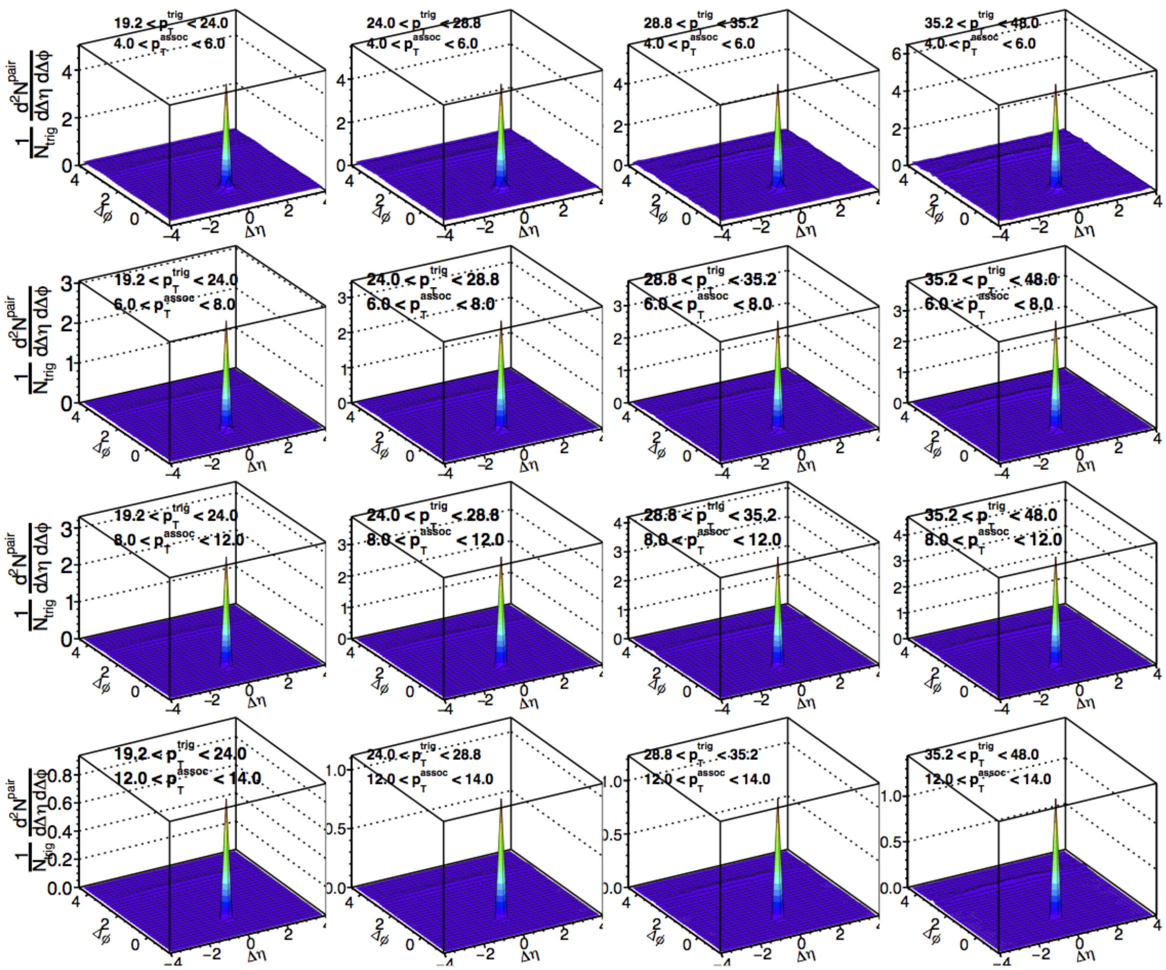

Figure A.2: The 2-D correlation functions as a function of $\Delta\eta$ and $\Delta\phi$ in all four $p_{\mathrm{T}}^{\mathrm{trig}}$ bins and the highest four $p_{\mathrm{T}}^{\mathrm{assc}}$ bins ($4 < p_{\mathrm{T}}^{\mathrm{assc}} < 14$ GeV/c) in the 0-10% most central Pb+Pb collisions.

A.1.2 Pb+Pb: 10-20% Centrality

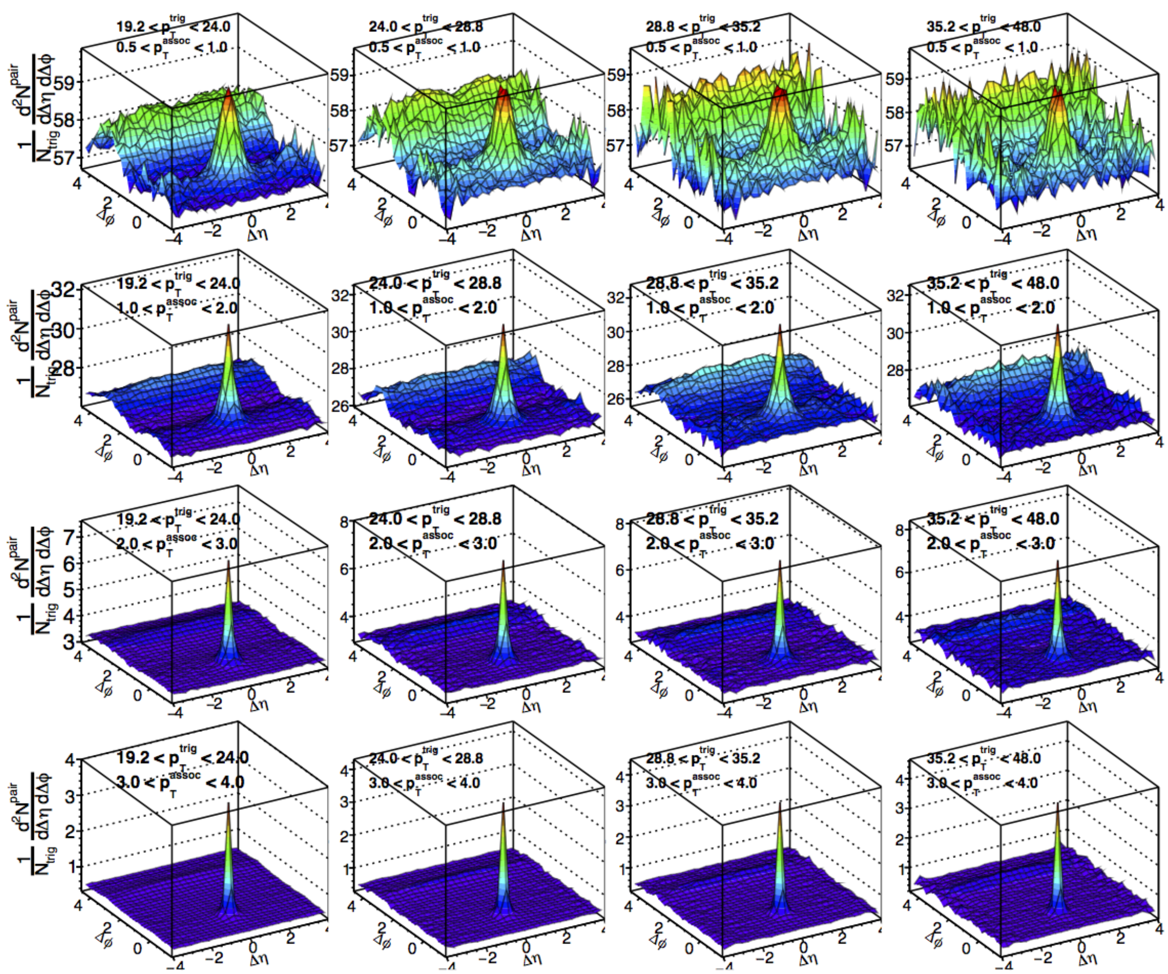

Figure A.3: The 2-D correlation functions as a function of $\Delta\eta$ and $\Delta\phi$ in all four $p_{\mathrm{T}}^{\mathrm{trig}}$ bins and the lowest four $p_{\mathrm{T}}^{\mathrm{assc}}$ bins ($0.5 < p_{\mathrm{T}}^{\mathrm{assc}} < 4$ GeV/c) in the 10-20% most central Pb+Pb collisions.

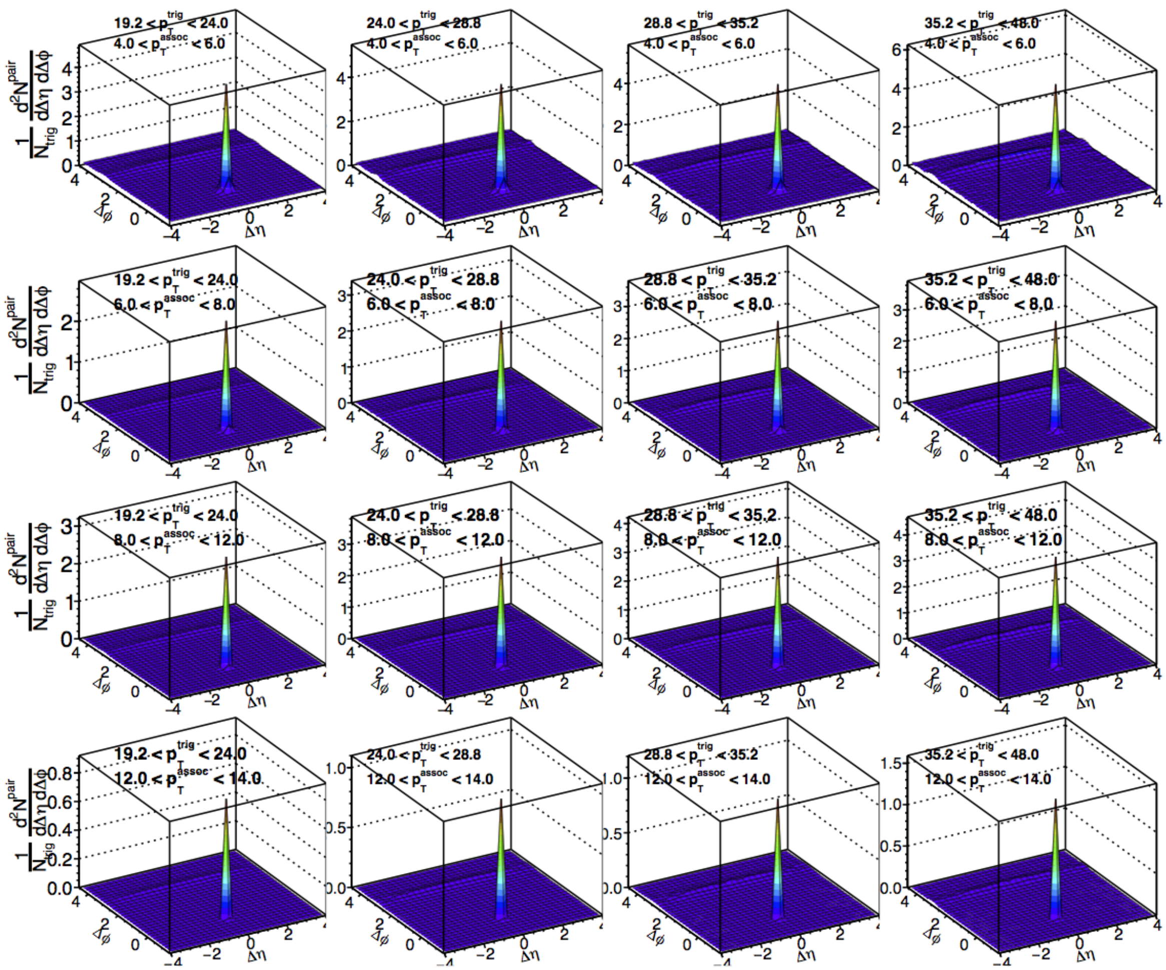

Figure A.4: The 2-D correlation functions as a function of $\Delta\eta$ and $\Delta\phi$ in all four $p_{\mathrm{T}}^{\mathrm{trig}}$ bins and the highest four $p_{\mathrm{T}}^{\mathrm{assc}}$ bins ($4 < p_{\mathrm{T}}^{\mathrm{assc}} < 14$ GeV/c) in the 10-20% most central Pb+Pb collisions.

A.1.3 Pb+Pb: 20-30% Centrality

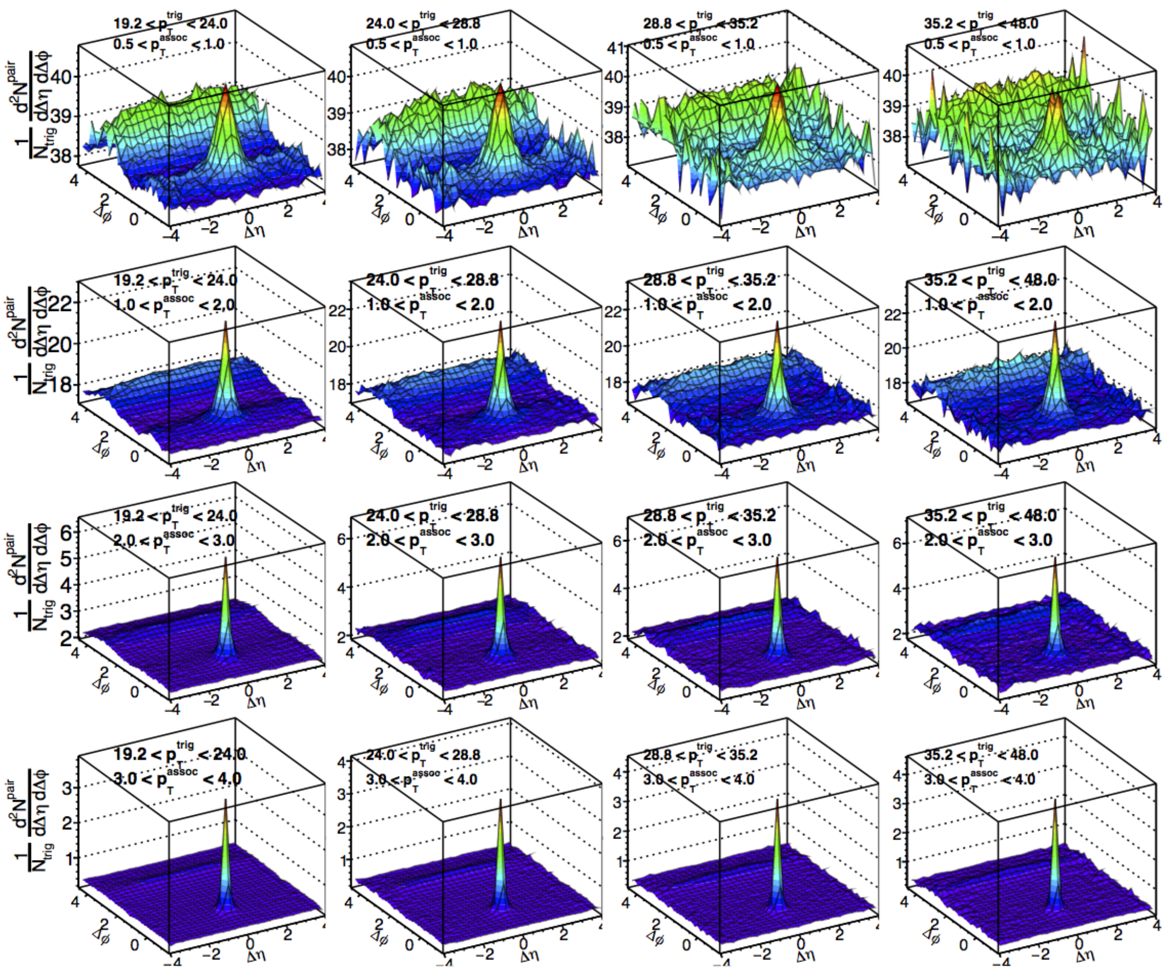

Figure A.5: The 2-D correlation functions as a function of $\Delta\eta$ and $\Delta\phi$ in all four $p_{\mathrm{T}}^{\mathrm{trig}}$ bins and the lowest four $p_{\mathrm{T}}^{\mathrm{assc}}$ bins ($0.5 < p_{\mathrm{T}}^{\mathrm{assc}} < 4$ GeV/c) in the 20-30% most central Pb+Pb collisions.

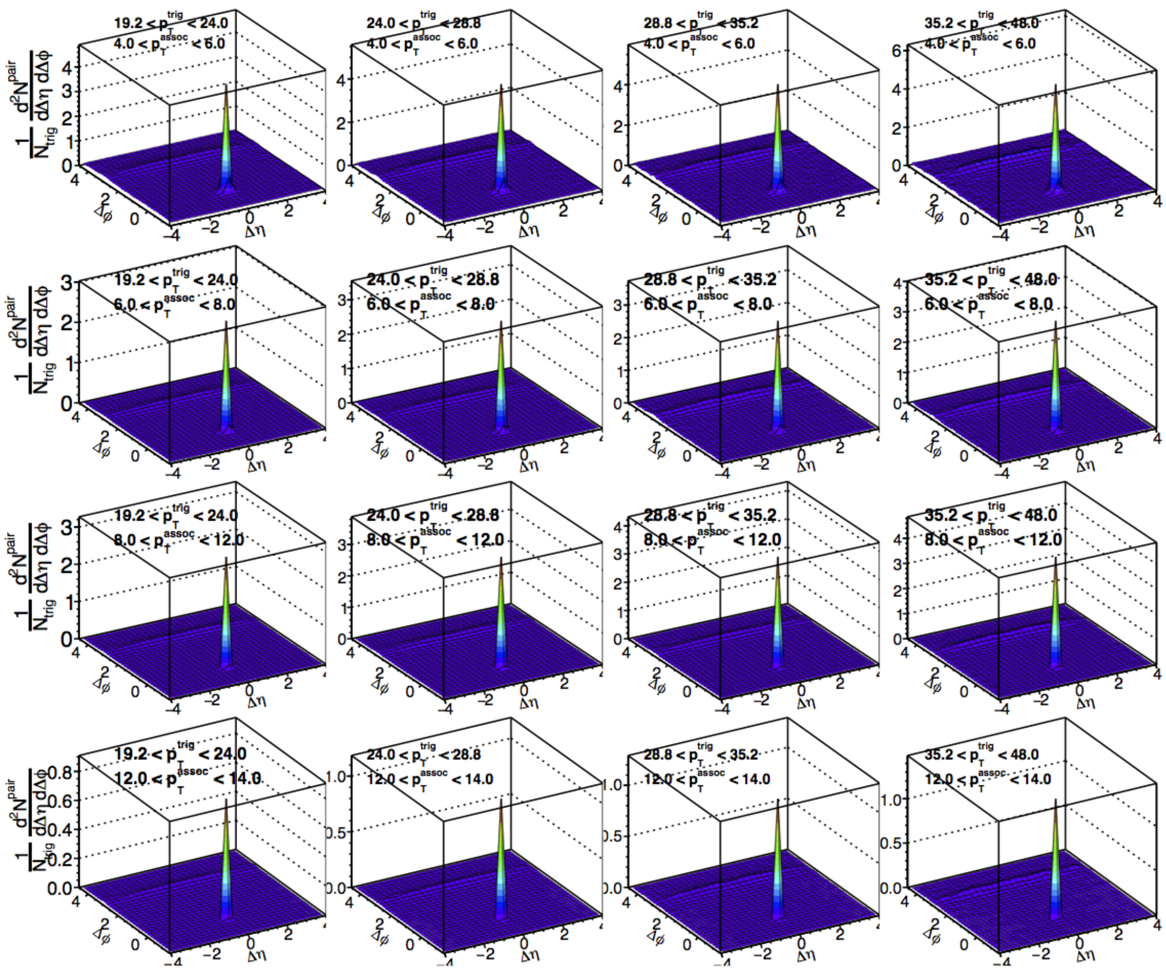

Figure A.6: The 2-D correlation functions as a function of $\Delta\eta$ and $\Delta\phi$ in all four $p_{\mathrm{T}}^{\mathrm{trig}}$ bins and the highest four $p_{\mathrm{T}}^{\mathrm{assc}}$ bins ($4 < p_{\mathrm{T}}^{\mathrm{assc}} < 14$ GeV/c) in the 20-30% most central Pb+Pb collisions.

A.1.4 Pb+Pb: 30-40% Centrality

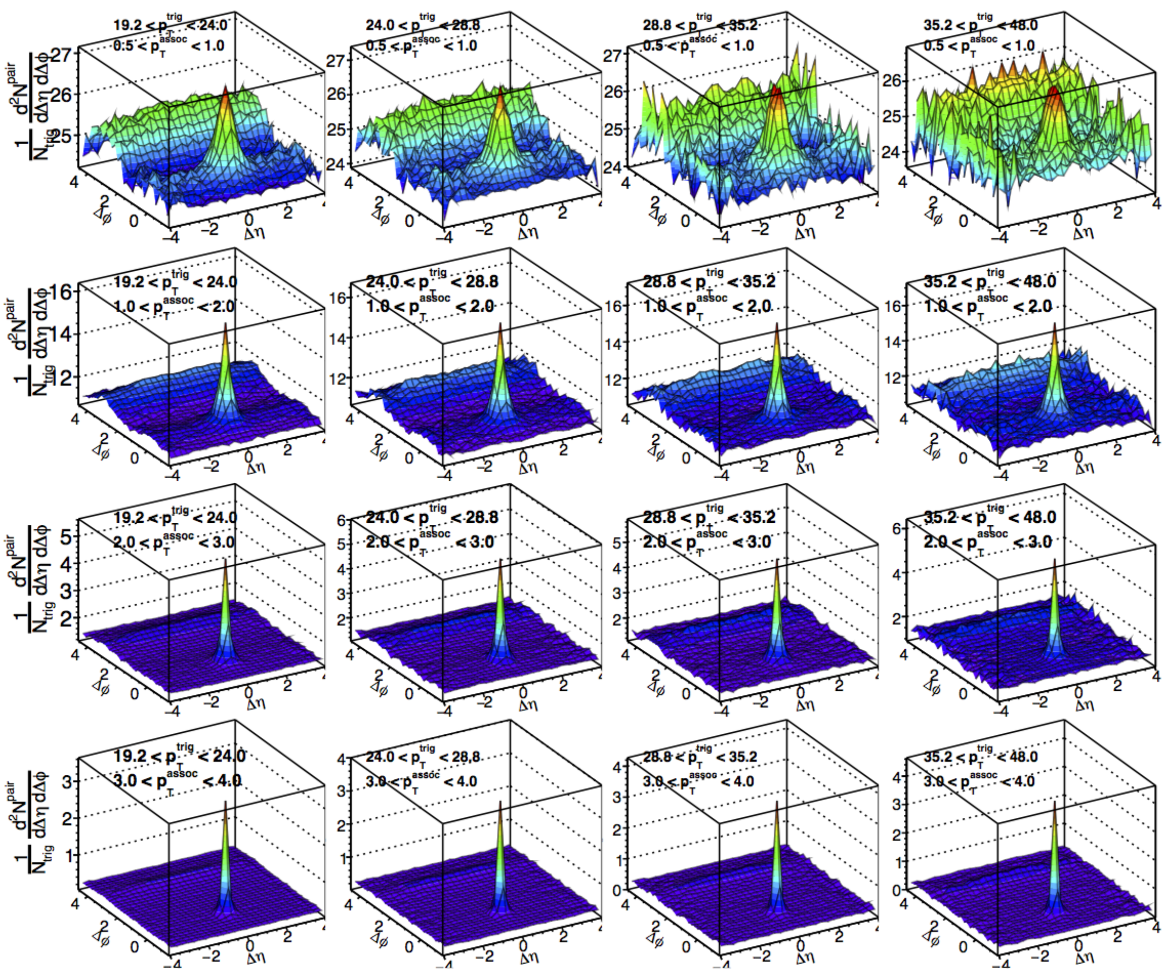

Figure A.7: The 2-D correlation functions as a function of $\Delta\eta$ and $\Delta\phi$ in all four $p_{\mathrm{T}}^{\mathrm{trig}}$ bins and the lowest four $p_{\mathrm{T}}^{\mathrm{assc}}$ bins ($0.5 < p_{\mathrm{T}}^{\mathrm{assc}} < 4$ GeV/c) in the 30-40% most central Pb+Pb collisions.

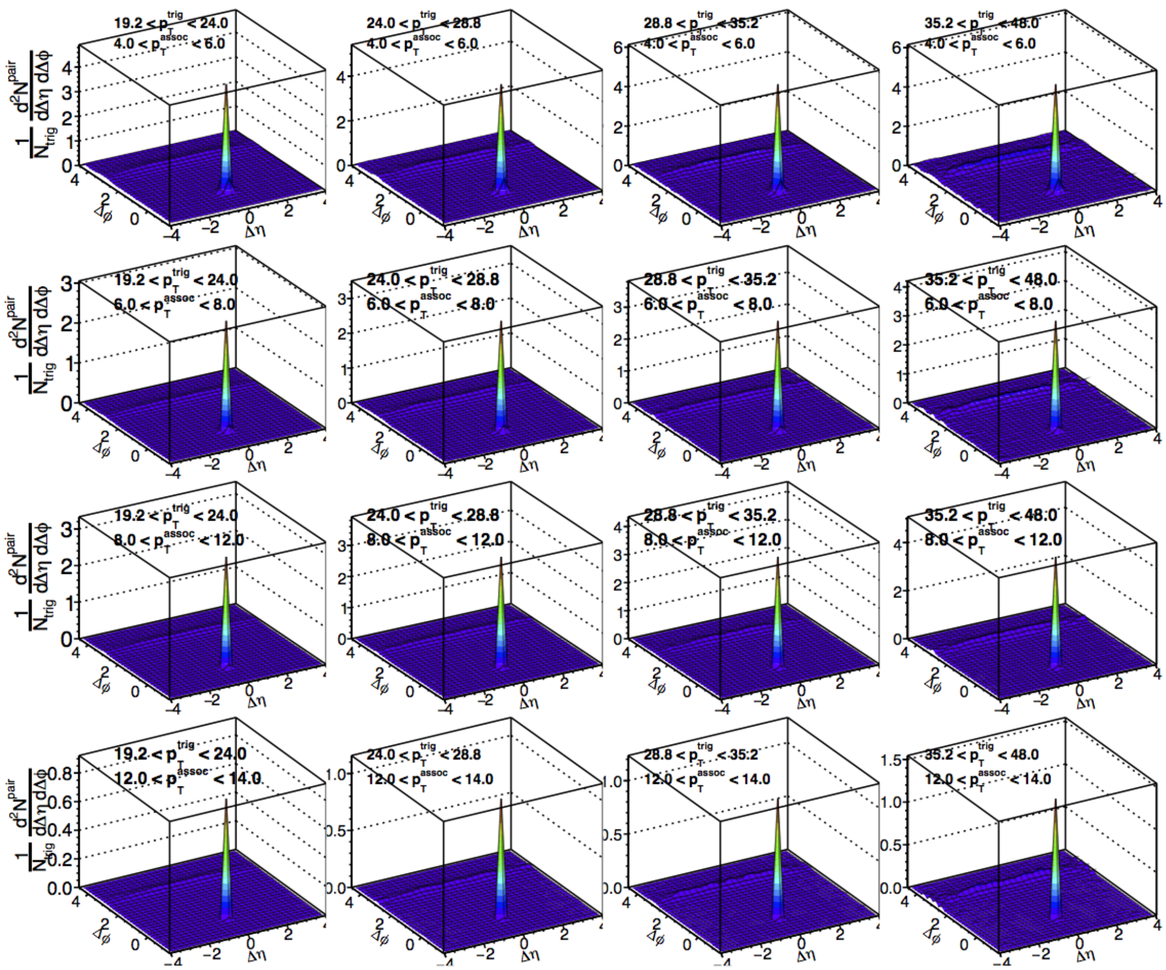

Figure A.8: The 2-D correlation functions as a function of $\Delta\eta$ and $\Delta\phi$ in all four $p_{\mathrm{T}}^{\mathrm{trig}}$ bins and the highest four $p_{\mathrm{T}}^{\mathrm{assc}}$ bins ($4 < p_{\mathrm{T}}^{\mathrm{assc}} < 14$ GeV/c) in the 30-40% most central Pb+Pb collisions.

A.1.5 Pb+Pb: 40-50% Centrality

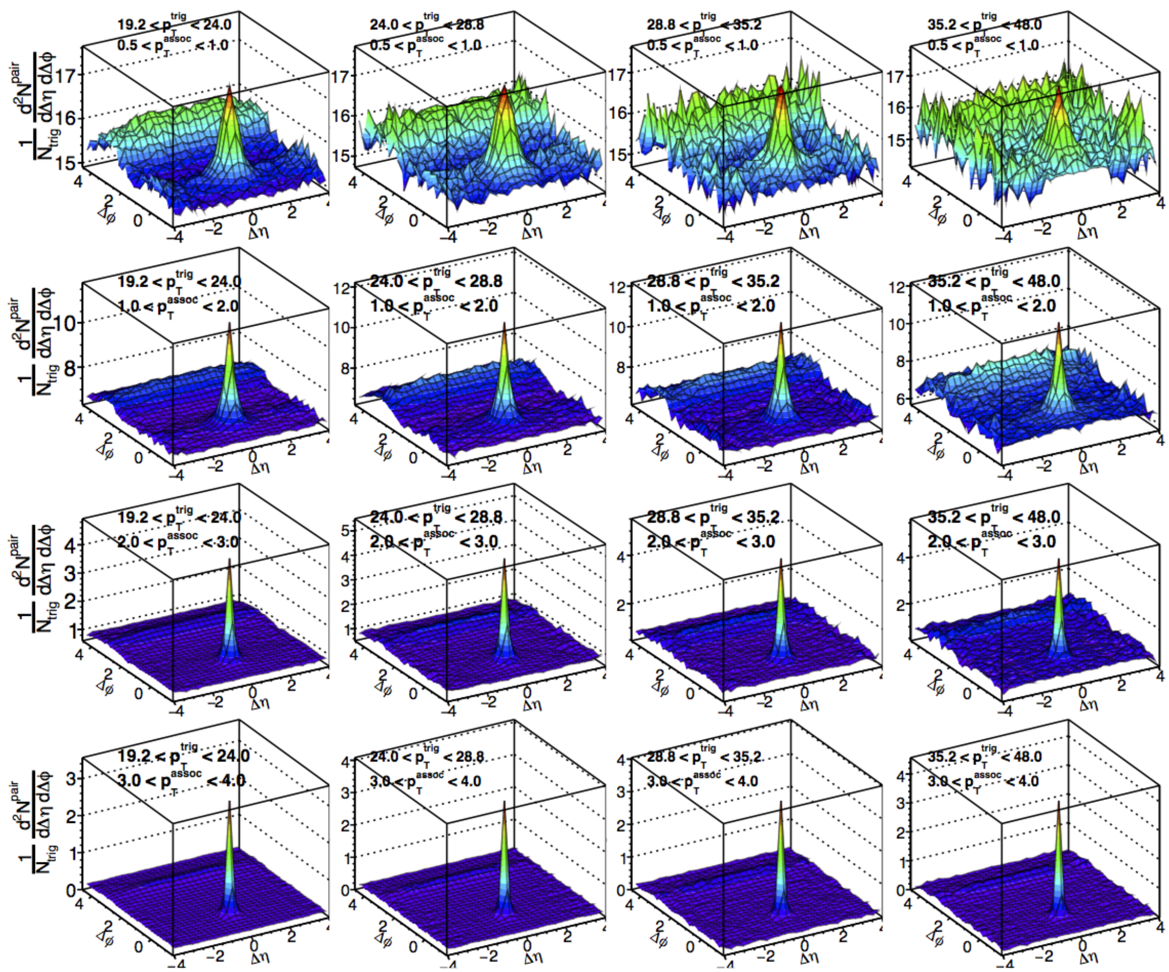

Figure A.9: The 2-D correlation functions as a function of $\Delta\eta$ and $\Delta\phi$ in all four $p_{\mathrm{T}}^{\mathrm{trig}}$ bins and the lowest four $p_{\mathrm{T}}^{\mathrm{assc}}$ bins ($0.5 < p_{\mathrm{T}}^{\mathrm{assc}} < 4$ GeV/c) in the 40-50% most central Pb+Pb collisions.

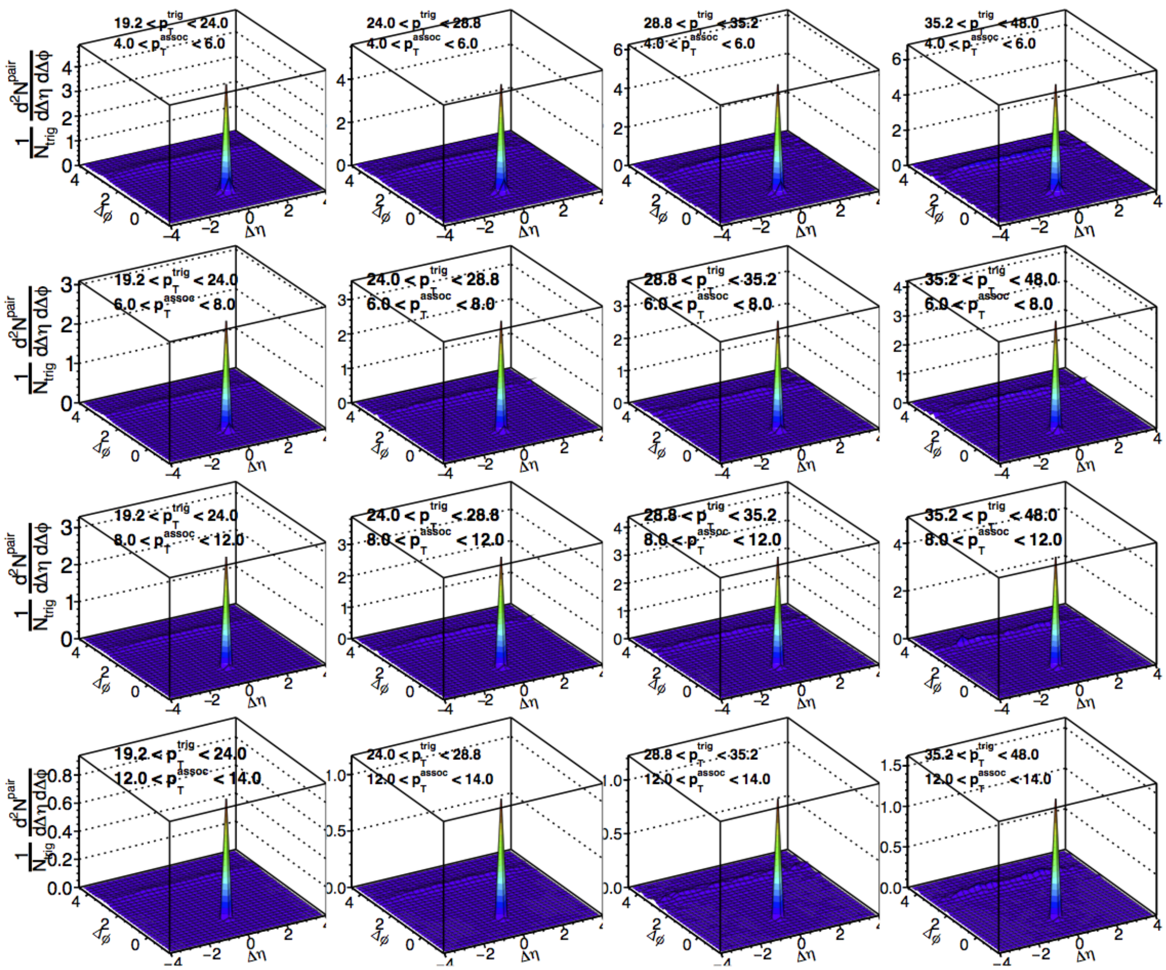

Figure A.10: The 2-D correlation functions as a function of $\Delta\eta$ and $\Delta\phi$ in all four $p_{\mathrm{T}}^{\mathrm{trig}}$ bins and the highest four $p_{\mathrm{T}}^{\mathrm{assc}}$ bins ($4 < p_{\mathrm{T}}^{\mathrm{assc}} < 14$ GeV/c) in the 40-50% most central Pb+Pb collisions.

A.1.6 Pb+Pb: 50-60% Centrality

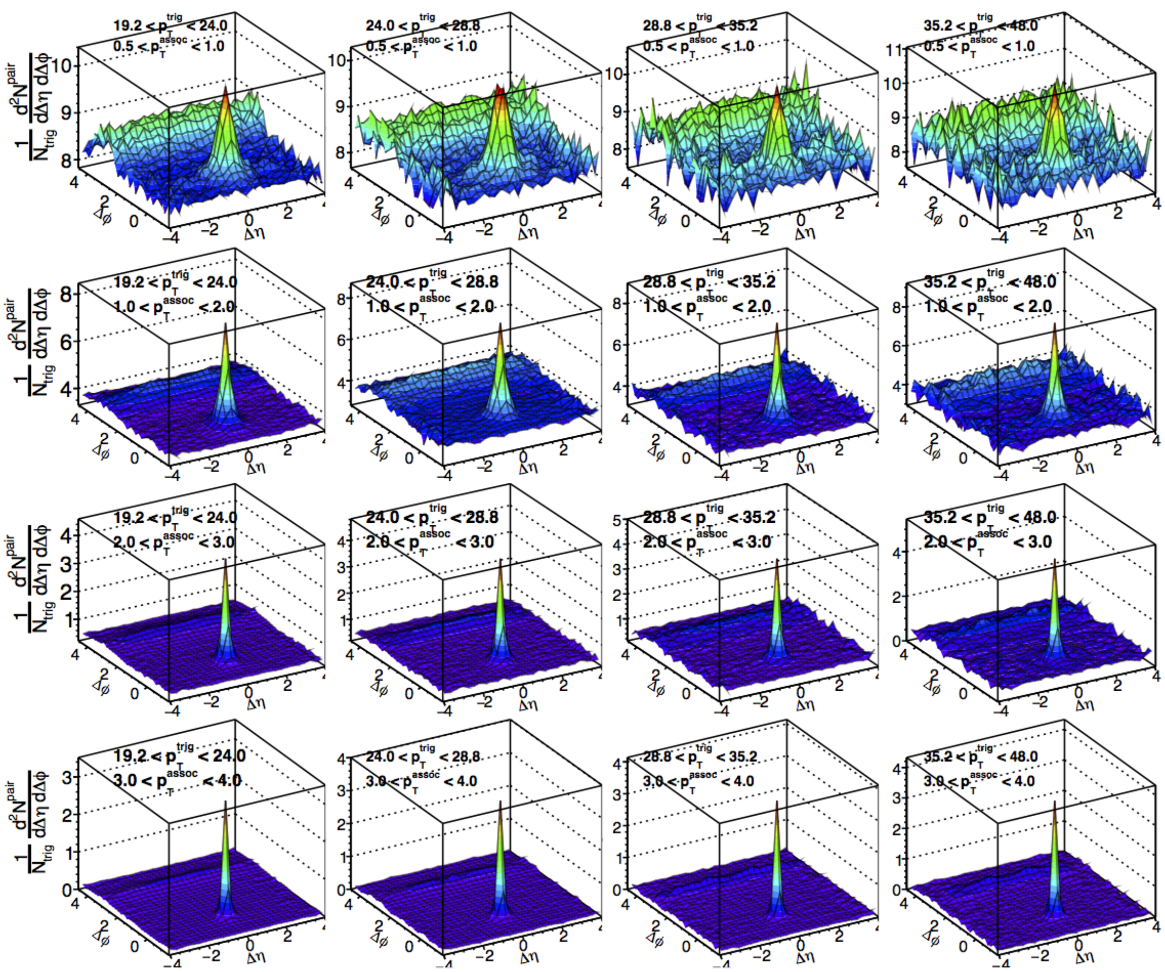

Figure A.11: The 2-D correlation functions as a function of $\Delta\eta$ and $\Delta\phi$ in all four $p_{\mathrm{T}}^{\mathrm{trig}}$ bins and the lowest four $p_{\mathrm{T}}^{\mathrm{assc}}$ bins ($0.5 < p_{\mathrm{T}}^{\mathrm{assc}} < 4$ GeV/c) in the 50-60% most central Pb+Pb collisions.

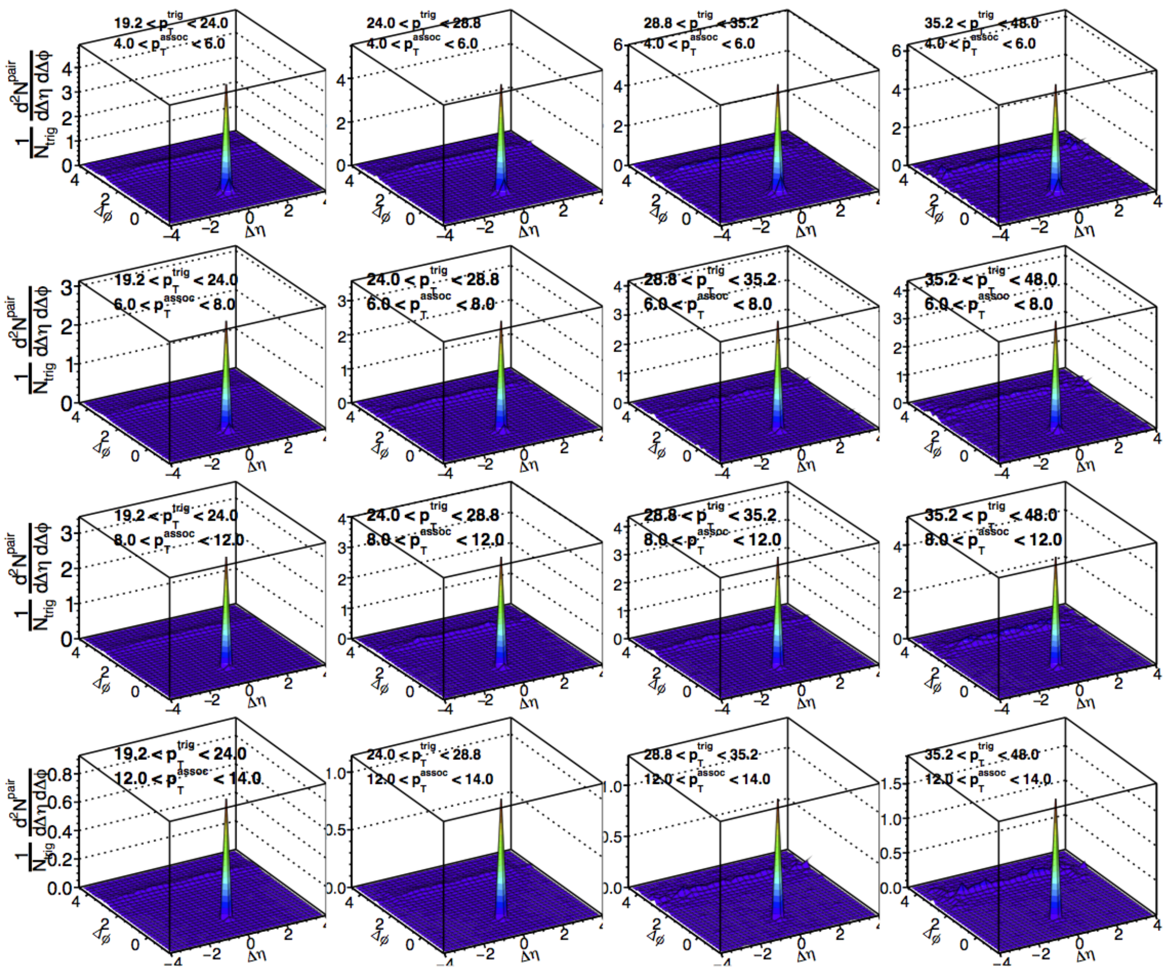

Figure A.12: The 2-D correlation functions as a function of $\Delta\eta$ and $\Delta\phi$ in all four $p_{\mathrm{T}}^{\mathrm{trig}}$ bins and the highest four $p_{\mathrm{T}}^{\mathrm{assc}}$ bins ($4 < p_{\mathrm{T}}^{\mathrm{assc}} < 14$ GeV/c) in the 50-60% most central Pb+Pb collisions.

A.1.7 $p+p$

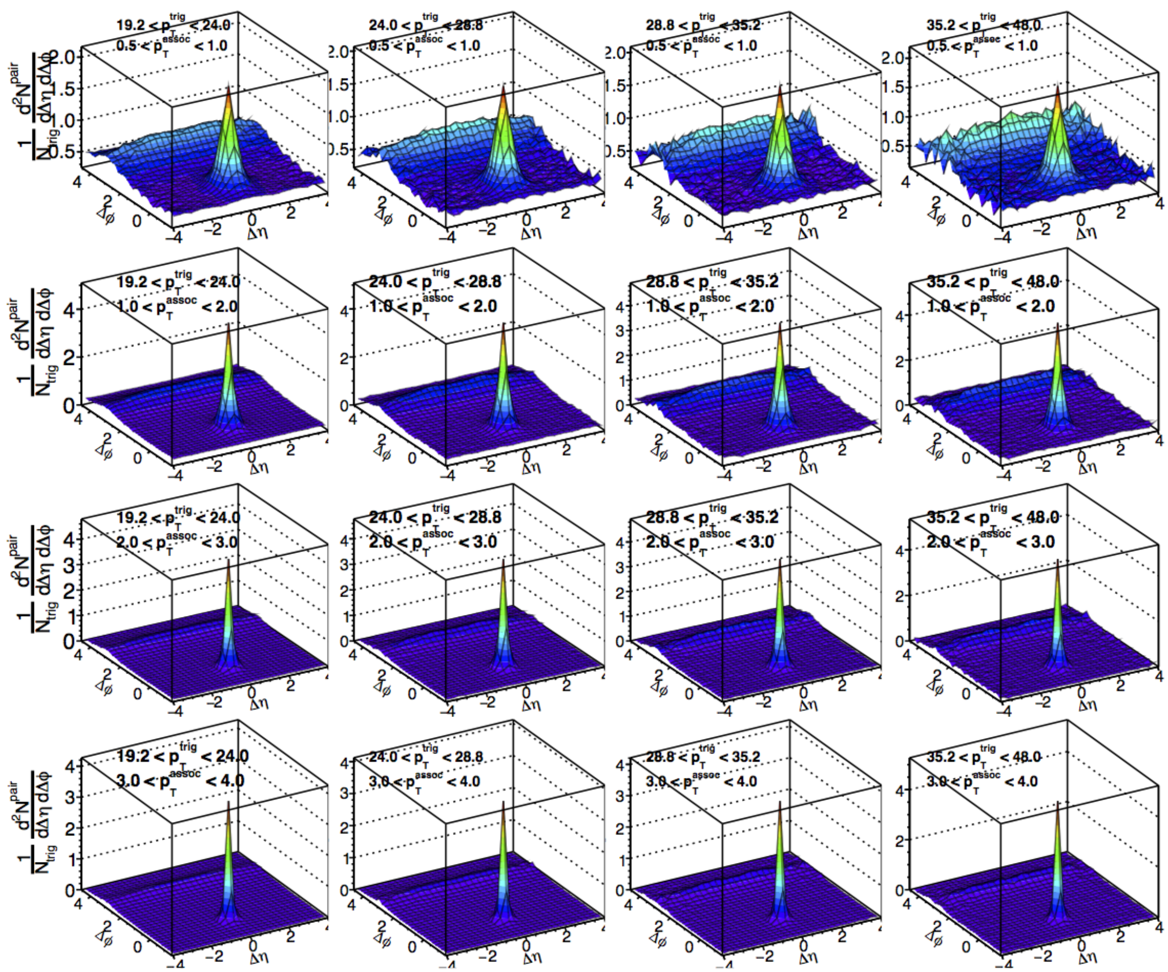

Figure A.13: The 2-D correlation functions as a function of $\Delta\eta$ and $\Delta\phi$ in all four $p_{\mathrm{T}}^{\mathrm{trig}}$ bins and the lowest four $p_{\mathrm{T}}^{\mathrm{assc}}$ bins ($0.5 < p_{\mathrm{T}}^{\mathrm{assc}} < 4$ GeV/c) in $p+p$ collisions.

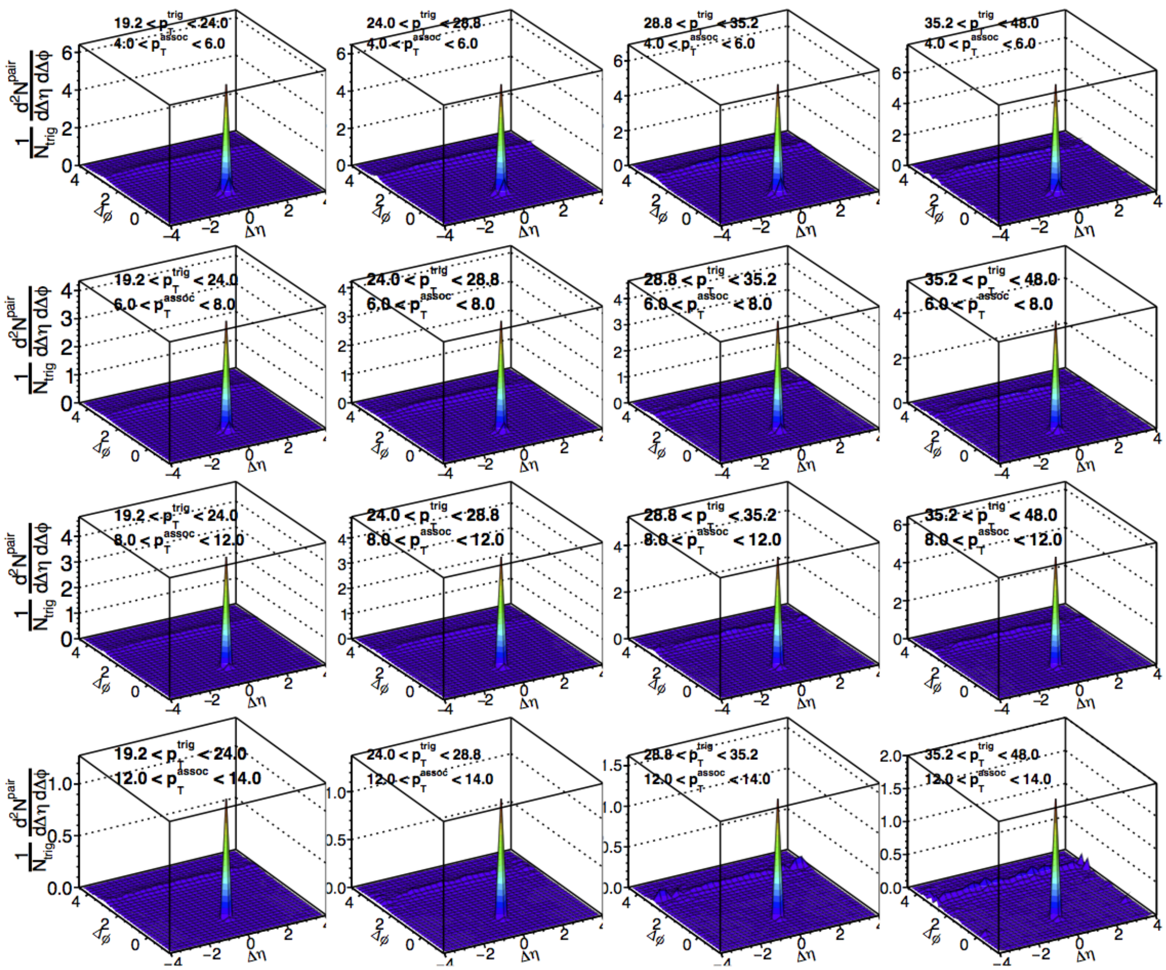

Figure A.14: The 2-D correlation functions as a function of $\Delta\eta$ and $\Delta\phi$ in all four $p_{\mathrm{T}}^{\mathrm{trig}}$ bins and the highest four $p_{\mathrm{T}}^{\mathrm{assc}}$ bins ($4 < p_{\mathrm{T}}^{\mathrm{assc}} < 14$ GeV/c) in $p+p$ collisions.

A.2 With Truncated Near Side Jet Peak

A.2.1 Pb+Pb: 0-10% Centrality

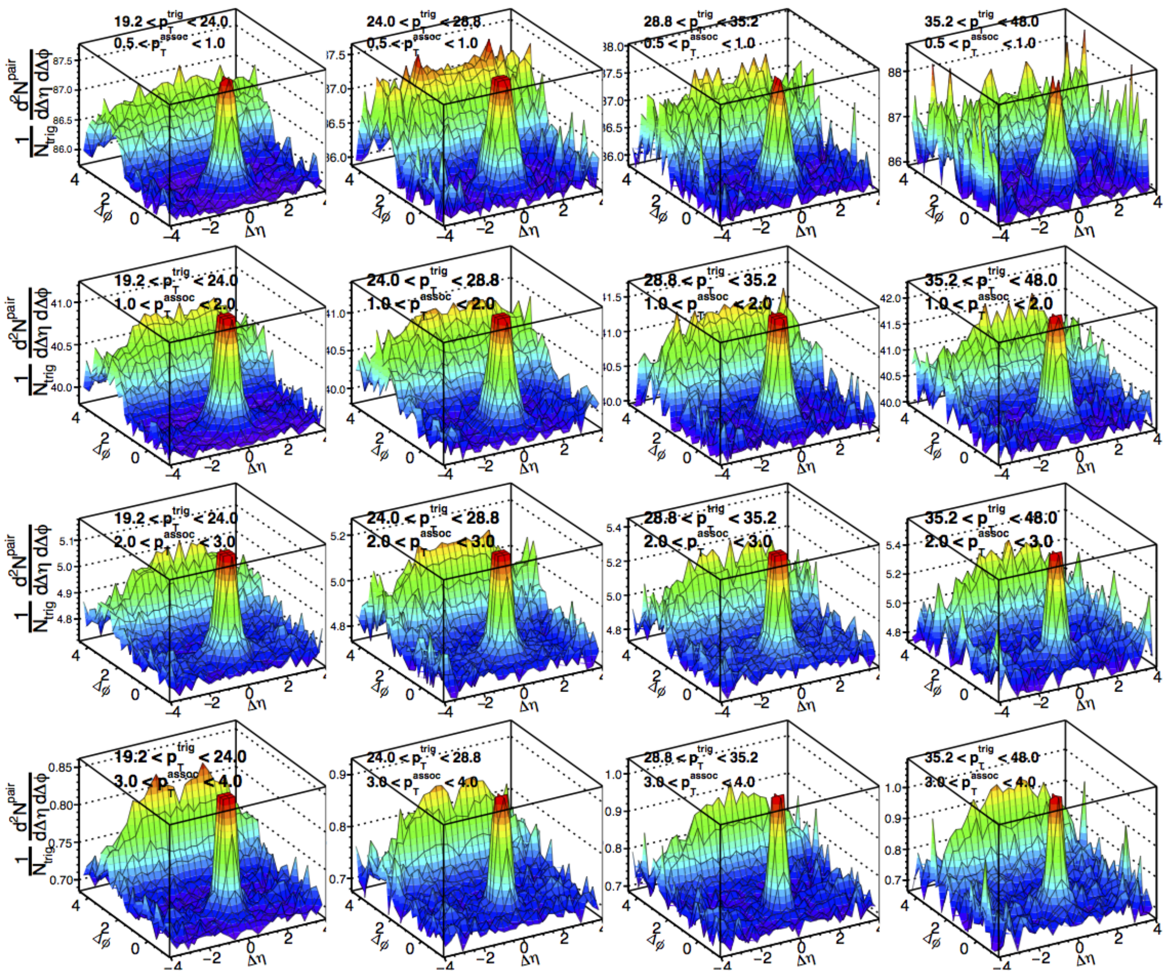

Figure A.15: The 2-D correlation functions as a function of $\Delta\eta$ and $\Delta\phi$ in all four $p_{\mathrm{T}}^{\mathrm{trig}}$ bins and the lowest four $p_{\mathrm{T}}^{\mathrm{assc}}$ bins ($0.5 < p_{\mathrm{T}}^{\mathrm{assc}} < 4$ GeV/c) in the 0-10% most central Pb+Pb collisions. The nearside peak is truncated to highlight the away side jet peak.

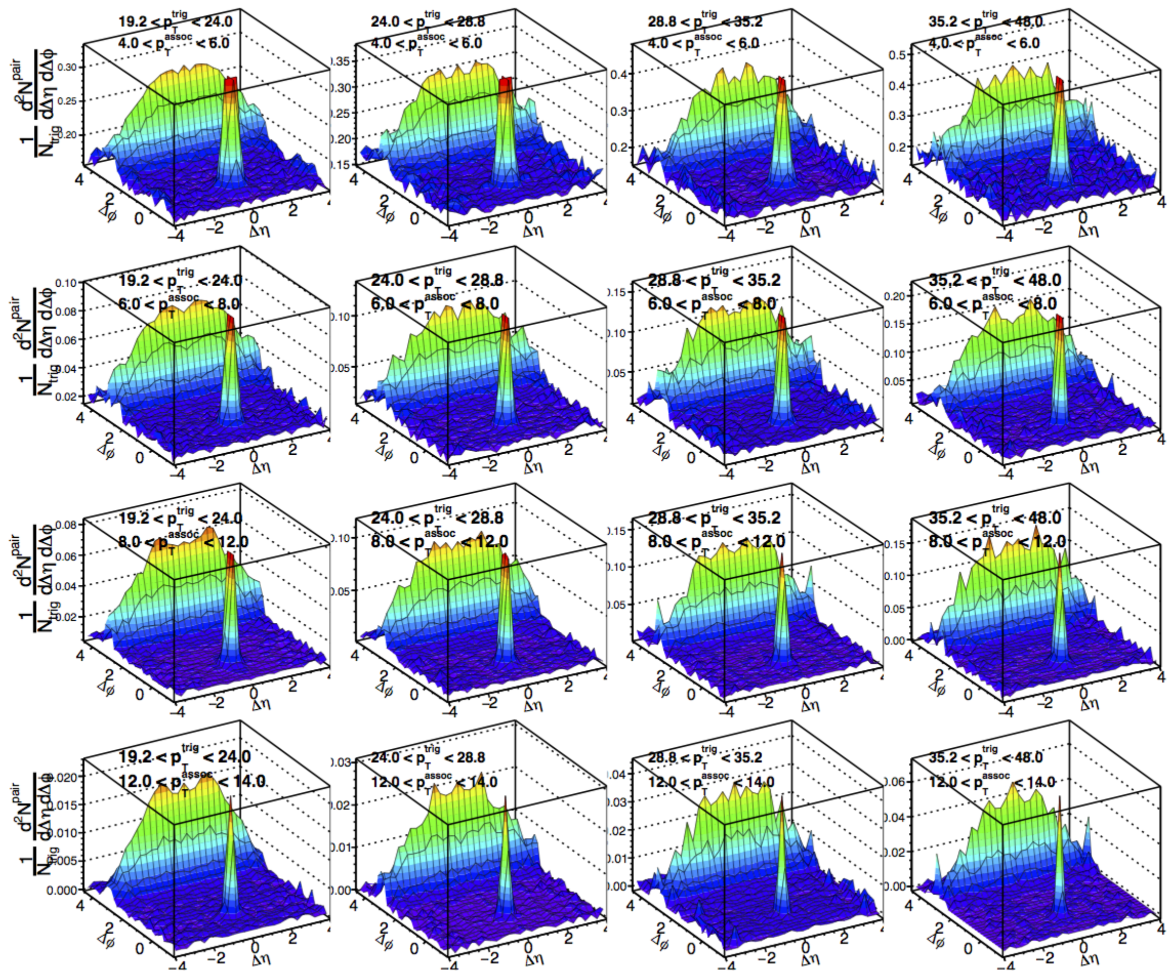

Figure A.16: The 2-D correlation functions as a function of $\Delta\eta$ and $\Delta\phi$ in all four p_T^{trig} bins and the highest four p_T^{assc} bins ($4 < p_T^{assc} < 14$ GeV/c) in the 0-10% most central Pb+Pb collisions. The nearside peak is truncated to highlight the away side jet peak.

A.2.2 Pb+Pb: 10-20% Centrality

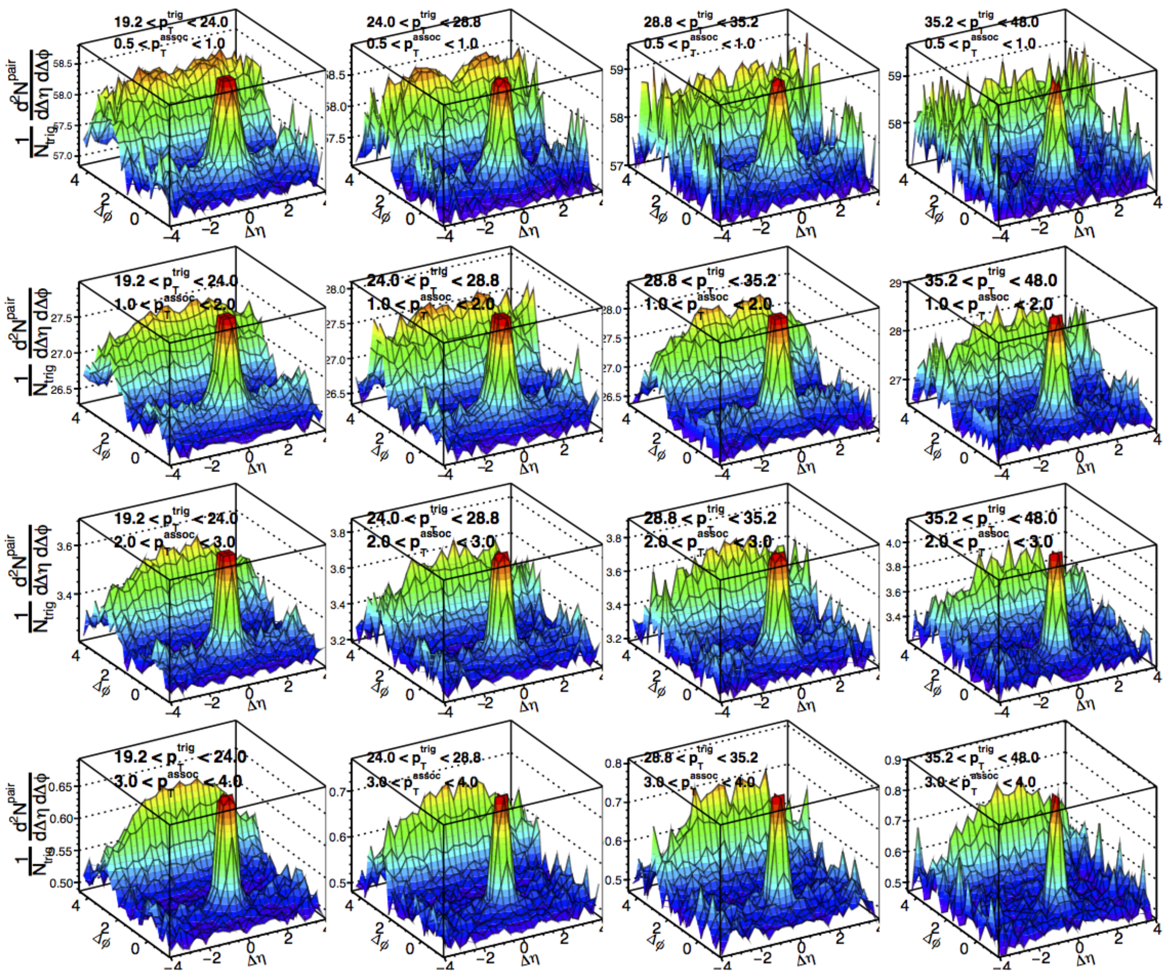

Figure A.17: The 2-D correlation functions as a function of $\Delta\eta$ and $\Delta\phi$ in all four $p_{\mathrm{T}}^{\mathrm{trig}}$ bins and the lowest four $p_{\mathrm{T}}^{\mathrm{assc}}$ bins ($0.5 < p_{\mathrm{T}}^{\mathrm{assc}} < 4$ GeV/c) in the 10-20% most central Pb+Pb collisions. The nearside peak is truncated to highlight the away side jet peak.

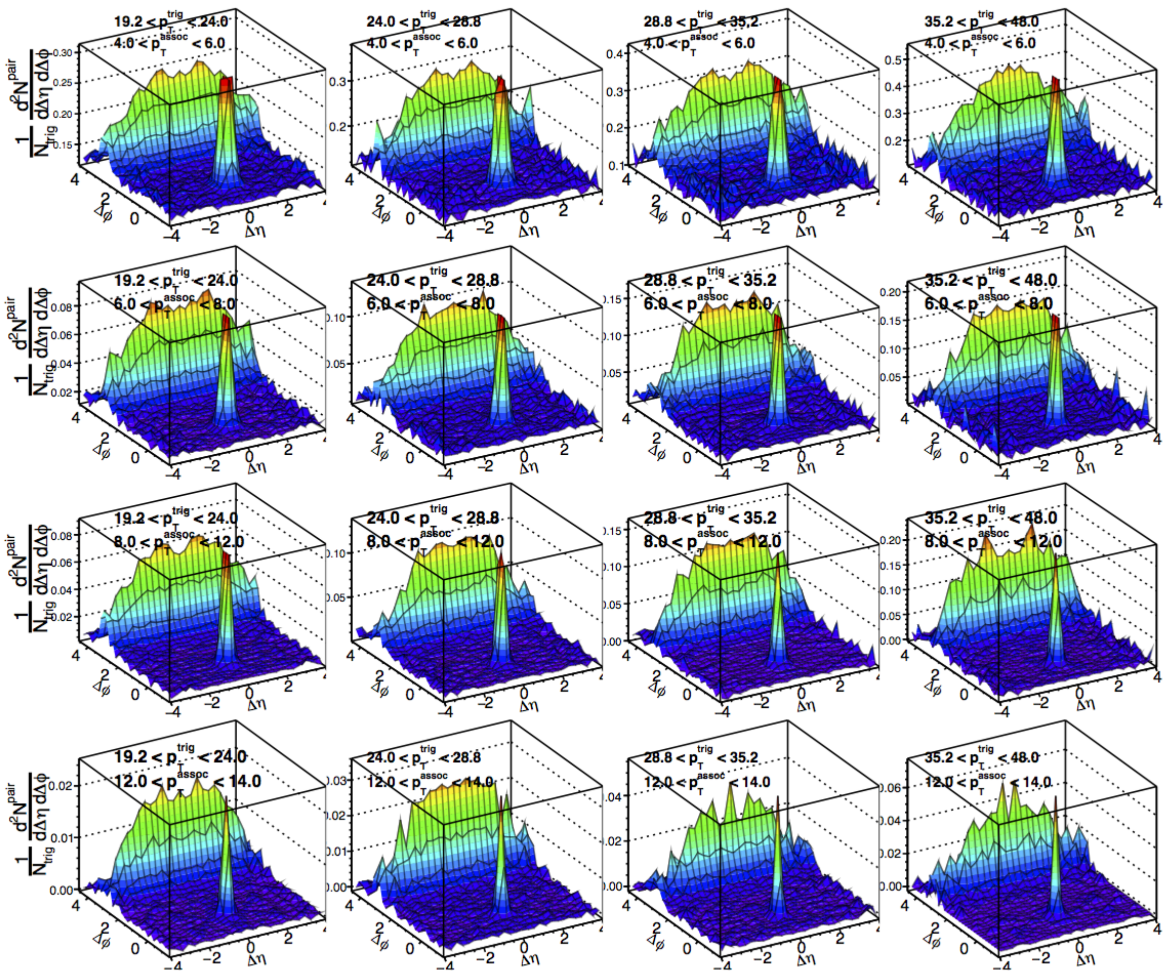

Figure A.18: The 2-D correlation functions as a function of $\Delta\eta$ and $\Delta\phi$ in all four $p_{\mathrm{T}}^{\mathrm{trig}}$ bins and the highest four $p_{\mathrm{T}}^{\mathrm{assc}}$ bins ($4 < p_{\mathrm{T}}^{\mathrm{assc}} < 14$ GeV/c) in the 10-20% most central Pb+Pb collisions. The nearside peak is truncated to highlight the away side jet peak.

A.2.3 Pb+Pb: 20-30% Centrality

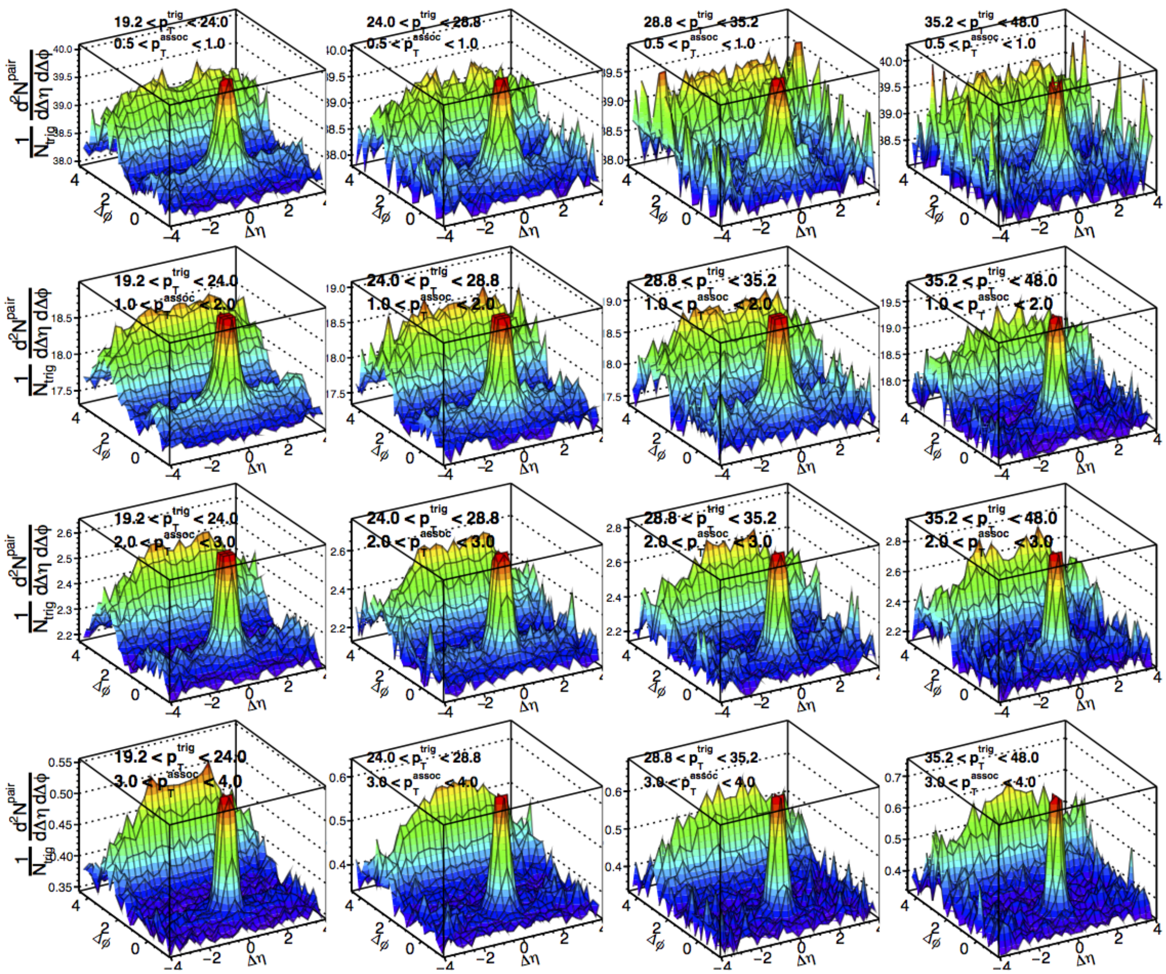

Figure A.19: The 2-D correlation functions as a function of $\Delta\eta$ and $\Delta\phi$ in all four $p_{\mathrm{T}}^{\mathrm{trig}}$ bins and the lowest four $p_{\mathrm{T}}^{\mathrm{assc}}$ bins ($0.5 < p_{\mathrm{T}}^{\mathrm{assc}} < 4$ GeV/c) in the 20-30% most central Pb+Pb collisions. The nearside peak is truncated to highlight the away side jet peak.

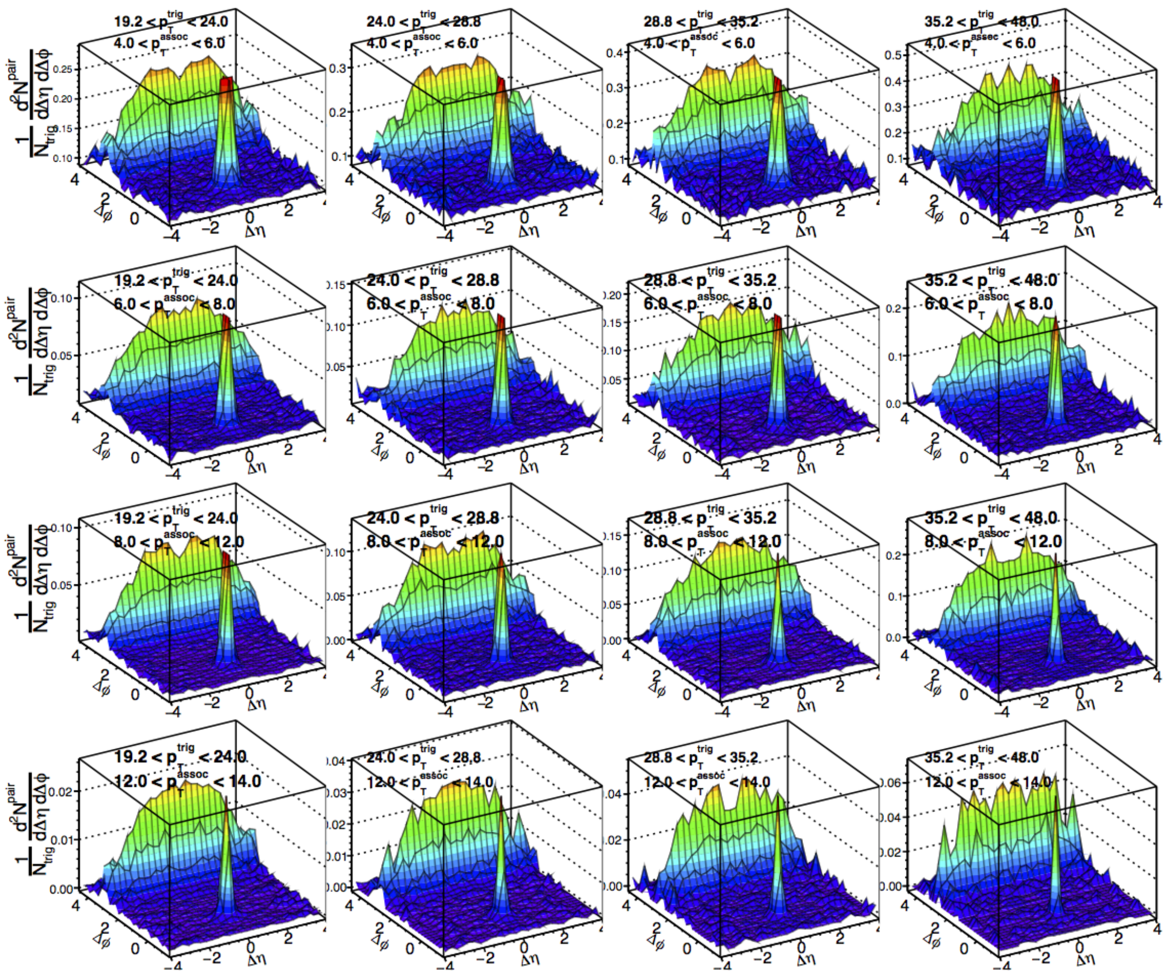

Figure A.20: The 2-D correlation functions as a function of $\Delta\eta$ and $\Delta\phi$ in all four $p_{\mathrm{T}}^{\mathrm{trig}}$ bins and the highest four $p_{\mathrm{T}}^{\mathrm{assc}}$ bins ($4 < p_{\mathrm{T}}^{\mathrm{assc}} < 14$ GeV/c) in the 20-30% most central Pb+Pb collisions. The nearside peak is truncated to highlight the away side jet peak.

A.2.4 Pb+Pb: 30-40% Centrality

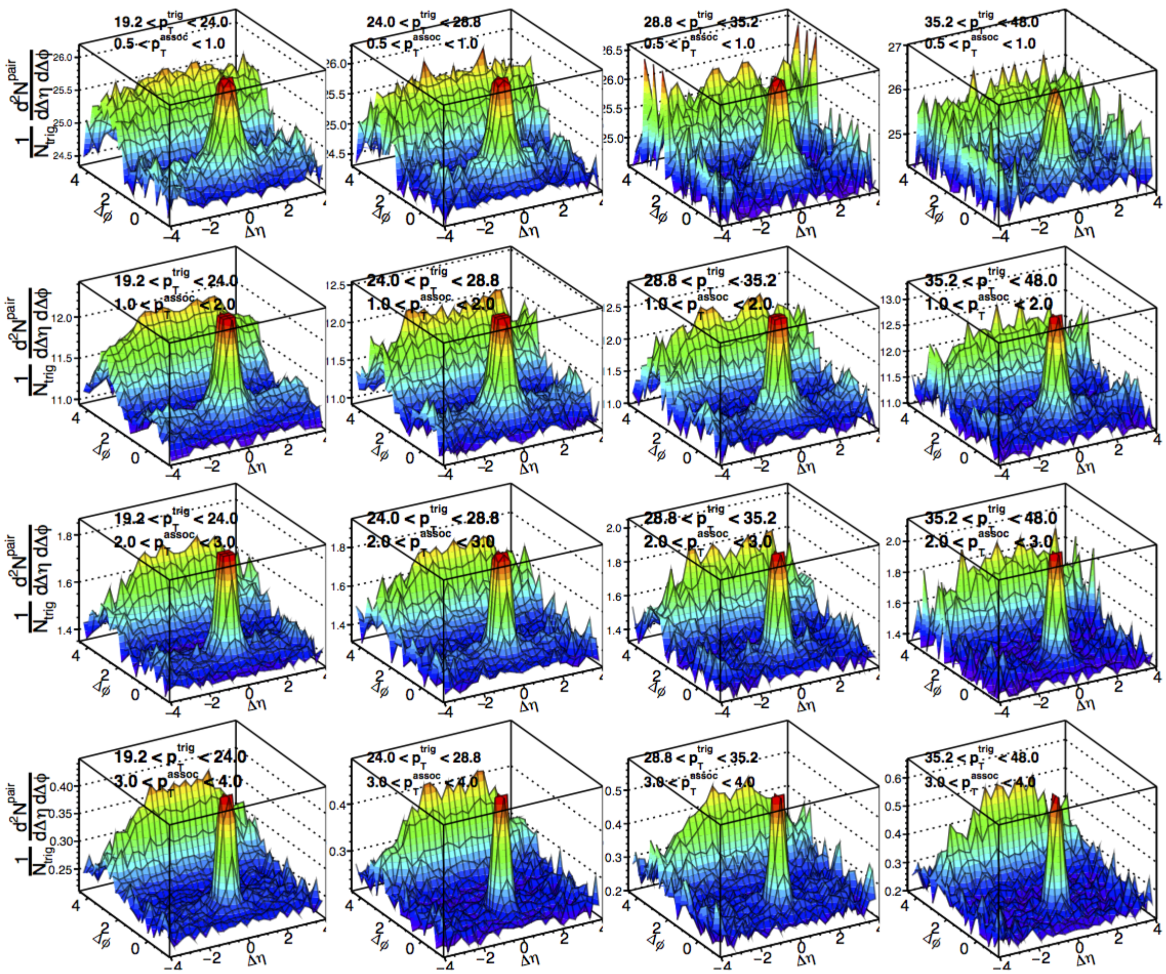

Figure A.21: The 2-D correlation functions as a function of $\Delta\eta$ and $\Delta\phi$ in all four $p_{\mathrm{T}}^{\mathrm{trig}}$ bins and the lowest four $p_{\mathrm{T}}^{\mathrm{assc}}$ bins ($0.5 < p_{\mathrm{T}}^{\mathrm{assc}} < 4$ GeV/c) in the 30-40% most central Pb+Pb collisions. The nearside peak is truncated to highlight the away side jet peak.

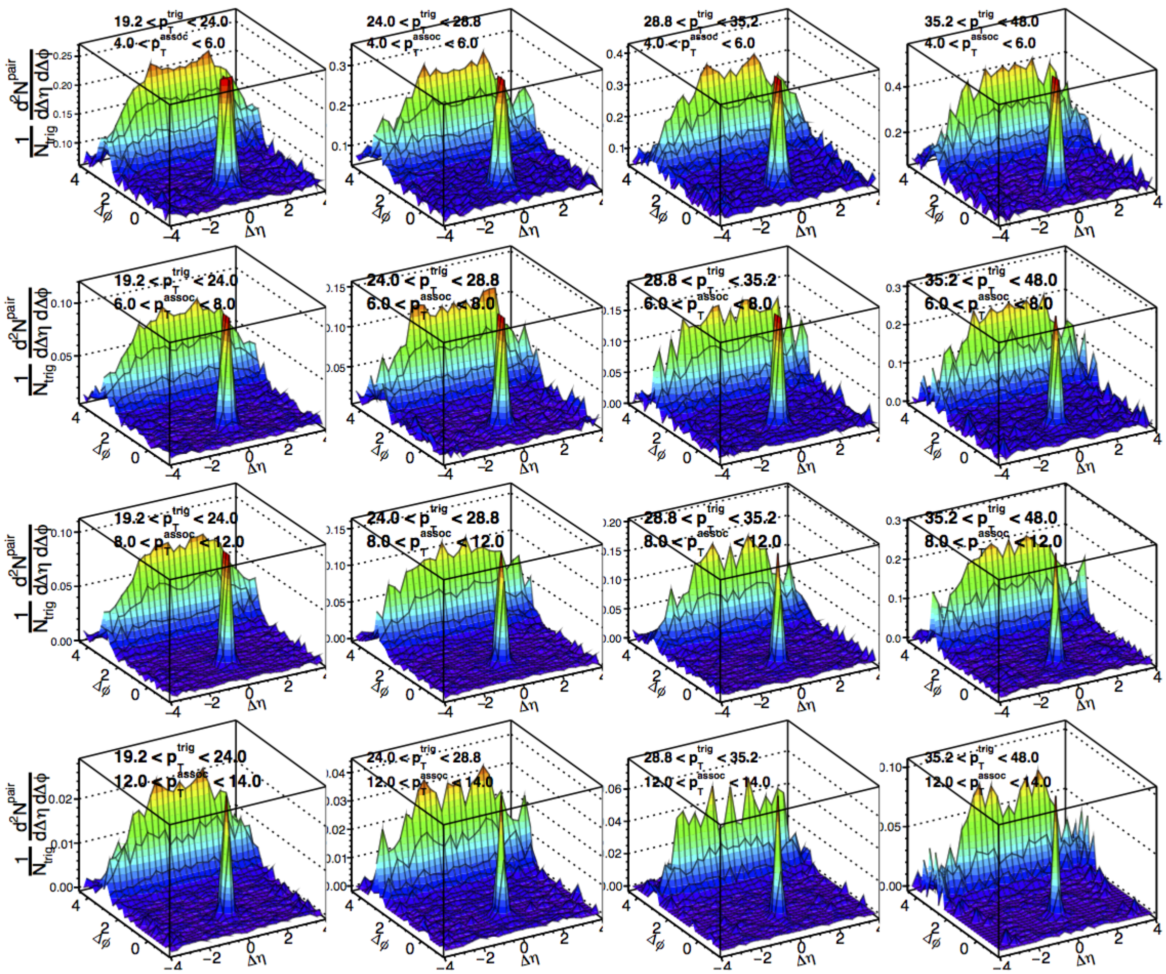

Figure A.22: The 2-D correlation functions as a function of $\Delta\eta$ and $\Delta\phi$ in all four $p_{\mathrm{T}}^{\mathrm{trig}}$ bins and the highest four $p_{\mathrm{T}}^{\mathrm{assc}}$ bins ($4 < p_{\mathrm{T}}^{\mathrm{assc}} < 14$ GeV/c) in the 30-40% most central Pb+Pb collisions. The nearside peak is truncated to highlight the away side jet peak.

A.2.5 Pb+Pb: 40-50% Centrality

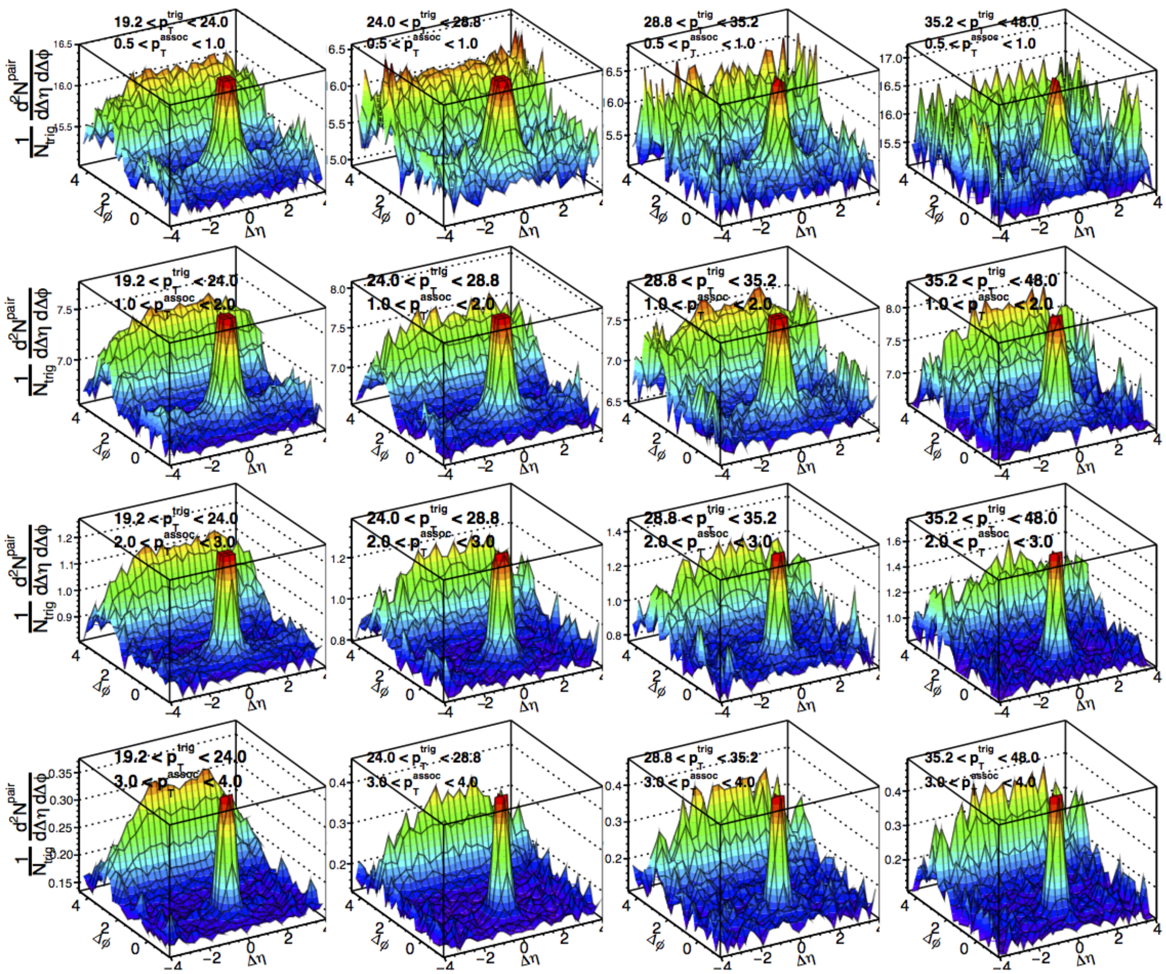

Figure A.23: The 2-D correlation functions as a function of $\Delta\eta$ and $\Delta\phi$ in all four $p_{\mathrm{T}}^{\mathrm{trig}}$ bins and the lowest four $p_{\mathrm{T}}^{\mathrm{assc}}$ bins ($0.5 < p_{\mathrm{T}}^{\mathrm{assc}} < 4$ GeV/c) in the 40-50% most central Pb+Pb collisions. The nearside peak is truncated to highlight the away side jet peak.

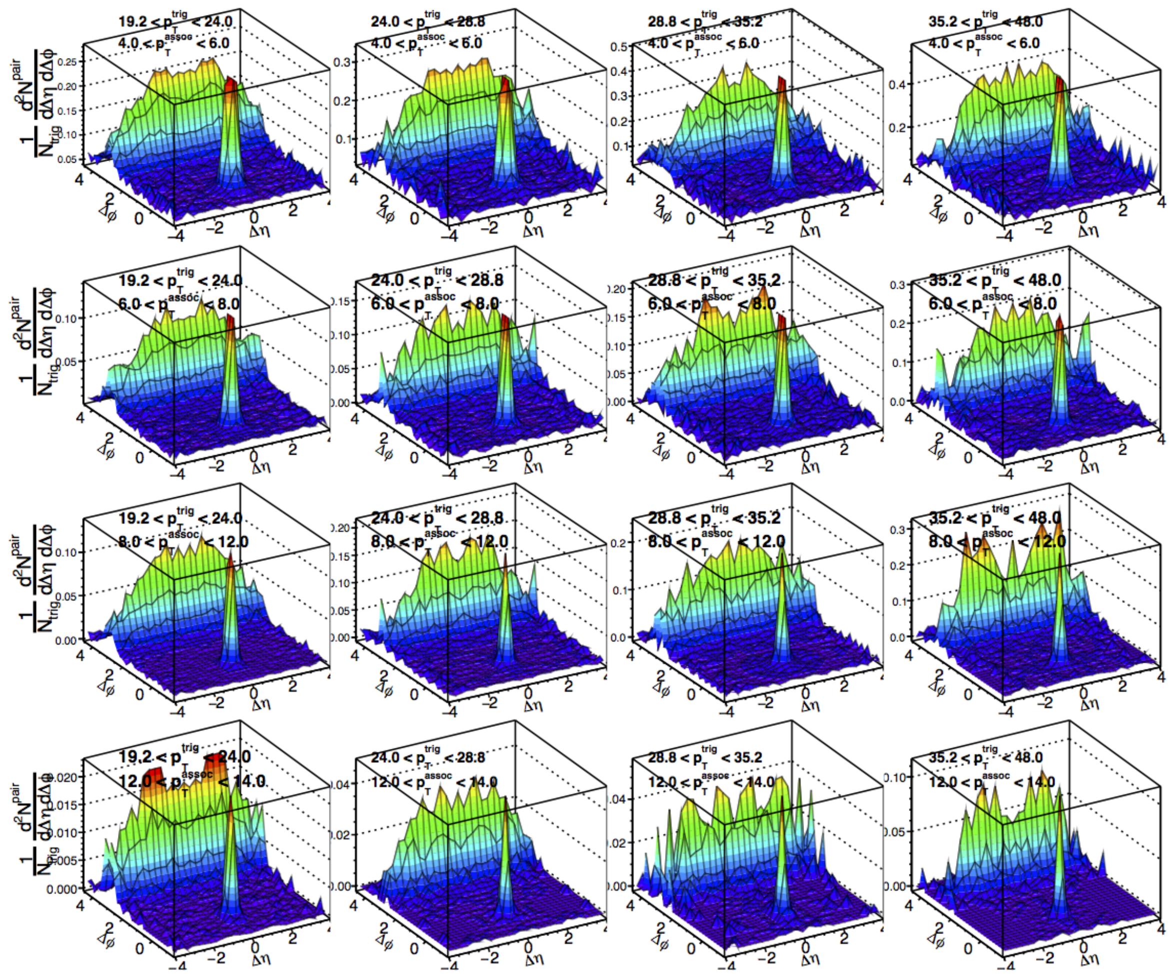

Figure A.24: The 2-D correlation functions as a function of $\Delta\eta$ and $\Delta\phi$ in all four $p_{\mathrm{T}}^{\mathrm{trig}}$ bins and the highest four $p_{\mathrm{T}}^{\mathrm{assc}}$ bins ($4 < p_{\mathrm{T}}^{\mathrm{assc}} < 14$ GeV/c) in the 40-50% most central Pb+Pb collisions. The nearside peak is truncated to highlight the away side jet peak.

A.2.6 Pb+Pb: 50-60% Centrality

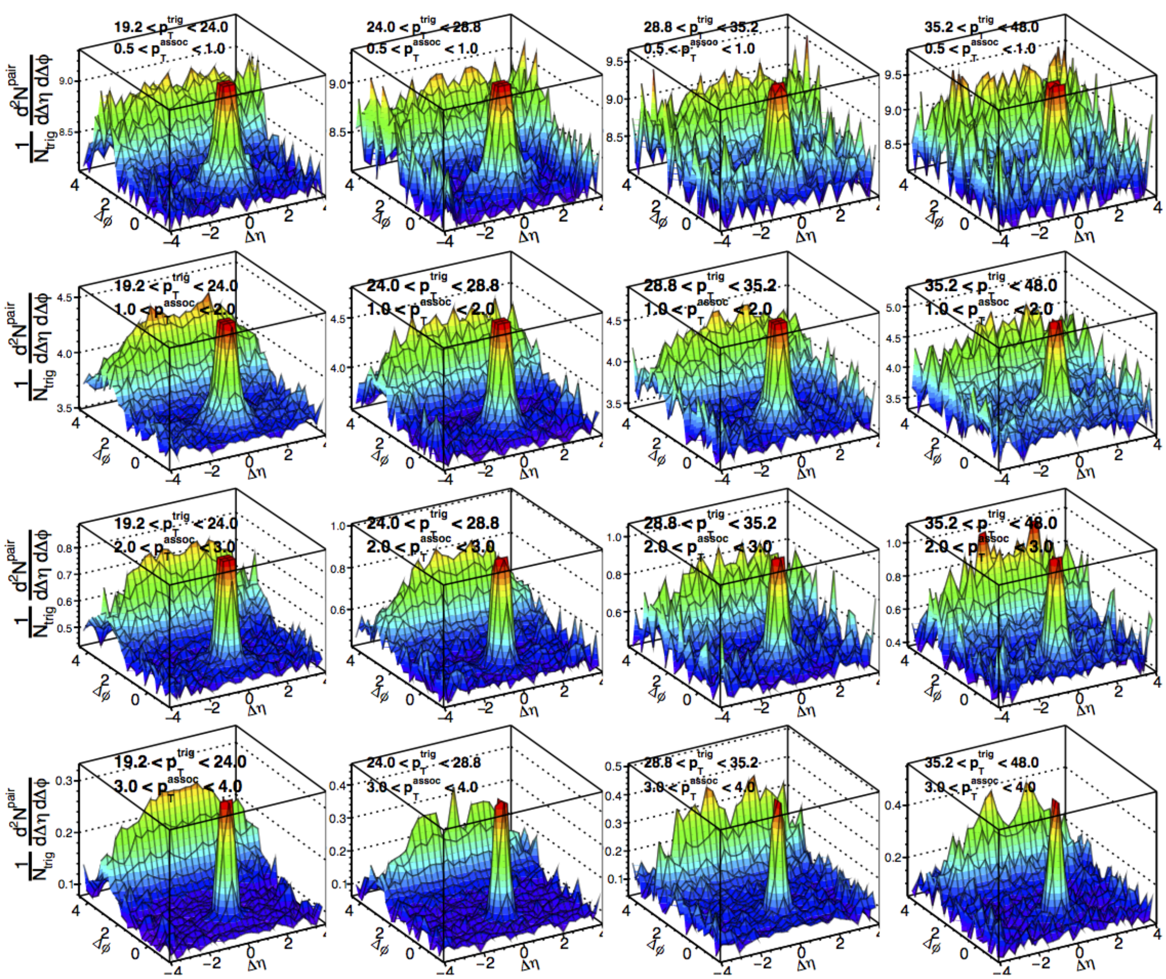

Figure A.25: The 2-D correlation functions as a function of $\Delta\eta$ and $\Delta\phi$ in all four $p_{\mathrm{T}}^{\mathrm{trig}}$ bins and the lowest four $p_{\mathrm{T}}^{\mathrm{assc}}$ bins ($0.5 < p_{\mathrm{T}}^{\mathrm{assc}} < 4$ GeV/c) in the 50-60% most central Pb+Pb collisions. The nearside peak is truncated to highlight the away side jet peak.

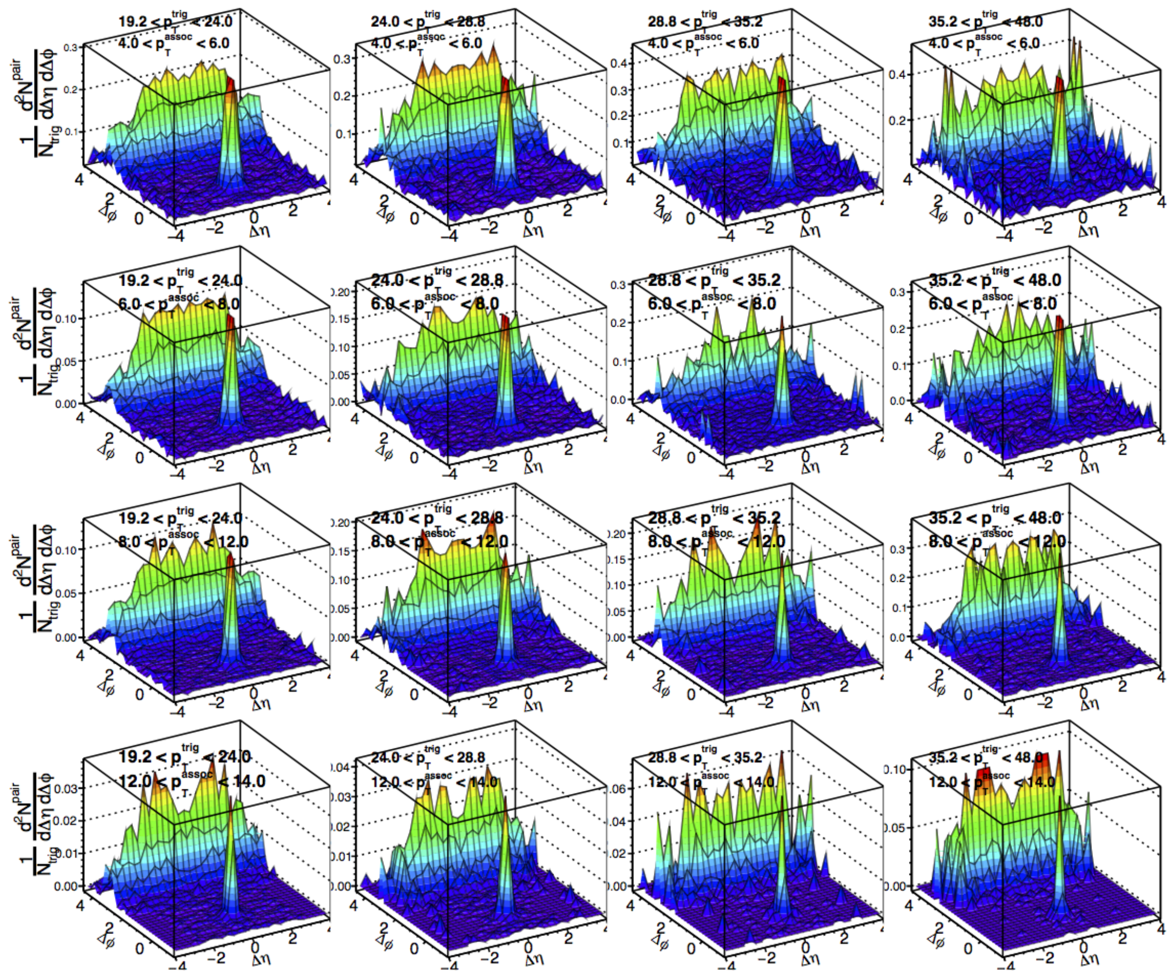

Figure A.26: The 2-D correlation functions as a function of $\Delta\eta$ and $\Delta\phi$ in all four $p_{\mathrm{T}}^{\mathrm{trig}}$ bins and the highest four $p_{\mathrm{T}}^{\mathrm{assc}}$ bins ($4 < p_{\mathrm{T}}^{\mathrm{assc}} < 14$ GeV/c) in the 50-60% most central Pb+Pb collisions. The nearside peak is truncated to highlight the away side jet peak.

A.2.7 $p + p$

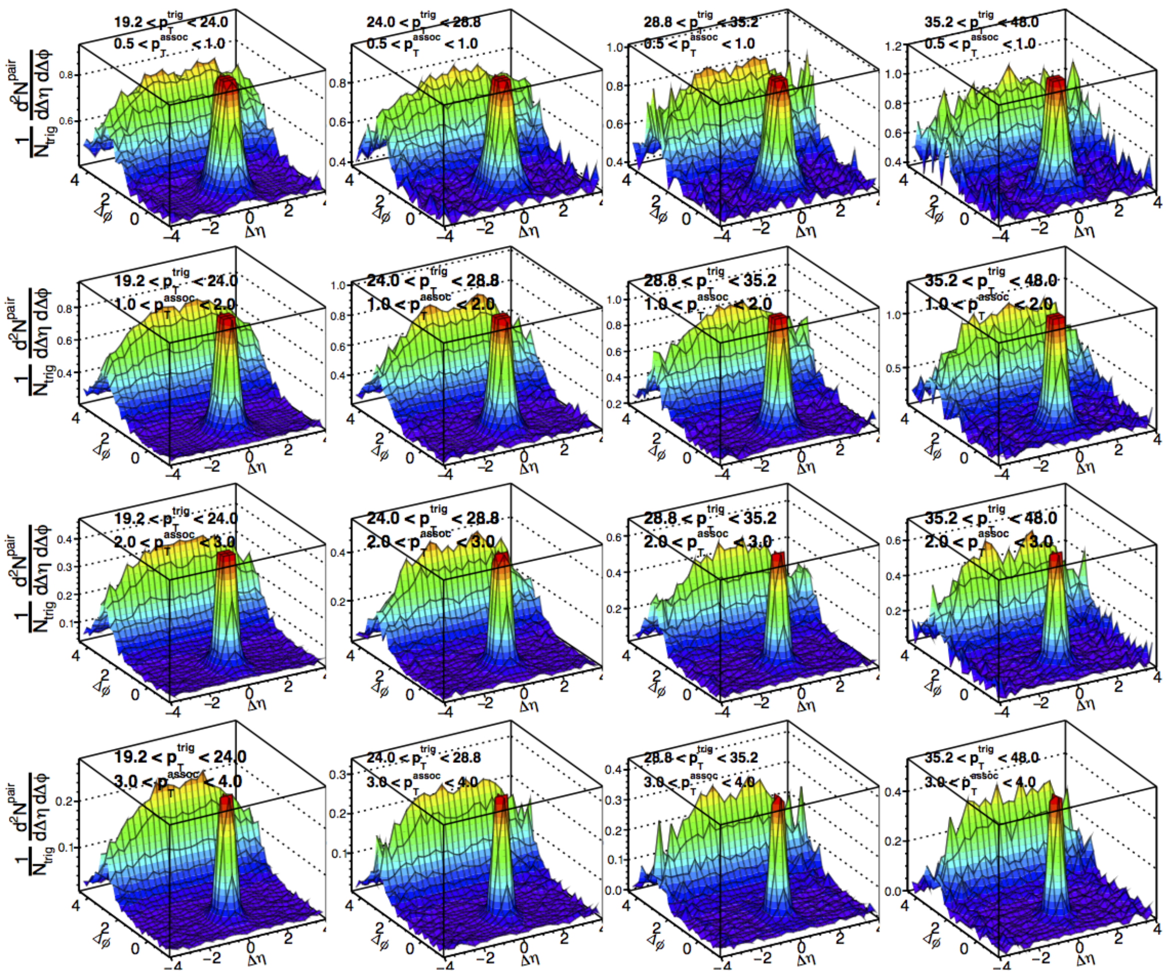

Figure A.27: The 2-D correlation functions as a function of $\Delta\eta$ and $\Delta\phi$ in all four $p_{\mathrm{T}}^{\mathrm{trig}}$ bins and the lowest four $p_{\mathrm{T}}^{\mathrm{assc}}$ bins ($0.5 < p_{\mathrm{T}}^{\mathrm{assc}} < 4$ GeV/c) in $p+p$ collisions. The nearside peak is truncated to highlight the away side jet peak.

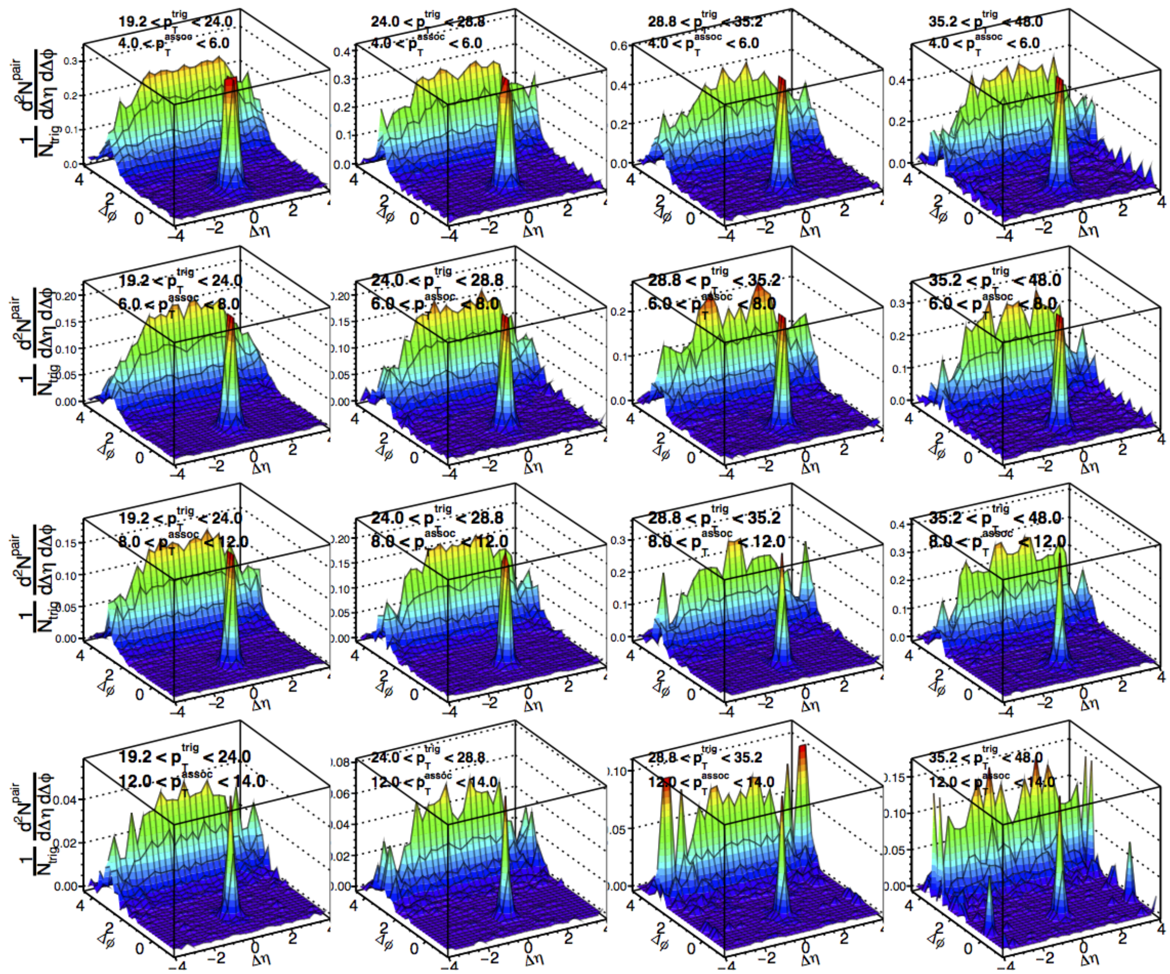

Figure A.28: The 2-D correlation functions as a function of $\Delta\eta$ and $\Delta\phi$ in all four $p_{\mathrm{T}}^{\mathrm{trig}}$ bins and the highest four $p_{\mathrm{T}}^{\mathrm{assc}}$ bins ($4 < p_{\mathrm{T}}^{\mathrm{assc}} < 14$ GeV/c) in $p + p$ collisions. The nearside peak is truncated to highlight the away side jet peak.

Bibliography

[1] Kyle Cranmer, "Quantum Diaries: A fresh look at the standard model." `http://www.quantumdiaries.org/2013/08/19/a-fresh-look-for-the-standard-model/`.

[2] P. W. Higgs, "Broken Symmetries and the Masses of Gauge Bosons," *Phys.Rev.Lett.*, vol. 13, pp. 508–509, 1964.

[3] F. Englert and R. Brout, "Broken Symmetry and the Mass of Gauge Vector Mesons," *Phys.Rev.Lett.*, vol. 13, pp. 321–323, 1964.

[4] The CMS Collaboration, "Observation of a new boson at a mass of 125 GeV with the CMS experiment at the LHC," *Phys. Lett. B*, vol. 716, no. 1, pp. 30 – 61, 2012.

[5] The ATLAS Collaboration, "Observation of a new particle in the search for the Standard Model Higgs boson with the ATLAS detector at the LHC," *Phys. Lett. B*, vol. 716, no. 1, pp. 1 – 29, 2012.

[6] R. Davis, D. S. Harmer, and K. C. Hoffman, "Search for Neutrinos from the Sun," *Phys. Rev. Lett.*, vol. 20, pp. 1205–1209, May 1968.

[7] Q. Ahmad *et al.*, "Measurement of the Rate of $\nu_e + d \to p + p + e^-$ Interactions Produced by ^8B Solar Neutrinos at the Sudbury Neutrino Observatory," *Phys. Rev. Lett.*, vol. 87, p. 071301, Jul 2001.

[8] Y. Fukuda *et al.* , "Evidence for Oscillation of Atmospheric Neutrinos," *Phys. Rev. Lett.*, vol. 81, pp. 1562–1567, Aug 1998.

[9] B. Pontecorvo, "Neutrino Experiments and the Problem of Conservation of Leptonic Charge," *Soviet Journal of Experimental and Theoretical Physics*, vol. 26, p. 984, May 1968.

[10] Z. Maki, M. Nakagawa, and S. Sakata, "Remarks on the Unified Model of Elementary Particles," *Progress of Theoretical Physics*, vol. 28, no. 5, pp. 870–880, 1962.

[11] T. Aoyama, M. Hayakawa, T. Kinoshita, and M. Nio, "Tenth-Order QED Contribution to the Electron $g-2$ and an Improved Value of the Fine Structure Constant," *Phys. Rev. Lett.*, vol. 109, p. 111807, Sep 2012.

[12] Particle Data Group, *Review of Particle Physics*. Philadelphia, USA: IOP Publishing, Inc., 2009. Chapter 9: Quantum Chromodynamics.

[13] R. Vogt, *Ultrarelativistic Heavy-Ion Collisions*. Amsterdam, The Netherlands: Elsevier, first ed., 2007.

[14] W. N. Cottingham and D. A. Greenwood, *An Introduction to the Standard Model of Particle Physics*. Cambridge, UK: Cambridge University Press, 2007.

[15] D. J. Gross and F. Wilczek, "Ultraviolet Behavior of Non-Abelian Gauge Theories," *Phys. Rev. Lett.*, vol. 30, pp. 1343–1346, Jun 1973.

[16] H. D. Politzer, "Reliable Perturbative Results for Strong Interactions?," *Phys. Rev. Lett.*, vol. 30, pp. 1346–1349, Jun 1973.

[17] S. Bethke, "Experimental tests of asymptotic freedom," *Progress in Particle and Nuclear Physics*, vol. 58, no. 2, pp. 351 – 386, 2007.

[18] M. Czakon, "The four-loop QCD β-function and anomalous dimensions," *Nucl. Phys. B*, vol. 710, no. 12, pp. 485 – 498, 2005.

[19] T. van Ritbergen, J. Vermaseren, and S. Larin, "The four-loop β-function in quantum chromodynamics," *Phys. Lett. B*, vol. 400, no. 34, pp. 379 – 384, 1997.

[20] F. Karsch and E. Laermann, "Thermodynamics and in-medium hadron properties from lattice QCD." `http://arxiv.org/abs/hep-lat/0305025`.

[21] The PHENIX Collaboration, "Formation of dense partonic matter in relativistic nucleus-nucleus collisions at RHIC: Experimental evaluation by the PHENIX Collaboration," *Nucl. Phys. A*, vol. 757, no. 12, pp. 184 – 283, 2005. First Three Years of Operation of RHIC.

[22] The STAR Collaboration, "Experimental and theoretical challenges in the search for the quark gluon plasma: The STAR Collaboration's critical assessment of the evidence from RHIC collisions," *Nucl. Phys. A*, vol. 757, no. 12, pp. 102 – 183, 2005. First Three Years of Operation of RHIC.

[23] The PHOBOS Collaborations, "The PHOBOS perspective on discoveries at RHIC," *Nucl. Phys. A*, vol. 757, no. 12, pp. 28 – 101, 2005. First Three Years of Operation of RHIC.

[24] The BRAHMS Collaboration, "Quark gluon plasma and color glass condensate at RHIC? The perspective from the BRAHMS experiment," *Nucl. Phys. A*, vol. 757, no. 12, pp. 1 – 27, 2005. First Three Years of Operation of RHIC.

[25] M. L. Miller, K. Reygers, S. J. Sanders, and P. Steinberg, "Glauber Modeling in High-Energy Nuclear Collisions," *Annual Review of Nuclear and Particle Science*, vol. 57, no. 1, pp. 205–243, 2007.

[26] J. Uphoff, F. Senzel, O. Fochler, C. Wesp, Z. Xu, and C. Greiner, "Elliptic Flow and Nuclear Modification Factor in Ultrarelativistic Heavy-Ion Collisions within a Partonic Transport Model," *Phys. Rev. Lett.*, vol. 114, p. 112301, Mar 2015.

[27] R. C. Hwa and X.-N. Wang, *Quark-Gluon Plasma*. Singapore: World Scientific, fourth ed., 2010.

[28] The CMS Collaboration, "Study of high-p_{T} charged particle suppression in Pb+Pb compared to $p+p$ collisions at $\sqrt{s_{NN}} = 2.76$ TeV," *EPJ C*, vol. 72, no. 3, 2012.

[29] University of Tokyo, "Quark Gluon Plasma." `http://qcdmof.cns.s.u-tokyo.ac.jp/index.php?Quark%20Gluon%20Plasma`.

[30] P. Romatschke and U. Romatschke, "Viscosity Information from Relativistic Nuclear Collisions: How Perfect is the Fluid Observed at RHIC?," *Phys. Rev. Lett.*, vol. 99, p. 172301, Oct 2007.

[31] J.-Y. Ollitrault, "Anisotropy as a signature of transverse collective flow," *Phys. Rev. D*, vol. 46, pp. 229–245, Jul 1992.

[32] A. M. Poskanzer and S. A. Voloshin, "Methods for analyzing anisotropic flow in relativistic nuclear collisions," *Phys. Rev. C*, vol. 58, pp. 1671–1678, Sep 1998.

[33] The STAR Collaboration, "Azimuthal anisotropy in Au+Au collisions at $\sqrt{s_{NN}} = 200$ GeV," *Phys. Rev. C*, vol. 72, p. 014904, Jul 2005.

[34] The CMS Collaboration, "Azimuthal anisotropy of charged hadrons in Pb+Pb collisions at $\sqrt{s_{NN}} = 2.76$ TeV," Tech. Rep. CMS-AN-10-394, CERN, 2010.

[35] David d'Enterria, "Jet Quenching." `http://arxiv.org/abs/0902.2011v2`.

[36] J. Bjorken, "Energy Loss of Energetic Partons in Quark - Gluon Plasma: Possible Extinction of High p_{T} Jets in Hadron - Hadron Collisions," 1982.

[37] American Physical Society, "Viewpoint: The Stopping Power of Hot Nuclear Matter." `http://physics.aps.org/articles/v7/97?referer=rss`.

[38] The CMS Collaboration, "Observation and studies of jet quenching in Pb+Pb collisions at $\sqrt{s_{NN}} = 2.76$ TeV," *Phys. Rev. C*, vol. 84, p. 024906, Aug 2011.

[39] The CMS Collaboration, "Jet momentum dependence of jet quenching in Pb+Pb collisions at $\sqrt{s_{NN}} = 2.76$ TeV," *Phys. Lett. B*, vol. 712, no. 3, pp. 176 – 197, 2012.

[40] The CMS Collaboration, "CMS HI Public Twiki: Approved Raa Zoo Plots." `https://twiki.cern.ch/twiki/bin/view/CMSPublic/HIRaaCompilation`.

[41] The CMS Collaboration, "Evidence of b-Jet Quenching in PbPb Collisions at $\sqrt{s_{NN}} = 2.76$ TeV," *Phys. Rev. Lett.*, vol. 113, p. 132301, Sep 2014.

[42] The CMS Collaboration, "Measurement of isolated photon production in pp and PbPb collisions at $\sqrt{s_{NN}} = 2.76$ TeV," *Phys. Lett. B*, vol. 710, no. 2, pp. 256 – 277, 2012.

[43] The CMS Collaboration, "Study of W boson production in PbPb and pp collisions at $\sqrt{s_{NN}} = 2.76$ TeV," *Phys. Lett. B*, vol. 715, no. 13, pp. 66 – 87, 2012.

[44] The CMS Collaboration, "Study of Z production in Pb+Pb and $p + p$ collisions at $\sqrt{s_{NN}} = 2.76$ TeV in the dimuon and dielectron decay channels," *JHEP*, vol. 2015, no. 3, 2015.

[45] The CMS Collaboration, "Suppression of non-prompt J/Ψ, prompt J/Ψ, and Υ (1S) in Pb+Pb collisions at $\sqrt{s_{NN}} = 2.76$ TeV," *JHEP*, vol. 2012, no. 5, 2012.

[46] The STAR Collaboration, "Evidence from $d+$Au Measurements for Final-State Suppression of High-p_T Hadrons in Au + Au Collisions at RHIC," *Phys. Rev. Lett.*, vol. 91, p. 072304, Aug 2003.

[47] The CMS Collaboration, "Centrality dependence of dihadron correlations and azimuthal anisotropy harmonics in Pb+Pb collisions at $\sqrt{s_{NN}} = 2.76$ TeV," *EPJ C*, vol. 72, no. 5, 2012.

[48] B. Alver and G. Roland, "Collision-geometry fluctuations and triangular flow in heavy-ion collisions," *Phys. Rev. C*, vol. 81, p. 054905, May 2010.

[49] The CMS Collaboration, "Observation of long-range, near-side angular correlations in proton-proton collisions at the LHC," *JHEP*, vol. 2010, no. 9, 2010.

[50] The CMS Collaboration, "Observation of long-range, near-side angular correlations in pPb collisions at the LHC," *Phys. Lett. B*, vol. 718, no. 3, pp. 795 – 814, 2013.

[51] The CMS Collaboration, "Multiplicity and transverse momentum dependence of two- and four-particle correlations in pPb and PbPb collisions," *Phys. Lett. B*, vol. 724, no. 45, pp. 213 – 240, 2013.

[52] The ATLAS Collaboration, "Measurement with the ATLAS detector of multi-particle azimuthal correlations in collisions at $\sqrt{s_{NN}} = 2.76$ TeV," *Phys. Lett. B*, vol. 725, no. 13, pp. 60 – 78, 2013.

[53] L. Evans and P. Bryant, "LHC Machine," *Journal of Instrumentation*, vol. 3, no. 08, p. S08001, 2008.

[54] CERN, "The Large Hadron Collider." `http://home.web.cern.ch/topics/large-hadron-collider`.

[55] S. MYERS, "The Large Hadron Collider 2008-2013," *International Journal of Modern Physics A*, vol. 28, no. 25, p. 1330035, 2013.

[56] SLAC Today, "The Large Hadron Collider." `https://news.slac.stanford.edu/image/large-hadron-collider`.

[57] The UA1 Collaboration, "Experimental observation of isolated large transverse energy electrons with associated missing energy at $\sqrt{s} = 540$ GeV," *Phys. Lett. B*, vol. 122, no. 1, pp. 103 – 116, 1983.

[58] The UA2 Collaboration, "Observation of single isolated electrons of high transverse momentum in events with missing transverse energy at the CERN $p + p$ collider," *Phys. Lett. B*, vol. 122, no. 56, pp. 476 – 485, 1983.

[59] Symmetry Magazine, "The skinny on the LHC's heavy ions." `http://www.symmetrymagazine.org/breaking/2010/11/05/the-skinny-on-the-lhcs-heavy-ions`.

[60] The CMS Collaboration, "The CMS experiment at the CERN LHC," *JINST*, vol. 3, p. S08004, 2008.

[61] The CMS Collaboration, "The CMS Detector Overview." `http://cms.web.cern.ch/news/detector-overview`.

[62] CERN Publications, "Building a crystal palace. Le palais de cristal," p. 2, Oct 2007.

[63] M. Brice, L. Vaillet, and L. Lazic, "Images of the CMS HCAL Barrel (HB)." CMS Collection., Nov 2008.

[64] J. R. Vlimant, "Track Reconstruction with the CMS Tracking Detector," tech. rep., UC Santa Barbara, 2007.

[65] The CMS Collaboration, "The CMS Detector Superconducting Magnet." `http://cms.web.cern.ch/news/superconducting-magnet`.

[66] inSPIRE HEP, "CERN Accelerator Complex." `https://inspirehep.net/record/1236817/plots`.

[67] D. E. Groom, N. V. Mokhov, and S. I. Striganov, "Muon Stopping Power and Range," *Atomic Data and Nuclear Data Tables*, vol. 76, July 2001.

[68] *The CMS hadron calorimeter project: Technical Design Report.* Technical Design Report CMS, Geneva: CERN, 1997.

[69] The CMS Collaboration, "The CMS Tracker Detector." `http://cms.web.cern.ch/news/tracker-detector`.

[70] V. Karimki, M. Mannelli, P. Siegrist, H. Breuker, A. Caner, R. Castaldi, K. Freudenreich, G. Hall, R. Horisberger, M. Huhtinen, and A. Cattai, *The CMS tracker system project: Technical Design Report.* Technical Design Report CMS, Geneva: CERN, 1997.

[71] V. Karimki, M. Mannelli, P. Siegrist, H. Breuker, A. Caner, R. Castaldi, K. Freudenreich, G. Hall, R. Horisberger, M. Huhtinen, and A. Cattai, *The CMS tracker system project: Technical Design Report.* Technical Design Report CMS, Geneva: CERN, 1997.

[72] The CMS Collaboration, "The CMS Detector Silicon Strips." `http://cms.web.cern.ch/news/silicon-pixels`.

[73] O. Djuvsland and J. Nystrand, "Single and double photonuclear excitations in Pb+Pb collisions at $\sqrt{s_{NN}} = 2.76$ TeV at the CERN Large Hadron Collider," *Phys. Rev. C*, vol. 83, p. 041901, Apr 2011.

[74] The CMS Collaboration, "Transverse-Momentum and Pseudorapidity Distributions of Charged Hadrons in $p+p$ Collisions at $\sqrt{s}=7$ TeV," *Phys. Rev. Lett.*, vol. 105, p. 022002, Jul 2010.

[75] The CMS Collaboration, "Transverse-momentum and pseudorapidity distributions of charged hadrons in $p+p$ collisions at $\sqrt{s}=0.9$ and 2.36 TeV," *JHEP*, vol. 2010, no. 2, 2010.

[76] The CMS Collaboration, "Azimuthal anisotropy of charged hadrons at high transverse momentum in Pb+Pb collisions at $\sqrt{s_{NN}}=2.76$ TeV," Tech. Rep. CMS-AN-11-436, CERN, 2011.

[77] The CMS Collaboration, "Azimuthal Anisotropy of Charged Particles at High Transverse Momenta in Pb+Pb Collisions at $\sqrt{s_{NN}}$=2.76 TeV," *Phys. Rev. Lett.*, vol. 109, p. 022301, Jul 2012.

[78] The CMS Collaboration, "Dependence on pseudorapidity and on centrality of charged hadron production in Pb+Pb collisions at $\sqrt{s_{NN}}=2.76$ TeV," *JHEP*, vol. 2011, no. 8, 2011.

[79] The CMS Collaboration, "Track reconstruction in the CMS tracker," Tech. Rep. CMS Note NOTE-2006-041, CERN, 2006.

[80] The CMS Collaboration, "Description and performance of track and primary-vertex reconstruction with the CMS tracker," *Journal of Instrumentation*, vol. 9, no. 10, p. P10009, 2014.

[81] The CMS Collaboration, "CMS tracking performance results from early LHC operation," *EPJ C*, vol. 70, no. 4, pp. 1165–1192, 2010.

[82] The CMS Collaboration, "Measurement of the elliptic anisotropy of charged particles produced in Pb+Pb collisions at $\sqrt{s_{NN}}=2.76$ TeV," *Phys. Rev. C*, vol. 87, p. 014902, Jan 2013.

[83] I. Lokhtin and A. Snigirev, "A model of jet quenching in ultrarelativistic heavy ion collisionsand high-p_{T} hadron spectra at RHIC," *EPJ C*, vol. 45, no. 1, pp. 211–217, 2006.

[84] T. Sjstrand, S. Mrenna, and P. Skands, "A brief introduction to PYTHIA 8.1," *Computer Physics Communications*, vol. 178, no. 11, pp. 852 – 867, 2008.

[85] S. Agostinelli *et al.*, "Geant4 simulation toolkit," *Nuclear Instruments and Methods in Physics Research Section A: Accelerators, Spectrometers, Detectors and Associated Equipment*, vol. 506, no. 3, pp. 250 – 303, 2003.

[86] The CMS Collaboration, "Very high-p_{T} triggered dihadron correlations in Pb+Pb and pp collisions at $\sqrt{s_{NN}} = 2.76$ TeV," Tech. Rep. CMS-PAS-HIN-12-010, CERN, Geneva, 2012.

[87] The ALICE Collaboration, "Measurement of event background fluctuations for charged particle jet reconstruction in Pb+Pb collisions at $\sqrt{s_{NN}} = 2.76$ TeV," *JHEP*, vol. 2012, no. 3, 2012.

[88] The CMS Collaboration, "Long-range and short-range dihadron angular correlations in central Pb+Pb collisions at $\sqrt{s_{NN}} = 2.76$ TeV," *JHEP*, vol. 2011, no. 7, 2011.

[89] The CMS Collaboration, "Observation of long-range, near-side angular correlations in proton-proton collisions at the LHC," *JHEP*, vol. 2010, no. 9, 2010.

[90] B. H. Alver, C. Gombeaud, M. Luzum, and J.-Y. Ollitrault, "Triangular flow in hydrodynamics and transport theory," *Phys. Rev. C*, vol. 82, p. 034913, Sep 2010.

[91] B. Schenke, S. Jeon, and C. Gale, "Elliptic and Triangular Flow in Event-by-Event D $= 3+1$ Viscous Hydrodynamics," *Phys. Rev. Lett.*, vol. 106, p. 042301, Jan 2011.

[92] D. Teaney and L. Yan, "Triangularity and dipole asymmetry in relativistic heavy ion collisions," *Phys. Rev. C*, vol. 83, p. 064904, Jun 2011.

[93] H. Petersen, G.-Y. Qin, S. A. Bass, and B. Müller, "Triangular flow in event-by-event ideal hydrodynamics in Au+Au collisions at $\sqrt{s_{NN}} = 200A$ GeV," *Phys. Rev. C*, vol. 82, p. 041901, Oct 2010.

[94] J. Xu and C. M. Ko, "Effects of triangular flow on di-hadron azimuthal correlations in relativistic heavy ion collisions," *Phys. Rev. C*, vol. 83, p. 021903, Feb 2011.

[95] S. Voloshin and Y. Zhang, “Flow study in relativistic nuclear collisions by Fourier expansion of azimuthal particle distributions,” *Zeitschrift fr Physik C Particles and Fields*, vol. 70, no. 4, pp. 665–671, 1996.

[96] The ALICE Collaboration, “Harmonic decomposition of two particle angular correlations in Pb+Pb collisions at $\sqrt{s_{NN}} = 2.76$ TeV,” *Phys. Lett. B*, vol. 708, no. 35, pp. 249 – 264, 2012.

[97] The CMS Collaboration, “Measurement of higher-order harmonic azimuthal anisotropy in Pb+Pb collisions at $\sqrt{s_{NN}} = 2.76$ TeV,” *Phys. Rev. C*, vol. 89, p. 044906, Apr 2014.

[98] N. N. Ajitanand, J. M. Alexander, P. Chung, W. G. Holzmann, M. Issah, R. A. Lacey, A. Shevel, A. Taranenko, and P. Danielewicz, “Decomposition of harmonic and jet contributions to particle-pair correlations at ultrarelativistic energies,” *Phys. Rev. C*, vol. 72, p. 011902, Jul 2005.

[99] T. A. Trainor, “Zero yield at minimum (ZYAM) method and v_2: Underestimating jet yields from dihadron azimuth correlations,” *Phys. Rev. C*, vol. 81, p. 014905, Jan 2010.

[100] The ALICE Collaboration, “Particle-Yield Modification in Jetlike Azimuthal Dihadron Correlations in Pb+Pb Collisions at $\sqrt{s_{\mathrm{NN}}} = 2.76$ TeV,” *Phys. Rev. Lett.*, vol. 108, p. 092301, Mar 2012.

[101] S. Peign and A. V. Smilga, “Energy losses in relativistic plasmas: QCD versus QED,” *Physics-Uspekhi*, vol. 52, no. 7, p. 659, 2009.

[102] J. Jia, W. A. Horowitz, and J. Liao, “Correlations between jet-quenching observables at energies available at the BNL Relativistic Heavy Ion Collider,” *Phys. Rev. C*, vol. 84, p. 034904, Sep 2011.

[103] B. Betz, M. Gyulassy, and G. Torrieri, “Fourier harmonics of high-p_T particles probing the fluctuating initial condition geometries in heavy-ion collisions,” *Phys. Rev. C*, vol. 84, p. 024913, Aug 2011.

[104] J. Jia and R. Wei, “Dissecting the role of initial collision geometry for jet quenching observables in relativistic heavy ion collisions,” *Phys. Rev. C*, vol. 82, p. 024902, Aug 2010.

[105] S. Wicks, W. Horowitz, M. Djordjevic, and M. Gyulassy, “Elastic, inelastic, and path length fluctuations in jet tomography,” *Nucl. Phys. A*, vol. 784, no. 14, pp. 426 – 442, 2007.

[106] T. Renk, “Path-length dependence of energy loss within in-medium showers,” *Phys. Rev. C*, vol. 83, p. 024908, Feb 2011.

[107] The PHENIX Collaboration, “Azimuthal Anisotropy of π^0 Production in Au + Au Collisions at $\sqrt{s_{NN}} = 200$ GeV: Path-Length Dependence of Jet Quenching and the Role of Initial Geometry,” *Phys. Rev. Lett.*, vol. 105, p. 142301, Sep 2010.

[108] B. Alver *et al.*, “Importance of correlations and fluctuations on the initial source eccentricity in high-energy nucleus-nucleus collisions,” *Phys. Rev. C*, vol. 77, p. 014906, Jan 2008.

[109] A. Ohlson, “Jet-hadron correlations in STAR,” *J. Phys. Conf. Ser.*, vol. 316, p. 012015, 2011.

[110] The Alice Collaboration, “Nuclear modification of hadron production measured by ALICE,” *J. Phys. Conf. Ser.*, vol. 381, no. 1, p. 012040, 2012.

[111] T. Renk and K. J. Eskola, “Hard dihadron correlations in heavy-ion collisions at RHIC and LHC.” `http://arxiv.org/pdf/1106.1740v2.pdf`.

[112] H. Zhang, J. F. Owens, E. Wang, and X.-N. Wang, “Dihadron Tomography of High-Energy Nuclear Collisions in Next-to-Leading Order Perturbative QCD,” *Phys. Rev. Lett.*, vol. 98, p. 212301, May 2007.

[113] R. Baier, Y. Dokshitzer, A. Mueller, S. Peign, and D. Schiff, “Radiative energy loss and p-broadening of high energy partons in nuclei,” *Nucl. Phys. B*, vol. 484, no. 12, pp. 265 – 282, 1997.